ABSTRACT

Title of Document: UNDERSTANDING AND TUNING NANOSTRUCTURED MATERIALS FOR CHEMICAL ENERGY CONVERSION

Guoqiang Jian, Doctor of Philosophy, 2014

Directed By: Professor Michael R. Zachariah, Department of Chemical and Biomolecular Engineering and Department of Chemistry and Biochemistry

The conversion of energy that employs chemical reaction is termed chemical energy conversion. In my dissertation, I have focused on chemical energy conversion systems involving energetic materials and lithium ion batteries, where performance is strongly dependent on the properties of materials and their architecture. The objective of this study is to enhance our understanding and tuning of nanostructured materials that might find application toward energetic materials and electrode materials in lithium ion batteries.

Rapid heating diagnostics tools, i.e. temperature-jump techniques, have been used to study the ignition of aluminum nanoparticles, nanothermite reaction mechanism and metal oxides nanoparticles decomposition under rapid heating conditions (~$10^5$-$10^6$ K/s). Time-resolved mass spectra results support the hypothesis that Al containing species diffuse outwards through the oxide shell. Low effective activation

energies were found for metal oxides nanoparticles decomposition at high heating rates, implying the mass transfer control at high heating rates. The role of oxygen release from oxidizer in nanothermite reactions have been examined for several different systems, including some using microsized oxidizer (i.e., nano-Al/micro-$I_2O_5$). In particular, for periodate based nanothermites, direct evidence from high heating rate SEM and mass spectrometry results support that direct gas phase oxygen release from oxidizer decomposition is critical in its ignition and combustion.

Efforts have also been made to synthesize nanostructured materials for nanoenergetic materials and lithium ion batteries applications. Hollow CuO spheres were synthesized by aerosol spray pyrolysis, employing a gas blowing mechanism for the formation of hollow structure during aerosol synthesis. The materials synthesized as oxidizers in nanothermite demonstrated superior performance, and of particular note, periodate salts based nanothermite demonstrated the best gas generating performance for nanothermite materials. Energetic composite nanofibrous mats (NC/Al-CuO, NC/Al-$Fe_2O_3$, and NC/Al-$Bi_2O_3$) were also prepared by an electrospinning method and evaluated for their combustion performance.

Aerosol spray pyrolysis was employed to produce carbon coated CuO hollow spheres, $Mn_3O_4$ hollow spheres, and $Fe_2O_3$ mesoporous spheres. These hollow/mesoporous spheres demonstrated superior electrochemical performance when used as anode materials in lithium ion batteries. The effects of the amorphous and crystal structures on the electrochemical performance and the structure evolution during electrochemical tests were also investigated.

# UNDERSTANDING AND TUNING NANOSTRUCTURED MATERIALS FOR CHEMICAL ENERGY CONVERSION

By

Guoqiang Jian

Dissertation submitted to the Faculty of the Graduate School of the
University of Maryland, College Park, in partial fulfillment
of the requirements for the degree of
Doctor of Philosophy
2014

Advisory Committee:
Professor Michael R. Zachariah, Chair
Professor Janice Reutt-Robey
Professor Bryan W. Eichhorn
Professor Zhihong Nie
Professor John Cumings, Dean's Representative

*"It is not enough to be industrious; so are the ants. What are you industrious about?"*

[*Letter to Harrison Gray Otis Blake*; November 16, 1857]

***— Henry David Thoreau***

# Dedication

To

My parents

Lin Jian and Yali Li,

And my wife

Ji An.

谨以此文献给我的父亲蹇林，母亲李亚利和我的妻子安冀。

Thank you for your unconditional love and support.

谢谢你们对我无条件的爱和支持。

# Acknowledgements

It is a great pleasure to thank those who made this dissertation possible.

First and foremost, I would like to gratefully thank my advisor, Dr. Michael Zachariah, for his invaluable encouragement, continuous support and careful guidance throughout my PhD study. I feel so fortunate for being his student and getting a chance to learn from his insights, experiences and professionalism. Everything he has taught me and all I have learned from him has been some of the most valuable assets throughout my life. I am grateful for everything Dr. Zachariah has done for me from the bottom of my heart.

I would also like to thank Professor Janice Reutt-Robey, Professor Bryan Eichhorn and Professor Zhihong Nie for serving on my advisory committee and giving me very helpful suggestions on my research. I must particularly thank Professor Janice Reutt-Robey. Her suggestion on the temperature probe system, the most critical element in my experimental setup, has been a major contribution to my first first-author work during my PhD study (Chapter 3). I am also grateful for Professor John Cumings for having agreed to serve on my committee. Special thanks also go to Professor Chunsheng Wang for his advice and suggestions on projects related to lithium ion batteries.

I would like to thank Dr. Yunhua Xu, with whom I collaborated with on the lithium ion batteries work. He did almost all of the electrochemical characterization in Chapter 9 and 10. In the last two years, we had a lot of discussions on how to better improve battery performance and I must admit, I learned a lot about batteries from him. I would also like to thank Dr. Shi Yan for teaching me how to use the

electrospinning setup. He also contributed to some parts of the work described in Chapter 8.

I would like to thank Dr. Lei Zhou, who mentored me in the first two years of my PhD study. I learned so much from his knowledge and experience on temperature-jump and high vacuum systems. I am also very grateful for his advice and help in my personal life and career development. My wife and I also owe a special thanks to him for serving as the witness in our wedding.

I must also thank all members of the Zachariah group for both contributing to the work presented in this dissertation and making my graduate study here an enjoyable experience. Special thanks go to Dr. Nichloas Piekiel, Dr. Snehaunshu Chowdbury, Lu Liu, Jeffery DeLisio, Garth Egan and Rohit Jacob, with whom I have had the great pleasure of collaborative work. In particular, I thank the help of Jeffery DeLisio for the language editing done with short notice. My thanks also go to Dr. Li-Chung Lai for assistance in electron microscopy, Dr. Greg Young and Jing Li for help in various samples tests, and Jack Touart for his help in electronics troubleshooting.

Last but definitely not least, I would like to thank my family for all their love and support. I am indebted to my parents for raising me and supporting me in all my pursuits. Most importantly, I am very grateful to my wife, Ji An, for her love, support and sacrifice. I believe she would be the one, if there is only one person who has faith with me on finishing my PhD. Thank you.

Guoqiang Jian
蹇国强

# Table of Contents

# List of Tables

# List of Figures

# List of Abbreviations

| | |
|---|---|
| SEM | Scanning Electron Microscopy |
| TEM | Transmission Electron Microscopy |
| HR | High Resolution |
| DTEM | Dynamic Transmission Electron Microscopy |
| SAED | Selected Area Electron Diffraction |
| EDS/EDX | Energy Dispersive X-ray Spectrometer |
| XRD | X-ray Diffraction |
| T-Jump | Temperature Jump |
| FTIR | Fourier Transform Infrared Spectroscopy |
| TOF | Time-of-Flight |
| TOFMS | Time-of-Flight Mass Spectrometer |
| MCP | Microchannel Plates |
| PMT | Photomultiplier Tube |
| FWHM | Full Width at Half Maximum |
| TGA | Thermogravimetry Analysis |
| DSC | Differential Scanning Calorimetry |
| DTA | Differential Thermal Analysis |
| BET | Brunauer-Emmett-Teller |
| DMA | Differential Mobility Analyzer |
| CPC | Condensation Particle Counter |
| MEMS/NEMS | Micro-/Nanoelectromechanical Systems |
| CCD | Charge-Coupled Device |

| | |
|---|---|
| CW | Continuous Wave |
| CEA | Chemical Equilibrium with Applications |
| MD | Molecular Dynamics |
| NIST | National Institute of Standards and Technology |
| APS | Advanced Photon Source |
| LLNL | Lawrence Livermore National Laboratory |
| JCPDS | Joint Committee on Powder Diffraction Standards |
| n-Al | Nanoaluminum |
| Al-NPs | Aluminum Nanoparticles |
| RDX | Cyclotrimethylenetrinitramine |
| TNT | 2, 4, 6-trinitrotoluene |
| NC | Nitrocellulose |
| MIC | Metastable Intermolecular Composites |
| ESD | Electrostatic Discharge |
| BOE | Bureau of Explosives |
| LIBs | Lithium Ion Batteries |
| CNTs | Carbon Nanotubes |
| CMC | Soidium Carboxymethyl Cellulose |
| EC/DEC | Ethylene Carbonate/Diethyl Carbonate |
| SEI | Solid-electrolyte Interface |
| CV | Cyclic Voltammogram |
| GITT | Galvanostatic Intermittent Titration Technique |
| SOD | State of Discharge |

# Chapter 1: Introduction

*"Energy cannot be created or destroyed, it can only be changed from one form to another."*

*—Albert Einstein*

## *1.1. Chemical Energy Conversion*

Chemical energy is a form of potential energy that is either stored or can be transformed to other forms of energy through a chemical reaction. Changes in the chemical energy of a system are commonly characterized through changes in the potential energy, as shown in Figure 1.1.

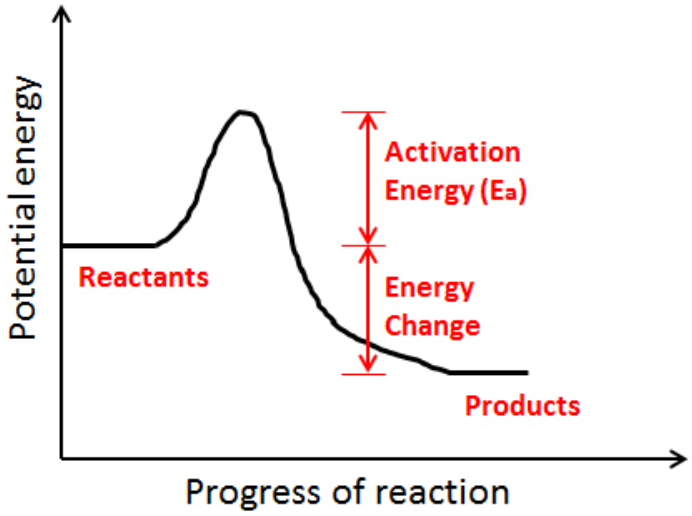


**Figure 1.1.** The potential energy diagram for an exothermic reaction.

All chemical reactions involve changes in potential energy, which can be transferred from or to several different types of energy (Figure 1.2). An example is

the explosive reaction of an energetic organic molecule, e.g., TNT, in which the energy stored in chemical bonds is transformed into thermal energy (heat) and mechanical energy (blast waves). In some chemical reactions, such as electrochemical reactions, there exist reversible transformations between electrical energy and chemical energy. Rechargeable batteries, e.g., lithium ion batteries, are batteries that feature these reversible electrochemical reactions, thus are capable of transforming electrical energy into or from chemical energy (Figure 1.2). Because the conversion of energy utilizes a chemical reaction, energy release/conversion rate in chemical energy conversion is directly dependent on the chemical reaction rate. In processes involving solid materials, mass transfer effects also play an important role in the final energy release rate.

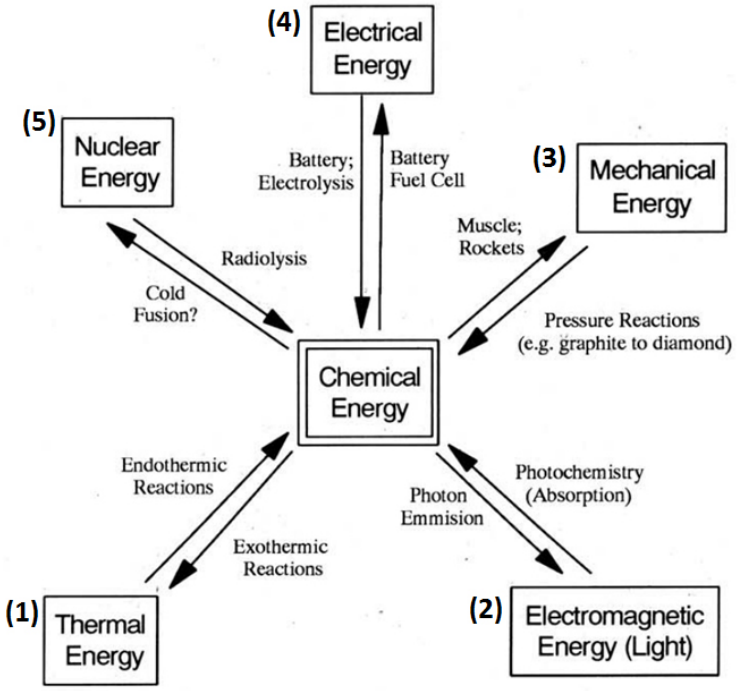


**Figure 1.2.** The energy conversion between chemical energy and other forms of energy. [1]

## *1.2. Advantages of Nanostructured Materials for Chemical Energy Conversion*

Nanostructured materials, or nanomaterials, have offered numerous advantages when compared to microsized and bulk materials, including high surface area to volume ratio, new physical or chemical properties etc. Specifically, for a chemical energy conversion system involving solid state reactions, nanostructured materials can have the following main advantages:

(a) Increased specific surface area and associated surface energy

(b) Increased mass, heat or/and charge transfer

(c) The ability to accommodate dimensional changes associated with some chemical reactions or phase transitions

## *1.3. Energetic Materials*

Energetic materials, in the most basic sense, are a class of materials with a large amount of stored chemical energy that can be released upon ignition. Technically, fuels such as diesel and gasoline fit into the definition of energetic materials, but, in conventional terms, energetic materials are usually limited to materials containing both a fuel and an oxidizer in a mixture or within a single compound. The first energetic material, gunpowder (i.e., black powder), can be dated back to 220 B.C. in ancient China. [2] This energetic material is comprised of saltpeter ($KNO_3$), sulfur, and carbon. Based on the modern definition, gunpowder belongs in the category of composite energetic materials, which contain fuel (sulfur and carbon) and oxidizer ($KNO_3$) in a mixture. In the later $19^{th}$ century, the first single organic compound containing both fuel and oxidizer was successfully synthesized and used as explosive.

Since then, a series of these monomolecular energetic materials, such as TNT, RDX, etc., had all emerged and have been widely used for both military and civilian applications. The advantage of monomolecular energetic materials is that the fuel and oxidizer exist in a single molecule, and thus can achieve a very rapid energy release. However, in terms of energy density, monomolecular energetic materials do not represent a significant advance. [3] On the other hand, tuning the release of energy from such materials is very difficult in consideration of the requirement that you would need to change the molecular structure during the organic synthesis process.

Metal based reactive materials are characterized by their high energy density. A well-known example is thermite, which is usually a mixture of aluminum and metal oxide powder. This reaction can release huge amounts of energy upon reaction, as shown below.

$$Al + \frac{3}{2} MO \rightarrow \frac{1}{2} Al_2O_3 + \frac{3}{2} M + \Delta H \qquad (1.1)$$

Traditional thermite reactions can also reach a very high temperature (>3000 K), and they have been widely used in exothermic welding. In principal, any reactive metal can be used as the fuel in the thermite reaction, but aluminum is employed as the fuel in most formulations because of its high reaction enthalpy and ready availability. [3] Figure 1.3 shows the energy density of some aluminum thermites in comparison to some of the most common monomolecular energetic materials. In regards to energy density, aluminum thermite systems have the potential to outperform the best monomolecular energetic materials, i.e., CL-20, as shown in Figure 1.3.

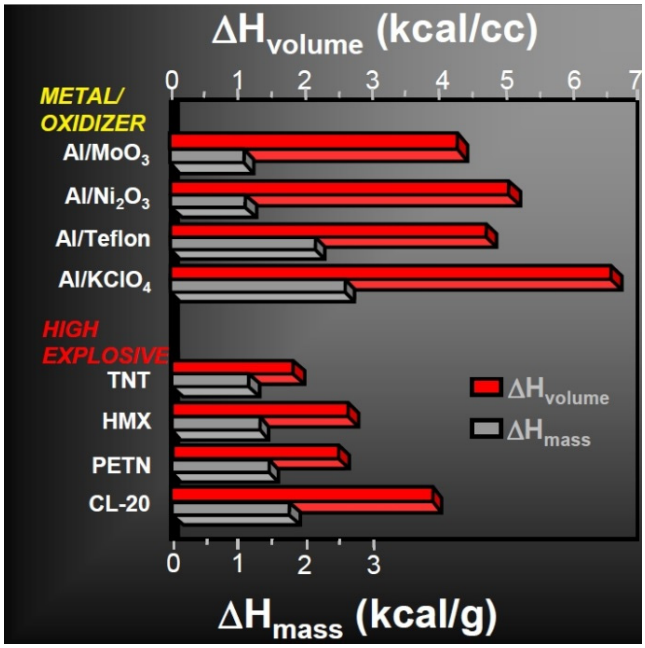


**Figure 1.3.** Energy density of various thermites and high explosives (adapted from [4]).

## *1.4. Nanocomposite Thermites*

Although thermites usually have much higher energy density than monomolecular energetic materials such as TNT (2, 4, 6-trinitrotoluene) etc., they suffer from slow rates of energy release, limited by the mass transfer rate between reactants. However, when the fuel and oxidizer are replaced by nanoparticles in a thermite system, the reactivity can increase by several orders of magnitude, leading to a much faster rate of energy release. In recent years, the application of nanostructured materials, particularly nanoparticles in energetic materials, have attracted great interest because of their enhanced energy release rate. [3, 5-11] This new class of nanocomposite energetic materials, comprised of a metallic fuel and an oxidizer at nanoscale, are called nanocomposite thermites or nanothermites. Sometimes, they are also called superthermites or metastable intermolecular composites (MICs). [8]

In nanocomposite thermites, the use of nanostructured materials is primarily used as a means to reduce diffusion lengths between reactive components and to increase the contact area between the fuel and the oxidizer. As a result, an enhanced flame-propagation rate of the wave front and energy-release rate of the nanoenergetic materials (up to three orders of magnitude) can be achieved when compared to their corresponding microsized formulations. [5] Moreover, it has been demonstrated that increasing the interfacial contact area between the oxidizer and the fuel at the nanoscale can significantly improve the performance of nanocomposite thermites. [12-15] A more practical advantage of using nanostructured materials in energetic materials system is that it allows for the ability to tune the reactivity of the nanocomposite thermites by changing the fuel/oxidizer, particle size, morphology or composition.

Recent development of ultra-high heating rate diagnostic tools has enabled the capability of probing fast condensed state reactions, e.g., nanothermite reactions. By applying rapid heating techniques and in-situ measurement tools, several important aspects of ignition and reaction mechanisms of nanocomposite energetic materials have been revealed. An overview of these tools for nanoenergetic materials research is provided in Chapter 2.

It can be foreseen that further understanding of nanothermite reaction mechanisms and the relationship between nanostructured materials and their reactivity in nanothermite reactions can greatly enhance the understanding and tuning of this new class of energetic materials.

## *1.5. Lithium-ion Batteries (LIBs)*

Rechargeable lithium ion batteries (LIBs) are a key component in portable electronics, and have become the most promising power medium in plug-in electric vehicles and integrated units for grid systems.

Figure 1.4 shows the schematic of a LIB. A typical LIB consists of two electrodes which are separated by the ion-conducting electrolyte. If the solid electrodes are separated by the liquid electrolyte, then an electrolyte-separator is needed. During the discharging process, as shown in Figure 1.4, lithium ions migrate from the high chemical potential anode, through the electrolyte separator, into the lower chemical potential cathode. At the same time, electrons travel from the anode to the external power source and finally reach to cathode. During the charging process, lithium ions are removed from the cathode and migrate into the anode.

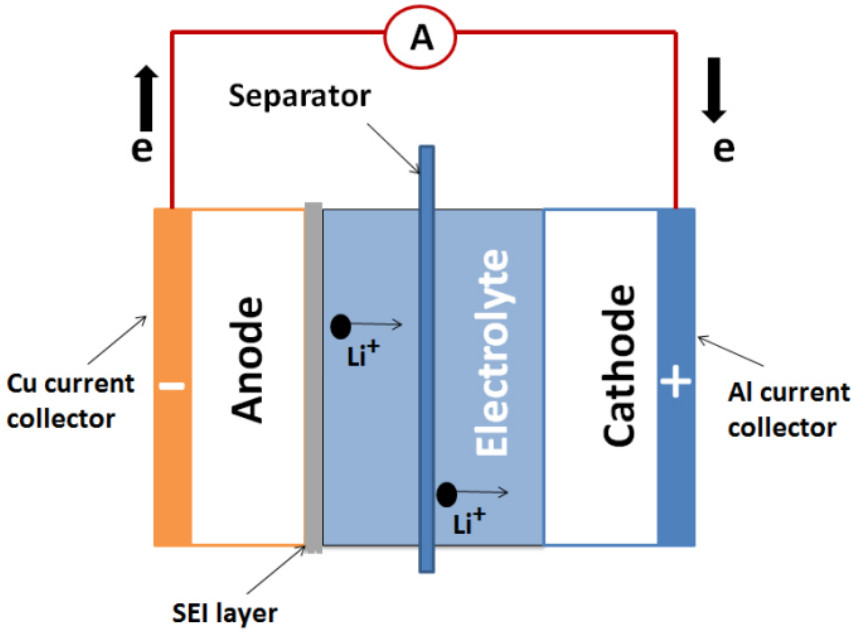


**Figure 1.4.** Schematic of a LIB. Note: Separator is not needed for nonaqueous electrolyte.

In a commercial $LiCoO_2$/C battery, the above process can be written as follow (Figure 1.5)

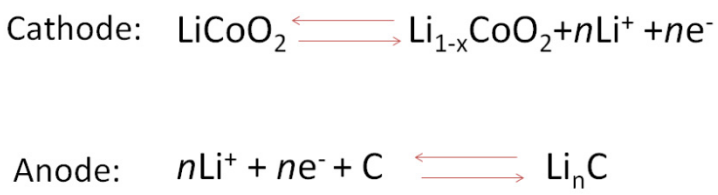


**Figure 1.5.** Electrode reactions in LIBs.

The cathode is often a Li-intercalation compound, such as $LiCoO_2$, characterized by a layered structure. The commercial used anode material in the LIBs, graphite carbon, is also characterized by a layer structure can store up to one Li ion per six carbon atoms ($LiC_6$). Graphite, as an anode material, has a theoretical capacity of 372 mAh $g^{-1}$, and is desired to be replaced by advanced electrode materials with high energy density. [16, 17]

## *1.6. Metal Oxide Nanoparticles as Anode Materials through Conversion Reactions*

In 2000, Tarascon et al. [18] firstly demonstrated the reversible electrochemical reaction of lithium with nanosized transition metal oxides (Figure 1.6), in which the metal oxide anode materials showed much higher discharge capacity than that of graphite. This conversion reaction differs from the classical Li insertion/disinsertion and Li-alloying process, and involves the formation and decomposition of $Li_2O$ matrix and reduction and oxidation of metal nanoparticles ($MO_x+2xLi \leftrightarrow M+xLi_2O$), as shown in Figure 1.6 and 1.7. Since the conversion reaction happens at the surface/interface, the specific area, surface energy and surface area play a pivotal role.

So, as schematically shown in Figure 1.7, the process can only become efficient and highly reversible with the usage of metal oxide nanomaterials. During the last decade, numerous efforts have been devoted to developing nanostructured metal oxide materials with superior electrochemical performance, and the progress in this field has been extensively reviewed. [19-24]

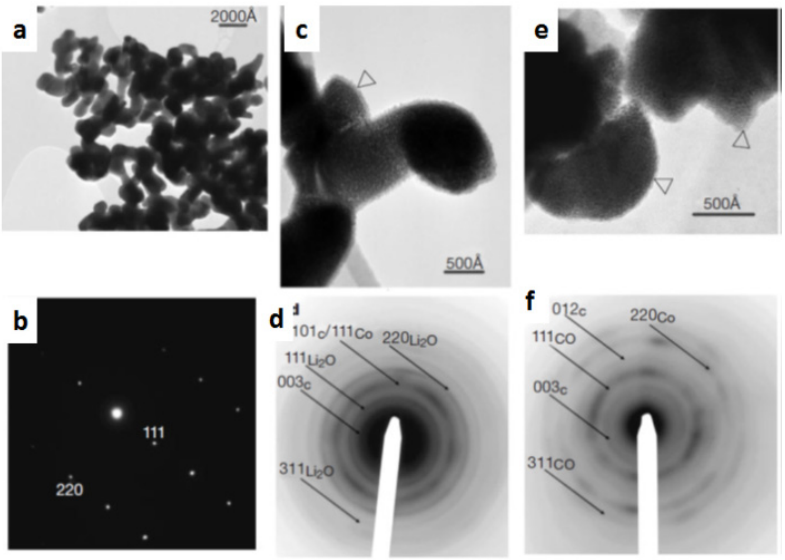


**Figure 1.6.** TEM and SAED images of CoO electrode before cycling (a, b), fully lithiated CoO (c, d) and delithiated CoO electrode (e, f). [18]

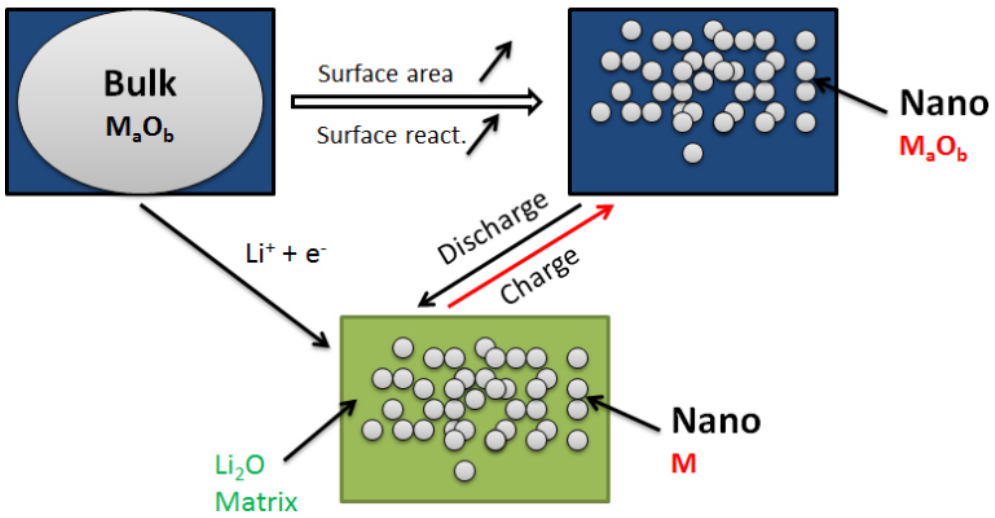


**Figure 1.7.** A schematic of conversion reaction process in LIBs.

## *1.7. Scope of the Dissertation*

As discussed in the previous sections, nanostructured materials have several advantages in chemical energy conversion systems involving energetic materials and lithium ion batteries. The objective of this dissertation is to enhance our understanding and tuning of nanostructured materials toward energetic materials and electrode materials in lithium ion batteries.

The work done in this dissertation will be discussed in three parts. Chapter 2 covers Part I and provides an overview of ultra-high heating rate diagnostic tools for nanoenergetic materials research. Most of the tools and techniques introduced in Chapter 2 are used in this dissertation (Chapter 3 to Chapter 8) to understand fast reactions of nanothermites and characterize their combustion performances. Part II presented in Chapter 3 to Chapter 8 is concerned with the study on reaction mechanisms, synthesis of new nanocomposite energetic materials and their combustion characteristics. In Chapter 3 and Chapter 4, a temperature-jump/time-of-flight mass spectrometer was used to study the ignition of aluminum nanoparticles, nanothermite reaction mechanism, and metal oxide nanoparticle decomposition under rapid heating conditions. Chapter 5-8 present the efforts to make new nanoenergetic composite materials using different methods, including aerosol spray pyrolysis/drying, milling and electrospinning. Part III includes Chapter 9 and 10, which describes the aerosol spray pyrolysis synthesis of hollow and mesoporous metal oxide nanostructures and their applications as anode materials in lithium ion batteries.

A summary of the works done in this dissertation and recommendations for future work are presented in Chapter 11.

## *1.8. References*


[1] Wink, D. J. *J. Chem. Educ.* **1992**, 69, 108-111.

[2] Akhavan, J. *The Chemistry of Explosives*. 2nd ed: The Royal Society of Chemistry, **2004**.

[3] Dreizin, E.L. *Prog. Energy Combust. Sci.* **2009**, *35*, 141-167.

[4] Fischer, S.H.; Grubelich, M.C. In: *32nd AIAA/ASME/SAE/ASEE Joint Propulsion Conference*. Lake Buena Vista, FL; **1996**.

[5] Aumann, C. E.; Skofronick, G. L.; Martin, J. A. *J. Vac. Sci. Technol. B, Microelectron. Process. Phenom.* **1995**, *13*, 1178-1183.

[6] Rossi, C.; Zhang, K.; Estéve, D.; Alphonse, P.; Thailhades, P.; Vahlas, C. *J. Microelectromech. Syst.* **2007**, *16*, 919-931.

[7] Yetter, R. A.; Risha, G. A.; Son, S. F. *Proc*. *Combust*. *Inst*. **2009**, *32*, 1819-1838.

[8] Piercey, D. G.; Klapötke, T. M. *Central Europ. J. Energ. Mat.* **2010**, *7*, 115-129.

[9] Martirosyan, K. S. *J. Mater. Chem.* **2011**, *21*, 9400-9405.

[10] Rossi, C.; Estéve, A.; Vashishta, P. *J. Phys. Chem. Solids* **2010**, *71*, 57-58.

[11] Zachariah, M. R. *Propellants Explos*. *Pyrotech*. **2013**, *38*, 7.

[12] Kim, S. H.; Zachariah, M. R. *Adv. Mater.* **2004**, *16*, 1821-1825.

[13] Malchi, J. Y.; Foley, T. J.; Yetter, R. A. *ACS Appl. Mater. Interfaces* **2009**, *1*, 2420-2423.

[14] Shende, R.; Subramanian, S.; Hasan, S.; Apperson, S.; Thiruvengadathan, R.; Gangopadhyay, K.; Gangopadhyay, S.; Redner, P.; Kapoor, D.; Nicolich, S.; Balas, W. *Propellants, Explos., Pyrotech.* **2008**, *33*, 122-130.

[15] Séverac, F.; Alphonse, P.; Estève, A.; Bancaud, A.; Rossi, C. *Adv. Funct. Mater.* **2012**, *22*, 323-329.

[16] Dunn, B.; Kamath, H.; Tarascon, J-M. *Science* **2011**, *334*, 928-935.

[17] Choi, N.S.; Chen, Z.H.; Freunberger, S.A.; Ji, X.L.; Sun, Y.K.; Amine, K.; Yushin, G.; Nazar, L.F.; Cho, J.; Bruce, P.G. *Angew. Chem. Int. Ed.* **2012**, *51*, 2-33.

[18] Poizot, P.; Laruelle, S.; Grugeon, S.; Dupont, L.; Tarascon, J-M. *Nature* **2000**, *407*, 496-499.

[19] Arico, A.S.; Bruce, P.; Scrosati, B.; Tarascon, J-M.; Schalkwijk, W.V. *Nature Mater.* **2005**, *4*, 366-377.

[20] Cabana, J.; Monconduit, L.; Larcher, D.; Rosa Palacin, M. *Adv. Mater.* **2010**, *22*, E170-E192.

[21] Zhang, Q.F.; Uchaker, E.; Candelaria, S.L.; Cao, G.Z. *Chem. Soc. Rev.* **2013**, *42*, 3127-3171.

[22] Wang, Z.Y.; Zhou, L.; Lou, X.W. *Adv. Mater.* **2012**, *24*, 1903-1911.

[23] Wu, H.B.; Chen, J.S.; Hng, H.H.; Lou, X.W. *Nanoscale* **2012**, *4*, 2526-2542.

[24] Reddy, M. V.; Subba Rao, G.V.; Chowdari, B.V.R. *Chem. Rev.* **2013**, *113*, 5364-5457.

# Chapter 2: Ultra-high Heating Rate Diagnostic Tools for Nanocomposite Energetic Materials Research: An Overview*

*"When it's too fast to see and too important not to." ®*

—*Vision Research*

## *Overview*

As I discussed in Chapter 1, nanocomposite energetic materials, e.g., nanothermites, have several advantages over their micro counterparts and traditional organic energetic materials. However, their applications in the fields of propellant, explosives and fast power sources are partially limited by the lack of understanding about these fast and intense reaction processes. Recent development of ultra-high heating rate diagnostic tools has enabled the capability of probing fast condensed state reactions, e.g., nanothermite reactions. By applying rapid heating techniques and *in situ* measurement tools, several important aspects of ignition and reaction mechanisms of nanocomposite energetic materials have been revealed. This chapter provides a brief overview of the development of rapid heating diagnostic tools for nanocomposite energetic materials research. In particular, a series of ultra-high heating rate techniques developed in our group, including temperature-jump/time-of-flight mass spectrometry, are described in detail. The progress made by using these techniques to study nanothermite reactions is highlighted. Other diagnostic tools relevant to

* Some results (Section 2.3) included in this chapter have been published in the following journal article: Jian, G.Q.; Chowdhury, S.; Sullivan, K.; Zachariah, M.R. Nanothermite Reactions: Is Gas Phase Oxygen Generation from the Oxygen Carrier an Essential Prerequisite to Ignition?, *Combust. Flame* **2013**, *160*, 432-437.

nanocomposite energetic materials research, such as combustion cell, are also included. Finally, a brief outline is given on rapid heating diagnostic tools used in each chapter of this dissertation.

## *2.1. Introduction*

Almost all solid state reactions, including thermite reactions, must be initiated by some kind of external stimulus, such as thermal heating, photoactivation, or application of pressure etc. Thermal heating is by far the most common external stimulus to initiate solid state reactions. [1]

Thermite is one kind of composite energetic materials, which usually contains a metal powder fuel and an oxidizer (usually metal oxide). When ignited by thermal heating, the thermite mixture undergoes a solid state thermite reaction, releasing large amounts of heat. However, due to the mass transfer limit between fuel and oxidizer, their reaction rate is slow compared to traditional organic energetic materials such as TNT and RDX. In nanocomposite thermite, fuel and oxidizer are mixed at the nanoscale so that diffusion lengths can be greatly reduced and the reaction surface area can be increased. As a result, the reaction rate can be greatly increased (several orders of magnitude higher) or even exceeds some other explosion reactions. [2]

Thermally activated solid state reaction processes and mechanisms are usually studied by commercial thermal analysis techniques such as thermogravimetry (TG), differential scanning calorimetry (DSC) and differential thermal analysis (DTA). [1] Other *in situ* characterization methods, including mass spectrometry, [3] infrared spectroscopy, [4, 5] Raman spectroscopy, [5] X-ray diffraction, [6] hot stage electron microscopy etc. [7], are often used to help reveal the reaction process and detailed

kinetics. All of these characterization instruments or techniques are performed at low heating rates, and characterized by low sampling rates. Despite the low heating rates, these experiments can be useful for determining some thermal properties of thermite and even nanothermite systems; [8, 9] however, they fail to probe the processes that occur during ignition and combustion process which occur at high heating rates. Our understanding of reaction mechanisms of nanothermites at high heating rates is very limited. Thus, to better understand the reaction mechanism of nanocomposite thermites, information about the dynamics/kinetics of fuel and oxidizer (decomposition) at high heating rates closer to that of real-time combustion events is necessary.

High heating rate heating sources directly combined with other diagnostic techniques have been shown to enable a better understanding of the ignition and reaction mechanisms of nanocomposite energetic materials. [10, 11] Two rapid heating methods have been used in nanocomposite energetic materials' studies. The first is laser rapid heating, which can effectively heat a nanothermite sample to a very high temperature in a very short time (as short as several *n*s). [11, 12] However, the sample's temperature-time history is unknown during the rapid heating, as is the ignition temperature. The other heating method, is hot filament heating, and is characterized by a known traceable temperature during rapid heating. This technique has been used to study the reaction kinetics of energetic materials under high heating rate conditions (up to ~$10^6$ K/s). In particular, temperature-jump/Fourier transform infrared spectroscopy (T-Jump/FTIR), developed by Brill et al., has been used to study reaction kinetics of organic energetics and condense phase propellants at a

heating rate of ~2000 K/s. [13-15] Recently, a series of ultra-high heating rate techniques based on the hot filament heating method were developed in our group, such as temperature-jump/time-of-flight mass spectrometry (T-Jump/TOFMS). [16] T-Jump/TOFMS has been used to study the decomposition of organic energetic materials, reaction mechanism of nanocomposite thermite reactions, etc. [16-19]

This chapter focuses on the development and key features of a series of ultra-high heating rate diagnostic tools in our group. In particular, temperature-jump/time-of-flight mass spectrometry, one of main techniques used in this dissertation, is presented as a tutorial. The progress made by using these techniques to study nanothermite reactions is highlighted. Other diagnostic tools relevant to nanocomposite energetic materials research, such as combustion cell, are also included. Finally, a brief outline is given on rapid heating diagnostic tools used in each chapter of this dissertation.

## *2.2. Summary of Rapid Heating Diagnostic Tools for Nanocomposite Energetic Materials Research*

### *2.2.1. High Heating Rate Diagnostic Tools: Desirable Features.*

The two most important features of a basic high heating rate diagnostic tool are its capabilities of heating the sample in a very short time (i.e., high heating rates) and collecting species/optical information during the rapid chemical reaction processes (i.e., high sampling rates). To study the reaction processes and mechanisms of combustion events including nanocomposite thermite reactions, additional features are also desirable when designing a diagnostic tool. Knowing the temperature time history during the rapid heating is a desirable and valuable feature from which we can

get different characteristic temperatures during ultra-fast solid state reactions. The temperature information at high heating rates, such as ignition temperature of nanothermite, decomposition temperature of oxidizers etc., are known to be very useful for analyzing reaction mechanisms. Another feature that would be beneficial when studying nanocomposite thermite reactions is the capability to run rapid heating experiments in an environment where secondary reactions could be eliminated or reduced.

*2.2.2. Temperature Jump Techniques: Up to ~$10^6$ K/s.*

The basic idea of the temperature jump (T-Jump) technique is to joule heat a fine metal wire coated with the sample to a high temperature (up to >2000 K) in a very short time (~2-20 ms), as shown schematically in Figure 2.1.

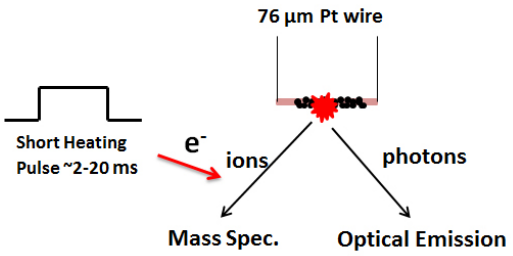


**Figure 2.1.** Schematic design of T-Jump technique.

The temperature of the platinum wire can be calculated from the resistance of the wire using the Calender-Van Dusen equation. [20] The high temperature measurement was calibrated against a blackbody source (Mikron M350, NIST calibrated) based on a two color pyrometry method. Detailed information about this temperature measurement and calibration can be found elsewhere. [21]

This technique enables rapid and controlled heating of samples on a 76 µm diameter Pt filament at a rate up to ~$10^6$ K/s with time resolved known temperature.

The T-Jump probe directly combined with other diagnostic techniques were later explored and proven as powerful procedures to understand the decomposition, ignition and reaction mechanisms of nanoparticles and energetic materials. A picture of temperature-jump techniques coupled with time-of-flight mass spectrometer system and high speed camera/photomultiplier tube detector is shown in Figure 2.2. The T-Jump mass spectrometer probe can be implemented into the system and an optical port can be used to do simultaneous high speed imaging using a Phantom® v12.0 digital camera. An example is shown in Figure 2.3, where the thermite reaction progression and intermediate reaction species, as well as the high speed imaging, can be obtained during rapid heating. Combining simultaneous optical and mass spectrometry data allows the distiguishing of decomposition, ignition and combustion processes, which will further the understanding of the nanothermite reaction process and mechanisms.

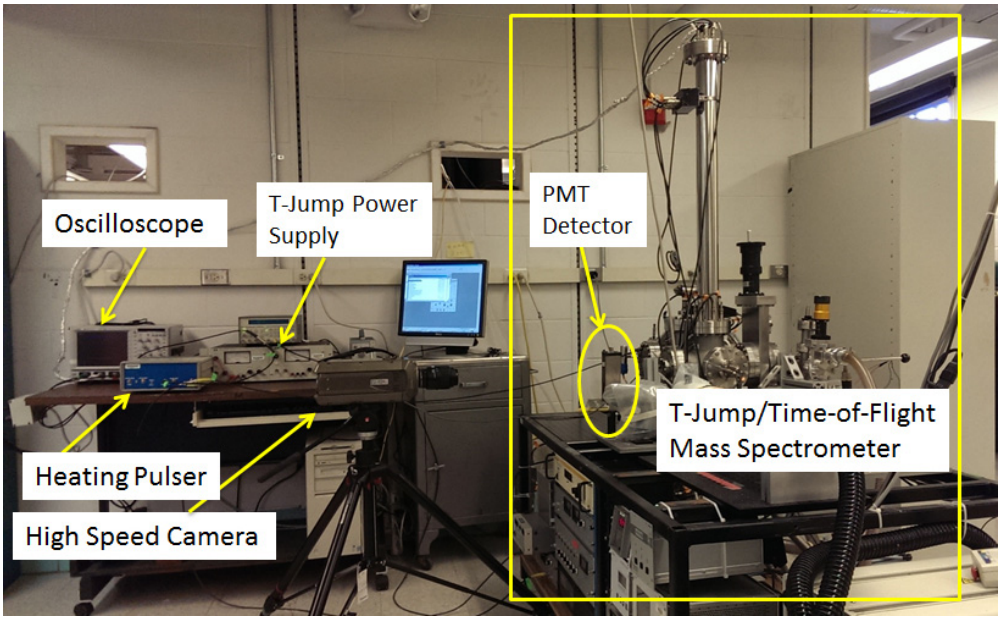


**Figure 2.2.** Image of the T-Jump/TOFMS system coupled with a PMT/high speed video camera.

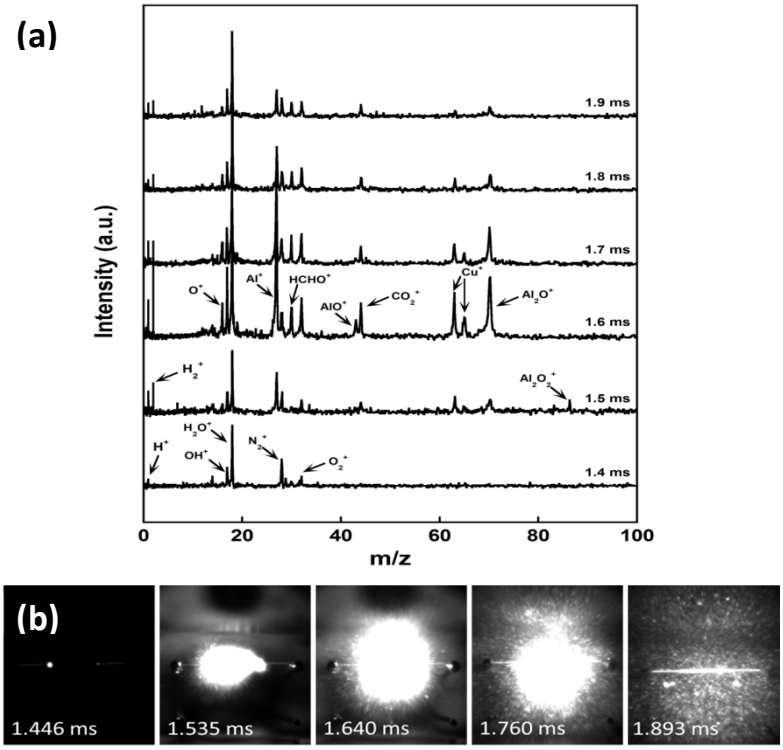


**Figure 2.3.** Time-resolved mass spectra obtained from fuel rich nano-Al/CuO thermite reaction. Selected images for a fuel rich ($\phi$=3) nano-Al/CuO reaction recorded by a high-speed digital camera.

There are several advantages of using rapid heating mass spectrometry methods to study nanocomposite thermite reactions. Firstly, the T-Jump/MS system can uniformly heat a sample at high heating rates, and the species produced during the decomposition, ignition and combustion can be studied by using only a very small amount of sample. Different from optical based tools which have limitations in the kinds of species that can be monitored, mass spectrometry can get complete characterization of species evolution during rapid heating. Also, the capability to probe a very small amount of sample is quite valuable, especially for studying newly synthesized materials where sample quantity is limited. Moreover, by heating the

samples in high vacuum, secondary reactions during rapid heating can be minimized or eliminated.

*2.2.3. T-Jump/TOFMS.*

A temperature-jump/time-of-flight mass spectrometer (T-Jump/TOFMS) consists of three major components, that is, the T-Jump probe with an electrical feedthrough, an ionization chamber and a time-of-flight tube, as schematically shown and pictured in Figure 2.4a-b. By operating the gate valve between sample loading chamber and the ionization chamber, the T-Jump sample holder can be inserted into the ionization chamber without breaking the high vacuum. The electron gun is normally set to 70 eV and 1 mA, to enable the efficient ionization of the reaction products. The T-Jump probe used in this system is a fine platinum filament with a 76 μm diameter and ~1 cm length. The Pt wire is soldered onto two tined-copper holders, and acts as the heater in the system. Using a homebuilt power source, the heating rate of the T-Jump probe can be varied by changing the pulse width and/or pulse voltage. The sampling rate of the MS is set to 10,000 Hz, which can enable mass spectra with a 100 μs time resolution. A schematic diagram of the control and data acquisition system is shown in Figure 2.5. The time-temperature measurement is achieved by the recording of the voltage and current across the Pt wire during the heating pulse. There is one observation window in the ionization chamber, therefore, the system can also be coupled with a high speed camera or a photomultiplier tube (PMT) to *in situ* record the optical images or traces during the rapid heating.

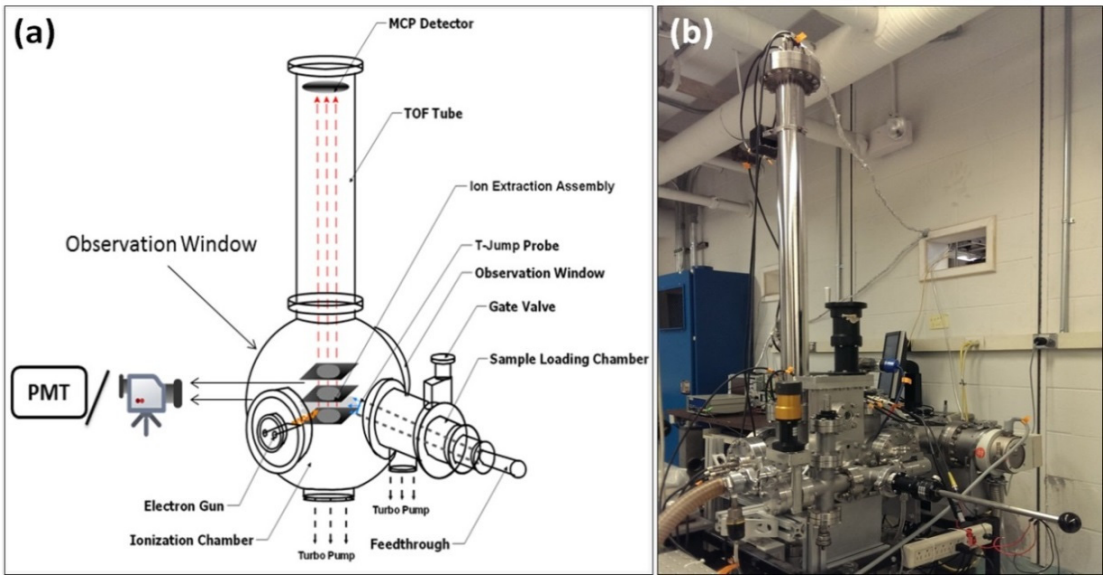


**Figure 2.4.** Schematic of the main components of T-Jump/TOFMS system. (a: Revised based on Figure 2 in [17])

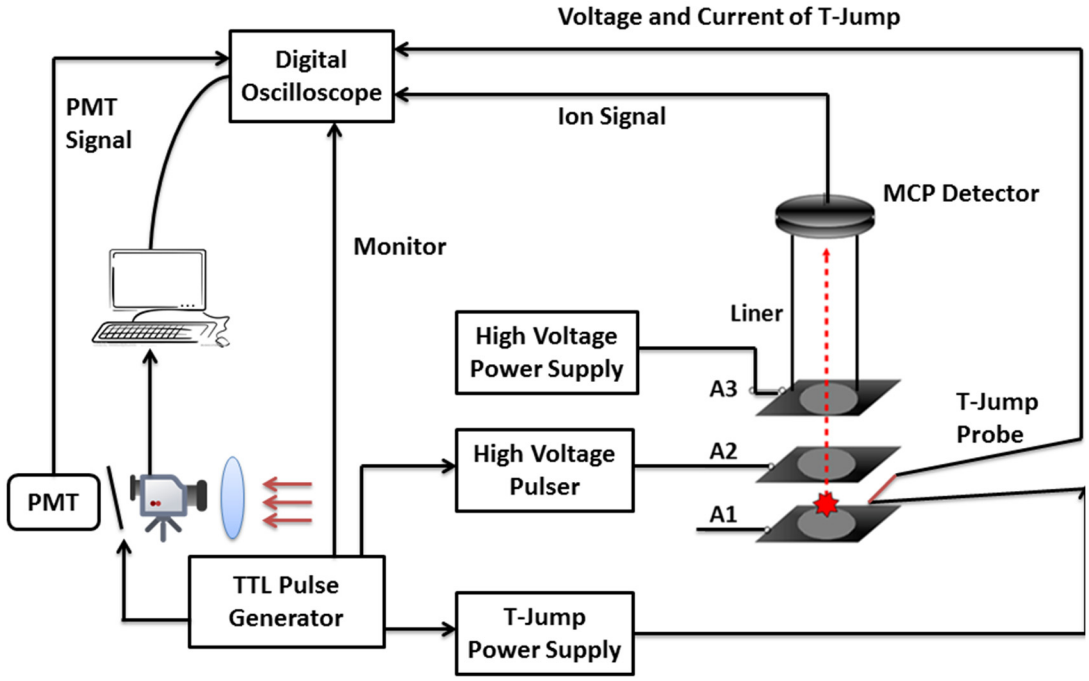


**Figure 2.5.** Schematic of the control and data acquisition systems of T-Jump/TOFMS. (A1: Ground, A2: Pulsed (Ground to -200 V), A3: -1500 V) and the voltage of the plates and liner is set to detect positive ions in this study.

The detailed setting and pulse sequence used in this dissertation study is shown in Figure 2.6. The ion optics consist of an ion repeller plate A1, an extraction plate A2 and an acceleration plate A3. The liner is used to ensure the field free ion drifting region in the TOF tube, and the MCP detector is used to detect the extracted ions. After the predetermined ionization process, the ions, the voltage on the A2 plate is changed to -200 V using a high voltage pulser, and the ions are extracted between the A1 and A2 plates to create the field for ion extraction. After the ion extraction process, the ions are accelerated between A2 and A3 plates, and drift into the TOF tube to be eventually detected by the MCP. The data are recorded with a 500 MHz digital oscilloscope and transferred to a computer for further analysis.

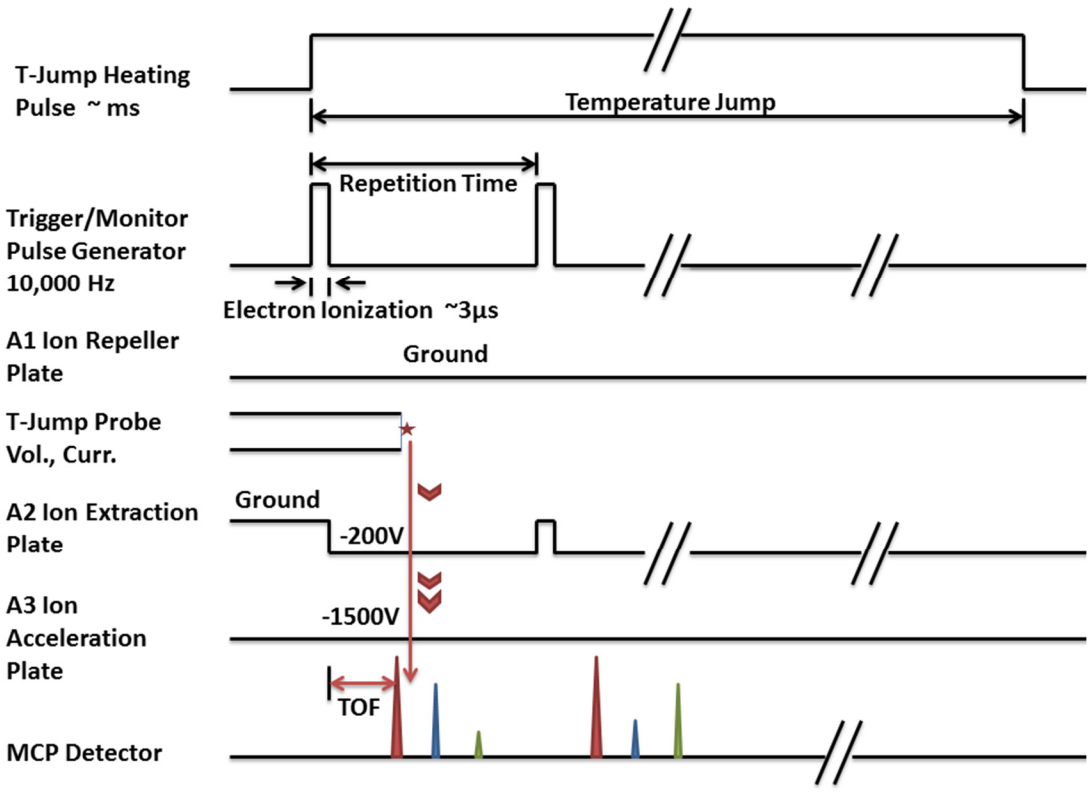


**Figure 2.6.** Detailed setting and pulse sequence used for positive ion detection in T-Jump/TOFMS.

*2.2.4. Optical Emission and High Speed Imaging.*

As shown in Figure 2.2 and Figure 2.3, optical emission from nanothermite in the mass spectrometer can be recorded using a PMT or a high speed video camera with high heating rates being used. The ignition and combustion of nanoparticles and nanothermites could also be studied by rapidly heating a sample on the wire in different gas environments in a wire ignition chamber, and collecting the optical emission data by recording the reaction process using a PMT or high speed video camera.

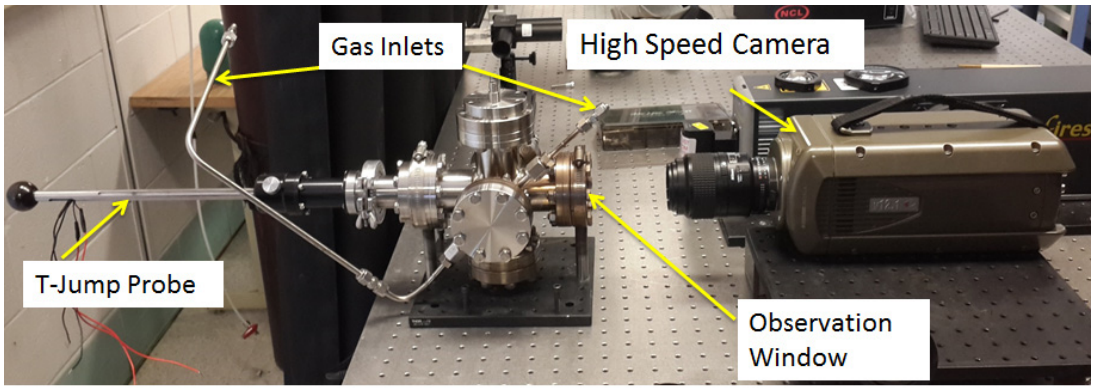


**Figure 2.7.** An image of T-Jump wire ignition chamber and high speed camera system. (High speed camera can be replaced by a PMT to record optical emission.)

Figure 2.7 shows an image of the wire ignition system, which is comprised of T-Jump probe, wire ignition chamber and high speed camera system (can be replaced with a PMT). The wire ignition chamber has the capability of introducing different gas environments under which the ignition behavior of nanothermites at different gas environments could be studied. Recently, Greg Young at the Naval Surface Warfare Center built an updated version of T-Jump wire ignition system, which can be used to study the ignition and burning of nanothermites in high pressure environments. [22]

An example of optical emission from nanothermite burning recorded by a PMT in the ignition chamber is shown in Figure 2.8. The ignition temperature is defined as the temperature at the onset of optical emission, and the burning time is taken by measuring the full width at half maximum (FWHM) of the optical emission curve. A PMT is most commonly used for collecting of broadband emission during the reaction, but by using filters, a PMT can also be used to study atomic emission during the combustion or explosion events.

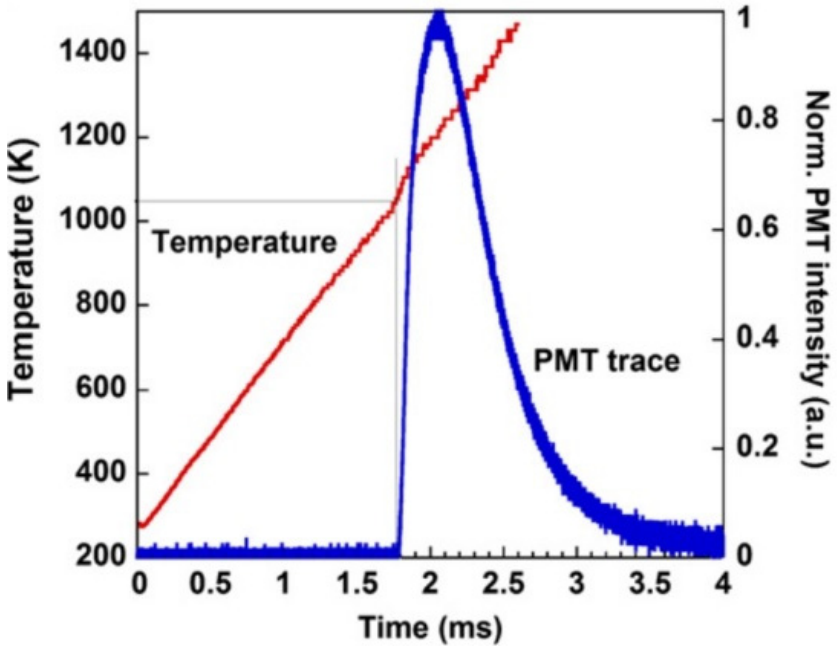


**Figure 2.8.** Optical emission signal of nano-Al/CuO thermite reaction recorded by a PMT. [23]

Our group has also explored high speed X-ray imaging of nanothermite reactions and metal oxide decompositions at high heating rates. [23] A high speed and high resolution movie was collected with the help of a real-time phase contrast imaging technique. [24] The experiments were performed with an X-ray beamline from the

Advanced Photon Source (APS) at Argonne National Laboratory and a CCD camera capable of X-ray imaging. An example of $Al/Fe_2O_3$ nanothermite reaction on the fast heating wire is shown in Figure 2.9, and the high resolution movie was recorded at a frame rate of 135780 fps (7.4 μs per image). It can be clearly seen from Figure 2.9 that the formation of micron-sized spherical particles and gas production happen in the reaction process.

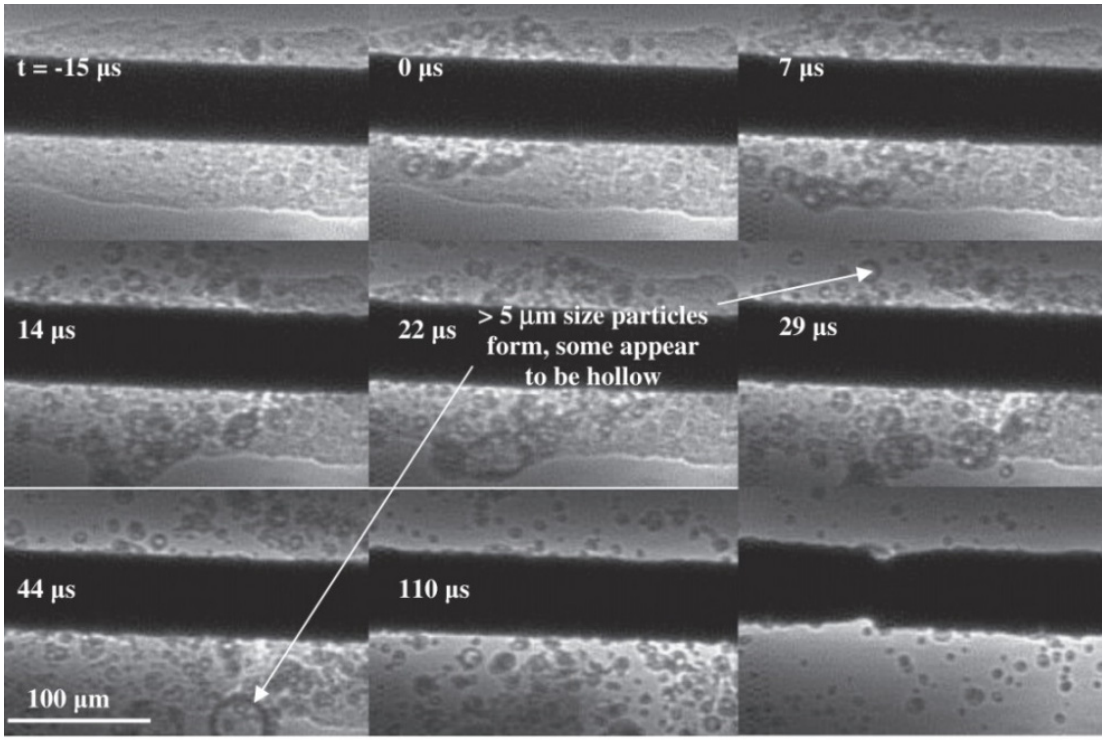


**Figure 2.9.** High speed X-ray imaging of $Al/Fe_2O_3$ nanothermite reaction. [23]

*2.2.5. Rapid Heating Electron Microscopy.*

Post-combustion product analysis of the solid products can be interrogated by electron microscopy, which can reveal information about ignition and the reaction mechanism. The primary barrier to achieve this objective arises from the difficulty of imaging the same nanoparticles before and after rapid heating events, or even during

rapid heating, when using standard microscopy techniques. Therefore, it is desirable to have the capability to rapidly heat sample inside of an electron microscope.

*2.2.5.1. Electrically Heated Microscopy Sample Holder.*

With the technical advances in both electron microscopy and nanofabrication, special holders and stages with rapid heating capabilities were introduced by Protochips Inc. that can be used inside a TEM or SEM. Special TEM holders and SEM stages have the capability of heating samples on a special Aduro thermal E-chip (Protochips Inc.) to a maximum temperature of 1473 K at a heating rate of up to $10^6$ K/s. The thermal E-chip, special TEM holder and SEM stage are shown in Figure 2.10. A schematic showing of the heating area (ceramic membrane) in the thermal E-chip is also shown as an inserted image in Figure 2.10c. The membrane in the thermal E-chip contains integrated heating elements and can be joule heated at high heating rates. Specifically, micro-sized holes are patterned which can be used for TEM imaging in which samples are placed over these holes. More detailed information about this technique can be found on the Protochips Inc.'s website.

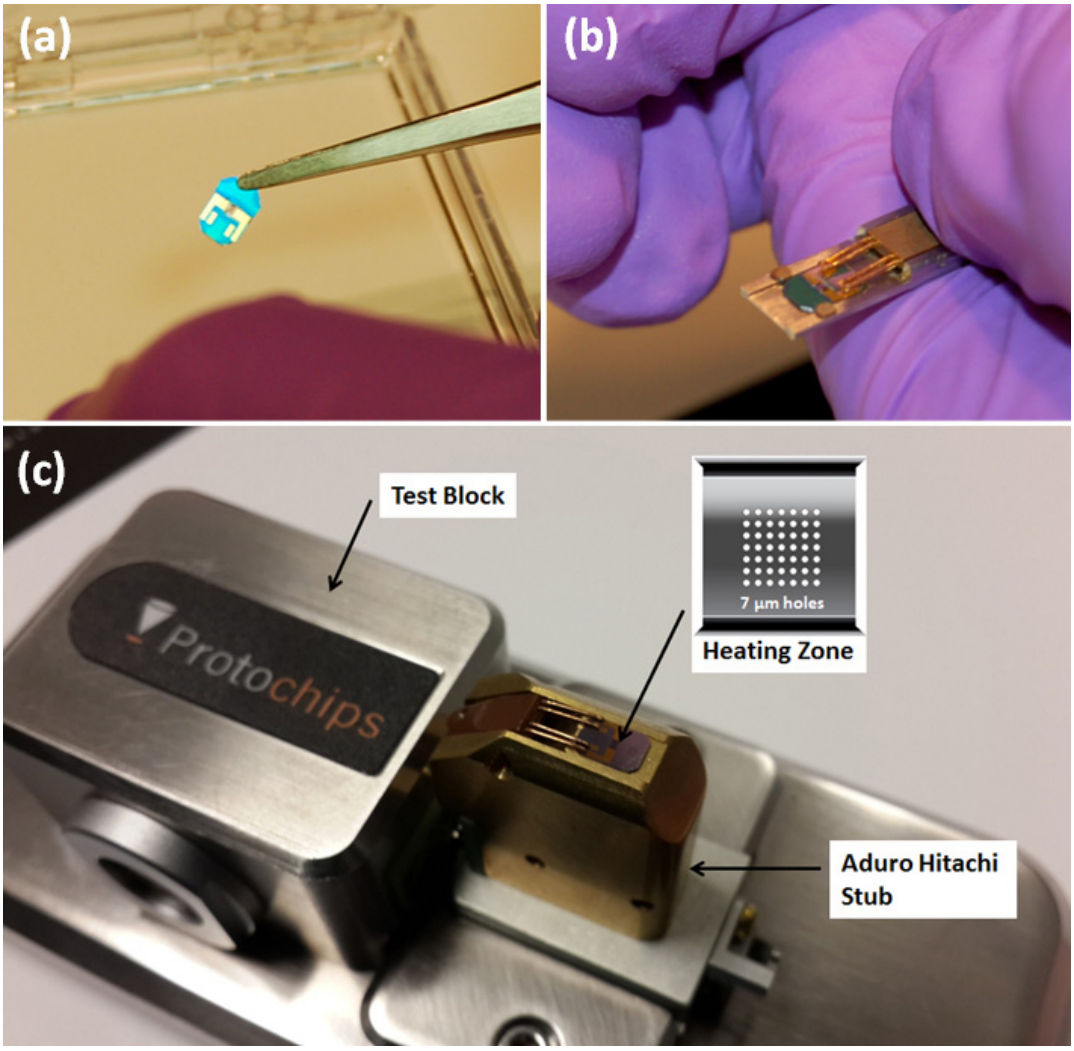


**Figure 2.10.** (a) Aduro thermal E-chip, (b) special TEM holder and (c) SEM stage. Note: a, b and inset heating zone images are taken from Protochips Inc. website.

Our group firstly used this technique to study the initiation and reaction mechanism of nano-Al and nano-Al thermite in a rapid heating environment. Figure 2.11 shows the TEM image of nano-Al before and after rapid heating, from which it suggests that the core migrated/diffused through the shell during the heating, supporting the diffusive mechanism for nano-Al.

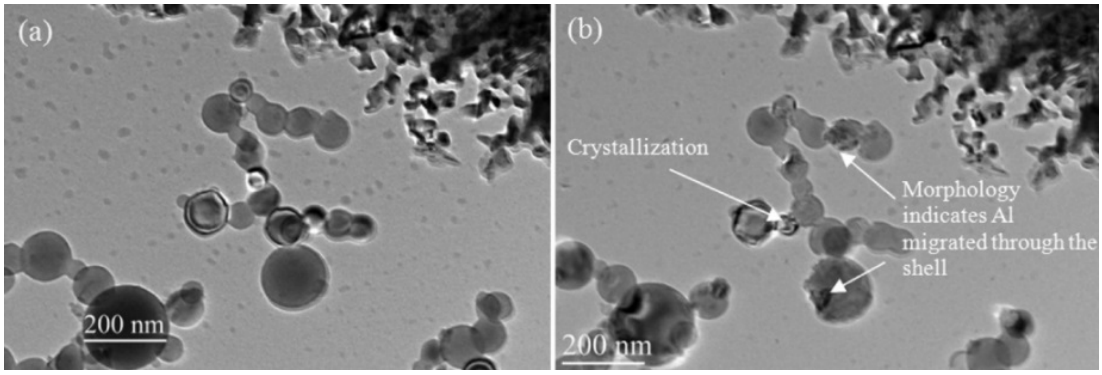


**Figure 2.11.** TEM images of nano-Al before and after rapid heating to 1473 K at $10^6$ K/s. [25]

The nanothermite sample, Al-NPs/$WO_3$ (fuel/oxidizer), was imaged using this technique in an SEM, and the images before and after rapid heating are shown in Figure 2.12. The back scattering image taken in an SEM show that significant morphology changes only occurred in regions where fuel and oxidizer were in physical contact. These direct imaging experiments provide strong, very useful information to study the reaction mechanism of nanothermites at high heating rates, from which a reactive sintering mechanism is supported.

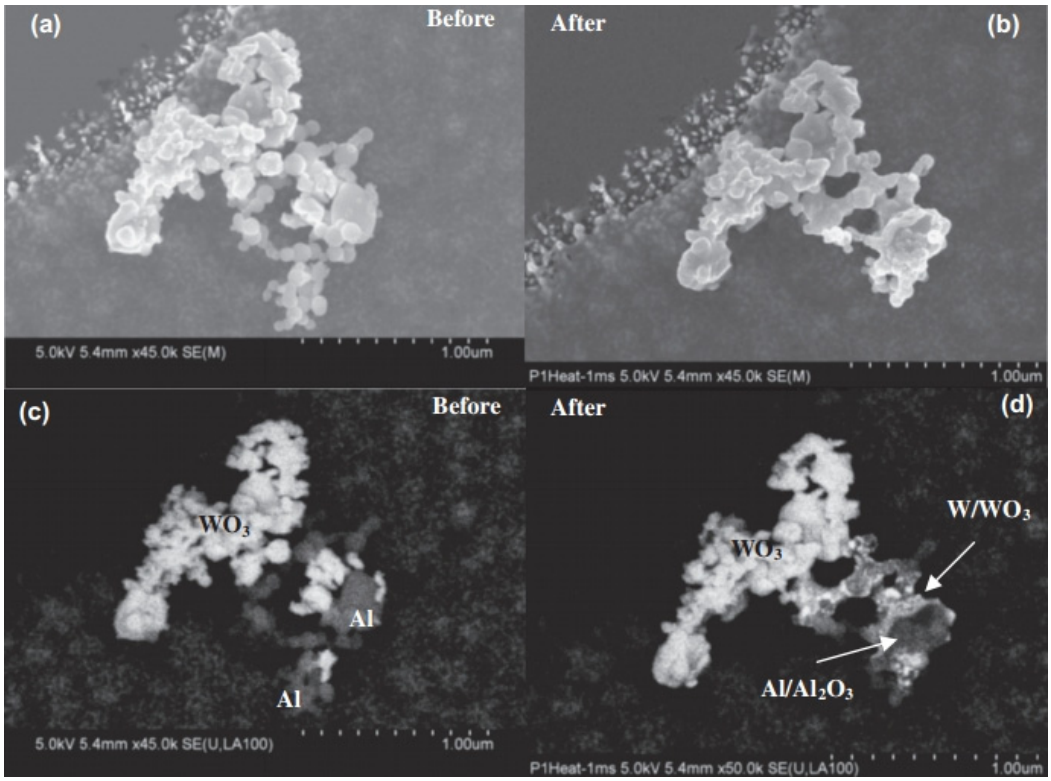


**Figure 2.12.** Secondary electron (a and b) and backscattered electron (c and d) SEM images of a nano-Al/$WO_3$ thermite sample before (a/c) and after (b/d) heating from 300-1473 K at $10^6$ K/s, and held for 1 ms. The labeled species were separately confirmed using energy dispersive X-ray spectroscopy (EDS). [23]

*2.2.5.2. Dynamic TEM.*

An alternative to obtaining images before and after rapid heating, the use of dynamic transmission electron microscopy (DTEM) developed at Lawrence Livermore National Laboratory (LLNL) allows visualization of nanostructure evolution during the rapid heating process. [26] In a collaborative work between our group and LLNL,[27] it has been shown that morphological changes in aluminum nanoparticle aggregates can occur in as little as a few nanoseconds after the onset of heating, as shown in Figure 2.13. The time-resolved TEM images reveal that the

morphological changes initiate within 15 ns and can be completed in less than 50 ns. The use of this technique to study the change of metal oxide nanoparticles during rapid heating will be useful in understanding the time scale of loss of surface area relative to reaction. However, application of DTEM to study the reaction mechanism of nanothermite reactions is still a great challenge. The biggest barrier is that efficient and uniform heating could not be achieved for metal and metal oxide nanoparticle mixtures.

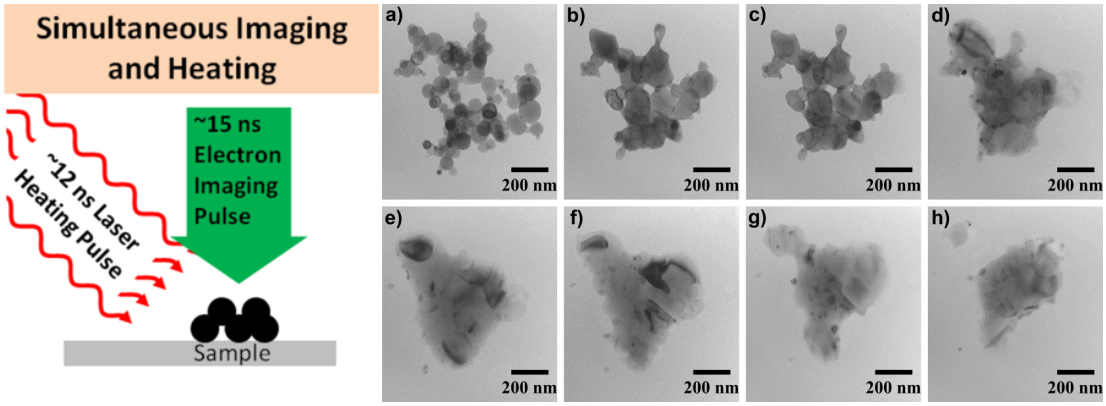


**Figure 2.13.** Left: Schematic illustration of the basic of DTEM. Right: An aggregate of Al-NPs before (a) and after (b-h) successive heating with 12 ns laser pulses with fluence 1.22 kJ/m$^2$. Images were taken with the DTEM in CW mode with long pauses between pulses for the taking of the micrographs. [27]

*2.2.6. Combustion Cell: Evaluating the Combustion Performance/Reactivity of Nanoenergetic Formulations.*

All of the rapid diagnostic tools mentioned in the above sections can be used to probe the reaction process of nanothermite reactions at high heating rates with the usage of a very small amount of sample. For a better understanding of the bulk behavior of nanothermite burning, a combustion cell is employed, from which

temporal pressure rise and optical emission information can be obtained for the reaction in a constant volume closed vessel. Figure 2.14 shows a schematic illustration of the combustion cell setup used in our lab. The combustion cell consists of four main components: a constant volume cell with an electrical feedthrough, a piezoelectric pressure transducer, a silicon photodetector and an oscilloscope. The most important features of nanothermite studies using the combustion cell are the measurement of pressurization rate and burning time, which are quite useful for evaluating the reactivity of nanothermites. Pressurization rate can be calculated as the peak pressure divided by the pressure rise time, and burning time is defined as the full width of half maximum (FWHM) of the optical emission signal.

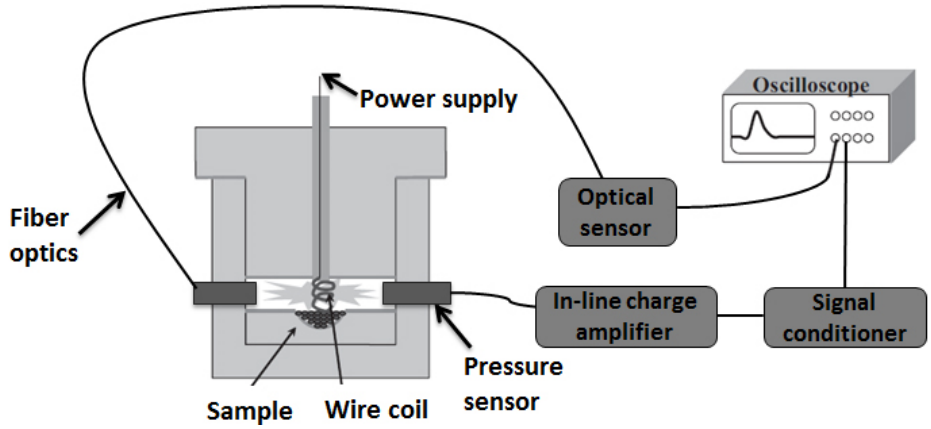


**Figure 2.14.** Schematic illustration of combustion cell setup.

Combustion cell techniques have not only been used for evaluating the reactivity/burning of nanothermites, but have also been demonstrated to be useful for studying nanothermite reaction mechanisms. Our group has investigated the reaction mechanisms of Al/CuO and Al/$Fe_2O_3$ nanothermites by collecting simultaneous pressure and optical signals during nanothermite reaction in a combustion cell. [28] Figure 2.15 shows simultaneous pressure and optical signals for nano-Al/CuO and

nano-Al/$Fe_2O_3$ thermites in a combustion cell. In nano-Al/CuO thermite (Figure 2.15a), a rapid pressure signal is seen followed by a prolonged optical signal, while for nano-Al/$Fe_2O_3$ (Figure 2.15b), the pressure and optical signals occur concurrently. Comparing between Figure 2.15a and Figure 2.15b, it is concluded that the burning of nano-Al/CuO thermite is rate limited by the aluminum, while the oxidizer decomposition is the rate-limiting step in nano-Al/$Fe_2O_3$ burning.

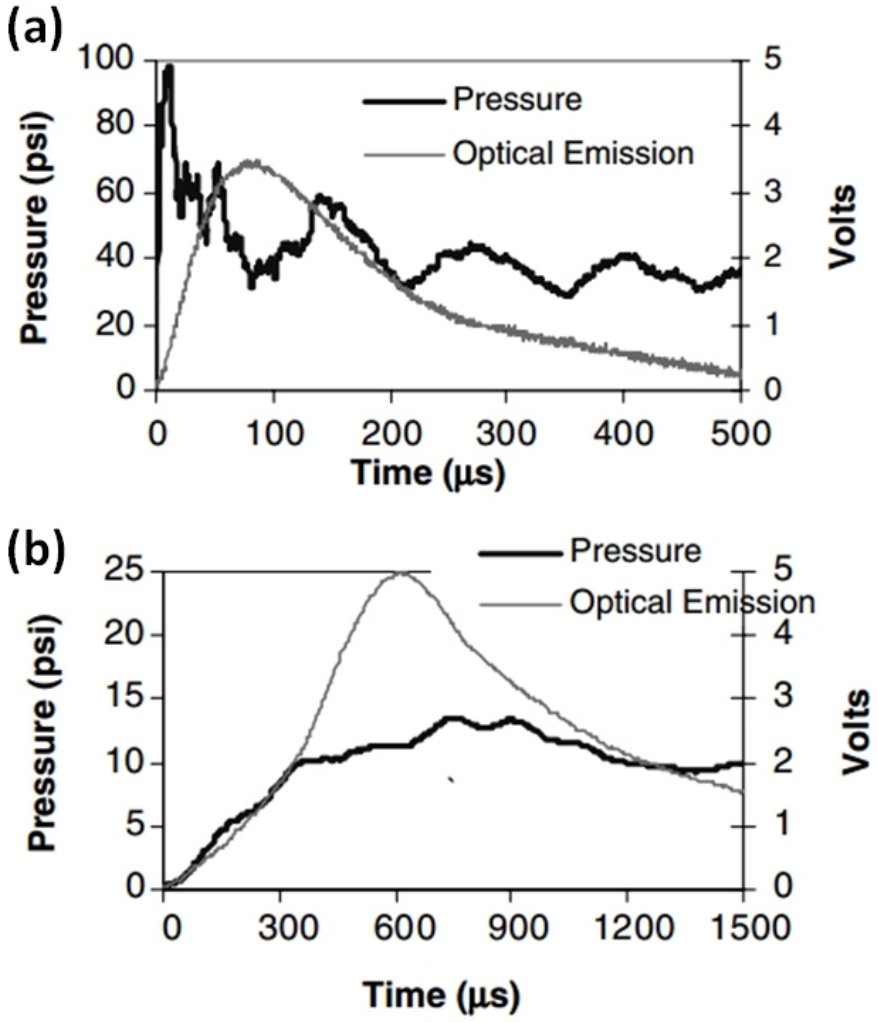


**Figure 2.15.** Simultaneous pressure and optical signals versus time for (a) nano-Al/CuO and (b) nano-Al/$Fe_2O_3$. [28]

## *2.3. Application of Ultra-high Heating Rate Diagnostic Tools in Nanothermite Reaction Mechanism Studies*

In 2008, our group first reported the time resolved analysis of organic energetic materials at high heating rates using T-Jump/TOFMS. [16] Since then, a significant amount of research efforts have been expanded to further develop this technique and its application to study the high heating rate decomposition of metal oxides nanoparticles, ignition, reaction mechanism of nanothermites etc. Some examples have been briefly introduced in the above section, and more examples of applications of ultra-high heating rate diagnostic tools can also be found in the following chapters of this dissertation.

This section describes one of our efforts to apply the rapid heating techniques in a nanothermite reaction mechanism study, i.e., to understand the role of gas phase oxygen generation from the oxygen carrier in the ignition event. [19] The objective of this study is to answer the question: "Is gas phase oxygen generation from the oxygen carrier an essential prerequisite to ignition?".

This question comes from the fact that the oxidizer acts as oxygen carrier, and could provide oxygen for usage in exothermic thermite reactions. But, how the oxidizer functions remains unknown. There are two most probable ways for the oxidizer to deliver oxygen for usage in reactions, as shown in the following equations:

Scheme 1: $MO\ (NP) \Rightarrow MO_{1-\delta}\ (NP) + \delta/2\ O_2\ (g)$

$2Al\ (NP) + 3/2\ O_2\ (g) \Rightarrow Al_2O_3\ (NP)$

Scheme 2: $2Al\ (NP) + 3MO\ (NP) \Rightarrow Al_2O_3\ (NP) + 3M$

One possibility is that the oxygen is firstly delivered in the gas phase and then reacts with aluminum (Scheme 1), while another is that the oxidizer directly reacts with aluminum in the condensed phase (Scheme 2). Although an early study for Al/CuO and Al/$Fe_2O_3$ systems show a clear correlation between the oxygen release temperature and ignition temperature, [17] whether this correlation still exists for a wider variety of oxidizers remains unknown.

The experiments were designed based on the above consideration, and a wide range of oxidizers were chosen (Table 2.1) and studied for their oxygen release temperature and ignition temperature at high heating rates.

**Table 2.1.** The list of source and primary particle size of fuel and oxidizers nanoparticles in this study. [19]

| Material | Supplier | Particle size (nm) |
|---|---|---|
| Nano-aluminum (ALEX) | Argonide Corp. | ~50 |
| Copper oxide (CuO) | Sigma–Aldrich | <50 |
| Iron oxide ($Fe_2O_3$) | Sigma–Aldrich | <50 |
| Tungsten oxide ($WO_3$) | Sigma–Aldrich | <50 |
| Bismuth oxide ($Bi_2O_3$) | Sigma–Aldrich | <50 |
| Silver iodate ($AgIO_3$) | NSW–China Lake | ~236 |
| Potassium Perchlorate ($KClO_4$) | Aerosol synthesized in our lab | ~300 |
| Tin (IV) oxide ($SnO_2$) | Sigma–Aldrich | <50 |
| Cobalt(II, III) oxide ($Co_3O_4$) | Sigma–Aldrich | <50 |
| Molybdenum oxide ($MoO_3$) | US Research Nanomaterials | 13–80 |
| Antimony (III) oxide ($Sb_2O_3$) | US Research Nanomaterials | 80–200 |

*2.3.1. The Measurement of Oxygen Release and Ignition Temperatures at High Heating Rates.*

To measure the oxygen release temperature of oxidizers at high heating rates (~$5\times10^5$ K/s), the bare oxidizers were rapidly heated in our T-Jump/TOFMS to measure the temperature during $O_2$ release from the individual oxidizers. An example of oxygen release from CuO nanoparticles is shown in Figure 2.16.

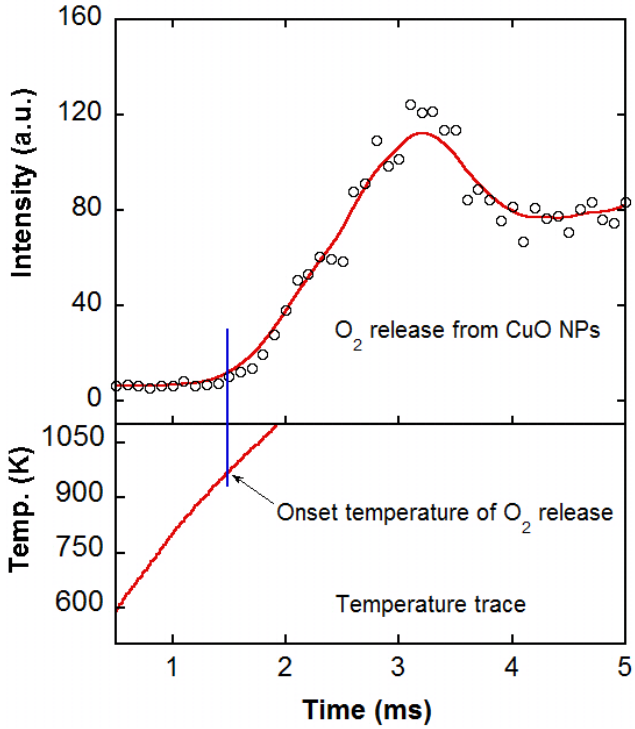


**Figure 2.16.** The temporal release of molecular oxygen from CuO nanoparticles when heated at ~$5\times10^5$ K/s. [19]

To obtain the ignition temperature, another set of experiments were carried out in the T-Jump/TOFMS with prepared stoichiometric nanothermite samples. A PMT was combined with the MS system, as schematically shown in Figure 2.4 (section 2.2.3). This system can collect the optical emission and mass spectra simultaneously, and therefore allows a direct comparison between the ignition point and the species

evolved during the thermite reaction, as shown in Figure 2.17 for the Al-CuO nanothermite reaction. It is seen from Figure 2.17 that the temperature of oxygen release from bare CuO nanoparticles (~975 K) is close to the ignition temperature of Al-CuO nanothermite (~1040 K).

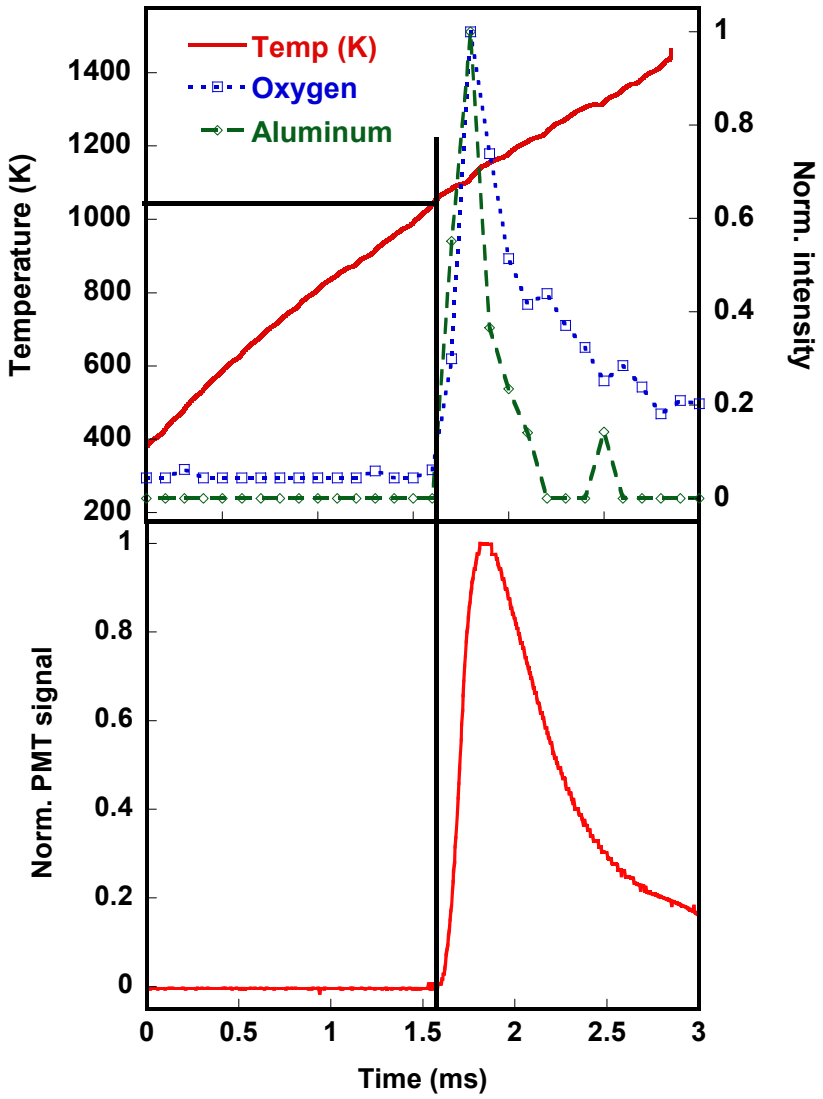


**Figure 2.17.** (top) Temporal profile of aluminum and oxygen species during the reaction of nano-Al/CuO mixture measured by T-Jump/TOFMS. (bottom) Simultaneous optical emission showing ignition as recorded by a PMT. [19]

*2.3.2. Oxygen Release Temperature from the Oxidizer vs. the Measured Ignition Temperature.*

Table 2.2 summarizes the results of oxygen release temperatures for all oxidizers and the corresponding ignition temperature of nanothermite mixtures (Heating rate ~ $5\times10^5$ K/s). The results of the measured $O_2$ release temperature from the oxidizer vs. the measured ignition temperature were also plotted and are shown in Figure 2.18.

**Table 2.2.** Ignition temperature of various n-Al based nanothermites is listed in terms of the oxidizer. The oxygen release temperature from the nanothermite reactions and the bare oxidizer as detected by TOFMS is also tabulated. [19]

| Nanothermite (Al + oxidizer) | Ignition temperature (K) (±50 K) | $O_2$ release temperature in thermite (K) (±50 K) | $O_2$ release from bare oxidizer (K) (±50 K) |
|---|---|---|---|
| $AgIO_3$ | 890 | 880 | 890 |
| $KClO_4$ | 905 | 905 | 875 |
| CuO | 1040 | 1050 | 975 |
| $Fe_2O_3$ | 1410 | 1400 | 1340 |
| $Co_3O_4$ | 1370 | 1020 | 1030 |
| $Bi_2O_3$ | 850 | 930 | 1620 |
| $Sb_2O_3$ | 950 | – | – |
| $MoO_3$ | 850 | – | – |
| $WO_3$ | 1030 | – | – |
| $SnO_2$ | 1050 | MS shutdown | 1680 |

It is seen from Table 2.2 that most oxidizers release $O_2$ during rapid heating, while some oxidizers do not release $O_2$. When analyzing the ignition temperature data, it is obvious that one would expect that oxygen release should be either earlier or close to the ignition point if gas phase oxygen is essential for ignition. From Figure 2.18, it is seen that there is a good correlation between oxygen release temperature from the oxidizer and the ignition temperature of nanothermites for Al-$AgIO_3$, Al-$KClO_4$, Al-

CuO, and Al-$Fe_2O_3$ nanothermites. However, several nanothermites tested in this study did not support the hypothesis that gas phase oxygen is required for the initiation/ignition of the nanothermite reactions. As shown in Figure 2.18, Al-$Bi_2O_3$ and Al-$SnO_2$ nanothermites have an ignition temperature that is lower than the oxygen release temperature of the corresponding oxidizers, while Al-$Co_3O_4$ nanothermite has an ignition temperature which is higher than the temperature of oxygen release from $Co_3O_4$. Some nanothermites, including Al-$Sb_2O_3$, Al-$MoO_3$, and Al-$WO_3$, can be ignited without the release of any oxygen gas.

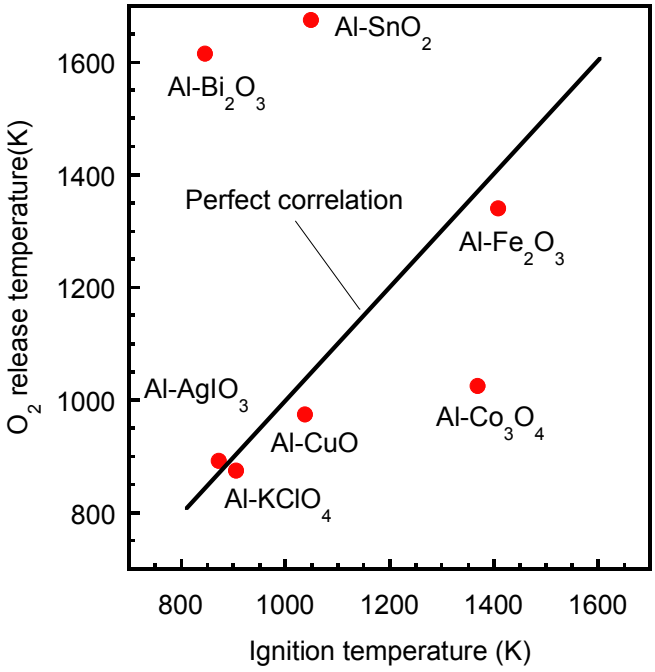


**Figure 2.18.** Oxygen release temperature from bare oxide vs. ignition temperature for various Al based nanothermites. The straight line indicates a perfect correlation. Nanothermites of oxidizers that do not release any oxygen are not shown. [19]

We thereby conclude that the initiation of nanothermite (ignition) before oxygen release or without oxygen release is likely a result of direct interfacial contact

between fuel and oxidizer, leading to condensed state mobility of reactive species. Thus in answer to the question posed before, “Is gas phase oxygen generation from the oxygen carrier an essential prerequisite to ignition?”, the answer is it might be in some cases, but certainly there are cases where it is not essential.

## *2.4. Conclusion and Outlook*

T-Jump/TOFMS is a powerful technique that was developed to probe fast condensed state reactions. The successful application of T-Jump/TOFMS in a study on decomposition of organic energetic materials at high heating rates promotes its application in the research topic of nanocomposite energetic materials. Our recent efforts on the application of T-Jump/TOFMS and other ultra-high heating rate diagnostic tools in nanocomposite energetic materials research greatly improve our understanding of decomposition, ignition and combustion of nanocomposite energetic materials at high heating rates.

The T-Jump/TOFMS technique is still in a stage of continuous development. Several ongoing technical improvements include interfacing with a fast heating micro-DSC chip, increasing sampling resolution etc. Applications of this technique in other research topics, such as fast heating destruction of biological spores, are in progress. In view of the convenience of combination of T-Jump/TOFMS with other diagnostic tools, more applications in a wide range of condensed phase materials are expected in the near future. More discussion about the future development of this technique will be included in Chapter 11.

## *2.5. Outline: Ultra-high Heating Rate Diagnostic Tools Used in This Dissertation*

Ultra-high heating rate diagnostic tools have been used extensively in this dissertation study. The following is the outline: (a) T-Jump/TOFMS: Chapter 3, 4, 5, 6 and 7; (b) High speed imaging: Chapter 3, 5, 6, 7 and 8; (c) Rapid heating electron microscopy: Chapter 6 and (d) Combustion cell: Chapter 5, 6 and 7.

## *2.6. References*


[1] Vyazovkin, S.; Wight, C. A. *Annu. Rev. Phys. Chem.* **1997**, *48*, 125-149.

[2] Rossi, C.; Estéve, A.; Vashishta, P. *J. Phys. Chem. Solids* **2010**, *71*, 57-58.

[3] Jian, G. Q.; Zhao, Y.; Wu, Q.; Yang, L. J.; Wang, X. Z.; Hu Z. *J. Phys. Chem.C* **2013**, *117*, 7811-7817.

[4] White, D.R.; White, R.L. *J. Appl. Polym. Sci.* **2005**, *95*, 351-357.

[5] Pérez-Ramírez, J.; Mul, G.; Kapteijn, F.; Moulijn, J. A. *J. Mater. Chem*. **2001**, *11*, 821-830.

[6] Pérez-Ramírez, J.; Abelló, S.; Van der Pers, N. M. *Chem. Eur. J.* **2007**, *13*, 870-878.

[7] Beattie, S. D.; Setthanan, U.; McGrady, G. S. *Int. J. Hydrogen Energy* **2011**, *36*, 6014-6021.

[8] Xu, D. G.; Yang, Y.; Cheng, H.; Li, Y. Y.; Zhang, K. L. *Combust. Flame* **2012** *159*, 2202-2209.

[9] Puszynski, J.A. *J. Therm. Anal .Calorim.* **2009***, 96*, 677-685.

[10] Moore, D. S.; Son, S.F.; Asay, B. W. *Propellants Explos. Pyrotech.* **2004,** *29*, 106-111.

[11] Zamkov, M.A.; Conner, R.W.; Dlott, D.D. *J. Phys. Chem. C* **2007**, *111,* 10278-10284.

[12] Granier, J.J.; Pantoya, M.L. *Combust. Flame* **2004**, *138*, 373-383.

[13] Brill, T.B.; Brush, P.J.; James, K.J.; Shepherd, J.E.; Pfeiffer, K.J. *Appl. Spectros.* **1992**, *46*, 900-911.

[14] Brill, T.B.; Ramanathan, H. *Combust. Flame* **2000**, 122, 165-171.

[15] Brill, T.B.; Arisawa, H.; Brush, P. J.; Gongwer, P. E.; Williams, G. K. *J. Phys.Chem.* **1995**, *99*, 1384-1392.

[16] Zhou, L.; Piekiel, N.; Chowdhury, S.; Zachariah, M. R. *Rapid Commun. Mass Spectrom*. **2009**, *23*, 194-202.

[17] Zhou, L.; Piekiel, N.; Chowdhury, S.; Zachariah, M. R. *J. Phys. Chem. C* **2010**, *114*, 14269-14275.

[18] Jian, G.Q.; Piekiel, N.W.; Zachariah, M.R. *J. Phys. Chem. C* **2012**, *116*, 26881-26887.

[19] Jian, G.Q.; Chowdhury, S.; Sullivan, K.; Zachariah, M.R. *Combust. Flame* **2013**, *160*, 432-437.

[20] Childs, P. R. N. *Practical Temperature Measurement,* Butterworth Heinemann: London, **2001**.

[21] Chowdhury, S. Ph.D. Dissertation, *University of Maryland*, **2012**.

[22] Young, G.; Jian, G.Q.; Jacob, R.; Zachariah, M.R. to be submitted.

[23] Sullivan, K.T.; Piekiel, N.W.; Wu, C.; Chowdhury, S.; Kelly, S.T.; Hufnagel, T.C.; Fezzaa, K.; Zachariah, M.R. *Combust. Flame* **2012**, *159*, 2-15.

[24] Wang, Y.J.; Liu, X.; Im, K-S.; Lee, W-K.; Wang, J.; Fezzaa, K.; Hung, D.L.S.; Winkelman, J.R. *Nature Phys.* **2008**, *4*, 305-309.

[25] Sullivan, K. T.; Chiou, W. A.; Fiore, R.; Zachariah, M. R. *Appl. Phys. Lett.* **2010**, *97*, 133104-1-3.

[26] Kim, J.S.; LaGrange, T.; Reed, B.W.; Taheri, M.L.; Armstrong, M.R.; King, W.E.; Browning, N.D.; Campbell, G.H. *Science* **2008**, 321, 1472-1475.

[27] Egan, G. C.; Sullivan, K.T.; LaGrange, T.; Reed, B. W.; Zachariah, M. R. *J. App. Phys.* **2014**, 115, 084903.

[28] Sullivan, K.; Zachariah, M.R. *J. Propul. Powe*r **2010**, *26*, 467-472.

# Chapter 3: Nano-Al and Nano-Al/CuO Thermite under Rapid Heating [*]

## *Highlights*

(a) The diffusive mechanism at high heating rate is supported by time-resolved mass spectrometry data of nano-Al.

(b) Time resolved mass spectra of nano-Al/CuO thermite show for the first time the existence of Al, $Al_2O$, AlO and $Al_2O_2$ intermediate reaction products.

## *Overview*

Aluminum nanoparticles (Al-NPs) and nano-Al/CuO thermite were investigated in a rapid heating environment by temperature jump time-of-flight mass spectrometry. Upon rapid heating ($10^5$ K/s-$10^6$ K/s), Al-containing vapor species (Al and $Al_2O$) are observed to slowly increase with increasing temperature, followed by a rapid increase in concentration at ~2030 K. The temporal evolution of Al, $Al_2O$ species observed in time-resolved mass spectra of rapid heated Al-NPs supports the hypothesis that Al containing species diffuse outwards through the oxide shell under high heating rate conditions. The rapid rise in Al-containing species above 2030 K, which is below the bulk melting point of $Al_2O_3$, implies that the penetration of Al into the shell probably decreases its melting point. The measurements lead to an effective overall diffusion

[*] The results presented in this chapter have been published in the following journal article: Jian, G.Q.; Piekiel, N.W.; Zachariah, M.R. Time-Resolved Mass Spectrometry of Nano-Al and Nano-Al/CuO Thermite under Rapid Heating: A Mechanistic Study, *J. Phys. Chem. C* **2012**, *116*, 26881-26887.

coefficient ~$10^{-10}$ $cm^2/s$. Time resolved mass spectra of nano-Al/CuO thermite show for the first time the existence of Al, $Al_2O$, AlO, and $Al_2O_2$ intermediate reaction products, with $Al_2O$ the main intermediate oxidation product, in agreement with thermochemical calculations.

## *3.1. Introduction*

The nanothermite reaction is a highly exothermic reaction between metal fuel and oxidizer particles at the nanoscale. Aluminum nanoparticles (Al-NPs) are the most commonly used fuel due to their ready availability, high energy density, and reactivity. [1-3] It is well known that a 2-5 nm thick oxide (typically amorphous $Al_2O_3$) coating is present on the surface of Al-NPs, which prevents the further oxidation of the metal at low temperature. [4, 5] In this regard, nanoaluminum can be considered as a core-shell nanoparticle with the oxide shell comprising a significant fraction of the particle mass, exceeding 50 % in some cases. [6]

The ignition of aluminum particles has been found to be very sensitive to particle size and closely related to the properties of the oxide shell. It has been found that Al-NPs can be ignited at as low as ~930 K which is close to the melting point of the Al (933 K). The micro-sized aluminum particles ignite at a much higher temperature of ~2300 K that is close to the melting point of the oxide shell.[7] Two mechanisms have been proposed to explain initiation/oxidation of Al-NPs. The first mechanism may be broadly classified as diffusion based phenomena where Al and oxygen species diffuse through the oxide shell. [8, 9] The second alternative mechanism, the so called “melt-dispersion mechanism”, suggests that the aluminum core expands and ruptures the oxide shell at high heating rates, resulting in ejection of small molten

clusters of aluminum at high velocities. [10-12] In melt-dispersion, mechanical breakdown of the aluminum oxide shell occurs at temperatures much lower than the melting point of the aluminum oxide shell, and plays an important role in the ignition of Al-NPs. [11] These two mechanisms offer radically different views of how nanoaluminum ignition is initiated.

In this chapter, temperature-jump time-of-flight mass spectrometer (T-Jump/TOFMS) was used to investigate the product speciation from Al-NPs and nano-Al/CuO thermite under rapid heating ($10^5$K/s-$10^6$K/s). Transmission electron microscopy (TEM) was used to characterize the morphological evolution of the Al-NPs, for which in some cases we found hollow structures in the heated Al-NPs. Our results indicate that aluminum core atoms diffuse outward thorough the oxide shell during the rapid heating.

## *3.2. Experimental Section*

### *3.2.1. Sample Preparation.*

Al-NPs purchased from Argonide Corporation (50 nm ALEX powder) are used in this study. The Al-NPs were found to contain ~70 % active Al by mass, as determined by TGA, due to the aluminum oxide shell. Copper oxide (CuO) nanoparticles are purchased from Sigma-Aldrich, and specified by the supplier to be <50 nm. $Al_2O_3$ particles are also purchased from Sigma Aldrich, with a purity of ≥ 98 %. For sample preparation, Al-NPs, $Al_2O_3$ particles and nano-Al/CuO were ultra-sonicated in hexane for 20 minutes, and then coated onto the T-Jump probe with a micropipette.

*3.2.2. T-Jump/TOFMS.*

The details of the T-Jump/TOFMS and operational setting can be found in Chapter 2 and previous papers. [13, 14] Typically, the T-Jump probe in this study is a ~12 mm long, 76 μm diameter platinum or iridium wire. In previous studies, the T-Jump system used a platinum filament that limited the heating temperature to around ~1800 K. In the present study, we also employ an iridium wire capable of temperatures in excess of 2000 K. A small portion of the central region (3-4 mm) of the wire is coated with the solid sample, and inserted into the vacuum chamber of the mass spectrometer, near to the electron ionization region. The electron beam is normally operated at 70 eV and 1 mA, with the background pressure in the TOF chamber at ~ $4.2\times10^{-6}$ torr. The T-Jump probe can be heated by an in-house built power source at a rate of up to ~$10^6$ K/s. From the current and voltage trace, a resistivity measurement can be obtained and related to the instantaneous temperature of the platinum [15] or iridium wire [16], which can be mapped against the mass spectra. Sample temperature is estimated to be ~5 K less than that of the wire temperature based on simulation results. [9] Time-resolved mass spectra combined with temperature information can be obtained and used for the characterization of the species produced during the rapid heating. The T-Jump mass spectrometer is also enabled with an optical port to enable simultaneous high speed imaging using a Phantom® v12.0 digital camera (67065 frames per second). This enables then the simultaneous temporal characterization of the temperature, species and visible combustion dynamics.

## *3.3. Results*

### *3.3.1. Rapidly Heated Nano Aluminum in T-Jump/TOFMS.*

In our previous T-Jump system, we used a platinum wire which limited the heating temperature to around ~1800 K, which is below the melting point of alumina. To address this limitation, we also employ an iridium wire which allows us to probe higher temperatures (>2000 K). We begin our analysis with the neat Al-NPs (without oxidizer), which was pulse heated to 2030 K in 3.1 ms in the TOFMS, at a heating rate of ~$6\times10^5$ K/s. During heating, a sequence of 95 spectra with mass to charge ratio (m/z) up to 380 were recorded at 100 μs intervals. We plot the mass spectra between t=2.3 ms and 3.3 ms in Figure 3.1a. Although we sampled up to m/z ~380, no high-mass ions were observed and major ions were only seen for m/z <100. Background species of the spectrometer consist of $H_2O^+$, $OH^+$ $N_2^+$ and $O_2^+$. Upon heating, we observe $Al^+$, $Al_2O^+$, $AlO^+$ (zoom-in view shown in Figure 3.1b) and $H_2^+$ product species and an increased intensity of $H_2O^+$. The major aluminum containing species observed are $Al^+$ and $Al_2O^+$, which we plot temporally in Figure 3.1c. Both $Al^+$ and $Al_2O^+$ appear simultaneously at t=2.3 ms, which corresponds to a wire temperature of 1720 K, and peaks at t=3.1 ms (T=2030 K). This is one of the key results of this chapter which we will interpret. Typical results of $H_2^+$ and $Al_2O^+$ species during the rapid heating are also plotted and shown in Figure 3.1d. Similar rapid heating experiment was also run for $Al_2O_3$ particles (Sigma Aldrich, ≥98 %), which were rapidly heated to 2070 K in 3 ms. The experiment yielded no observable $Al_2O$.

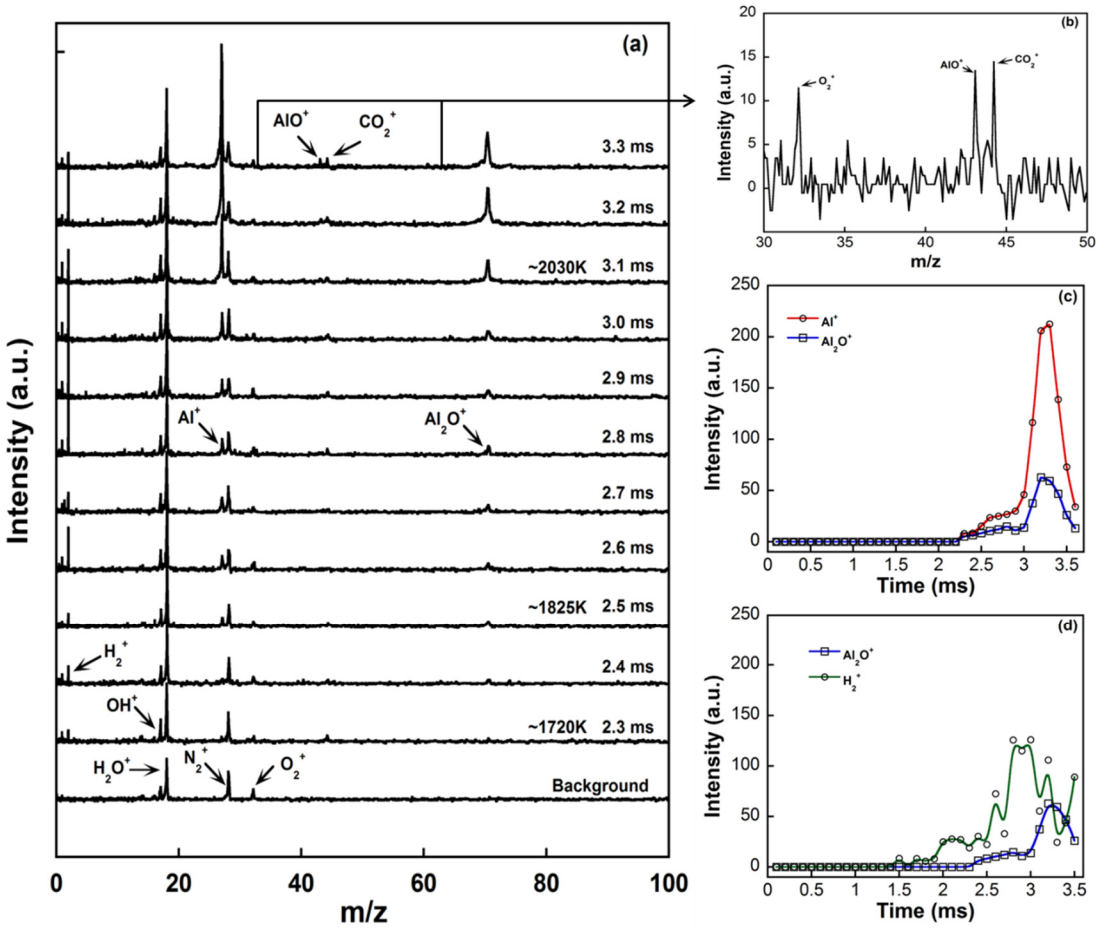


**Figure 3.1.** (a) Time-resolved mass spectra obtained from rapid heated Al-NPs on iridium wire, (b) the zoom-in view of the mass spectrum at t=3.3 ms, (c) typical results of $Al^+$ and $Al_2O^+$ ion species and (d) $H_2^+$ and $Al_2O^+$ ion species during rapid heating.

The known ionization cross sections (σ) for different Al containing species [17] are used for the estimation of their partial pressure ($p$) (i.e., concentrations) from the measured ion intensities ($I \propto p \times \sigma$), to enable comparison of the concentrations of different species. The ionization cross section data for Al, $Al_2O$, AlO and $Al_2O_2$ are summarized in Table 3.1. [18-20]

**Table 3.1.** Electron impact ionization cross section of Al, $Al_2O$, AlO, and $Al_2O_2$ at 70 eV. [18-20]

| Species | Al | $Al_2O$ | AlO | $Al_2O_2$ |
|---|---|---|---|---|
| σ ($Å^2$) | 7.5 | 11.8 | 4.8 | 6.0 |

To study the effect of the heating rate, we changed the heating pulse to ~2 ms and 5 ms, which correspond to a heating rate of ~$9\times10^5$ K/s and $3\times10^5$ K/s, respectively. In these runs, we observe $Al^+$ appearance at 1825 K and 1705 K, respectively. Similar to the 3 ms heating pulse, we also observe $H_2$ produced at ~1250 K, as well as an increased intensity of $H_2O$ upon rapid heating.

To further investigate the possibility that at lower temperatures elemental aluminum is reacting with adsorbed water, we measured the evolution of hydrogen production, which is shown in Figure 3.2. We rapidly heated the Al-NPs to 1650 K at a heating rate of ~$5\times10^5$ K/s and observe $H_2^+$ onset at t=2.3 ms, corresponding to a temperature of ~1250 K. This implies that significant aluminum diffusion is occurring and possibly reacting with adsorbed water in the alumina shell, which we will discuss further later. The TEM images of the heated Al-NPs (up to 1650 K in 3 ms) are shown in Figure 3.3a-b. Many of the particles appear unchanged after rapid heating; however, a few are seen to be hollow implying that aluminum can diffuse out of the shell without a catastrophic change in the shell structure. A similar hollow structure was also reported in Al-NPs oxidation at high temperatures by Rai et al. [8]

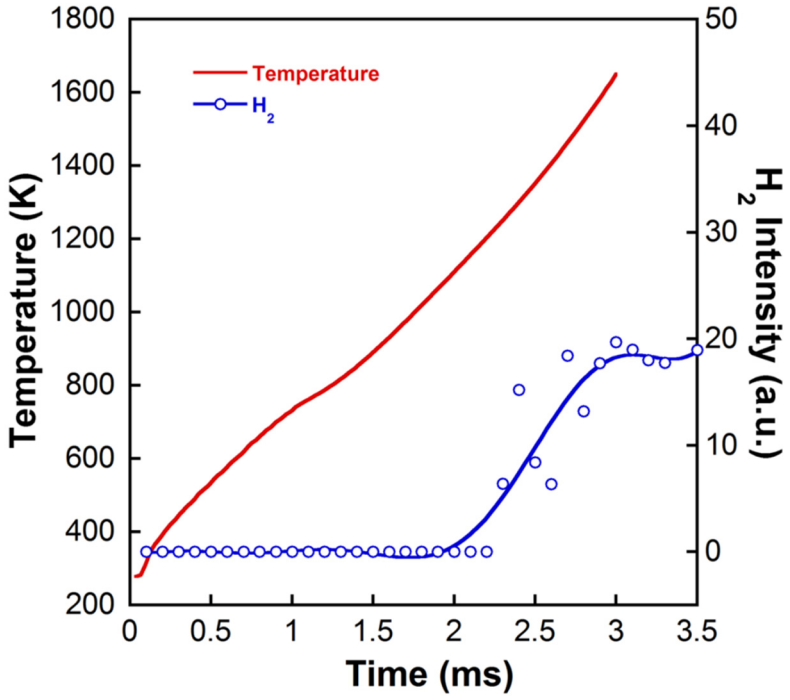


**Figure 3.2.** Temporal evolution of hydrogen peak intensity of rapid heating of Al-NPs up to 1650 K in 3 ms.

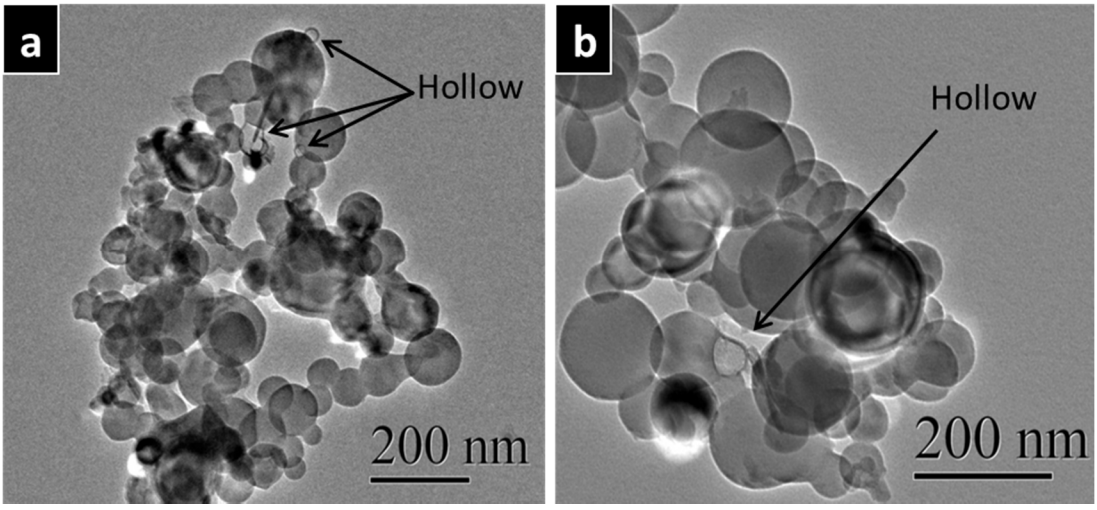


**Figure 3.3.** (a, b) TEM images of Al-NPs after rapid heating up to 1650K.

*3.3.2. Nano-Aluminum/CuO Thermite Reaction in T-Jump/TOMFS.*

A more vigorous reaction of nano-Al was probed with a thermite mixture using CuO as the oxidizer at a heating rate of ~$5\times10^5$ K/s. To better study the intermediate reaction species during the thermite reactions, especially those related to Al species, fuel rich (equivalence ratio $\phi$=3) nano-Al/CuO thermites were probed. The T-Jump mass spectrometer probe has been implemented with an optical port to enable simultaneous high speed imaging using a Phantom® v12.0 digital camera.

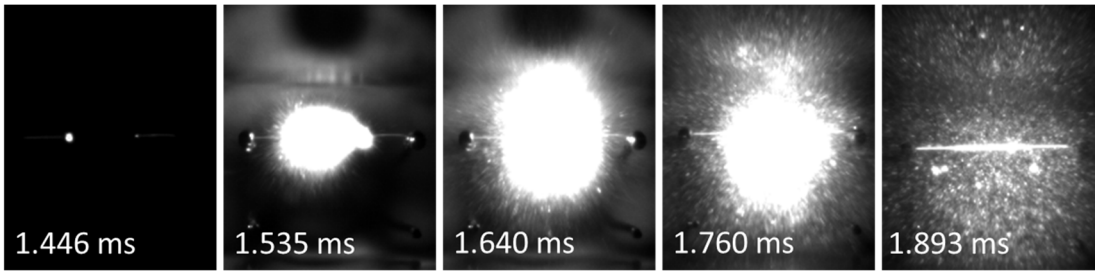


**Figure 3.4**. Selected images for a fuel rich nano-Al/CuO reaction recorded by a high-speed digital camera.

Figure 3.4 shows sequential snapshots of fuel rich nano-Al/CuO ignited on the Pt wire at a heating rate of ~$5\times10^5$ K/s. It is seen from Figure 3.4 that the optical signal is first observed at the two ends of the sample coating at a time of 1.446 ms (~1000 K), indicating the ignition of the thermite sample. The ignition front then propagates from the two ends toward the center, and ignites the whole thermite sample at a time of 1.535 ms. Time resolved mass spectra for the reaction is shown in Figure 3.5.

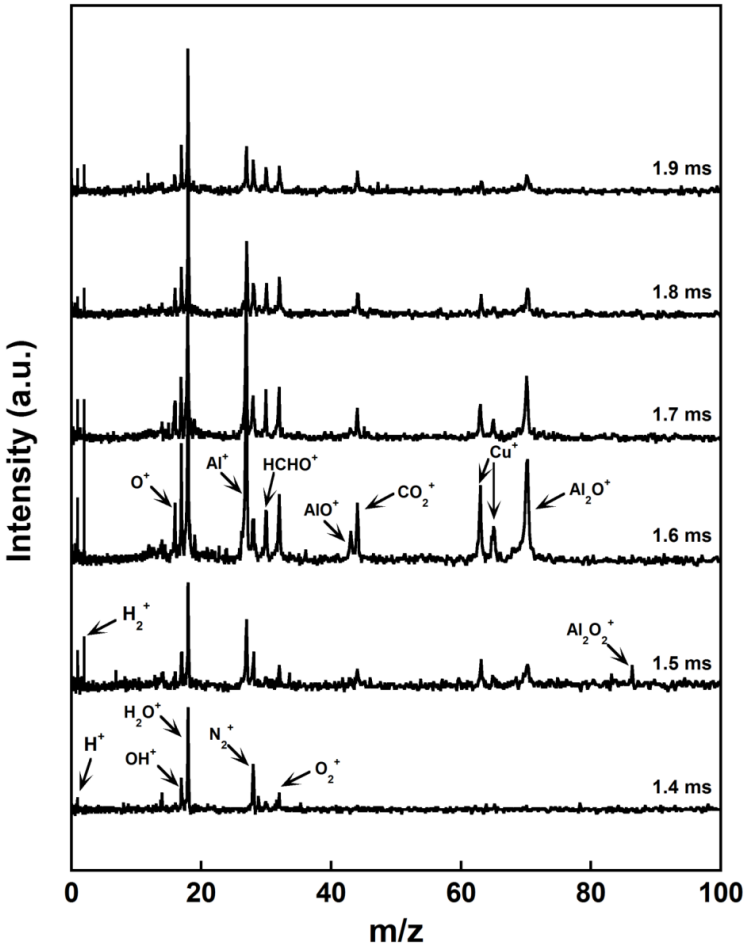


**Figure 3.5.** Time-resolved mass spectra obtained from fuel rich nano-Al/CuO thermite reaction.

The mass spectra in Figure 3.5 clearly show the thermite reaction progression and intermediate reaction species, which corresponds to the high speed imaging in Figure 3.4. In Figure 3.6, we plot the time dependent evolution of different species from fuel rich nano-Al/CuO thermite reaction, to be discussed later. From time-resolved mass spectra shown in Figure 3.5, we can see Al at ~1.5 ms (~1015 K). At later times, we see the strongest intermediate ions peaks, which include $Al^+$, $Al_2O^+$, $AlO^+$, $Al_2O_2^+$, $O_2^+$, $Cu^+$, $H_2^+$, and some carbon containing species of $CH_2O^+$ and $CO_2^+$. $Cu^+$ is a product from the Al/CuO thermite reaction, while $O_2^+$ is from the thermal

decomposition of the CuO nanoparticles.[21] Similar to the rapid heating of Al NPs, we also observed a strong $H_2^+$ peak, presumably from the reaction between the outward radially diffused Al and adsorbed water in the shell. Carbon containing species are likely from the decomposition of the thin layer of $CuCO_3$ on the surface of CuO nanoparticles. [21]

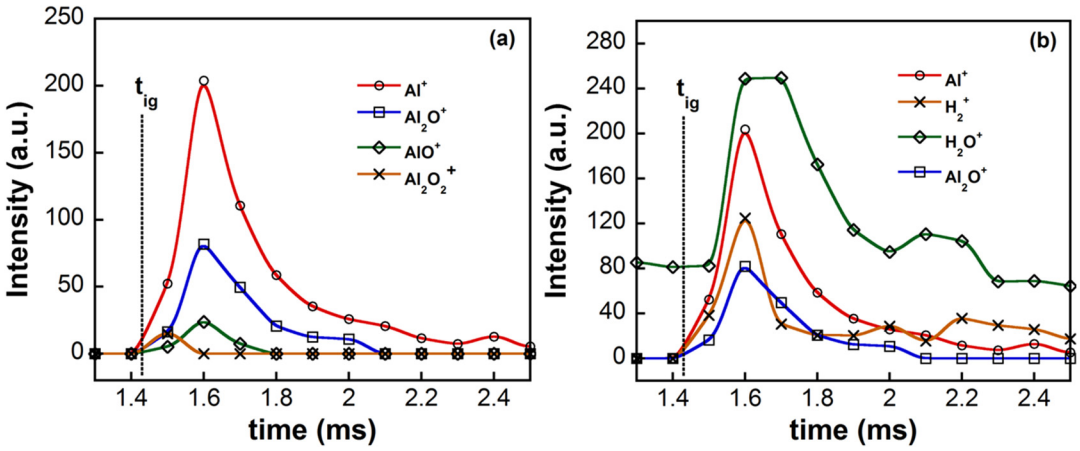


**Figure 3.6.** Time dependent evolution of (a) $Al^+$, $Al_2O^+$, $AlO^+$, $Al_2O_2^+$ and (b) $Al^+$, $Al_2O^+$, $H_2O^+$, $H_2^+$ from a fuel rich nano-Al/CuO thermite reaction.

*3.3.3. Calculated Equilibrium Mole Fraction of Alumina Decomposition and Thermite Reaction at High Temperature.*

Thermodynamic equilibrium mole fractions of $Al_2O$ and AlO products for pure alumina decomposition as well as 30wt % $Al_2O_3$+70wt % Al (similar mass ratio to Al NPs) at high temperature 1900 K to 2000 K are shown in Table 3.2 using NASA CEA code. From Table 3.2, it shows that only a small fraction of $Al_2O$ and AlO exist for both cases. Moreover, AlO mole fraction is always higher than $Al_2O$ species at high temperature from 1900~2000 K.

**Table 3.2.** Thermodynamic equilibrium mole fraction of $Al_2O$ and AlO products using NASA CEA code for aluminum oxide decomposition [a]

| Starting materials | Species | T=1900 K | T=1950 K | T=2000 K |
|---|---|---|---|---|
| Pure $Al_2O_3$ | $Al_2O$ | $2.19\times10^{-3}$ | $4.2\times10^{-4}$ | $8\times10^{-5}$ |
| | AlO | $2.691\times10^{-2}$ | $1.209\times10^{-2}$ | $5.53\times10^{-3}$ |
| 30wt% $Al_2O_3$+70wt% Al | $Al_2O$ | $3.10\times10^{-3}$ | $5.8\times10^{-4}$ | $1.2\times10^{-4}$ |
| | AlO | $1.873\times10^{-2}$ | $8.51\times10^{-3}$ | $3.91\times10^{-3}$ |

[a] Constant pressure and constant temperature thermochemical calculation. $P=10^{-9}$ atm.

Thermochemical equilibrium calculation results from the NASA CEA code for fuel rich Al/CuO thermites ($\phi$=3) are shown in Figure 3.7 at pressures of $10^{-4}$ and 1 atm. As shown in Figure 3.7a-b, Al, $Al_2O$, AlO and $Al_2O_2$ are the main products species predicted by thermodynamic calculations, in agreement with what we observed in fuel rich nano-Al/CuO thermite reaction shown in Figure 3.5. From Figure 3.7a-b, the species mole fractions predicted by thermochemical equilibrium calculation results follow the order of $Al_2O$>AlO>$Al_2O_2$, which is consistent with mass spectrometry results of nano-Al/CuO thermite reaction in Section 3.3.2.

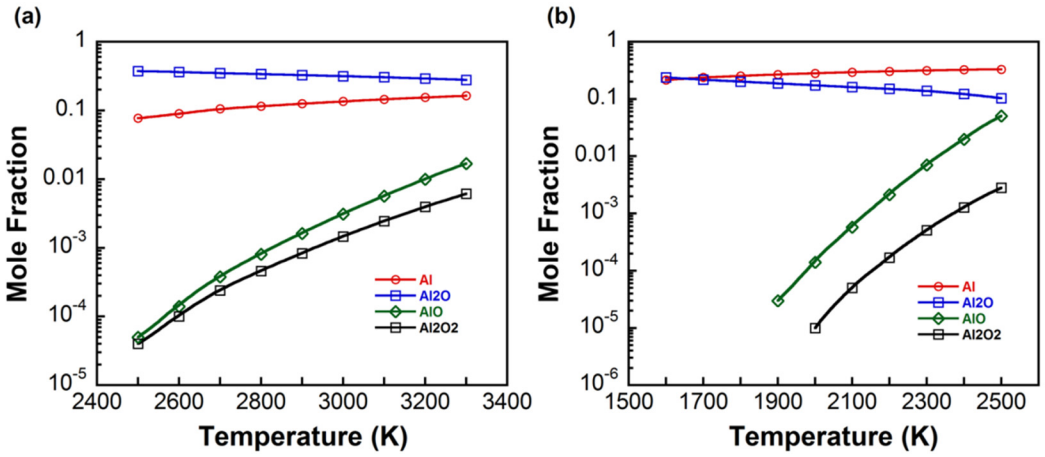


**Figure 3.7.** Calculated equilibrium mole fraction of major Al-containing species of fuel rich Al/CuO (phi=3) using NASA CEA code. Pressure: (a) 1 atm and (b) $10^{-4}$ atm. (Considering 30% $Al_2O_3$ in Al NPs by mass)

## *3.4. Discussion*

### *3.4.1. Rapid Heating of Nano-Al in Vacuum and Diffusion Based Mechanism.*

Heating of the Al-NPs to the melting point of Al, should in the absence of any constraint from the shell result in a volumetric expansion ($\rho_{Al(l)}$=2.38 g/cm$^3$, $\rho_{Al(s)}$=2.70 g/cm$^3$). Since the thermal expansion coefficient of aluminum is much larger than that of alumina (linear coefficient of aluminum being approximately four times that of alumina), it is expected that melted Al will be driven outward through the shell, or possibly rupture the shell. Nevertheless, we see no Al in the spectra (Figure 3.1a) until ~1720 K, and thus well above the melting point of elemental aluminum. One possibility for the lack of aluminum in the spectrum at temperatures above its melting point is that the aluminum diffusion does not produce a high enough signal for detection by the TOFMS. However, from prior work it is well known that the ignition temperature of nanoaluminum is well below this temperature. Another possibility is that we are observing Al containing species from the direct heating of the alumina shell. However, thermodynamic calculations (NASA CEA code) in Table 3.2 show that if that were the case we should: a) see less $AlO_2$ species with increasing temperature above 1900 K; b) the concentration of AlO should be higher than $Al_2O$. In fact we see the opposite effect with ~2.2 times higher concentration of $Al_2O$ (see calculation steps in Appendix A-Supplemental Information).

A more likely explanation for lack of aluminum at lower temperatures is that aluminum diffusing through the shell is reacting with adsorbed water in alumina shell to produce hydrogen, which we do observe in the mass spectra at 1.5 ms (~1250 K). This point will be discussed later in this part. The absence of any higher order clusters

of either Al or $AlO_x$ implies that at least up to 2030 K no catastrophic mechanical breakdown of the aluminum oxide shell has occurred. Previous in-situ high heating rate TEM experiment shows that aluminum oxide shell cracking can be seen, but no particle "spallating" was found after rapid heating to 1473 K in 1 ms, indicating that the aluminum core migrated outwards through the shell during the heating. [22]

Recent reactive molecular dynamics (MD) simulation results by Chakraborty and Zachariah suggest that the diffusion of core Al ions into the shell changes the aluminum oxide structure into the aluminum rich metastable sub-oxide shell, which can melt at a temperature considerably lower than the melting point of aluminum oxide. [23] The sudden increase in the aluminum peak at 2030 K suggests the shell is now melting, some 350 K below the reported alumina melting point, and results in a rapid increase in the rate of aluminum transport.

Our observations of $H_2$ under rapid heating of Al-NPs suggest a reaction between Al and $H_2O$ which can produce $H_2$ ($Al+3H_2O=Al(OH)_3+3/2H_2$), and an increase of $H_2O$ upon heating Al-NPs. In fact, Navrotsky et al. has reported on water adsorption in nanoscale alumina. [24] They found that up to three percent (by weight) of adsorbed water exists in both $\alpha$-$Al_2O_3$ and $\lambda$-$Al_2O_3$ alumina, and residual water (e.g. 0.48 % weight for $\lambda$-$Al_2O_3$ with a surface area of 161 $m^2/g$ ) still exists even after heating the sample in vacuum at 1023 K for 2 hours. Hence, we conclude that the increase in water intensity in the mass spectra should be from desorption of adsorbed water in the alumina shell.

Considering the above, we propose a diffusion based mechanism that Al containing species diffuse outwards through the oxide shell of Al-NPs under rapid heating shown

schematically in Figure 3.8. A typical aluminum nanoparticle is shown in Figure 3.8a with aluminum core, alumina shell and some absorbed water within the shell. Initially, the Al core melts upon rapid heating and diffuses outwards thorough the shell, and reacts with the adsorbed water in the shell to produce hydrogen (Figure 3.8b). Hydrogen is observed when the Al-NPs are heated to ~1250 K. Higher temperatures will enhance the aluminum ion-mobility through the oxide shell, which can be further enhanced by stress induced cracking or thinning of the oxide shell [22, 25] and the built-in electric field induced by the oxide shell [26]. By 1720 K, Al and $Al_2O$ species are observed (Figure 3.8c), and above T=1720 K, more Al and $Al_2O$ species migrate outwards but show a slow increase in mass spectra. With the increasing aluminum ion diffusion through the shell, and counter-diffusion of oxygen anion radially inward, the shell region thickens and leads to the formation of an aluminum rich sub-oxide shell. This sub-oxide as we have shown through molecular dynamics simulation [23] has a lower melting point than pure alumina, resulting in a much enhanced transport of aluminum. At this point ~ 2030 K (Figure 3.8d), both Al and $Al_2O$ show a significant increase, and the appearance of AlO is also seen. Based on the proposed mechanism, we make a rough estimate of the effective diffusion coefficient $D=L^2/t_{delay}$ $\sim 10^{-10}$ $cm^2/s$; where L=shell thickness and $t_{delay}$=the time difference between the melting point of the aluminum, as determined by the wire temperature and the time when we observe the first appearance of aluminum in the mass spectrometer.

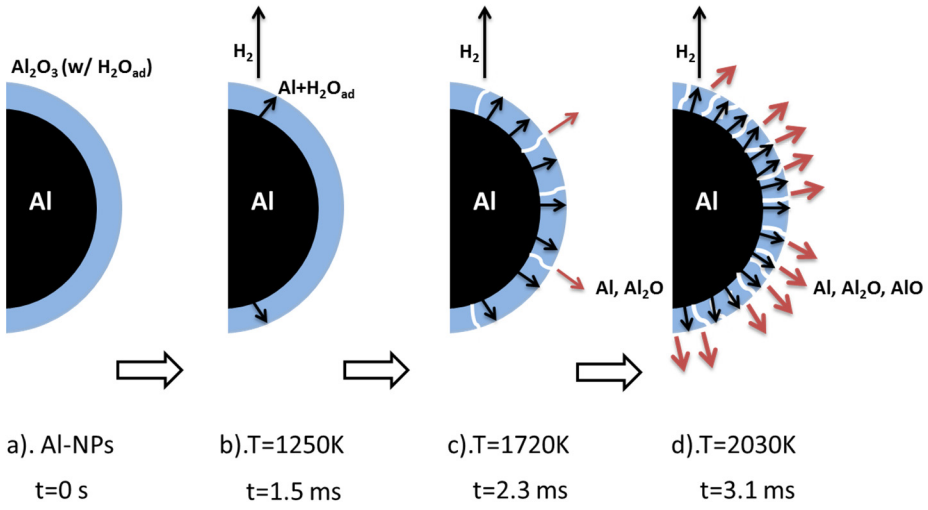


**Figure 3.8.** Schematics illustrate the rapid heating of the Al-NPs in vacuum. (a) Initial Al-NPs with Al core-$Al_2O_3$ shell structure and adsorbed water in alumina shell. (b) Upon heating to Al melting point, Al species start to diffuse outwards and react with adsorbed water to produce $H_2$. (c) At T=1720 K, more Al species diffuse/migrate outwards and start to appear in mass spectra. (d) At $T$ = 2030 K, the shell changes to suboxide and melts, more Al and $Al_2O$ diffuse/migrate outward and AlO starts to appear in mass spectra.

The lack of any observed small clusters of aluminum or aluminum oxides, as well as no catastrophic mechanical breakdown of the aluminum oxide shell below 2030 K, suggest a diffusion process in our T-Jump rapid heating experiment of the Al-NPs.

*3.4.2. Al-containing Species in Rapid Heating of Al-NPs and Nano-Al/CuO Thermite Reaction.*

Many intermediate reaction products have been found or suggested in the oxidation of the aluminum through experiments [27-32], thermodynamic calculation [33] and molecular simulation [34,35], but only AlO has been experimentally observed by in-

situ optical absorption/emission spectrum. By contrast, AlO, $Al_2O$, and $Al_2O_2$ are predicted to be the main intermediate oxidation reaction products by thermodynamic calculation [33] and MD simulation. [34] In part the difference between observation and prediction is due to the limitations of available optical transitions of the optical methods which are limited to detecting Al and AlO. Mass spectrometry method has no constraints on species type and as shown in Figure 3.1a, we find Al and $Al_2O$ as the main products species of the rapidly heated Al-NPs. A small peak of $AlO^+$ was found to appear at t=3.1 ms (2030 K), and a typical zoom in spectra with $AlO^+$ is shown in Figure 3.1b. Thus, in contrast to optical measurements, we expect $Al_2O$ as the main intermediate oxidation product based on its existence as a major intermediate species of rapidly heated Al-NPs.

Yuasa et al. has proposed the following mechanism for $Al_2O$ formation: [27]

$$Al(l) \rightarrow Al(g)$$

$$Al(g) + O_2(g) \rightarrow AlO + O$$

$$Al(g) + O + M \rightarrow AlO + M$$

$$AlO + Al(l) \rightarrow Al_2O$$

This mechanism suggests that the AlO and Al are precursors of the $Al_2O$. This mechanism was developed for the burning of micron sized aluminum in a droplet burning or diffusion flame configuration. Nanoparticles will burn much differently, [32] and typically by surface reaction processes. Moreover, unlike the mechanism above, our $O_2$ concentration as observed in Figure 3.1, are too small to account for $Al_2O$ production ( i.e. $Al_2O >> O_2$). The mechanism above implies that $Al_2O$ is formed from an AlO precursor, which we find it occur in very low to non-measurable

concentrations. Our results imply that $Al_2O$ is formed directly from the surface without volatilization of AlO.

One might expect that existence of adsorbed $H_2O$ could contribute to the production of $AlO_x$; however, $H_2^+$ and $Al_2O^+$ peaks in Figure 3.1d do not follow the same trend with increasing temperature, indicating that $Al_2O$ is not coming from direct reaction of diffused Al and adsorbed $H_2O$ in the shell. To determine if the origin of the $Al_2O$ species could be attributed to the decomposition of the rapidly heated alumina shell, $Al_2O_3$ particles (Sigma Aldrich, ≥98%) were rapidly heated to 2070 K in 3 ms and the experiment yielded no observable $Al_2O$. Moreover, Puri and Yang's simulation results have shown Al-containing fragments from 5 nm alumina particles when heated beyond 4000 K. [36] Thus we may conclude that the observed $Al_2O$ cannot be attributed to dissociation or decomposition of the oxide shell, and must involve the migration of the aluminum core atoms.

MD simulations of rapid heating Al-NPs in vacuum by Chakraborty and Zachariah have shown that Al from the core can diffuse into the shell and react with oxygen in the shell to form a metastable sub-oxide with lower O to Al ratio. [23] Similar results were also reported by Wang et al. [37] As the $Al^+$ and $Al_2O^+$ appear almost simultaneously and the intensity behaves similarly upon heating as shown in Figure 3.1c, we can speculate that $Al_2O$, might come from the reaction between diffused Al core and oxygen in the shell rather than from the dissociation of the oxide shell.

Given its existence as a major intermediate species in rapidly heated Al-NPs, we expect $Al_2O$ as one of the main intermediate oxidation product of aluminum oxidation. As shown in Figure 3.5 and Figure 3.6a, $Al^+$, $Al_2O^+$, $AlO^+$ and $Al_2O_2^+$ species

predicted by thermochemical calculations appear after ignition point, and $Al^+$ and $Al_2O^+$ are the main species similar to that seen for rapid heating of Al-NPs. In fact, $Al^+$ and $Al_2O^+$ species were also observed in our previous time-resolved mass spectrometry study of stoichiometry nano-Al/CuO. [9, 21] Time dependent species evolutions show that $Al^+$, $Al_2O^+$ and $AlO^+$ follow the same trend, while $Al_2O_2^+$ peaks earlier than other aluminum species. The earlier appearance and quick decreasing of $Al_2O_2^+$ peak may indicate that $Al_2O_2$ decomposition contributes to the formation of AlO species, which has been previously proposed by Huang *et al.* [7]

Notice that, similar to the mass spectra of rapidly heated Al-NPs, only elemental Al is observed in the mass spectra shown in Figure 3.5, and no high order Al and $AlO_x$ clusters are observed. Also, the high concentration of $H_2^+$ shown in Figure 3.5 further supports the existence of the adsorbed water. Figure 3.6b again shows that $H_2^+$ is produced by the reaction between Al and adsorbed water, which can be seen after the Al/CuO thermite reaction begins. The above results further support a diffusive mechanism in nanothermite reactions.

While prior works [28,29,32,33]have shown Al and AlO species, to our knowledge, this is the first experimental evidence of the existence of these four aluminum species during aluminum combustion and nanoparticles oxidation process.

## *3.5. Conclusions*

In conclusion, we have used T-Jump/TOFMS to investigate Al-NPs and nano-Al/CuO thermite reactions at high heating rates ~$10^5$-$10^6$ K/s. Time-resolved mass spectra were obtained for rapid heating of Al-NPs and fuel rich nano-Al/CuO thermite mixtures in which for the first time four Al-containing intermediate species

have been observed (Al, $Al_2O$, AlO, $Al_2O_2$). Temporal evolution of Al, $Al_2O$ and $H_2$ species observed in time-resolved mass spectra of rapid heated Al-NPs supports the hypothesis that Al containing species diffuse outwards through the oxide shell under high heating rate conditions.

## *3.6. Appendix A: Supplemental Information*

*3.6.S1. Temporal Evolution of Water Peak Intensity of Rapid Heating of Al-NPs up to ~ 2000 K.*

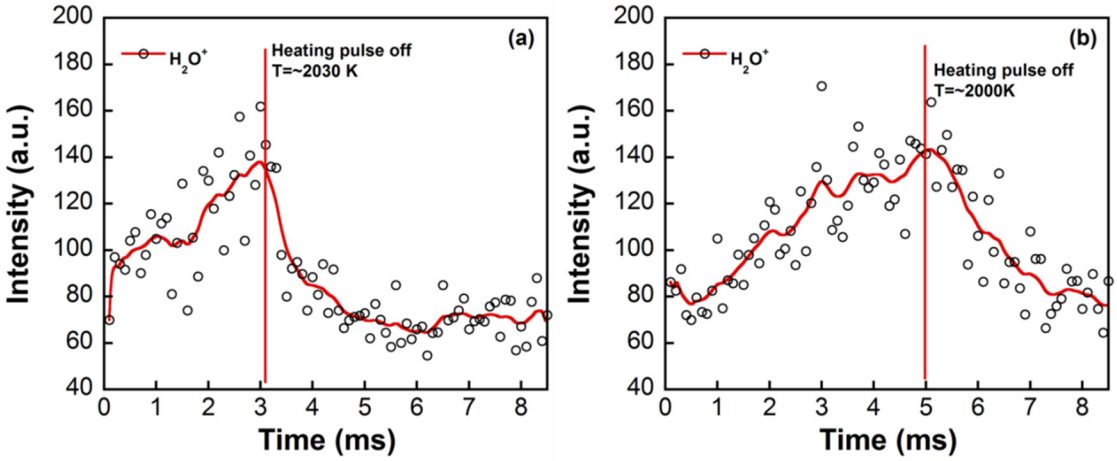


**Figure 3.S1.** Temporal evolution of water peak intensity from rapid heating of Al-NPs (a) ~3 ms heating pulse (heating rate ~$3\times10^5$ K/s) and (b) ~5 ms heating pulse (heating rate ~$6\times10^5$ K/s).

In Figure 3.S1a-b, we plot the temporal evolution of $H_2O^+$ peak intensity at two different heating pulse times (~3 ms and ~5 ms). From Figure 3.S1a-b, we can see that the $H_2O^+$ peak increases as the temperature goes up in both cases, indicating the water release from the Al-NPs upon heating.

*3.6.S2.Temporal Evolution of $H_2O^+$, $OH^+$ and $H_2^+$ Peaks Intensities of Rapid Heating of Al-NPs up to 1650 K in 3 ms.*

We plot the temporal trends for $H_2O^+$, $OH^+$ and $H_2^+$, as shown in Figure 3.S2. No $AlO_x$ and O were found in mass spectra since the maximum temperature is 1650 K. Different trends of $H_2^+$ and $OH^+$ indicate that no water decomposition process happens here. We also want to point out that we have never observed $H_2$ signal in the background mass spectra as well as the rapid heating of bare metal oxide nanoparticle cases. However, the $H_2$ peak can be seen either in rapid heating of Al-NPs or aluminum nanothermite cases, indicating the reaction of aluminum with water leading to the production of $H_2$.

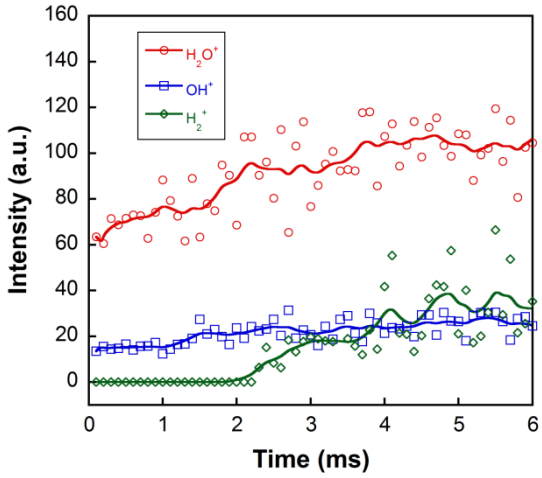


**Figure 3.S2.** Temporal evolution of $H_2O^+$, $OH^+$ and $H_2^+$ peaks intensities of rapid heating of Al-NPs up to 1650 K in 3 ms.

In Figure 3.S1a-b, we plot the temporal evolution of $H_2O^+$ peak intensity at two different heating pulse times (~3 ms and ~5 ms). From Figure 3.S1a-b, we can see that the $H_2O^+$ peak increases as the temperature goes up in both cases, indicating the water release from the Al-NPs upon heating.

*3.6.S3. Comparison of $Al_2O$ and AlO Species Concentration in TOFMS.*

By knowing the ionization cross section values for different species, we are able to calculate the partial pressures from the measured ion intensities based on the following equation Eq. (S1)

$$\mathrm{I_{Al}} = \mathrm{A}\sigma_{\mathrm{Al}}\mathrm{C_{Al}},\ \mathrm{I_{Al_2O}} = \mathrm{A}\sigma_{\mathrm{Al_2O}}\mathrm{C_{Al_2O}},\ \mathrm{I_{AlO}} = \mathrm{A}\sigma_{\mathrm{AlO}}\mathrm{C_{AlO}} \quad \text{(S1)}$$

A is the constant associated with the mass spectrometer,$\sigma_{\mathrm{Al}}$,$\sigma_{\mathrm{Al_2O}}$ and $\sigma_{\mathrm{AlO}}$ are the electron-impact cross section, $\mathrm{C_{Al}}$, $\mathrm{C_{Al_2O}}$ and $\mathrm{C_{AlO}}$ are the concentration of species. When electron beam is set at 70 eV, $\sigma_{\mathrm{Al}} \approx 7.5\ \mathrm{A}^2$, $\sigma_{\mathrm{Al_2O}} \approx 11.8\ \mathrm{A}^2$ and $\sigma_{\mathrm{AlO}} \approx 4.8\ \mathrm{A}^2$.

It is obvious that the cross section of AlO is less than half of the cross section of $Al_2O$. That means, for the same concentration of species, AlO peak in mass spectrometer should be less than half of $Al_2O$ species. However, as shown in Figure 3.1 at t=3.3 ms, $Al_2O$ intensity is ~70, while AlO intensity is ~13. A rough calculation shows that the $Al_2O$ concentration is ~2.2 times higher than AlO concentration.

$$70 = \mathrm{A} \times 11.8 \times \mathrm{C}_{Al_2O},\ 13 = \mathrm{A} \times 4.8 \times C_{AlO}$$

$$\frac{C_{Al_2O}}{C_{AlO}} \approx 2.2$$

*3.6.S4. Estimation of Background Water Flux in TOFMS.*

Since $H_2O$ is the main background species as we saw in Figure 3.1a, we need to consider the possibility of gas phase water reacting with aluminum. For our background pressure ($P \approx 4.2\times10^{-6}$ torr), the Knudsen number $K_n$>>1, and we can estimate the water vapor flux using Eq. (S2),

$$J_{H_2O} = \frac{p_{H_2O}}{N_A\sqrt{2\pi mkT}} \qquad \text{(S2)}$$

Here, $p_{H_2O}$ is the partial pressure of water vapor in vacuum, $N_A$ is the Avogadro constant, $m$ is the mass of a water molecule, $k$ is the Boltzmann constant, and $T$ is the temperature of the water vapor in vacuum. $H_2O$, $N_2$ and $O_2$ are the main three background species shown in Figure 3.1a, and the intensities of these species are identified as $I_{H_2O}$, $I_{N_2}$, $I_{O_2}$. The observed ion intensities are related to the concentration through the ionization cross-section (at same temperature).

$$I_{H_2O} = A\sigma_{H_2O}C_{H_2O}, I_{N_2} = A\sigma_{N_2}C_{N_2}, I_{O_2} = A\sigma_{O_2}C_{O_2} \quad \text{(S3)}$$

A is the constant associated with the mass spectrometer, $\sigma_{H_2O}$, $\sigma_{N_2}$ and $\sigma_{O_2}$ are the electron-impact cross section, and $C_{H_2O}$, $C_{N_2}$ and $C_{O_2}$ are the concentration of species. The calculated concentration of background species was then used to determine the partial pressure for each component, and listed in Table 3.S1.

**Table 3.S1.** Estimation of partial pressure from measured intensity in mass spectrometer [a]

| Gas Species | Intensity $I$ (a.u.) | e-impact cross section σ (Å$^2$) at 70 eV [38] | Partial pressure $p$ (Pa) |
|---|---|---|---|
| $H_2O$ | ~100 | 2.275 | ~$3.8\times10^{-4}$ |
| $N_2$ | ~40 | 2.508 | ~$1.4\times10^{-4}$ |
| $O_2$ | ~10 | 2.441 | ~$3.4\times10^{-5}$ |

[a] Pressure in ionization chamber is $P \approx 4.2\times10^{-6}$ torr $\approx 5.6\times10^{-4}$ Pa.

Using Eq. (S2), the water vapor flux $J_{H_2O}$ is estimated to be ~$3.9\times10^{-31}$ mol/(cm$^2$.s). The extremely low flux rate of water vapor in the mass spectrometer indicates that the detected hydrogen production in the mass spectrometer could not be the result of

reaction between the aluminum and gas phase water vapor, but rather absorbed water incorporated within the alumina shell.

## *3.7. References*


[1] Yetter, R. A.; Risha, G. A.; Son, S. F. *Proc. Combust. Inst.* **2009**, *32*, 1819-1838.

[2] Dreizin, E. L. *Prog. Energy Combust. Sci.* **2009**, *35*, 141-167.

[3] Wen, D. S. *Energy Environ. Sci.* **2010**, *3*, 591-600.

[4] Trunov, M. A.; Schoenitz, M.; Dreizin , E. L. *Combust. Theor. Model.* **2006**, *10*, 603-623.

[5] Firmansyah, D. A.; Sullivan, K.; Lee, K. S.; Kim, Y. H.; Zahaf, R.; Zachariah, M. R.; Lee, D. G. *J. Phys. Chem. C* **2012**, *116*, 404-411.

[6] Granier, J. J.; Pantoya, M. L. *Combust. Flame* **2004**, *138*, 373-383.

[7] Huang, Y.; Risha, G. A.; Yang, V.; Yetter, R. A. *Combust. Flame* **2009**,*156*, 5-13.

[8] Rai, A.; Park, K.; Zhou, L.; Zachariah, M. R. *Combust. Theor. Model* **2006**, *10 (5)*, 843-859.

[9] Chowdhury, S.; Sullivan, K.; Piekiel, N.; Zhou, L.; Zachariah, M. R. *J. Phys. Chem. C* **2010**, *114*, 9191-9195.

[10] Levitas, V. I.; Asay, B. W.; Son, S. F.; Pantoya, M. *Appl. Phys. Lett.* **2006**, *89*, 071909-1-3.

[11]Levitas, V. I.; Asay, B. W.; Son, S. F.; Pantoya, M. *J. Appl. Phys.* **2007**, *101*, 083524-1-20.

[12] Levitas, V. I.; Pantoya, M. L.; Dikici, B. *Appl. Phys. Lett.* **2008**, *92*, 011921-1-3.

[13] Zhou, L.; Piekiel, N.; Chowdhury, S.; Zachariah, M. R. *Rapid Commun. Mass Spectrom.* **2009**, *23*, 194-202.

[14] Zhou, L.; Piekiel, N.; Chowdhury, S.; Lee, D. G.; Zachariah, M. R. *J. Appl. Phys.* **2009**, *106*, 083306-1-8.

[15] Childs, P. R. N. *Practical Temperature Measurement,* Butterworth Heinemann: London, **2001**.

[16] Wimber, R.T.; Halvorson, J.J. *Journal of Materials, JMLSA* **1972**, *7*, 564-567.

[17] Hilpert, K. *Rapid Commun. Mass Spec.* **1991**, *5*, 175-187.

[18] Deutsch, H.; Hilpert, K.; Becker, K.; Probst, M.; Märk, T. D. *J. Appl. Phys.* **2001**, *89*, 1915-1-7.

[19] Drowart, J.; Chatillon, C.; Hastie, J.; Bonnell, D. *Pure Appl. Chem.* **2005**, *77*, 683-737.

[20] Chervonnyi, A. D. *Russ. J. Inorg. Chem.,* **2010**, *55*, 556-559.

[21] Zhou, L.; Piekiel, N.; Chowdhury, S.; Zachariah, M. R. *J. Phys. Chem. C* **2010**, *114*, 14269-14275.

[22] Sullivan, K. T.; Chiou, W. A.; Fiore, R.; Zachariah, M. R. *Appl. Phys. Lett.* **2010**, *97*, 133104-1-3.

[23] Chakraborty, P.; Zachariah, M. R. *Combust. Flame* **2013**, DOI: 10.1016/j.combustflame.2013.10.017.

[24] McHale, J. M.; Auroux, A.; Perrotta, A. J.; Navrotsky, A. *Science*, **1997**, *277*, 788-791.

[25] Sullivan, K. T.; Piekiel, N. W.; Wu, C.; Chowdhury, S.; Kelly, S. T.; Hufnagel, T. C.; Fezzaa, K.; Zachariah, M. R. *Combust. Flame* **2012**, *159*, 2-15.

[26] Henz, B. J.; Hawa, T.; Zachariah, M. R. *J. Appl. Phys.* **2010**, *107*, 024901-1-9.

[27] Yuasa, S.; Zhu, Y. X.; Sogo, S. *Combust. Flame* **1997**, *108*, 387-396.

[28] Pangilinan, G. I.; Russell, T. P. *J. Chem. Phys.* **1999**, *111*, 445-448.

[29] Wang, S. F.; Yang, Y. Q.; Sun, Z. Y.; Dlott, D. D. *Chem. Phys. Lett.* **2003**, *368*, 189-194.

[30] Moore, D. S.; Son, S. F.; Asay, B. W. *Propellants Explos. Pyrotech.* **2004,** *29*, 106-111.

[31] Piehler, T. N.; DeLucia, F. C.; Munson, C. A.; Homan, B. E.; Miziolek, A. W.; McNesby, K. L. *Appl. Opt.*. **2005**, *44*, 3654-3660.

[32] Lynch, P.; Fiore, G.; Krier, H.; Glumac, N. *Combust. Sci. and Tech.* **2010**, *182*, 842-857.

[33] Goroshin, S.; Mamen, J.; Higgins, A.; Bazyn, T.; Glumac, N.; Krier, H. *Proc. Combust. Inst.* **2007**, *31*, 2011-2019.

[34] Wang, W. Q.; Clark, R.; Nakano, A.; Kalia, R. K.; Vashishta, P. *Appl. Phys. Lett.* **2010**, *96*, 181906-1-3.

[35] Campbell, T. J.; Aral, C.; Ogata, S.; Kalia, R. K.; Nakano, A.; Vashishta, P. *Phy. Rev. B* **2005**, *71*, 205413-1-14.

[36] Puri, P.; Yang, V. *J Nanopart Res*. **2010**, *12*, 2989-3002.

[37] Wang, W. Q.; Clark, R.; Nakano, A.; Kalia, R. K.; Vashishta, P. *Appl. Phys. Lett.* **2009**, *95*, 261901-1-3.

[38] Kim, Y. K.; Irikura, K.K.; Rudd, M.E.; Ali, M.A.; Stone, P.M.; Chang, J.; Coursey, J.S.; Dragoset, R. A.; Kishore, A. R.; Olsen, K. J.; Sansonetti, A. M.; Wiersma, G. G.; Zucker, D. S.; Zucker, M. A. NIST Electron-Impact Cross Section Database, http://physics.nist.gov/PhysRefData/Ionization/molTable.html (accessed January 16, 2014).

# Chapter 4: Characterizing Oxygen Release from Metal Oxides at High Heating Rates*

## *Highlights*

(a) Effective activation energies using the Flynn-Wall-Ozawa isoconversional method are much lower than the activation energies under low heating rates.

(b) Oxygen transport may be rate controlling at high heating rates.

## *Overview*

Oxygen release from metal oxides at high temperatures is relevant to many thermally activated chemical processes, including chemical looping combustion, solar thermochemical cycles and energetic thermites. In this study, we evaluate the thermal decomposition of nanosized metal oxides under rapid heating (~$10^5$ K/s) with time-resolved mass spectrometry. We find that effective activation energies using the Flynn-Wall-Ozawa isoconversional method are much lower than the activation energies under low heating rates, indicating that oxygen transport may be rate controlling at high heating rate.

## *4.1. Introduction*

Metal oxides are employed as oxygen carriers in chemical looping combustion, [1] thermite reactions [2] and as part of a redox couple in solar thermochemical fuels

* The results presented in this chapter have been submitted in the following journal article: Jian, G.Q.; Zhou, L.; Piekiel, N.W.; Zachariah, M.R. Low Effective Activation Energies for Oxygen Release from Metal Oxides: Evidence for Mass Transfer Limits at High Heating Rates, *ChemPhysChem* **2014**, DOI: 10.1002/cphc.201301148.

production. [3] Central to each of the above applications is oxygen storage and release kinetics at high heating rates. Although extensive work has been carried out on the decomposition kinetics of solid system, [4, 5] very few studies of decomposition kinetics of metal oxides at high heating rates have been reported. The primary reason could be that the traditional quantitative measurements of the solid state reaction kinetics are usually performed by commercial thermal analysis techniques at low heating rates, [4, 5] thus fail in the measurement of the rapid chemical processes. Recently, the usage of metal oxides as oxygen carriers in combustion/explosive reactions [2] motivates the study of metal oxide decomposition at high heating rate conditions closer to that of real-time combustion events. For these investigations, a temperature-jump/time-of-flight mass spectrometer system (T-Jump TOFMS) was developed based on coupling a mass spectrometer with a pulse heating temperature-jump probe, which enables one to characterize the chemical transformations under rapid heating conditions of up to ~$10^6$ K/s in a time resolved manner. [6] The T-Jump/TOFMS system has been used to study the decomposition of nitrocellulose, RDX as well as nanothermite reactions. [6-9] Specific to our investigation of nanothermite reactions, it was found that for some cases oxygen release from the metal oxide nanoparticles as an oxidizer might be closely related to the reactivity of nanothermites. [7]

In contrast to the kinetic parameters obtained from traditional thermal analysis techniques (usually mass loss), the T-Jump/TOFMS system measures the temporal behavior of product species under high heating rate conditions, which can then be used to determine the overall activation energy based on an isoconversional approach.

Vyazovkin et al. [10] have demonstrated that effective activation energies can be derived by measuring the species produced in a heating process using mass spectrometry. White et al. [11-14] calculated the species-specific isoconversion effective activation energies, and showed that species-specific thermal analysis provides information of a specific thermal process, which could be useful for the analysis of complex reaction processes.

In this chapter, we describe a new approach to calculate the effective activation energies of nanosized metal oxide decomposition under rapid heating by measuring the chemical species produced using T-Jump/TOFMS (Figure 4.1). The effective activation energies obtained using the Flynn-Wall-Ozawa method are also compared with activation energies obtained at lower heating rates. Effective activation energies are found to be much lower than those reported at low heating rates, demonstrating the possible presence of mass transfer limitation during the reaction at high heating rates. The diffusional effects on the decomposition of nanosized metal oxides at high heating rates are analyzed.

## *4.2. Experimental Section*

### *4.2.1. Materials.*

Samples used in this study included CuO, $Fe_2O_3$ and $Co_3O_4$ nanoparticles, and were all obtained from Sigma-Aldrich, designated as <50 nm by the supplier. Transmission electron microscope (TEM, JEOL 2100F, Japan) analysis show that the primary particle size distribution is around 30-50 nm, while some particles larger than 50 nm also exist in the sample. (See Appendix A: Supplemental Information.)

*4.2.2. High Heating Rates Kinetics Measurement.*

The fast heating experiments were conducted in a temperature-jump time-of-flight mass spectrometer (T-Jump/TOFMS) at heating rates ranging from ~1 to $7\times10^5$ K/s. A schematic drawing of the T-Jump/TOFMS system is shown in Figure 4.1.

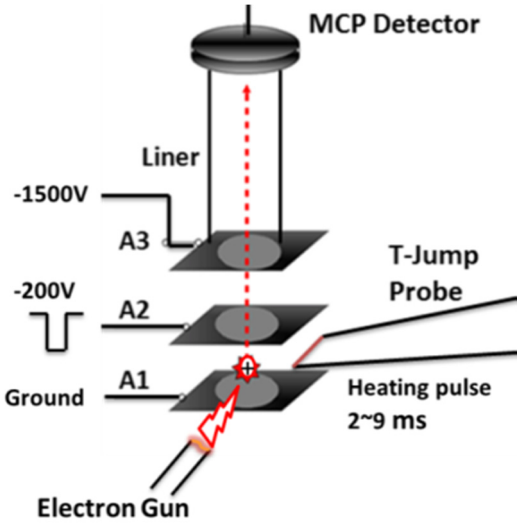


**Figure 4.1.** Schematic drawing of the T-Jump/TOFMS system.

The instrument is comprised of a linear time-of-flight chamber, an electron gun ionization source, a T-Jump probe with a platinum filament for sample heating and an in-house built power source to supply a tunable current pulse for rapid heating. The filament was inserted within the ion-extraction region of the TOF mass spectrometer, which has a background pressure of ~$10^{-6}$ torr. A detailed description of the instrument and its operating procedures can be found from in Chapter 2 and our previous papers. [6-9] The advantage of T-Jump/TOFMS system is its capability of achieving simultaneous measurement of species evolution and temperature. There is effectively no time delay between T-Jump heating probe and mass spectrometer system since the T-Jump probe is closely located in the ionization region as shown in

Figure 4.1. The product species are directly produced under high vacuum in a non-collisional environment and are transported to the micro channel plate detector in less than ~10 μs. Briefly, mass spectra are continuously recorded at a temporal resolution of 100 μs, while voltage and current data from the heating pulse are recorded simultaneously and used to calculate the temperature. By varying the duration of heating pulse from ~2-9 ms, heating rates can be changed in a range of ~1-7×$10^5$ K/s. A new Pt wire was employed for each experimental run. Time resolved mass spectra combined with temperature information were then used for characterization of the metal oxide decomposition at high heating rates.

Prior to heating, the metal oxide nanoparticles were ultrasonicated for 20 min in hexane. The prepared sample suspensions were coated on the central region of the T-Jump probe (length ~ 12 mm, diameter ~76 μm) with a pipette. A dense sample coating was formed after hexane evaporation. The mass of the coating materials on the wire was estimated to be ~90 μg by a high precision balance (readability d=0.001 mg).

*4.2.3. Low Heating Rates Kinetics Measurement.*

The slow heating experiments were conducted in a thermogravimetric analysis (TGA) system (SDT Q600, TA Instruments) under flow of argon, at a flow rate of 50 ml/min. For each run, ~5 mg sample was placed inside an alumina crucible pan and heated to the set temperature (1273 K for CuO, 1373 K for $Co_3O_4$ and 1573 K for $Fe_2O_3$) in an argon environment. Thermal analysis experiments for each sample were performed at heating rates of 5, 10, 15, 20 and 30 K/min.

## *4.3. Results and Discussion*

### *4.3.1. Oxygen Release from Nanosized Metal Oxides Measured by Temperature-Jump Mass Spectrometer.*

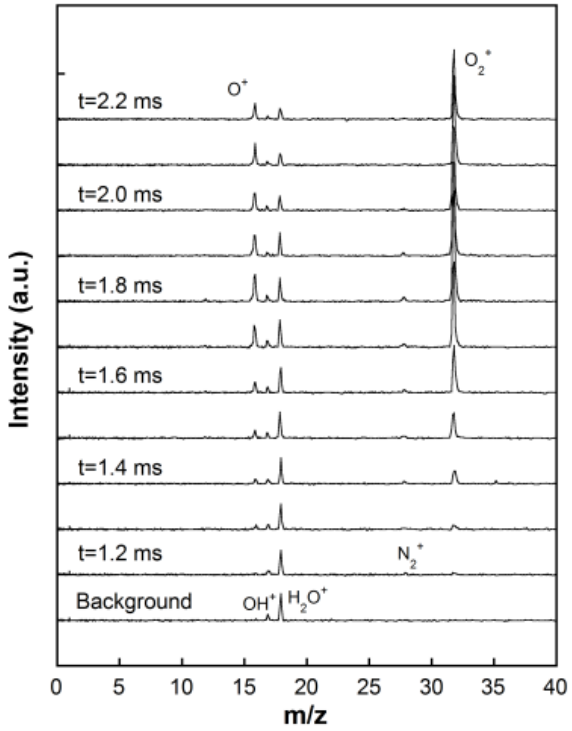


**Figure 4.2.** Time resolved mass spectra of CuO nanoparticles decomposition at a heating rate ~$6\times10^5$K/s.

Time-resolved mass spectra obtained from rapid heating of CuO nanoparticles are shown in Figure 4.2. In this experiment the heating duration is about 2.1 ms with a heating rate of ~$6\times10^5$ K/s. We selectively plot the mass spectra obtained between 1.0-2.2 ms in Figure 4.2, and a background spectrum taken at t=0 ms is also shown. As seen in Figure 4.2, a strong peak of m/z=18 ($H_2O$) and smaller peaks at m/z of 17 (OH), 28 ($N_2$), are from background species. Mass spectra taken at t=1.2-2.2 ms clearly show oxygen (m/z=16, 32) produced upon rapid heating, and its intensity

increases with increasing temperature. The temporal behaviour of $O_2$ release is presented in Figure 4.3 and shows the onset temperature of $O_2$ release is ~1020 K at a heating rate of ~$6\times10^5$ K/s for CuO nanoparticles. Figure 4.3 shows that oxygen intensity increases very fast upon heating and reaches to a peak value then starts to decrease. Since the fully release of oxygen from CuO NPs could significantly increase of the background pressure level, the oxygen intensity does not go back to initial value but remains at a relatively high level for a couple of milliseconds.

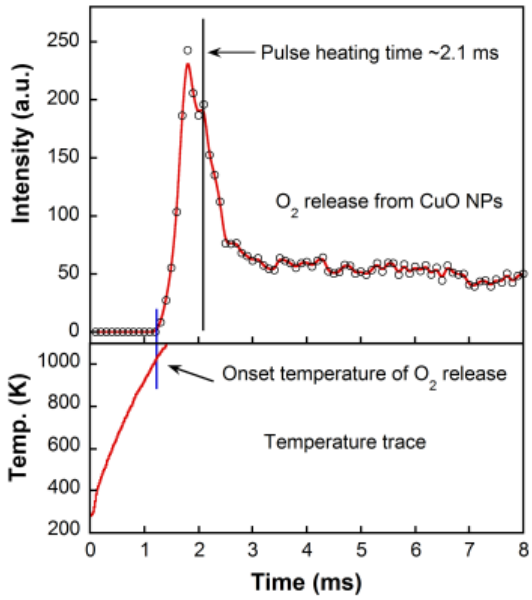


**Figure 4.3.** Temporal profile of oxygen release from rapid heating of CuO NPs at a heating rate ~$6\times10^5$K/s.

Variable heating rate experiments using the same conditions were performed to study the decomposition kinetics at heating rates from ~$1.5\times10^5$ K/s- ~$6.5\times10^5$ K/s, which enables us to extract the onset temperature of oxygen release, as shown in Figure 4.4. Similar experiments were also conducted for $Fe_2O_3$ and $Co_3O_4$ nanoparticles.

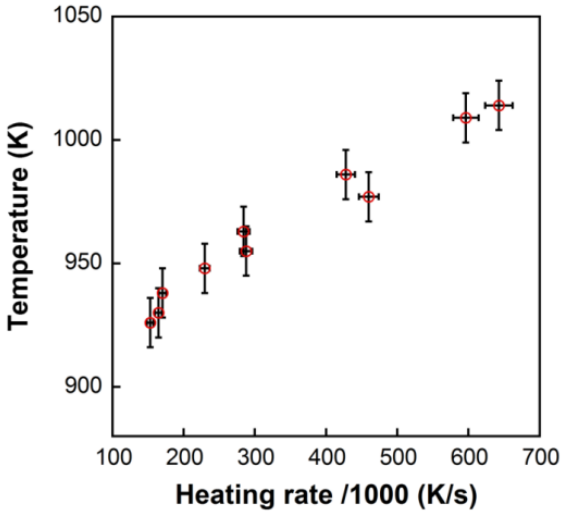


**Figure 4.4.** Oxygen release temperatures from CuO NPs as a function of heating rate. Error bars represent the standard deviation caused by the noise in resistance measurement (±10K).

*4.3.2. Activation Energy of Oxygen Release from Nanosized Metal Oxides at High Heating Rates.*

Since the decomposition of metal oxides at high temperature produces a sub-oxide and oxygen gas (e.g., CuO decomposition shown below), the measured oxygen evolution was used to evaluate effective activation energies.

$$2\mathrm{CuO}(s) \rightarrow \mathrm{Cu_2O}(s) + 0.5\mathrm{O_2}(g) \qquad (1)$$

Effective activation energies ($E_a$) were calculated from species-specific intensity versus temperature profiles using the Flynn-Wall-Ozawa method. [15-17] The isoconversion method is based on the principle that the reaction rate at constant extent of conversion is a function of only the temperature, which allows for model-free estimates of the activation energy.

Based on the single step kinetics derived from the Arrhenius equation, we can get

$$\frac{d\alpha}{dt} = \mathrm{A}exp\left(^{-\mathrm{E_a}}/_{RT}\right) f(\alpha) \quad (2)$$

Here, the subscript α is a given value of conversion, A is the pre-exponential frequency factor, $R$ is the gas constant, T is the temperature, $f(\alpha)$ is the reaction model in terms of conversion, and $\mathrm{E_a}$ is the activation energy. [18] Following the isoconversion principle, the kinetics of the solid sample reactions can be described as

$$\left[\frac{dln(^{d\alpha}/_{dt})}{dT^{-1}}\right]_{\alpha} = -\,^{E_a}/_{R} \qquad (3)$$

For non-isothermal conditions at a constant heating rate β, integration of Eq.(2) will involve solving the temperature integral I ($E_a$, T)

$$\mathrm{g}(\alpha) \equiv {}^{A}/_{\beta} \int_0^{T_\alpha} exp\left(^{-\mathrm{E}_a}/_{RT}\right) dT = {}^{A}/_{\beta}\, I(E_a, T) \qquad (4)$$

In Eq. (4), g(α) is the integral form of the reaction model. By using Doyle's linear approximation, [19] one arrives at the Flynn-Wall-Ozawa isoconversion method:

$$\ln(\beta) = \mathrm{Const.} - 1.05\,{}^{\mathrm{E}_a}/_{RT_\alpha} \qquad (5)$$

The isoconversion method is often employed because it does not require an *a priori* presumption of the reaction model to extract activation energies. [4, 5]

Detailed information regarding the interpretation and procedures of using isoconversion methods can be found in a series of publications by Vyazovkin *et al.* [4, 5, 18]

As shown in Figure 4.3 and Figure 4.4, the $O_2$ release profile can be obtained for different heating rates. For the kinetic analysis using the Flynn-Wall-Ozawa method, the effective activation energy is dependent on the extent of conversion, and will vary in some complex systems with degree of transformation in a manner that reflects the contributions of individual processes. However, we employ the T-Jump/TOFMS

system for identifying the activation energy at the initial stage of metal oxide decomposition reaction, by employing the onset temperature of $O_2$ release as the isoconversion point. The effective activation energy obtained at the initial stage of metal oxide decomposition would not be complicated by further decomposition of suboxide to pure metal and oxygen which requires much higher reaction temperature in non-reducing environments (e.g., $2Cu_2O \rightarrow 4Cu+O_2$). [20, 21]

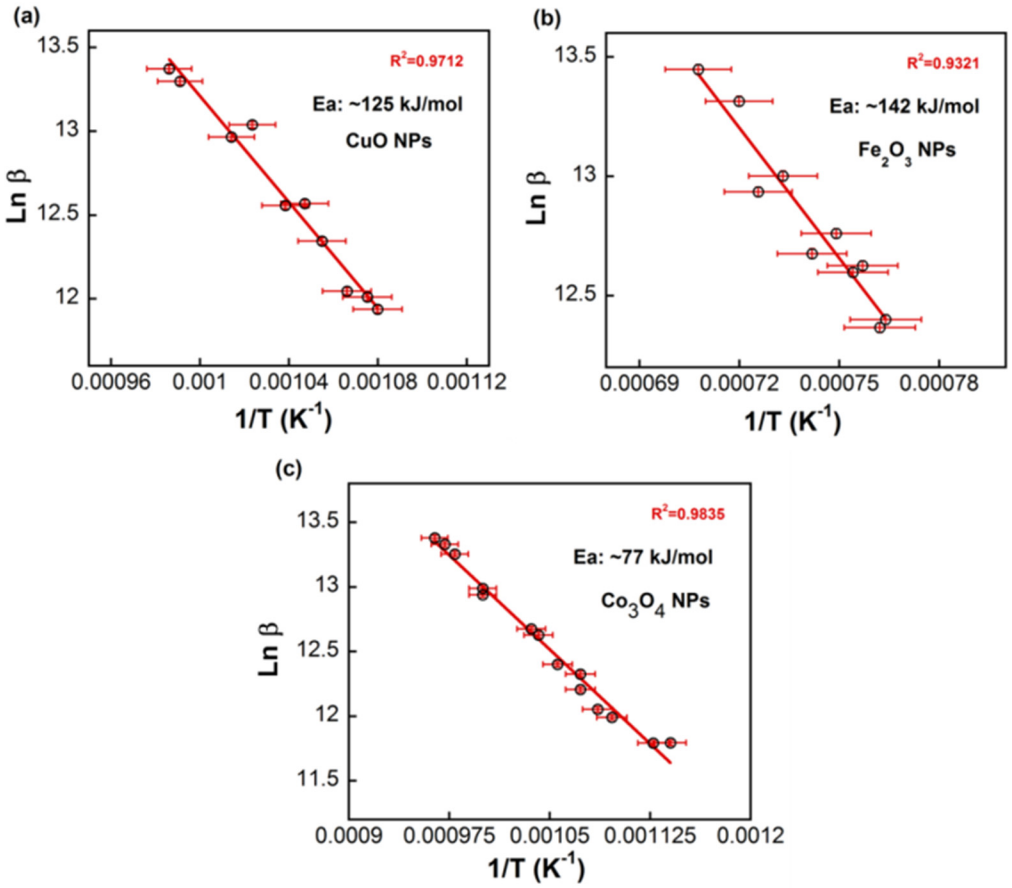


**Figure 4.5.** Natural logarithm of heating rate versus the reciprocal absolute temperature for onset oxygen release from decomposition of metal oxides nanoparticles. (a: CuO, b: $Fe_2O_3$, c: $Co_3O_4$)

By applying Eq. (5), the effective activation energies can be determined from the slope of the Arrhenius plot in Figure 4.5. The metal oxide nanoparticles in Figure 4.5 demonstrate an acceptable degree of linearity with a correlation coefficient R of 0.96 The effective activation energy calculated from m/z 32 $O_2$ ion signals temperature profile are 125±17, 144±32 and 77±6 kJ/mol for CuO, $Fe_2O_3$ and $Co_3O_4$ nanoparticles, respectively. Uncertainties were estimated based on the linear regression slope error calculated from a linear fit in Figure 4.5 with 95% confidence bounds.

**Table 4.1.** Effective activation energies measured by the isoconversional method at low and high heating rates. a. Low heating rates in TGA based on a 10 % conversion. b. High heating rates in T-Jump MS.

| Metal oxides NPs | CuO NPs | $Fe_2O_3$ NPs | $Co_3O_4$ NPs |
|---|---|---|---|
| **a.** $E_a$ (kJ/mol) | 191 | 334 | 269 |
| **b.** $E_a$ (kJ/mol) | 125 | 142 | 77 |

Our experiments which are conducted in high-vacuum are directly probing the decomposition of the metal–oxygen complex within a nanoparticle at high heating rates and the subsequent escape of molecular oxygen or a volatile metal sub-oxide.

Although most reported experiments were focused on the kinetics study of metal oxide reacting with reducing reagents (carbon, hydrogen etc.), [22-25] there exist some reported values of activation energies for direct metal oxide decomposition at low heating rates. Chadda et al. reported an activation energy for CuO decomposition

in air at low heating rates of ~313 kJ/mol. [26] A value of ~238 kJ/mol was reported for CuO decomposition in argon. [27] For $Co_3O_4$ decomposition, the activation energy was reported to be ~293 kJ/mol in argon. [27] Later, Malecki et al. reported $E_a$ of ~153 and 164 kJ/mol for $Co_3O_4$ powder and single crystal in a rough vacuum (oxygen partial pressure ~0.67 Pa). [28] As far as we are aware, no activation energy of direct $Fe_2O_3$ decomposition was reported, possibly because of the high decomposition temperature of $Fe_2O_3$ which hindered the usage of traditional thermal analysis to obtain kinetics parameters.

The previously reported activation energies in the literature are all for microsized metal oxides particles. To address this point we run the low heating rates kinetics measurements for metal oxides nanoparticles in a TGA by the same isoconversional approach. The activation energies for the initial decomposition were found to be 191, 334 and 269 kJ/mol for CuO, $Fe_2O_3$, and $Co_3O_4$ nanoparticles respectively. Obviously, the activation energies at low heating rates are much higher than those obtained values at high heating rates, as complied in Table 4.1. Additionally, we did not notice significant reduction in activation energies for nanosized metal oxides, compared to the reported values for microsized particles under low heating rates.

For condensed phase kinetics studied by the isoconversion method, the measured effective activation energies can reflect several factors such as surface properties of the solid, diffusion effects of products or/and reactants, reducing environment etc. [23, 29, 30] In particular two primary factors could contribute to the observed lower effective activation energies: size effects and high heating rates. It has been reported that kinetic parameters could change as particle size decreases into the nanoscale.

Yue et al. [31] found a diminution in the effective activation energy of up to 70-80 kJ/mol for nanosized calcite decomposition. The reduction of activation energy was also found in nanoscale metal oxidation. [32] This has been attributed to the excessive surface energies of nanoparticles. Navrotsky et al. [33, 34] studied the stability of metal oxide systems at the nanoscale, and found that nanophase metal oxides show large thermodynamic driven shifts in oxidation-reduction equilibria. Based on the available surface enthalpy data for iron oxide and cobalt oxides systems, [33, 34] we estimated the contribution of surface enthalpy of ~50 nm nanoparticles, to the total reaction enthalpy is less than ~5%, indicating that size effects could not lead to a significant lowering of the observed activation energy.

Indeed our measured activation energies for metal oxides nanoparticles (Table 4.1) at low heating rates are not much different from those reported for microsized particles. We attribute the lower activation energies to the high heating rates, which is also consistent with high heating rate micro-differential scanning calorimetery, [35] which also showed lower activation energies at high heating rates. Similar lower activation energies at high heating rates were also reported by other groups for thin film sample, biomass etc., though their heating rates are still much lower than ours. [36-38]

It is not unreasonable to assume then that at some level of heating rate, that the observed reaction rate is constrained by the oxygen transport within the material.

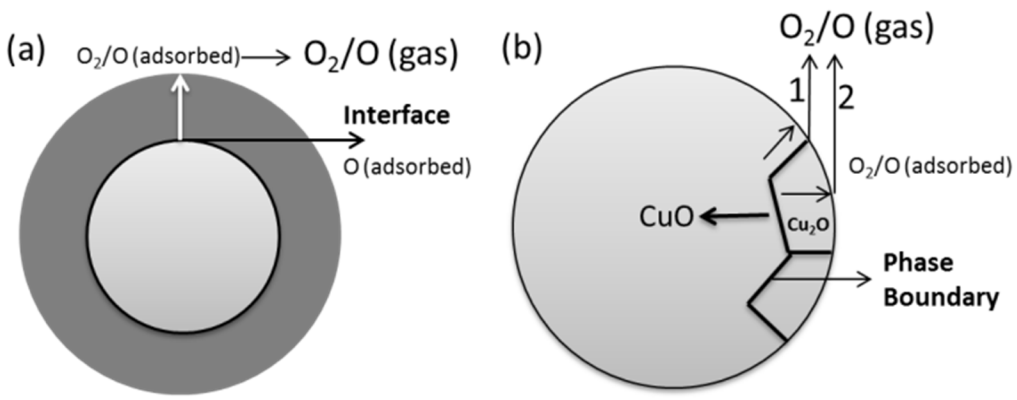


**Figure 4.6.** Models for CuO NPs decomposition: (a) a shrink core model and (b) boundary diffusion model. Note: two possible paths of phase boundary diffusion-1 and bulk diffusion-2 in (b).

In their review paper, Malinin and Tolmachev [27] summarized two different types of metal oxide decomposition pathways. Type one produces both atomic and molecular oxygen, whereas type two involves only molecular oxygen in the decomposition (e.g. $Ag_2O \rightarrow Ag$). [27, 39] Available experimental data indicate that $CuO \rightarrow Cu_2O$ and $Co_3O_4 \rightarrow CoO$ processes release both atomic and molecular oxygen and thus belong to the first type. $Fe_2O_3 \rightarrow Fe_3O_4$ has also been found to produce both oxygen atoms and molecules. [39, 40] Therefore, all three metal oxides in this study belong to the type one which produces both atomic and molecular oxygen. The generally accepted scheme for the type one decomposition is: [27, 39]

(a) $O^{2-}$ (lattice) $\rightarrow$ 2e + O (surface)

(b) 2O (surface) $\rightarrow O_2$ (adsorbed) $\rightarrow O_2$ (gas) or

2O (surface) $\rightarrow$ 2O (gas)

(c) Formation and growth of nuclei of a new phase.

Since all the materials studied in this work fall into the type one category, we use the example of CuO. The decomposition of CuO is known to form a dense product by in-situ TEM [41, 42] and scanning electron microscopy (SEM) experiments. [43] This is possibly because the initial volume of CuO does not greatly differ from the oxide products.[27] (e.g. density of CuO: 6.3 g/cm$^3$, $Cu_2O$: 6.0 g/cm$^3$) Therefore, the oxygen formed in the phase boundary should either diffuse out through bulk or grain boundary of $Cu_2O$, as shown in Figure 4.6b. Perinet et al systematically studied the oxygen self-diffusion in $Cu_2O$ by an $^{18}O$ tracer technique, and reports that neutral interstitial oxygen is responsible for the diffusion in both grain boundaries and the bulk.[44] Ideally, the decomposition process should proceed like a shrinking core model, as shown in Figure 4.6a. However, it is more likely to proceed thorough a phase boundary moving process shown in Figure 4.6b since boundary diffusion processes have a much lower energy barrier. In an *in-situ* TEM study of CuO reduction to $Cu_2O$ in vacuum, Li et al. found that grain boundaries provide easy paths for oxygen release, with an activation energy of ~106 kJ/mol.[41, 42] They estimated a diffusion coefficient of $\sim 10^{-9}$~$10^{-10}$ cm$^2$/s (at ~1000K) for oxygen diffusion in $Cu_2O$ grain boundaries, [45] which is higher than the $\sim 10^{-11}$-$10^{-12}$ cm$^2$/s value obtained for bulk $Cu_2O$. [44, 45]

If we propose as in Figure 4.6b, that oxygen diffusion occurs along the $Cu_2O$ grain boundaries, and is the rate limiting step in oxygen release at high heating rates, we can test the reasonableness of this hypothesis by estimating the diffusion time ($t_d$) for oxygen thorough the phase boundary with a simple scaling analysis, $t_d \approx L^2/D$ , where $D$ is the grain boundary diffusion coefficient $\sim 10^{-9}$-$10^{-10}$ cm$^2$/s, and $L$ is the

particle radius ~25 nm. This yields time scales on the order of milliseconds (~6-60 ms), which is consistent with the time scales we observed in our mass spectra.

If we continue our assumption, based on Li et al.[41, 42], that transport is primarily through the phase boundary we can liken this to reaction/diffusion problems that have been previously investigated for reactions within catalyst particles.[46] Borrowing directly from that analysis one can define the effectiveness factor $\eta$, as the observed reaction rate divided by the intrinsic reaction rate.

$$R_{obs}=k_{obs}f(c) = \eta k f(c) = \eta A e^{-\frac{E_a}{RT}} f(c) \quad (6)$$

where $R_{obs}$ is the observed reaction rate, $f(c)$ is dependent on the reactant concentration, $k$ is the intrinsic reaction rate constant, and A is pre-exponential factor, and $E_a$ is the intrinsic chemical activation energy.

In the limit of low effectiveness factors $\eta$ (internal diffusion controlled) is

$$\eta \propto h_T \quad (7)$$

$h_T$ is the Thiele modulus, and its square is proportional to the ratio of the reaction to diffusion. Based on its definition, we can get

$$h_T \propto \sqrt{\frac{k}{D_c}} \quad (8)$$

where $D_c$ is the diffusivity of oxygen species. From eqs. 6-8, we can get

$$k_{obs} \propto \frac{k}{\sqrt{\frac{k}{D_c}}} = \sqrt{kD_c} \quad (9)$$

Diffusivity $D_c$ (oxygen diffusivity in phase boundary) can be written as

$$D_c = \mathrm{A}_d e^{-\frac{E_d}{RT}} \quad (10)$$

where $\mathrm{A}_d$ is a temperature independent quantity and $\mathrm{E}_d$ is the activation energy for diffusion process, then we can get

$$k_{obs} \propto \sqrt{kD_c} = \sqrt{\left(Ae^{-\frac{E_a}{RT}}\right)\left(A_d e^{-\frac{E_d}{RT}}\right)}$$

$$= A^{1/2} \times {A_d}^{1/2} e^{-\frac{(E_a+E_d)}{2RT}} \quad (11)$$

and

$$E_{eff} = \frac{(E_a+E_d)}{2} \sim \frac{E_a}{2} \quad (12)$$

From eqs. 12, the effective activation energy $E_{eff}$ in the limit of transport control reduces to half the intrinsic chemical activation energy. In other words, at high heating rates, oxygen donation from oxygen carriers is limited by condensed state transport processes.

## *4.4. Conclusions*

In conclusion, we employ T-Jump/TOFMS to study the kinetics of decomposition for three metal oxide nanoparticles (CuO, $Fe_2O_3$ and $Co_3O_4$) at high heating rates of ~$10^5$K/s. The isoconversion effective activation energies were calculated based on the time-resolved mass spectra information and temperature profiles, and are found to be significantly lower than activation energies at slow heating rates. The lower activation energies obtained in this study implies that even for nanoparticles which have small diffusional length scales, high heating rates can result in a situation where mass transfer constraints are observed. This should have implication on how systems that employ metal oxides as oxygen carrier are selected. The results imply that the choice of oxygen carrier/donor is not simply selected on the thermochemical constraints.

## *4.5. Appendix A: Supplemental Information*

### *4.5.S1. TEM Images of Commercial CuO, $Fe_2O_3$ and $Co_3O_4$ Nanoparticles.*

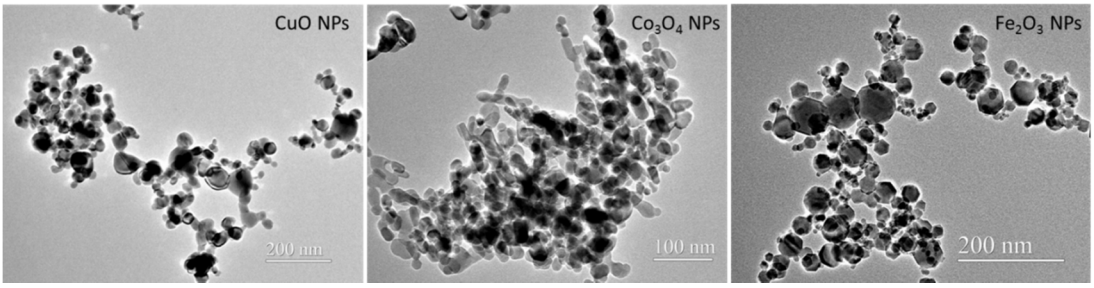


**Figure 4.S1.** TEM images of CuO, $Fe_2O_3$ and $Co_3O_4$ nanoparticles.

### *4.5.S2. Oxygen Release Profile of Heating CuO Nanoparticles at a Heating Rate of ~$3\times10^3$ K/s.*

At a relatively low heating rate (~$3\times10^3$ K/s), we were able to differentiate the two individual processes, as shown in Figure 4.S2.

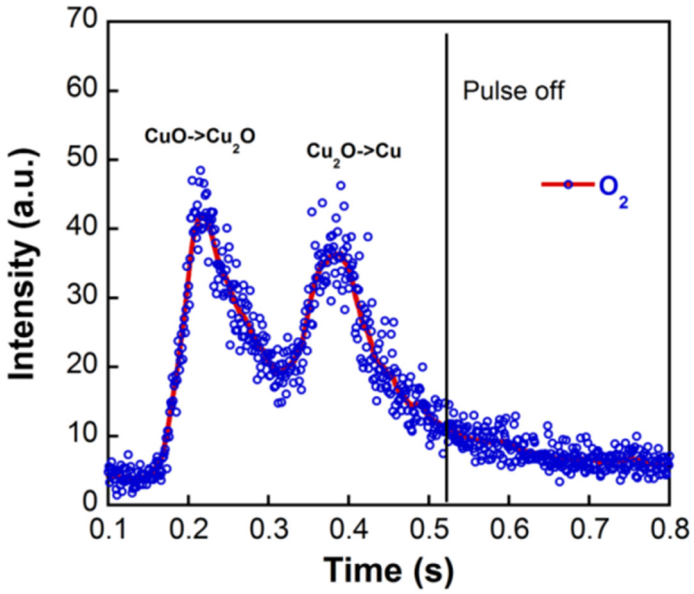


**Figure 4.S2.** $O_2$ release profile for CuO NPs at a heating rate of ~$3\times10^3$ K/s. (Heating pulse: 0.53 s, final temperature: 2000 K.)

*4.5.S3. Mass Spectrometry Results of Oxygen Release from CuO Nanoparticle at a Heating Rate of 10 °C/min in the Argon Environment.*

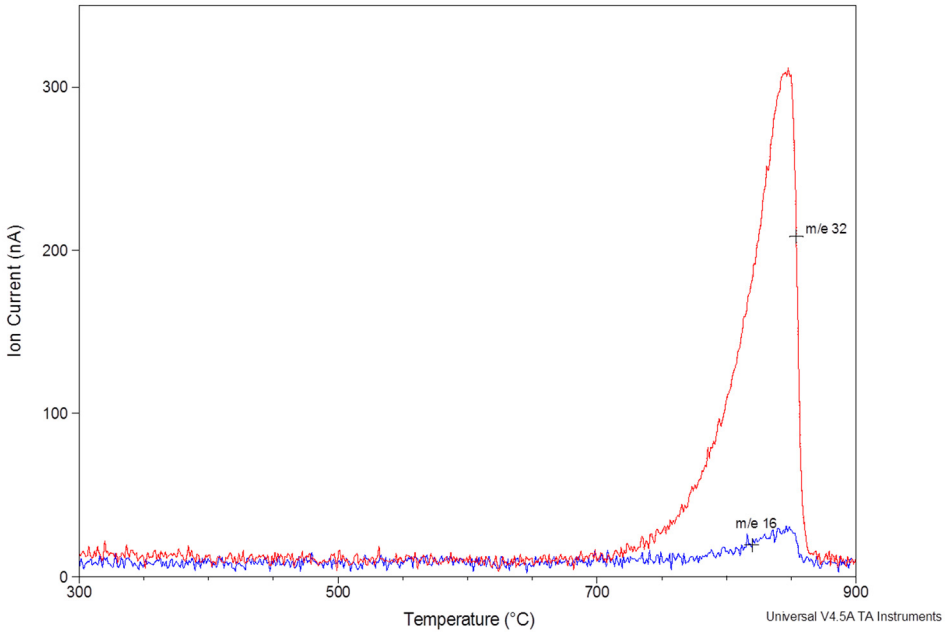


**Figure 4.S3.** Mass spectrometry results of oxygen release from metal oxide NPs at a heating rate of 10 °C/min.

CuO nanoparticles were heated at a heating rate of 10 °C/min in the argon flow. The experiments were run in a thermogravimetric analysis (TGA)-mass spectrometer (MS) system (SDT Q600 and Discovery MS, TA Instruments) under flow of argon, at a flow rate of 50 ml/min.

*4.5.S4. The Ratio of $O_2$/O in Mass Spectra (Figure 4.2) Measured by the Mass Spectrometry during Rapid Heating.*

Oxygen gas was purged into our T-Jump mass spectrometer system via a leak valve, and the ionization pattern at 70 eV shows a ratio of $O_2$/O ~5.2, which is very similar to the results ($O_2$/O ratio ~5) shown in NIST/EPA/NIH Mass Spectral Library.

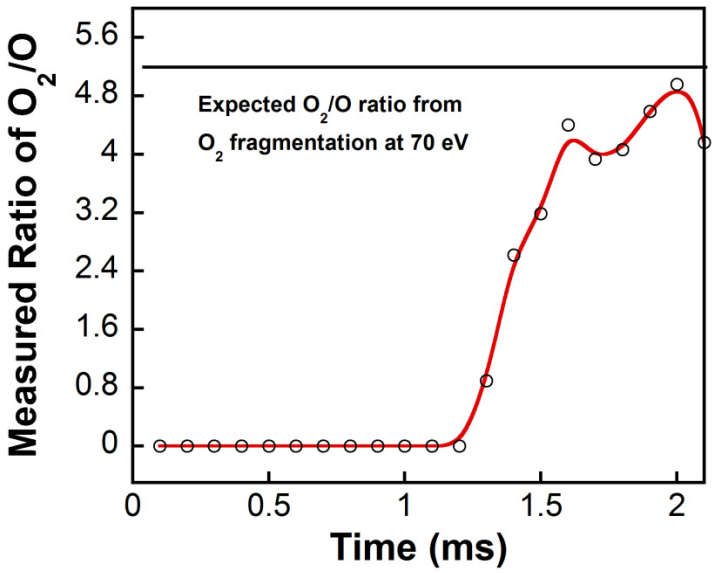


**Figure 4.S4.** The ratio of $O_2$/O in mass spectra (Figure 4.2) measured by the mass spectrometry during rapid heating. Note: Expected $O_2$/O ratio was estimated based on ionization pattern of pure $O_2$ at 70 eV.

## *4.6. References*

[1] Cho, P.; Mattisson, T.; Lyngfelt, A. *Fuel* **2004**, *83*, 1215-1225.

[2] Dreizin, E. L. *Prog. Energy Combust. Sci.* **2009**, *35*, 141-167.

[3] Steinfeld, A. *Solar Energy* **2005**, *78*, 603-615.

[4] Vyazovkin, S.; Wight, C.A. *Annu. Rev. Phys. Chem.* **1997**, *48*, 125-149.

[5] Vyazovkin, S. *Int. Rev. Phys. Chem.* **2000**, *19*, 45-60.

[6] Zhou, L.; Piekiel, N.; Chowdhury, S.; Zachariah, M. R. *Rapid Commun. Mass Spectrom.* **2009**, 23, 194-202.

[7] Zhou, L.; Piekiel, N.; Chowdhury, S.; Zachariah, M. R. *J. Phys. Chem. C* **2010**, *114*, 14269-14275.

[8] Jian, G.Q.; Piekiel, N.W.; Zachariah, M.R. *J. Phys. Chem. C* **2012**, *116*, 26881-26887.

[9] Jian, G.Q.; Chowdhury, S.; Sullivan, K.; Zachariah, M.R. *Combust. Flame* **2013**, *160*, 432-437.

[10] Vyazovkin, S.; Goryachko, V.; Bogdanova, V.; Guslev, V. *Thermochim. Acta* **1993**, *215*, 325-328.

[11] Bonnet, E.; White, R.L. *Thermochim. Acta* **1998**, *311*, 81-86.

[12] White, D.R.; White, R.L. *J. Appl. Polym. Sci.* **2005**, *95*, 351-357.

[13] White, R.L. *Int. J. Mass Spectrom.* **2009**, *287*, 128-133.

[14] White, D.R.; White, R.L. *Appl. Spectrosc.* **2008**, *62*, 116-120.

[15] Ozawa, T. *Bull. Chem. Soc. Jpn.* **1965**, *38*, 1881-1886.

[16] Flynn, H.; Wall, L.A. *J. Res. Natl. Bur. Stand.* **1966**, *70A*, 487-523.

[17] Ozawa, T. *Thermochim. Acta* **1992**, *203*, 159-165.

[18] Vyazovkin, S.; Sbirrazzuoli, N. *Macromol. Rapid Commun.* **2006**, *27*, 1515-1532.

[19] Doyle, C. D. *J. Appl. Polym. Sci.* **1962**, *6*, 639-642.

[20] Roberts, H. S.; Smyth, F.H. *J. Am. Chem. Soc.* **1921**, *43*, 1061-1079.

[21] Galvita, V.V.; Poelman, H.; Rampelberg, G.; Schutter, B.D.; Detavenier, C.; Marin, G.B. *Catal. Lett.* **2012**, *142*, 959-968.

[22] Arjmand, M.; Keller, M.; Leion, H.; Mattisson, T.; Lyngfelt, A. *Energy Fuels* **2012**, *26*, 6528-6539.

[23] Tiernan, M.J.; Barnes, P.A.; Parkes, G.M.B. *J.Phys.Chem.B* **1999**, *103*, 338-345.

[24] Kim, J.Y.; Rodriguez, J.A.; Hanson, J.C.; Frenkel, A.I.; Lee, P.L. *J. Am. Chem. Soc.* **2003**, *125*, 10684-10692.

[25] Pineau, A.; Kanari, N.; Gaballah, I. *Thermochim. Acta* **2006**, *447*, 89-100.

[26] Chadda, D.; Ford, J.D.; Fahim, M.A. *Int. J. Energy Res.* **1989**, *13*, 63-73.

[27] Malinin, G.V.; Tolmachev, Y.M. *Russian Chemical Reviews* **1975**, *44*, 392-397.

[28] Malecki, A.; Prochowska-Klisch, B. *J. Therm. Anal.* **1994**, *41*, 1109-1117.

[29] Maciejewski, M. *J. Therm. Anal*. **1992**, *38*, 51-70.

[30] Vyazovkin, S. *Thermochim. Acta* **2003**, *397*, 269-271.

[31] Yue, L.H.; Shui, M.; Xu, Z.D. *Thermochim. Acta* **1999**, *335*, 121-126.

[32] Song, P.X.; Wen, D.S.; Guo, Z. X.; Korakianitis, T. *Phys. Chem. Chem. Phys.* **2008**, *10*, 5057–5065.

[33] Navrotsky, A.; Ma, C.C.; Lilova, K.; Birkner, N. *Science* **2010**, *330*, 199-201.

[34] Navrotsky, A. *ChemPhysChem* **2011**, *12*, 2207-2215.

[35] Piekiel, N.W.; Cavicchi, R.E.; Zachariah, M.R. *Thermochim. Acta* **2011**, *521*, 125-129.

[36] Choi, Y.; Jung, M.; Lee, Y.K. *Electrochem. Solid-State Lett.* **2009**, *12*, F17-F19.

[37] Fushimi, C.; Araki, K.; Yamaguchi, Y.; Tsutsumi, A. *Ind. Eng. Chem. Res.* **2003**, *42*, 3922-3928.

[38] Chen, D.T.Y. *J. Therm. Anal.* **1975**, *7*, 61-64.

[39] Galwey, A.K.; Brown, M.E. *Thermal Decomposition of Ionic Solids, Volume 86: Chemical Properties and Reactivities of Ionic Crystalline Phases* (Studies in Physical and Theoretical Chemistry), Elsevier Science, **1999**, 1st edition.

[40] Bergermayer, W.; Schweiger, H.; Wimmer, E. *Phys.Rev.B* **2004**, *69*, 195409-1-12.

[41] Li, J.; Wang, S.Q.; Mayer, J.W.; Tu, K.N. *Phys. Rev. B* **1989**, *39*, 12367-12372.

[42] Li, J.; Mayer, J.W. *Mater. Chem. Phys.* **1992**, *32*, 1-24.

[43] Sullivan, K.T.; Piekiel, N.W.; Wu, C.; Chowdhury, S.; Kelly, S.T.; Hufnagel, T.C.; Fezzaa, K.; Zachariah, M.R. *Combust. Flame* **2012**, *159*, 2-15.

[44] Perinet, F.; Duigou, J.L.; Monty, C. *in Non-Stoichiometric Compounds Surfaces, Grain Boundaries and Structural Defects;* Nowotny, J.; Weppner, W., Ed.; Kluwer Academic Publishers: Boston, **1989**; Vol. *276*; p 387-397.

[45] Moore,W.J.; Selikson, B. *J. Chem. Phys.* **1951**, *19*, 1539-1543.

[46]Hill, C.G. *An Introduction to Chemical Engineering Kinetics and Reactor Design*, Wiley: **1977**.

# Chapter 5: Aerosol Synthesis of Hollow CuO Spheres as Oxidizers in Nanoenergetic Gas Generators [*]

## *Highlights*

(a) Hollow CuO spheres with nanosized building blocks are fabricated using a "droplet-to-particle" aerosol spray pyrolysis method.

(b) Hollow structure is produced by adding sucrose and $H_2O_2$ in the precursor solution as gas blowing agents.

(c) The nanoaluminum thermite with hollow CuO as oxidizer ignites in a very violent manner and significantly outperforms commercial CuO nanoparticles in both pressurization rate and peak pressure.

## *Overview*

Thermochemical metal/metal oxide redox reactions have twice the energy density of 2, 4, 6-trinitrotoluene (TNT). They suffer, however, from low pressure-volume work due to low gas expansion from the reaction. This study focuses on the development of a nanocomposite that delivers a high energy density and the potential of rapid gas release. Hollow CuO spheres with nanosized building blocks are fabricated using a "droplet-to-particle" aerosol spray pyrolysis method with the introduction of gas-blowing agents in the synthesis procedure. Nanoaluminum with hollow CuO as an oxidizer ignites in a very violent manner and exhibits excellent

[*] The results presented in this chapter have been published in the following journal article: Jian, G.Q.; Liu, L.; Zachariah, M.R. Facile Aerosol Route to Hollow CuO Spheres and its Superior Performance as an Oxidizer in Nanoenergetic Gas Generators, *Adv. Funct. Mater.* **2013**, *23*, 1341-1346.

gas-generation behavior, demonstrating a high pressurization rate of 0.745 MPa $\mu s^{-1}$ and a transient peak pressure of 0.896 MPa with a charge density of 1 mg $cm^{-3}$, as well as a rapid oxygen release. Compared with wet-chemistry methods, gas-phase processes are relatively low cost, nominally offer a higher purity product, and are usually configured as continuous production processes, with a limited number of steps. The synthesis strategy demonstrated is simple and should be extendable to the preparation of other hollow metal oxide structures.

## *5.1. Introduction*

Hollow metal oxide micro/nanostructures are of interest for their potential applications in catalysis, nano-/microreactors, energy storage and conversion, drug delivery, and chemical sensors. [1-7] Several methods have been employed to fabricate hollow metal oxide structures, which can be broadly classified as templating and template-free methods. [1-3, 8, 9] Although hard-template methods are effective in producing well-defined structures, the synthetic procedures can be complex and involve a template-removal step. Recently, processes based on Ostwald ripening have been employed as a template-free strategy to produce metal oxide hollow structures, [3] through an "inside-out" mechanism. [10, 11] In this approach, nanocrystallites in the core of colloidal aggregate, which are energetically less stable, dissolve, diffuse out, and redeposit to the outer surface, leading to a continuous evacuation of the core materials and the formation of the hollow structure. Compared with wet-chemistry methods, gas-phase processes are relatively low cost, nominally offer a higher purity product, and usually are configured as continuous production processes, with a limited number of steps. In fact, many modifications of gas-phase methods including

chemical vapor deposition, sputtering, microplasma synthesis, combustion and flame, and aerosol/spray pyrolysis have been developed and aim to achieve large-scale industrial production of nanoparticles. [12-16] Among these methods, aerosol/spray pyrolysis offers the advantages of simplicity, high purity, relatively low cost, environmental friendliness, and continuous production. [15, 16]

Nanoenergetic materials, or so called nanothermites, a subset of metastable intermolecular composites (MIC), are a relatively new class of energetic materials comprising a metallic fuel and an oxidizer at the nanoscale that can rapidly release heat and pressure. They have found application as propellants and explosives, as well as in propulsion power in micro-/nanoelectromechanical systems (MEMS/NEMS).[17-19] In most formulations, aluminum is employed as the fuel because of its high reaction enthalpy and ready availability, and low-cost metal oxides such as CuO and $Fe_2O_3$ are commonly used as oxidizers (Eqs. 1): [17]

$$Al + \frac{3}{2} MO \rightarrow \frac{1}{2} Al_2O_3 + \frac{3}{2} M + \Delta H \qquad (1)$$

In nanoenergetic-material formulations, the use of nanoparticles is primarily used as a means to reduce diffusion lengths between reactive components, and to increase the contact area between the fuel and the oxidizer. As a result, an enhanced flame-propagation rate of the wave front and energy-release rate of the nanoenergetic materials (up to three orders of magnitude) can be achieved compared with their corresponding microsized formulations. [20] Moreover, it has been demonstrated that increasing the interfacial contact area between the oxidizer and the fuel at the nanoscale can significantly improve the performance of nanoenergetic formulations. [21-24] In particular, Al/CuO has been found to be a very vigorous formulation that

can rapidly release a large amount of gaseous products and will be the subject of this chapter. [25-27]

In this chapter, we focus on developing an Al/CuO nanocomposite that can deliver a high energy density and with the potential of rapid gas release. For this purpose, we have developed a novel and facile approach to fabricate hollow CuO spheres by a "droplet-to-particle" aerosol spray pyrolysis route. In particular, the shells of hollow CuO spheres were found to comprise ≈10 nm CuO nanoparticles as building blocks, indicating their potential large interfacial contact with fuel nanoparticles when forming a nanocomposite with aluminum nanoparticles. The energetic performance of the as-prepared nanocomposites that contained hollow CuO spheres was then tested for their combustion behavior and enhanced performance was found.

## *5.2. Experimental Section*

### *5.2.1. Aerosol Spray Pyrolysis and Material Characterization.*

Hollow CuO spheres were prepared by an aerosol spray pyrolysis method as illustrated in Scheme 5.1. 0.9664 g (0.004 mol) of copper nitrate trihydrate ($Cu(NO_3)_2 \cdot 3H_2O$) (Strem Chemical), 0.1711 g ($5.0 \times 10^{-4}$ mol) of sucrose ($C_{12}H_{22}O_{11}$) (Sigma-Aldrich) and 5 mL of hydrogen peroxide solution (30 wt%. $H_2O_2$) (Sigma-Aldrich) were dissolved into 45 mL of water. Aerosol droplets containing the dissolved precursors were generated using compressed air at a pressure of 0.24 MPa in a collision-type atomizer. The geometric mean diameter of the droplets was measured to be ≈1 μm using a laser aerosol spectrometer. The produced aerosol droplets were passed through a silica-gel diffusion dryer to remove most of the solvent, and passed to a tube furnace at 600 °C. The normal residence time was

around 1 s for a total gas flow rate of 3.5 L $min^{-1}$.The products were collected on a 0.4 µm (pore size) HTTP Millipore filter and further heated at 350 °C for 1 h in air to remove any possible carbon residue in the sample. As a comparison, CuO particles were also synthesized through the same process with no sucrose and $H_2O_2$ added to the precursor solution. Typical product yields exceeded 30%. Online particle-size measurement was obtained by using a home-built differential mobility analyzer (DMA) system and a condensation particle counter (CPC) (CPC model 3025, TSI Inc.). The materials were characterized by transmission electron microscopy (TEM) and selected area electron diffraction (SAED) (JEOL JEM 2100F), scanning electron microscopy (SEM) (Hitachi, SU-70 FEG-SEM) and powder X-ray diffraction (XRD) (Bruker D8 Advance using Cu $K_\alpha$ radiation).

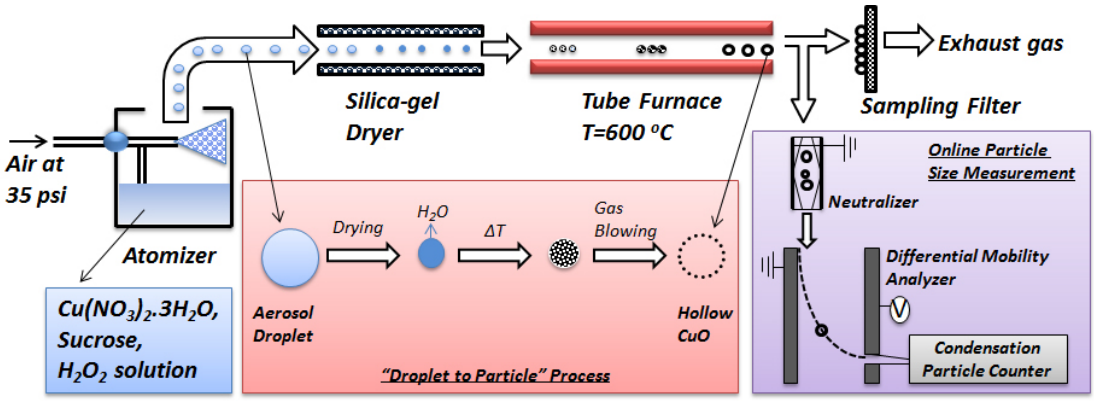


**Figure 5.1.** Illustration of aerosol spray pyrolysis route to hollow CuO spheres and online particle size measurement system.

*5.2.2. Combustion Cell Characterization.*

CuO oxidizers were mixed with aluminum nanoparticles with 70 % active Al determined by TGA (Argonide Corporation, designated as 50 nm ALEX) with a

stoichiometric ratio. Approximately 10 mL of hexane was then added and the thermite mixture was ultrasonicated for 30 min to ensure intimate mixing. After the evaporation of hexane in air, the powder was then gently broken apart. A constant-volume combustion cell (≈13 $cm^3$) was used to measure the pressure and optical emission of thermite sample simultaneously. [27] In this study, 12.5 mg of the loose thermite sample was placed inside the combustion cell and ignited by Joule heating of a nichrome coil on top of the loose powder. One attached piezoelectric pressure transducer together with an in-line charge amplifier and signal conditioner were used to measure the pressure change. The optical signal was simultaneously collected by a lens tube assembly, containing a planoconvex lens ($f$ = 50 mm) and a photodetector to collect the broadband emission. In comparison, commercial CuO nanoparticles (<50 nm) (Sigma-Aldrich) were also tested as an oxidizer in the combustion cell.

*5.2.3. Time-Resolved Mass Spectrometry Measurement and High-Speed Imaging*.

The recently developed temperature-jump/time-of-flight mass spectrometer (T-Jump/TOFMS) was used to study the oxygen release from the CuO oxidizers. [26] Typically, a ≈10 mm-long Pt wire (76 μm) was coated with a thin layer of CuO sample powder (ultrasonicated in hexane for 30 min). The coated wire was rapidly heated to approximately 1800 K at a heating rate of $5 \times 10^5$ K $s^{-1}$. Time-resolved mass spectra combined with wire temperature were then used for characterization of the species produced during the rapid heating. High-speed digital-video imaging of sample combustion on the wire was conducted using a Vision Research Phantom v12.0 digital camera. The high-speed video was taken at a resolution of 256 × 256 pixels and a frame rate of 67065 fps (14.9 μs per frame).

## *5.3. Results and Discussions*

### *5.3.1. Hollow-CuO-Sphere Synthesis and Characterization.*

A schematic illustration for the preparation and online particle-size measurement of hollow CuO nanospheres is presented in Figure 5.1. The process is a "droplet-to-particle" aerosol spray pyrolysis approach, whereby precursor solutions are atomized and decomposed thermally to form particles. The key to the formation of the hollow CuO structure with small nanoparticles as building blocks is the introduction of sucrose and hydrogen peroxide ($H_2O_2$) to the copper nitrate starting solution as an in situ blowing agent. As shown in Scheme 5.1, online particle-size characterization is used to obtain the size distribution of the product particles.

Scanning electron microscopy (SEM) and transmission electron microscopy (TEM) images, (Figure 5.2a, b) show that the as-prepared particles have hollow structures comprising a thin shell with a 5-10 nm wall thickness. The High-resolution TEM (HR-TEM) image shown in Figure 5.2c confirms the shell of the hollow structure is actually an assembly of ≈10 nm nanoparticles. The inset lattice-fringe image shown in Figure 5.2c shows a crystallinity that is indexed to the monoclinic phase of CuO, which was further verified with a bulk sample from by X-ray diffraction (XRD), as shown in Figure 5.2e. To ensure the removal of any carbon residue as a remnant of the sucrose, the as-collected samples were further heated in air at 350 °C for 1 h. The TEM images in Figure 5.3 show no observable morphology change as compared with Figure 5.2b, c, indicating no phase growth occurred during heating. The XRD and the selected area electron diffraction (SAED) results in Figure 5.3b confirm the single phase of CuO (JCPDS No. 48-1548).

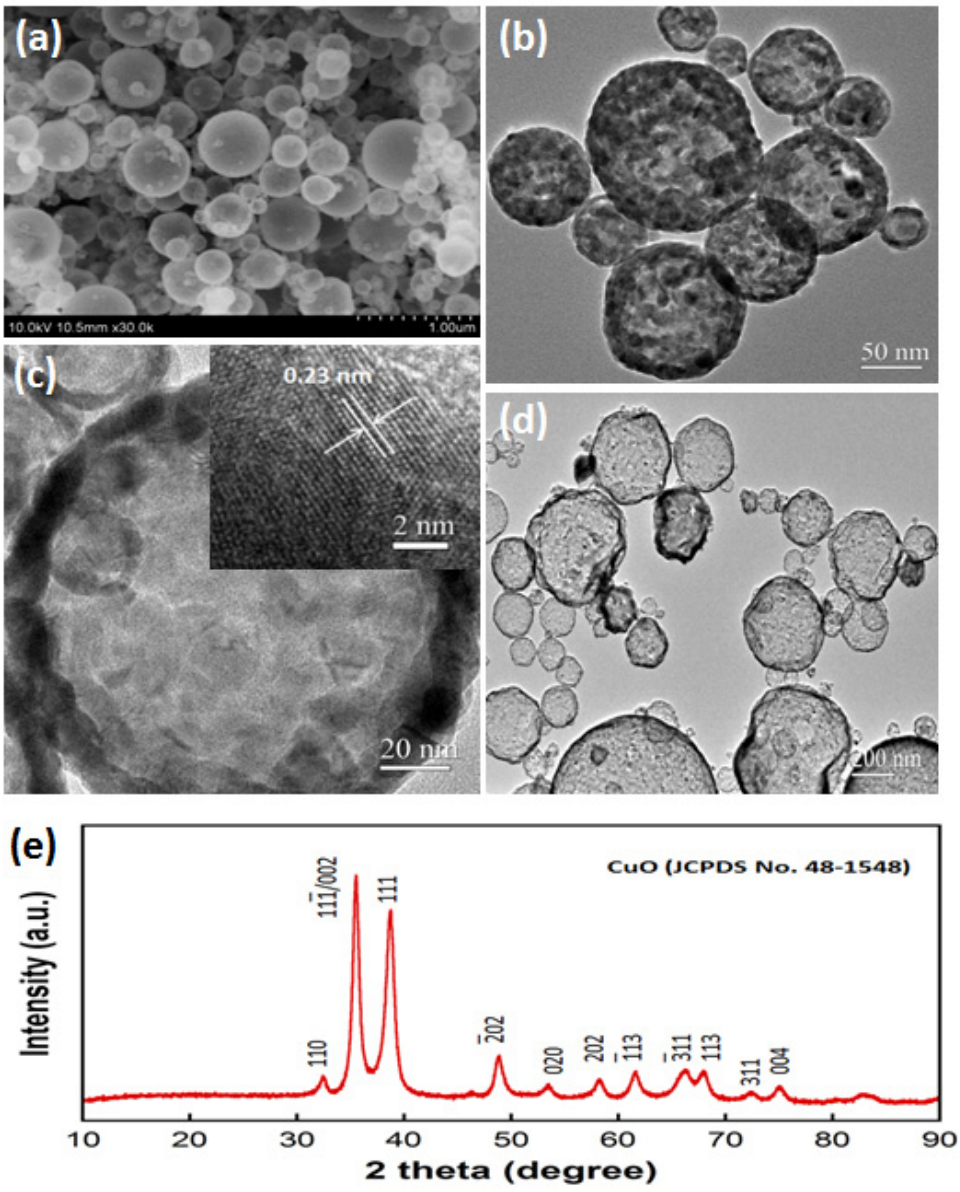


**Figure 5.2.** SEM (a), TEM and HRTEM images (b-d) and XRD (e) of prepared hollow CuO spheres collected from sample filter. Note: (d) is the TEM image of the hollow CuO spheres synthesized from solution with higher precursor concentration and more gas blowing agents. (Precursor: $Cu(NO_3)_2.3H_2O$: 0.9664g (0.004 mol), $C_{12}H_{22}O_{11}$: 0.3423g (0.001 mol), $H_2O_2$ (70%): 5ml, and $H_2O$: 15ml.)

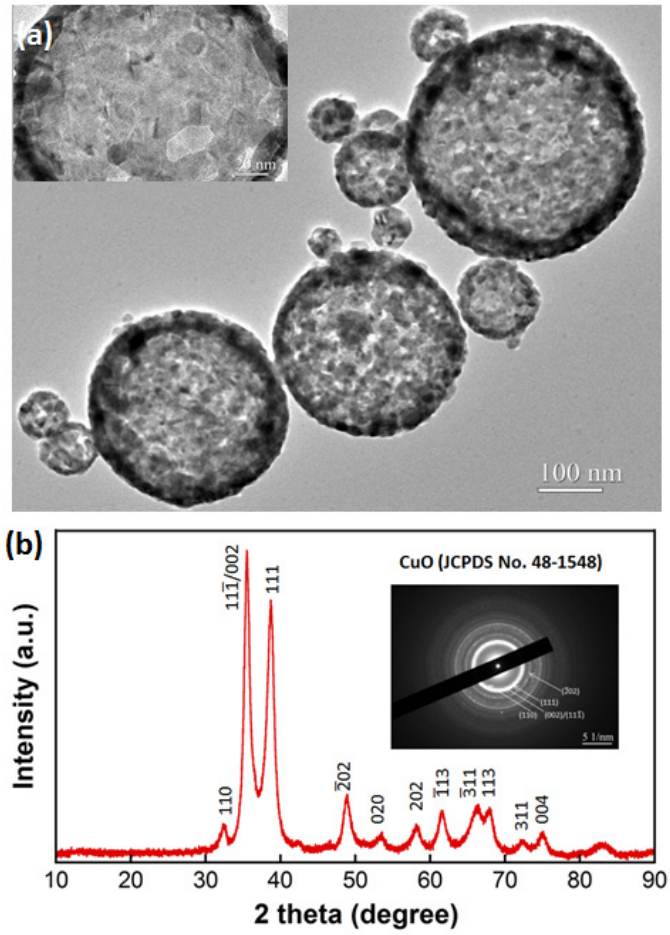


**Figure 5.3.** TEM image (a) and XRD spectrum (b) of prepared hollow CuO spheres after heat treatment in air (350 $^{o}$C, 1 hour). Inset of (a) is the high magnification TEM image showing the shell and crystallite. Inset of (b) is the SAED pattern of the hollow CuO spheres after heat treatment in air.

To investigate the effect of sucrose and $H_2O_2$ on the morphology and composition of the products, an experiment was carried out using the same concentration of copper nitrate solution but without any sucrose and $H_2O_2$. In this case, product particles only show a partially hollow interior as seen in Figure 5.4a, implying that copper nitrate precursor decomposition is also acting like a blowing agent.

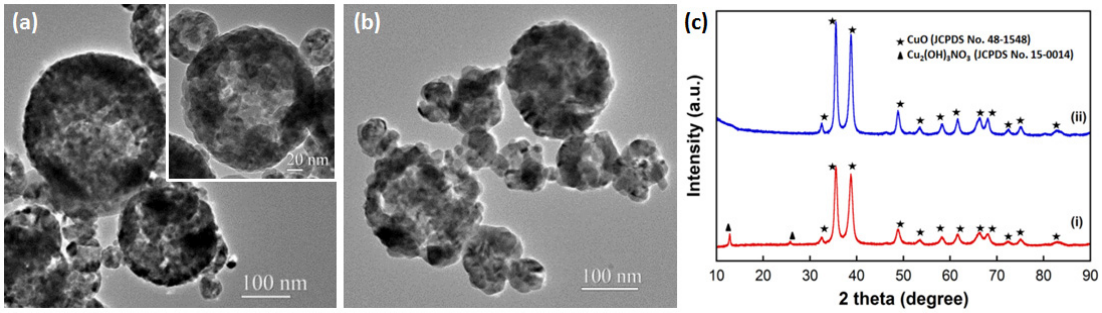


**Figure 5.4.** TEM images of as prepared partial hollow product from precursor solution without sucrose and $H_2O_2$ (a) and after post heat treatment in air at 350°C for 1 hour (b). Corresponding XRD spectra (c): i-as prepared, ii-after heat treatment.

The XRD patterns shown in Figure 5.4c (XRD spectrum i) shows that the product contains CuO (JCPDS No.48-2548) and $Cu_2(OH)_3NO_3$(JCPDS No.15-0014) phases, indicating incomplete reaction of the precursor, contrary to the addition of sucrose and $H_2O_2$ case (Figure 5.2e). Post-treatment of this sample in air at 350 °C for 1 h produces phase-pure CuO (Figure 5.4a, and XRD spectrum ii in Figure 5.4c). Prior work has shown that nitrate decomposition can be promoted by sucrose oxidation, [28] which also suggests why, even though the nitrate should have ample gas products to create a hollow, it did not. The sucrose, under the assumption of oxidation to $CO_2$ and water should only produce about a third as much gas as the nitrate under our conditions, but can form hollow structures because of faster gas-production kinetics (Appendix A: Supplemental Information, Figure 5.S1). The role of the $H_2O_2$ is to catalyze the oxidation of the sucrose, which is also known to rapidly polymerize into a tar-like substance in the absence of a very strong oxidizer, as shown in Figure 5.S2a in the Supporting Information. It has been shown in Figure 5.S2b in the Supplemental Information that a reduced formation of carbon species occurs

when adding $H_2O_2$ to the precursor solution. The observation that complete decomposition of the copper precursor was aided by sucrose and $H_2O_2$ addition seems to imply that possible exothermic reactions in the particle promote complete precursor decomposition. Based on the above observations, we conclude that the addition of a gas generator, sucrose (forming $CO_2$, $H_2O$), in addition to the inherent gas-generation properties of a nitrate salt, can promote the formation of large, thin-walled cavities in metal oxide particles.

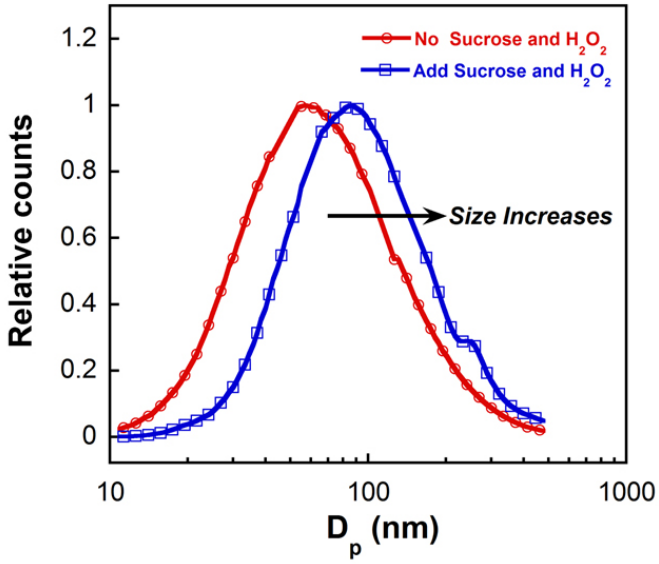


**Figure 5.5.** Particle size distributions of CuO produced by aerosol spray pyrolysis measured by a differential mobility analyzer (DMA) coupled with a condensation particle counter (CPC).

Online particle sizing was employed with a differential mobility analyzer (DMA) system and a condensation particle counter (CPC). For these experiments, the copper nitrate concentration in the precursor solutions was fixed and the size distribution of the aerosol was determined with and without the gas-blowing agents. The distributions shown in Figure 5.5 clearly show a shift in the size distribution, which

peaks at ≈57 nm without the blowing agents, to ≈85 nm with the added sucrose and $H_2O_2$. Indeed larger hollow particles can be produced by employing higher concentrations of copper nitrate precursor and blowing agents, which can be seen in Figure 5.2d.

*5.3.2. Performance of Hollow CuO as an Oxidizer in Nanoenergetic Formulations.*

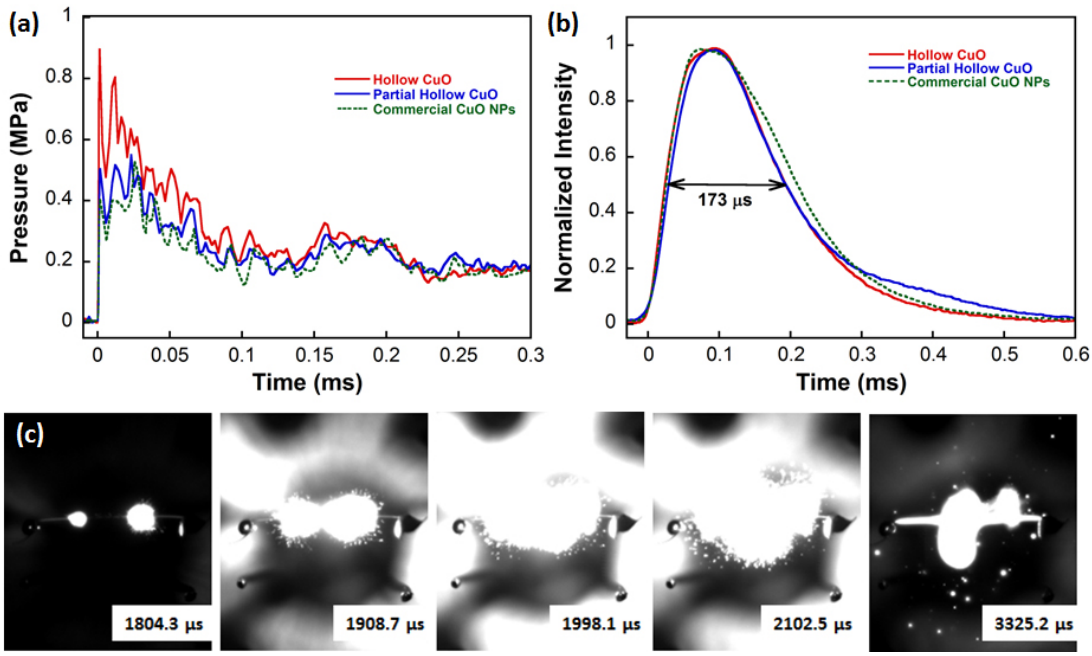


**Figure 5.6.** Pressure (a) and optical (b) traces for nanoaluminum based thermite formulations with hollow CuO spheres (red line), partial hollow CuO (blue line) and commercial CuO nanoparticles (green line) as oxidizers in a combustion cell. (c) Sequential snapshots of hollow CuO containing nanoaluminum thermite burning on fast-heating wire. The labeled times are time elapsed (µs) after triggering.

To evaluate the effect of this new morphology in a nanoenergtic-type application, the hollow CuO was ultrasonically mixed with aluminum nanoparticles in a stoichiometric ratio, and after drying, 12.5 mg were ignited in a combustion cell (≈13

$cm^3$). For comparison, the partially hollow CuO (Figure 5.4b) and commercial CuO nanoparticles (<50 nm, TEM image shown in Figure 5.S3 in the Supporting Information) were also tested. Figure 5.6a shows the temporal pressure traces in the combustion cell for the various mixtures. All of the pressure traces show a rapid rise, which occurs on the order of microseconds, with the hollow CuO spheres containing thermite achieving a pressure rise of ≈0.896 MPa in only 1.2 μs, significantly outperforming the partially hollow CuO (0.496 MPa in 1.6 μs) and commercial CuO NPs (0.400 MPa in 1.6 μs). From Figure 5.6a, we also found that hollow CuO spheres achieve the maximum pressure value in the first 1.2 μs, while the other two reach the maximum pressure value at a much later time, 23.2 and 25.6 μs for partial hollow CuO spheres and CuO NPs respectively. Comparing the absolute pressure rise with systems that are known to have the highest pressurization rate $P_{max}/t_{rise}$, e.g., $KMnO_4$ nanoparticles (1.999 MPa $\mu s^{-1}$ for Al/$KMnO_4$) [29] and perchlorate-containing core-shell nanostructures (0.772-2.454 MPa $\mu s^{-1}$ for Al/$KClO_4$+CuO), [30] we find that these hollow CuO structures yield comparable results of ≈0.745 MPa $\mu s^{-1}$. High-speed imaging of Al/hollow CuO thermite on the fast-heating wire (≈$10^6$ K $s^{-1}$) shows a violent flame front, as shown in Figure 5.6c.

The corresponding optical-emission traces for all three thermite formulations are shown in Figure 5.6b. The burning times for all three formulations are roughly the same: full width at half maximum (FWHM) = 173 μs for hollow CuO, which is much longer than the pressure rise time, suggesting that in all of the cases, the burning behavior is rate limited by the aluminum fuel, or at least is independent of the oxide morphology. The high pressurization rate of the hollow CuO spheres may be

associated with their higher surface area, which is composed of very fine ≈10 nm primary particles. In essence, this is really an aggregate of the primary particles, which are sufficiently less agglomerated and thus more ready to interfacially react with the fuel. In conjunction, we explored the temporal oxygen-release kinetics from these oxidizers. Based on our previous work on oxygen-release kinetics, we expected that the faster-reacting material would release $O_2$ faster. [26]

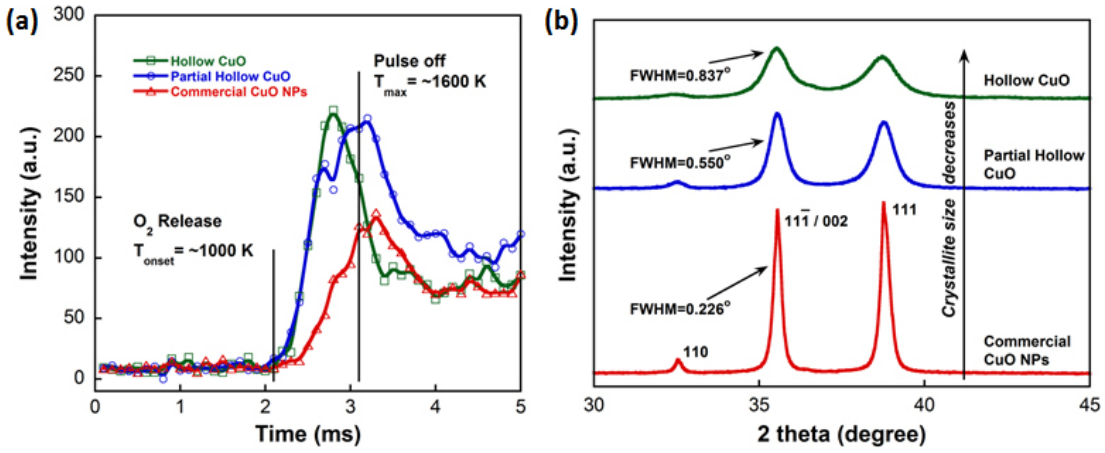


**Figure 5.7.** (a) Temporal profile of oxygen release upon heating hollow and partial hollow CuO spheres and commercial CuO NPs (labeled as <50 nm). The heating pulse time was 3.1 ms. (b) XRD spectra for hollow CuO, partial hollow CuO and commercial CuO NPs.

To compare the oxygen release kinetics of all three CuO structures, we rapidly heated the oxidizers on a 76 μm Pt wire at a heating rate of $5\times10^5$ K $s^{-1}$. The temporal profile of oxygen release from the three CuO structures is shown in Figure 5.7a. We observed no difference in the onset temperature for oxygen release ≈1000 K. However, quite clearly the hollow CuO spheres release oxygen at a faster rate than the partially hollow material and the commercial CuO aggregated NPs. These

differences in performance may be attributed to differences in the crystallite sizes of the CuO primary particle building blocks, as shown in Figure 5.7b. The line widths of the XRD patterns indicate differences in crystallite size, which can be estimated by the Scherrer equation, giving average crystallite sizes of 40.1 nm for commercial CuO, 16.4 nm for the partial hollow CuO and 10.8 nm for the hollow CuO, consistent with the TEM observations. It is reasonable to expect that smaller crystallite sizes lead to a higher oxygen fugacity. [31] Additionally, we have measured a lower activation energy for oxygen release kinetics per unit mass by high-heating-rate mass spectrometry. [32] We note that the temporal profiles for the oxygen release shown in Figure 5.7a get wider with increasing crystallite size, and are similar to the trend observed in the combustion cell. Part of this may be attributed to the narrow primary-particle-size distribution in the hollow spheres (Figure 5.3a) relative to the other structures (Figure 5.4b).

## *5.4. Conclusions*

In summary, this chapter reports on the development of an Al/CuO nanocomposite which shows a better performance than previous ones adopted with nanoparticles. The hollow CuO spheres with thin shell thickness employed in the nanocomposite were prepared by a simple aerosol spray pyrolysis method with the introduction of gas-blowing agents in the synthesis procedure. The resultant hollow CuO spheres comprised small nanosized building blocks with a crystallite size of ≈10 nm. The CuO hollow spheres exhibit excellent gas-generation behavior, demonstrating a high pressurization rate of 0.745 MPa $\mu s^{-1}$ and a transient peak pressure of 0.896 MPa, as

well as a rapid oxygen release. The synthesis strategy demonstrated is simple and should be extendable to the preparation of other hollow metal oxide structures.

## *5.5. Appendix A: Supplemental Information*

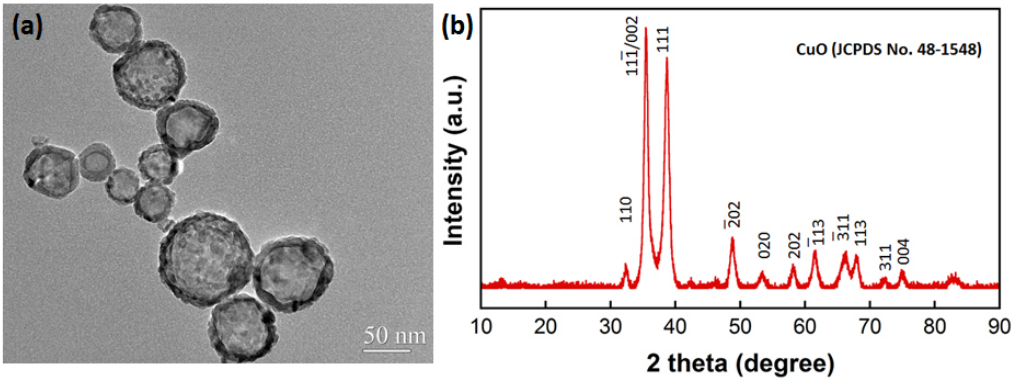


**Figure 5.S1.** TEM image (a) and XRD spectrum (b) of as prepared CuO without $H_2O_2$ in the precursor solution. Experimental details: 0.9664 g copper nitrate trihydrate ($Cu(NO_3)_2.3H_2O$), 0.1711g sucrose ($C_{12}H_{22}O_{11}$, Sigma-Aldrich) and were dissolved into 18.5 ml water.

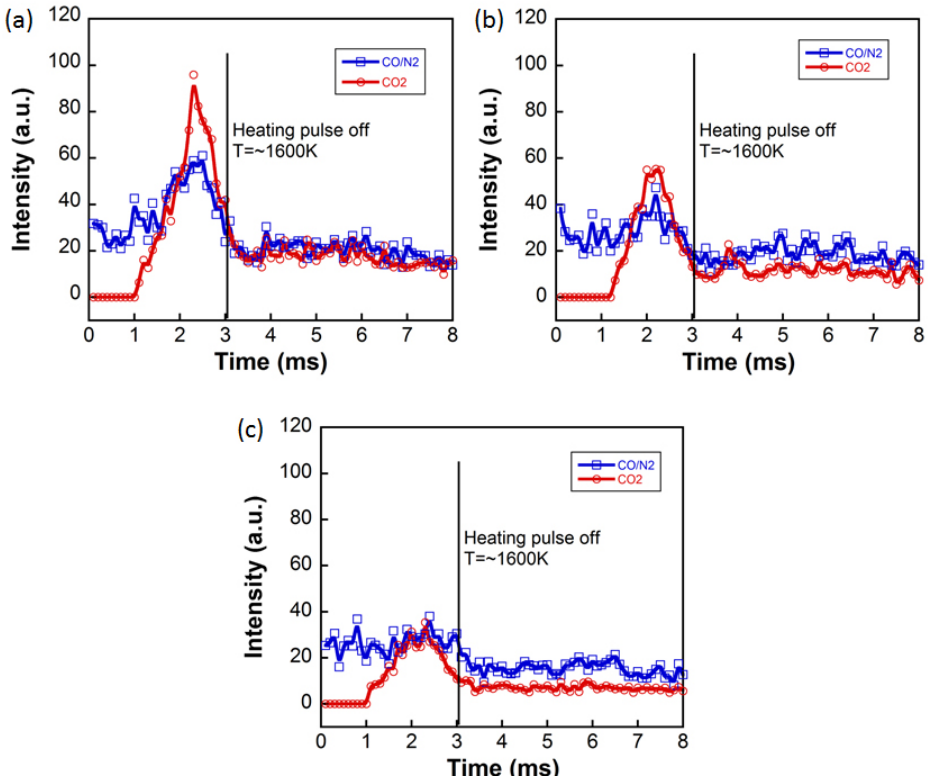


**Figure 5.S2.** Time-resolved mass spectrometry measurement of the carbon species upon heating the CuO products obtained from precursor solution without $H_2O_2$ (a), with $H_2O_2$ (b), without $H_2O_2$ and sucrose (c). The heating pulse was 3.1 ms. All samples are ultrasonicated in hexane for 30 mins before testing.

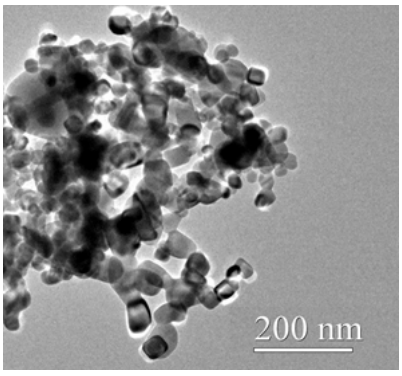


**Figure 5.S3.** TEM image of commercial CuO nanoparticles (Sigma Aldrich, <50 nm designated by supplier).

## *5.6 References*


[1] Lou, X.W.; Archer, L.A.; Yang, Z.C. *Adv. Mater.* **2008**, *20*, 3987-4019.

[2] Zhang, Q.; Wang, W. S.; Goebl, J.; Yin, Y. D. *Nano Today* **2009**, *4*, 494-507.

[3] Hu, J.; Chen, M.; Fang, X.S.; Wu, L.M. *Chem. Soc. Rev.* **2011**, *40*, 5472-5491.

[4] Liu, J.; Qiao, S.Z.; Chen, S.J.; Lou, X.W.; Xing, X.R.; Lu, G.Q. *Chem. Commun.* **2011**, *47*, 12578-12591.

[5] Lai, X. Y.; Halpert, J. E.; Wang, D. *Energy Environ. Sci.* **2012**, *5*, 5604-5618.

[6] Wang, Z.Y.; Zhou, L.; Lou, X.W. *Adv. Mater.* **2012***, 24,* 1903-1911.

[7] Lee, J.H. *Sens. Actuators, B* **2009***, 140,* 319-336.

[8] Yin, Y.D.; Rioux, R.M.; Erdonmez, C.K.; Hughes, S.; Somorjai, G.A.; Alivisatos, A.P. *Science* **2004,** 304, 711-714.

[9] Railsback, J.G.; Johnston-Peck, A.C.; Wang, J.W.; Tracy, J.B. *ACS Nano* **2010**, 4, 1913-1920.

[10] Yang, H.G.; Zeng, H.C. *J. Phys. Chem. B* **2004**, *108*, 3492-3495.

[11] Lou, X.W.; Wang, Y.; Yuan, C.; Lee, J.Y.; Archer, L.A. *Adv. Mater.* **2006**, *18*, 2325-2329.

[12] Kruis, F.E.; Fissan, H.; Peled, A. *J. Aerosol Sci.* **1998**, *29*, 511-535.

[13] Mariotti, D.; Sankaran, R.M. *J. Phys. D: Appl. Phys.* **2010** *43,* 323001-21.

[14] Schimmoeller, B.; Pratsinis, S.E.; Baiker, A. *ChemCatChem* **2011**, *3*, 1234-1256.

[15] Okuyama, K.; Lengoro, I.W. *Chem. Eng.Sci.* **2003**, 58, 537-547.

[16] Boissiere, C.; Grosso, D.; Chaumonnot, A.; Nicole, L.; Sanchez, C. *Adv. Mater.* **2011***, 23,* 599-623.

[17] Dreizin, E.L. *Prog. Energy Combust. Sci.* **2009**, *35*, 141-167.

[18] Piercey, D.G.; Klapötke, T.M. *Central Europ. J. Energ. Mat.* **2010**, *7*, 115-129.

[19] Rossi, C.; Zhang, K.; Estéve, D.; Alphonse, P.; Thailhades, P.; Vahlas, C. *J. Microelectromech. Syst.* **2007**, *16*, 919-931.

[20] Aumann, C. E.; Skofronick, G. L.; Martin, J. A. *J. Vac. Sci. Technol. B,Microelectron. Process. Phenom.* **1995**, *13*, 1178-1183.

[21] Kim, S. H.; Zachariah, M. R. *Adv. Mater.* **2004**, *16*, 1821-1825.

[22] Malchi, J. Y.; Foley, T. J.; Yetter, R. A. *ACS Appl. Mater. Interfaces* **2009**, *1*, 2420-2423.

[23] Shende, R.; Subramanian, S.; Hasan, S.; Apperson, S.; Thiruvengadathan, R.; Gangopadhyay, K.; Gangopadhyay, S.; Redner, P.; Kapoor, D.; Nicolich, S.; Balas, W. *Propellants, Explos., Pyrotech.* **2008**, *33*, 122-130.

[24] Séverac, F.; Alphonse, P.; Estève, A.; Bancaud, A.; Rossi, C. *Adv. Funct. Mater.* **2012**, *22*, 323-329.

[25] Martirosyan, K.S. *J. Mater. Chem.* **2011**, *21*, 9400-9405.

[26] Zhou, L.; Piekiel, N.; Chowdhury, S.; Zachariah, M.R. *J. Phys. Chem. C* **2010**, *114*, 14269-14275.

[27] Sullivan, K.; Zachariah, M. R. *J. Propul. Power* **2010***, 26,* 467-472.

[28] Amarilla, J. M.; Rojas, R. M.; Rojo, J. M. *J. Power Sources* **2011**, *196*, 5951-5959.

[29] Prakash, A.; McCormick, A.V.; Zachariah, M.R *Adv. Mater.* **2005**, *17*, 900-903.

[30] Wu, C.W.; Sullivan, K.; Chowdhury, S.; Jian, G.Q.; Zhou, L.; Zachariah, M.R. *Adv. Funct. Mater.* **2012**, *22*, 78-85.

[31] Navrotsky, A.; Ma, C.C.; Lilova, K.; Birkner, N. *Science*, **2010**, *330*, 199-201.

[32] Jian, G.Q.; Zhou, L. Piekiel, N.; Zachariah, M.R. Probing Oxygen Release Kinetics of Nanosized Metal Oxides by Temperature-Jump Time of Flight Mass Spectrometry. Fall Meeting, the Eastern States Section of the Combustion Institute, Storrs, CT, Oct 9-12, **2011**.

# Chapter 6: Periodate Salts Based Nanothermites as Nanoenergetic Gas Generators [*]

## *Highlights*

(a) Periodate salt nanoparticles were synthesized by a facile aerosol spraying drying process, and demonstrate highly reactive properties as oxidizers in an aluminum-based nanoenergetic formulation.

(b) Direct evidence has been shown to support that gas phase oxygen release from the oxidizer decomposition is critical in the ignition and combustion of periodate nanoenergetic formulations.

## *Overview*

While aluminum is the most widely used fuel, there are a wide range of potential oxidizers with various properties. In this chapter, we have prepared periodate salt ($KIO_4$ and $NaIO_4$) nanoparticles which are known to have low toxicity and hygroscopicities, but extremely high oxidative power. Our results show that when formulated into nanocomposites with aluminum, periodate nanoparticles demonstrate highly reactive properties as well as superior gas generating behavior (the best performance known so far). Several in-situ techniques at high heating rates as well as TG-DSC have been employed to probe the reaction mechanisms. The results suggest that exothermic decomposition of periodate salts contributes to the low ignition

[*] The results presented in this chapter have been published in the following journal article: Jian, G.Q.; Feng, J.Y.; Jacob, R.J.; Egan, G.C.; Zachariah, M.R. Super-reactive Nanoenergetic Gas Generators Based on Periodate Salts, *Angew. Chem. Int. Ed.* **2013**, *52*, 9743-9746.

temperature of its nanoenergetic formulations. This study also shows, for the first time, clear evidence to support that direct gas phase oxygen release, from oxidizers in a nanoenergetic formulation is responsible for the combustion performance.

## *6.1. Introduction*

Composite energetic materials are simple mixtures of the fuel and oxidizer (e.g., thermite). Although composite energetic materials usually have much higher energy density than monomolecular energetic materials such as TNT (2,4,6-trinitrotoluene), nitrocellulose, RDX (cyclotrimethylenetrinitramine) etc., they suffer from the slow rates of energy release, limited by the mass transfer rate between reactants. In large part, the idea of nanoenergetics is to promote intimate mixing between the fuel and oxidizer by decreasing the length scale. [1-3] This relatively new class of energetic materials has been a topic of extensive research and has been investigated for applications involving gas generators, initiators, propellants and explosives as well as propulsive power in micro-/nanoelectromechanical systems (MEMS/NEMS). [4-7]

In the most widely studied nanoenergetic formulations, nanoaluminum is employed as the fuel because of its high reaction enthalpy and ready availability, and metal oxides nanoparticles serve as oxidizers (e.g. $Fe_2O_3$, CuO and $MoO_3$). [4-9] More recently, some other oxidizers, including $KMnO_4$, [10] $I_2O_5$, [11] $NaClO_4$, [12, 13] have been introduced into the nanoenergetic formulations for their high oxygen content and strong oxidizing nature. These strong oxidizers also display very promising gas generating behavior; however, most of them have a reduced shelf life compared to metal oxides nanoparticles, for reasons of light sensitive or hygroscopicity. [14, 15] Recent efforts have been explored to encapsulate perchlorate

salt nanoparticles with less reactive metal oxide layers as a moisture barrier. [16] However, perchlorate salts, particularly potassium perchlorate ($KClO_4$), have raised environmental and public health concerns during manufacture, transport, and applications, and have been targeted for elimination from many traditional pyrotechnic formulations. [17-20] In a recent report, Moretti and Sabatini et al. introduced periodate salts as an alternative to perchlorates salts as pyrotechnic oxidizers because of their low toxicity and hygroscopicities. Their results show that periodate salt based formulations have good performance in illumination applications. [20] The fabrication of periodate salt nanoparticles and their applications as gas generators, however, remains a challenge.

In this chapter, we present an example of gas generators based on periodate salts as oxidizers in nanoenergetic formulations. A simple yet versatile aerosol spray drying approach was developed to produce periodate salt nanoparticles. The aerosol spray drying method is a promising method to produce high oxygen content salt oxidizer nanoparticles, and for fabricating salt nanoparticles not accessible by wet chemistry methods. [21, 22] The prepared periodate salt nanoparticles were then tested as oxidizers in nanoenergetic formulations with nanoaluminum as the fuel. These periodate salt nanoparticles exhibit superior reactivity when evaluated as the oxidizers in nanoenergetic formulation, producing the highest reported gas pressure pulses. Fast heating scanning electron microscopy and temperature jump mass spectrometry techniques were employed to probe the initiation/reaction mechanism, and provided direct evidence that gas phase oxygen release is responsible for the initiation of the periodate nanoenergetic formulations.

## *6.2. Experimental Section*

### *6.2.1. Synthesis of $KIO_4$ and $NaIO_4$ Nanoparticles.*

The $KIO_4$ and $NaIO_4$ nanoparticles were synthesized by an aerosol spray-drying process as illustrated in Figure 6.1. 0.4 g $KIO_4$ or $NaIO_4$ (Sigma-Aldrich) was dissolved into 100 ml deionized water. Aerosol droplets (mean diameter ~1 μm) containing the dissolved salts were generated using compressed air at a pressure of 35 psi in a collision type atomizer. The produced aerosol droplets were passed through a silica-gel diffusion dryer to remove most of the moisture, and passed to a tube furnace at 180 $^oC$ for $KIO_4$ and 200$^oC$ for $NaIO_4$. The nanoparticles were collected on a 0.4 μm (pore size) HTTP Millipore filter and characterized by scanning electron microscopy (SEM, Hitachi, SU-70 FEG-SEM), transmission electron microscopy (TEM, JEOL JEM 2100F), and powder X-ray diffraction (XRD) (Bruker D8 Advance using Cu Kα radiation). The $KClO_4$ and $NH_4ClO_4$ nanoparticles were also produced by the same approach. $NaClO_4$ nanoparticles could not be collected by this approach since its high hygroscopic nature. All starting perchlorate salts were from Sigma-Aldrich and used as received. CuO nanoparticles (<50 nm, Sigma-Aldrich) were used for this study as a reference material.

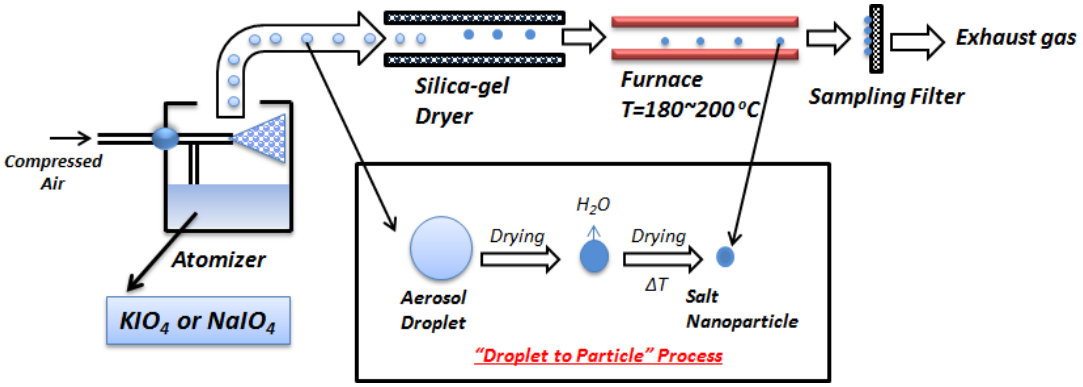


**Figure 6.1.** Schematic illustration of periodate salt nanoparticles formation.

*6.2.2. Combustion Cell Characterization.*

$KIO_4$ or $NaIO_4$ nanoparticles were stoichiometrically mixed with aluminum nanoparticles (Argonide Corporation, designated as 50 nm ALEX; 70 wt % active Al). Al/$KIO_4$ formulation contains 30.9 wt % aluminum nanoparticles and 69.1 wt % $KIO_4$ nanoparticles. Al/$NaIO_4$ formulation contains 32.5 wt % aluminum nanoparticles and 67.5 wt % $NaIO_4$ nanoparticles. Approximately 10 ml of hexane was then added, and the mixture was ultrasonicated for 30 min to ensure intimate mixing. After the evaporation of hexane in air, the powder was then gently broken apart. A constant volume combustion cell (~13 $cm^3$) was used to simultaneously measure the pressure rise and optical emission of Al/$KIO_4$ and Al/$NaIO_4$ samples. In this study, 25.0 mg thermite sample was placed inside the combustion cell and ignited by joule heating of a nichrome coil on top of the loose powder. Other oxidizers samples (control experiments) were also tested in combustion cell for comparison purpose. The post combustion products were further characterized by SEM coupled with an energy-dispersive X-ray detector (Bruker).

*6.2.3. Time Resolved Mass Spectrometry and High Speed Imaging.*

The temperature-jump/time-of-flight mass spectrometer (T-Jump/TOFMS) [23, 24] (also see Chapter 2) was used to study the decomposition of the periodate nanoparticles. Typically, a ~10 mm long Pt wire (76 μm) was coated with a thin layer of oxidizer sample powder (ultrasonicated in hexane for 30 min). The coated wire was rapidly heated to ca. 1600 K at a heating rate of $\sim 5\times10^5$ K/s. Time-resolved mass spectra combined with wire temperature were then used for characterization of the decomposition species. The high speed digital imaging of sample combustion on the wire was taken at a resolution of 256×256 and frame rate of 67065 fps (14.9 μs per frame) by a Vision Research Phantom® v12.0 digital camera. The high speed imaging experiment was conducted in air at atmospheric pressure. The ignition temperature of the nanoenergetic reactions was obtained from the correlated emission signal with temperature profile of the T-Jump filament. The same high speed imaging experiments were also conducted in argon environment at atmospheric pressure.

*6.2.4. Thermogravimetric/Differential Scanning Calorimetry (TG/DSC) Measurement.*

A Netzsch F3 Jupiter STA was employed to study the decomposition of $KIO_4$, $NaIO_4$, $KClO_4$, and $NH_4ClO_4$ nanoparticles. This apparatus combines a TGA instrument and a heat flux DSC implemented using a Netzsch TGA–DSC sample carrier. About 5 mg of sample was loaded into the TG analyzer, and the temperature was programmed to 700 $^oC$ (973 K) at the rate of 10 $^oC$ /min in 100 sccm $N_2$ flow.

*6.2.5. High Heating Rate Microscopy.*

A specially designed sample holder (Aduro holder, Protochips, Inc.) was used to heat samples with a 1 ms heating pulse *in situ* inside a scanning electron microscopy

(SEM, Hitachi, SU-70 FEG-SEM), from room temperature up to 1173 K and at a rate as fast as $10^6$ K/s. The sample was further held at 1173 K for 1 ms. SEM images were taken before and after heating.

## *6.3. Results and Discussions*

### *6.3.1. Synthesis and Characterization of Periodate Salt Nanoparticles.*

The general pathway of preparing periodate salt nanoparticles via an aerosol spray drying method is illustrated in Figure 6.2a (for details see Figure 6.1.). Briefly, periodate nanoparticles were formed thorough an aerosol "droplet-to-particle" process, whereby precursor aqueous solutions are continuously atomized to form micron-size droplets and subsequent solvent evaporation enables the formation of nanoparticles. The nanoparticles size ranges from 50 to 300 nm based on the scanning electron microscopy (SEM) images (Figure 6.2b-c) and transmission electron microscopy (TEM) images (Figure 6.3), which is mainly dependent on the aerosol droplet size distribution. The prepared nanoparticles were further confirmed to be single crystal phase of $KIO_4$ and $NaIO_4$ by X-ray diffraction (XRD) analysis, as shown in Figure 6.4.

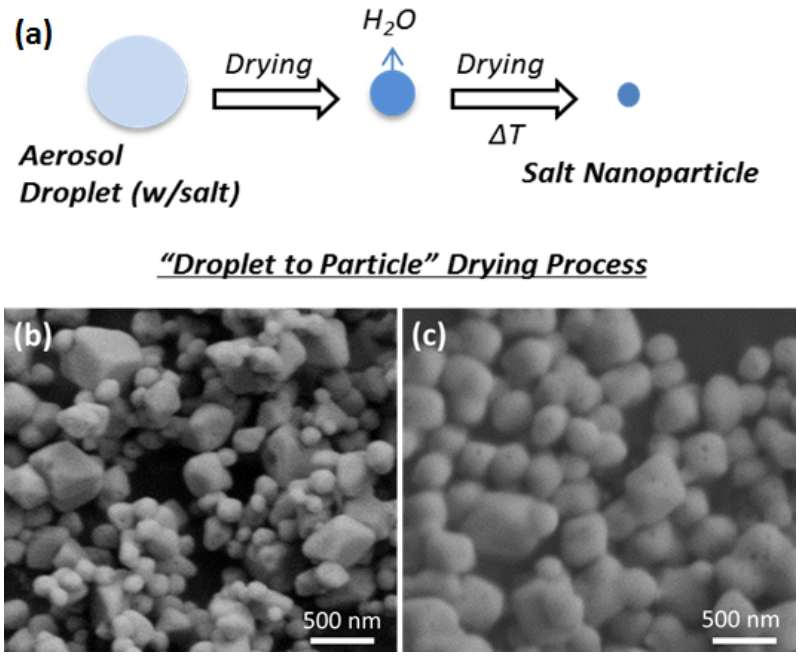


**Figure 6.2.** (a) Schematic illustration of preparing periodate salt nanoparticles by aerosol spraying drying. (b, c) SEM images of $KIO_4$ (b) and $NaIO_4$ (c) nanoparticles.

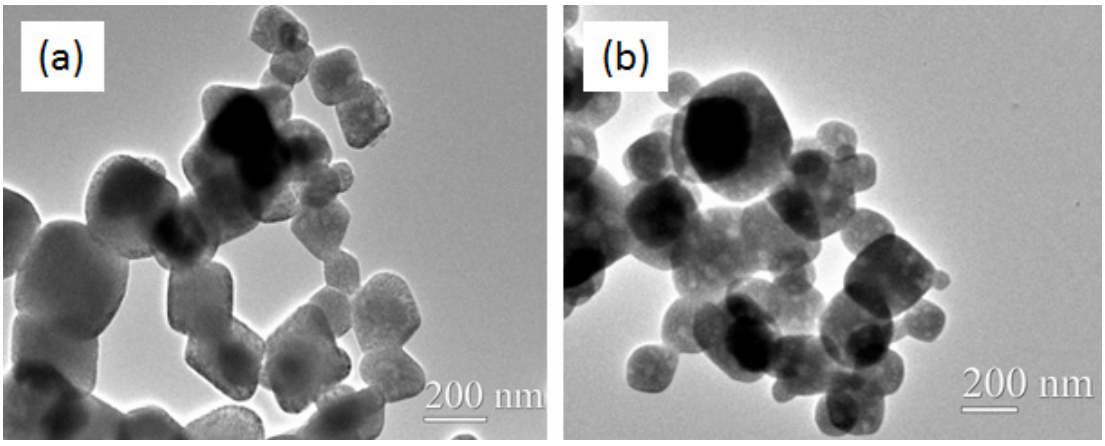


**Figure 6.3.** TEM images of (a) $KIO_4$ and (b) $NaIO_4$ nanoparticles.

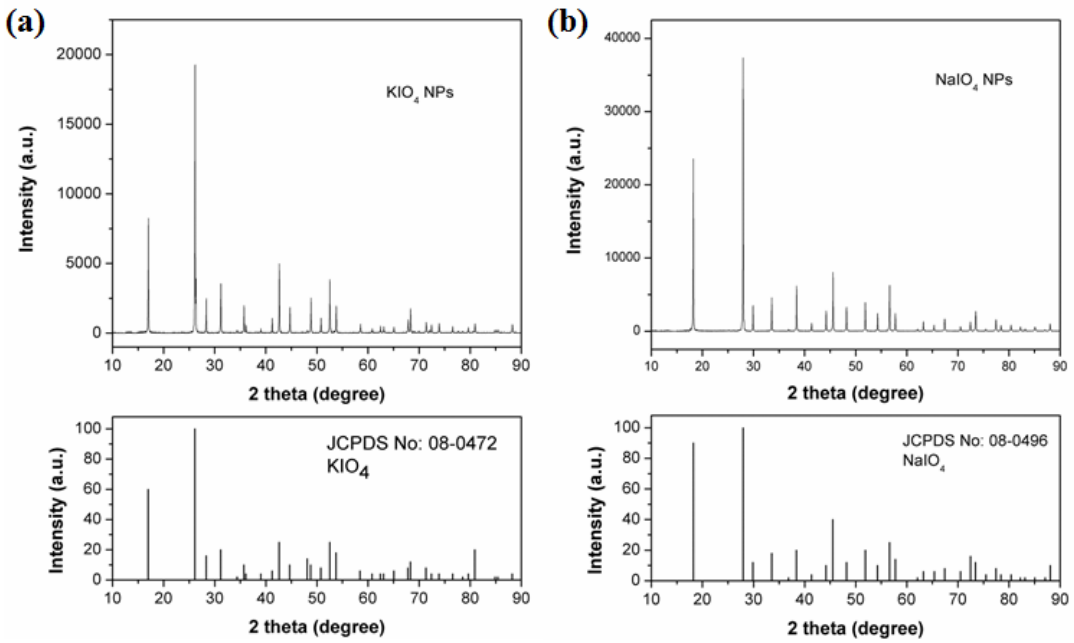


**Figure 6.4.** (a) XRD pattern of $KIO_4$ nanoparticles and standard XRD pattern of $KIO_4$ (JCPDS: 08-0472). (b) XRD pattern of $NaIO_4$ nanoparticles and standard XRD pattern of $NaIO_4$ (JCPDS: 08-0496).

Periodate nanoenergetic formulations were prepared by mixing oxidizer nanoparticles with nanoaluminum (<50 nm) in a stoichiometric ratio shown in Eqs. (1, 2).

$$8Al+3KIO_4 \rightarrow 3KI+4Al_2O_3 \quad (1)$$

$$8Al+3NaIO_4 \rightarrow 3NaI+4Al_2O_3 \quad (2)$$

Backscattering electron images of $KIO_4$ and $NaIO_4$ nanoenergetic composite materials are shown in Figure 6.5.

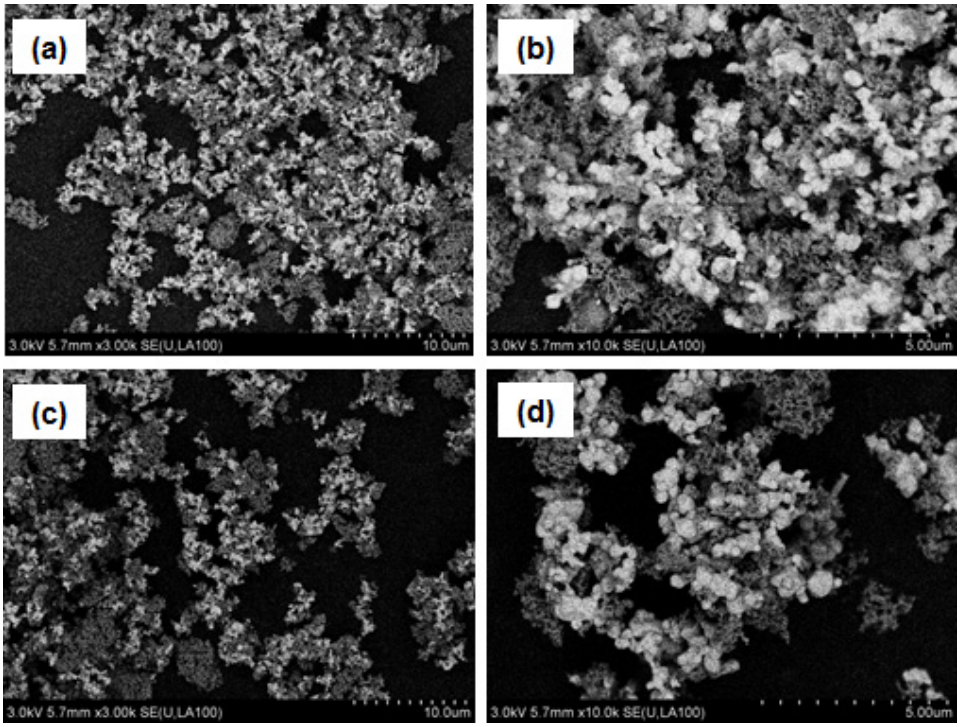


**Figure 6.5.** (a-d) Backscattering electron (BSE) images of nano-Al/nano-$KIO_4$ (a-b) and nano-Al/nano-$NaIO_4$ (c-d) samples. Note: Bright spots are $KIO_4$ and $NaIO_4$ nanoparticles.

*6.3.2. Periodate Salt Nanoparticles as Oxidizers in Nanoenergetic Gas-Generators.*

The relative reactivity of the periodate nanoenergetic formulations was evaluated using a combustion cell (Figure 6.6a), from which temporal pressure rise and optical emission information can be obtained for the reaction in a small closed vessel. The pressure rise and optical emission of nanoenergetic reactions with synthesized periodate nanoparticles as oxidizers in the combustion cell are shown in Figure 6.6b-c, and peak pressure, pressurization rate and full width at half maximum (FWHM) burn time are summarized in Table 6.1, along with CuO nanoparticles (<50 nm) as the reference material. [16]

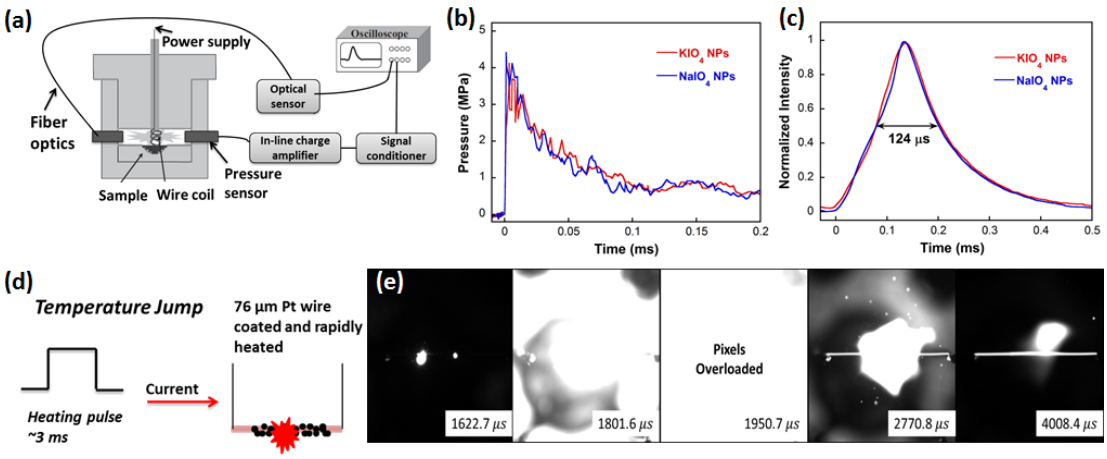


**Figure 6.6.** (a) Schematic showing of combustion cell. (b, c) Pressure vs. time (b) and normalized optical emission vs. time (c), for nanoaluminum-based energetic formulations with $KIO_4$ and $NaIO_4$ nanoparticles as oxidizers. (d) Schematic showing temperature jump experiment. (e) Sequential snapshots of Al/$KIO_4$ nanothermite burning on a fast-heating wire in atmosphere (air).

**Table 6.1.** Combustion cell results of nanoenergetic formulations with different oxidizer nanoparticles.

| Oxidizer (w/Al NPs, $\varphi$=1)[a] | $P_{max}$ [MPa] | *Pressurization rate* [MPa µs$^{-1}$] | *FWHM Burn time* [µs] |
|---|---|---|---|
| $KIO_4$ NPs | 3.8 | 2.4 | ~124 |
| $NaIO_4$ NPs | 4.0 | 2.6 | ~124 |
| CuO NPs[4e] | 0.7 | 0.06 | ~170 |

[a] The pressurization rate (dP/dt) is defined as the initial slope of the pressure curve. FWHM burn time is defined as the full-width half-maximum of the optical emission curve obtained in the combustion cell tests. The results are the average values of three experiments.

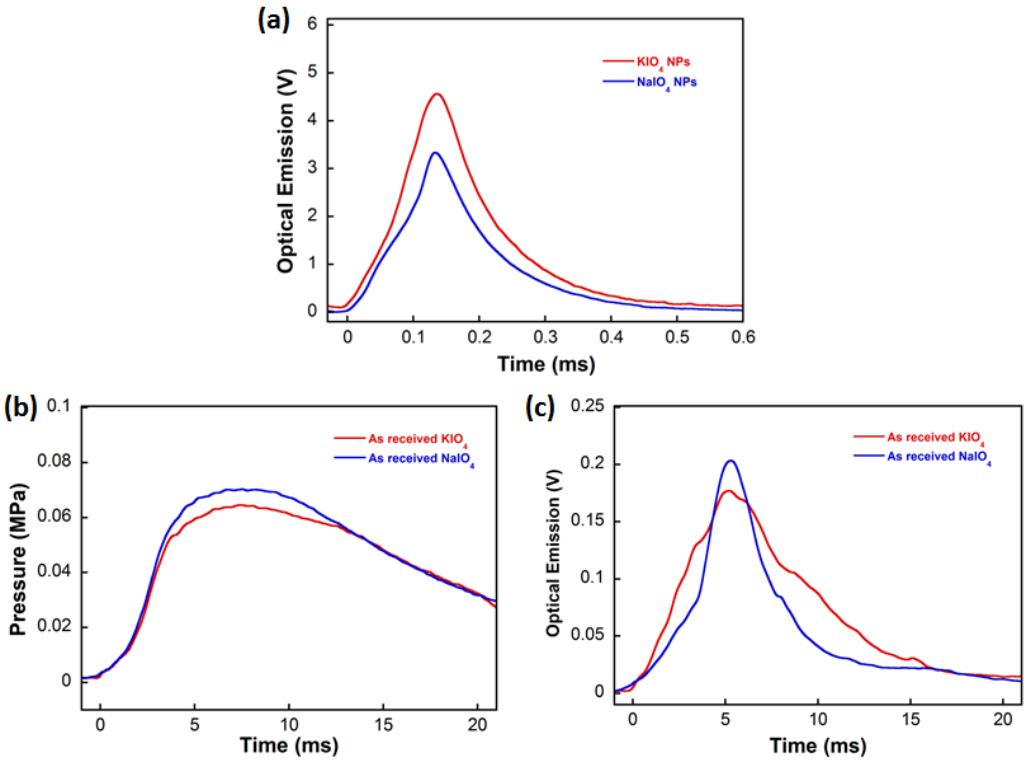


**Figure 6.7.** (a) Optical traces for nanoaluminum-based energetic formulations with $KIO_4$ and $NaIO_4$ nanoparticles as oxidizers in combustion cell. (b, c) Pressure (b) and optical (c) traces for nanoaluminum-based energetic formulations with as received $KIO_4$ and $NaIO_4$ (micron sized) as oxidizers in combustion cell.

From Figure 6.6b, all pressure profiles show a rapid rise which occurs in a few microseconds, with peak pressures as high as ~4 MPa, and average pressurization rates of 2.4 and 2.6 MPa $\mu s^{-1}$ for $KIO_4$ and $NaIO_4$ NPs (Table 6.1) respectively. Both the maximum pressure achieved and pressurization rate of Al/$KIO_4$ and Al/$NaIO_4$ significantly outperform CuO NPs (normally used as a standard), as presented in Table 6.1. We also compared the results with energetic formulations comprising aluminum nanoparticles and as received $KIO_4$ and $NaIO_4$ (~100 μm) shown in Figure 6.7, and found a very significant increase in the maximum peak pressure (>60x) and

pressurization rate (>>1000x), emphasizing the importance of employing nanosized oxidizers to improve the reactivity. In comparison to the reported values of pressurization rate for other nanoenergetic systems, e.g. a) 2.0 MPa $\mu s^{-1}$ for $Al/KMnO_4$ [10] and b) 0.77-2.4 MPa $\mu s^{-1}$ for $Al/KClO_4$+CuO,[16] periodate nanoenergetic formulations deliver the highest values. Since we tested all the samples at a fixed mass of 25 mg, $Al/KIO_4$ and $Al/NaIO_4$ nanoenergetic formulations demonstrate the highest pressurization rates per mole of Al considering the relatively high molecular weight of periodate salts.

In Figure 6.6c, we show the normalized optical emission traces for periodate based nanoenergetic formulations, from which we see that the burning time for both $KIO_4$ and $NaIO_4$ systems are roughly the same ~124 μs, which is much longer than the pressure rise time, suggesting the burning behavior is rate limited by the aluminum since the pressure rise is primarily due to oxygen release. [25, 26] The similar pressurization rates and burning time of $KIO_4$ and $NaIO_4$ imply, not surprisingly, that they have a similar reaction mechanism, which we will further explore later in the paper. Additionally, we found that the burning time of periodate salt based nanoenergetic formulations are shorter than the Al/CuO nanothermite (~170 μs), as presented in Table 6.1. In the periodate systems, the gas contributing to the pressurization is mainly through oxygen release from periodate salts decomposition, which should enhance the burning rate of nanoaluminum. This point has been previously confirmed by Glumac et al. [27] in the combustion of nanoaluminum in a pressurized oxygen environment. It has been found that the burning time of

nanoaluminum can be significantly reduced, in some cases by 4x, in a pressurized environment.

(a) Nano Al+nano $KIO_4$. $T_{ig}$= 950 K.

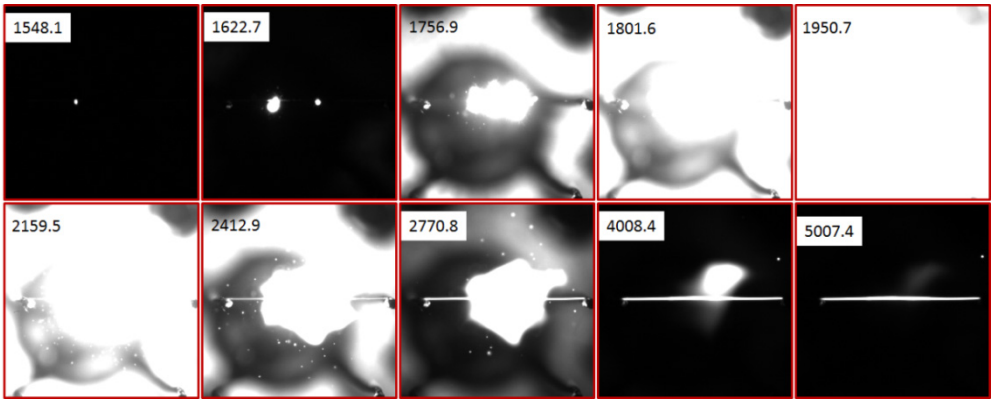


(b) Nano Al+nano $NaIO_4$. $T_{ig}$= 880 K.

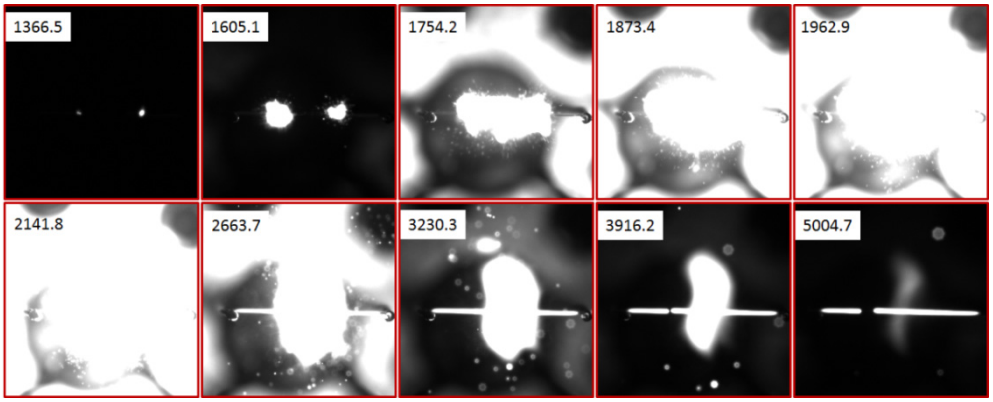


(c) Nano Al+nano CuO. $T_{ig}$= 1040 K.

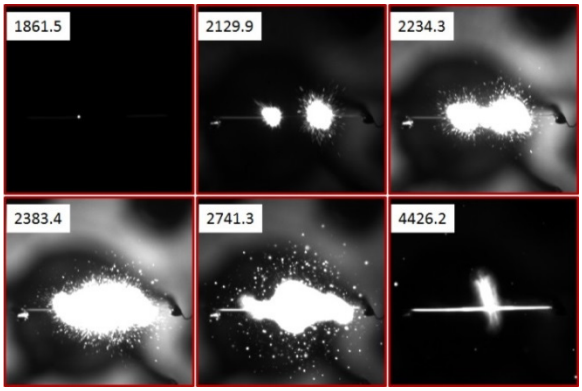

(d) Nano Al.

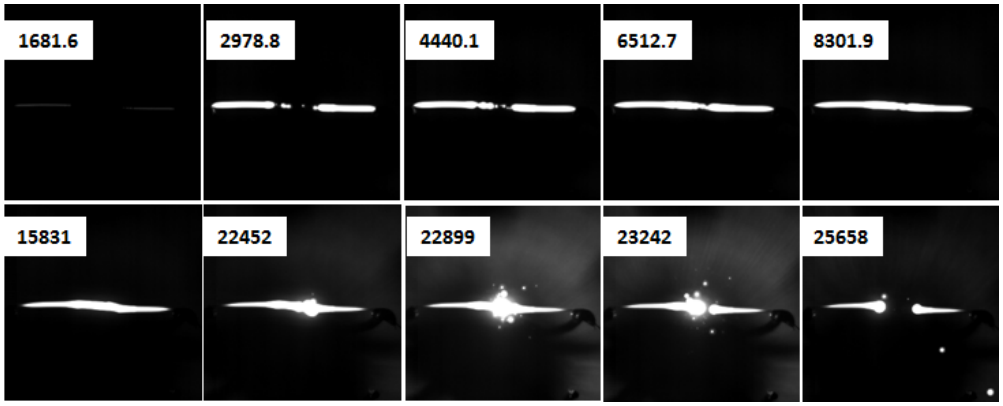


**Figure 6.8.** (a-d) High speed imaging of nanoenergetic formulations, nanoaluminum burning on the rapid heated wire. (a) nano Al+nano $KIO_4$, (b) nano Al+nano $NaIO_4$, (c) nano Al+ nano CuO and (d) nano Al. Note: The wire was rapidly heated to ~1600 K in 3 ms at the atmospheric pressure. Label unit: μs.

High speed imaging experiments of periodate nanoenergetic formulations in open air ignition (see supporting movie 2) and rapid wire ignition (Figure 6.6d-e, and details in Figure 6.8) show that periodate salt nanoparticles demonstrate much more violent reactions and brighter emission than CuO nanoparticles, indicating much faster energy release and pressurization rate for periodate nanoenergetic formulations. While we have not spectroscopically evaluated the emission, it is quite possible the enhanced brightness could in part be attributed to alkali atomic emission. Indeed the work of Moretti and Sabatini et al. have shown that incorporation $NaIO_4$ into pyrotechnics greatly enhances luminous efficiency and its potential application as the illuminant. [20] We should expect that with the more vigorous reaction expected using the nanomaterials, that this property would be significantly more enhanced and

our combustion cell results do show a ~15-30x increase in optical emission (Figure 6.7a) as compare to the micron sized material (Figure 6.7c).

Wire ignition experiments were employed to determine the ignition temperature of the nanoenergetic formulations at high heating rates (~$5\times10^5$ K/s) by applying a rapid heating pulse, as illustrated in Figure 6.6d. The measured ignition temperature of Al/$KIO_4$ and Al/$NaIO_4$ nanoenergetic formulations are 950 K and 880 K (Figure 6.8), respectively, which are lower than the ignition temperature of Al/CuO nanothermite (~1040 K). [28] We note that for Al/$NaIO_4$ nanoenergetic formulations, the ignition temperature is even lower than the melting point of aluminum (933 K).

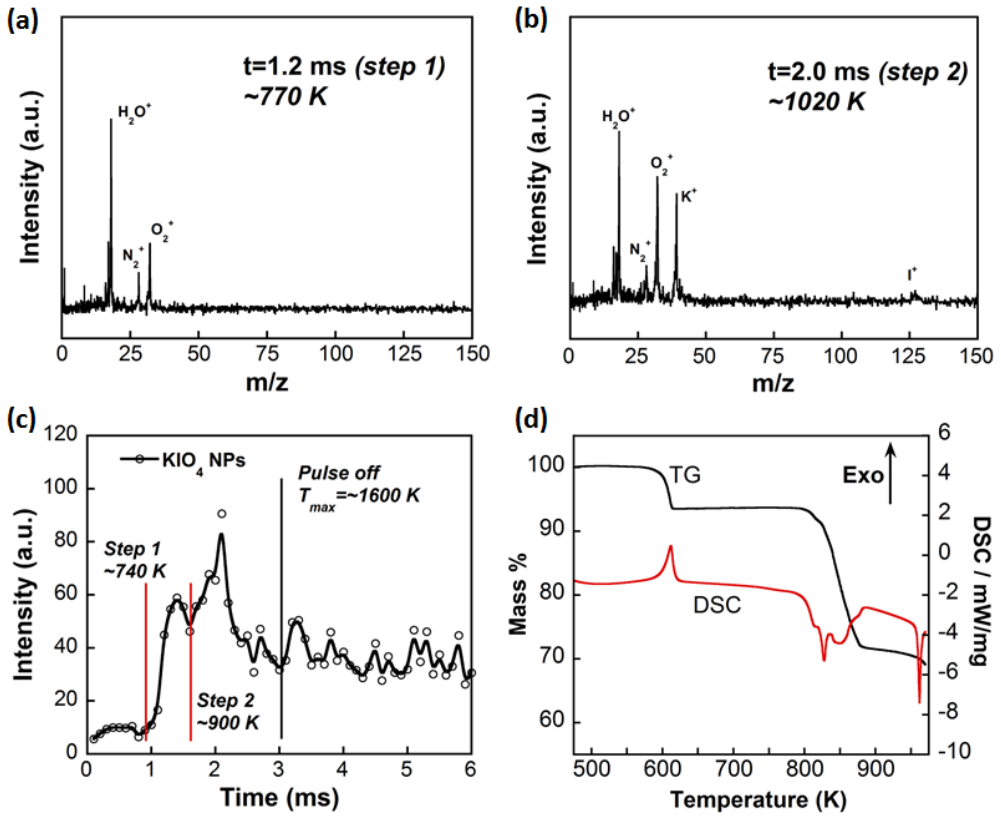


**Figure 6.9.** (a, b) Selected mass spectra obtained from rapid heating of $KIO_4$ nanoparticles. (c) Temporal profile of oxygen release upon heating $KIO_4$ nanoparticles. (d) TG/DSC curves of $KIO_4$ nanoparticles.

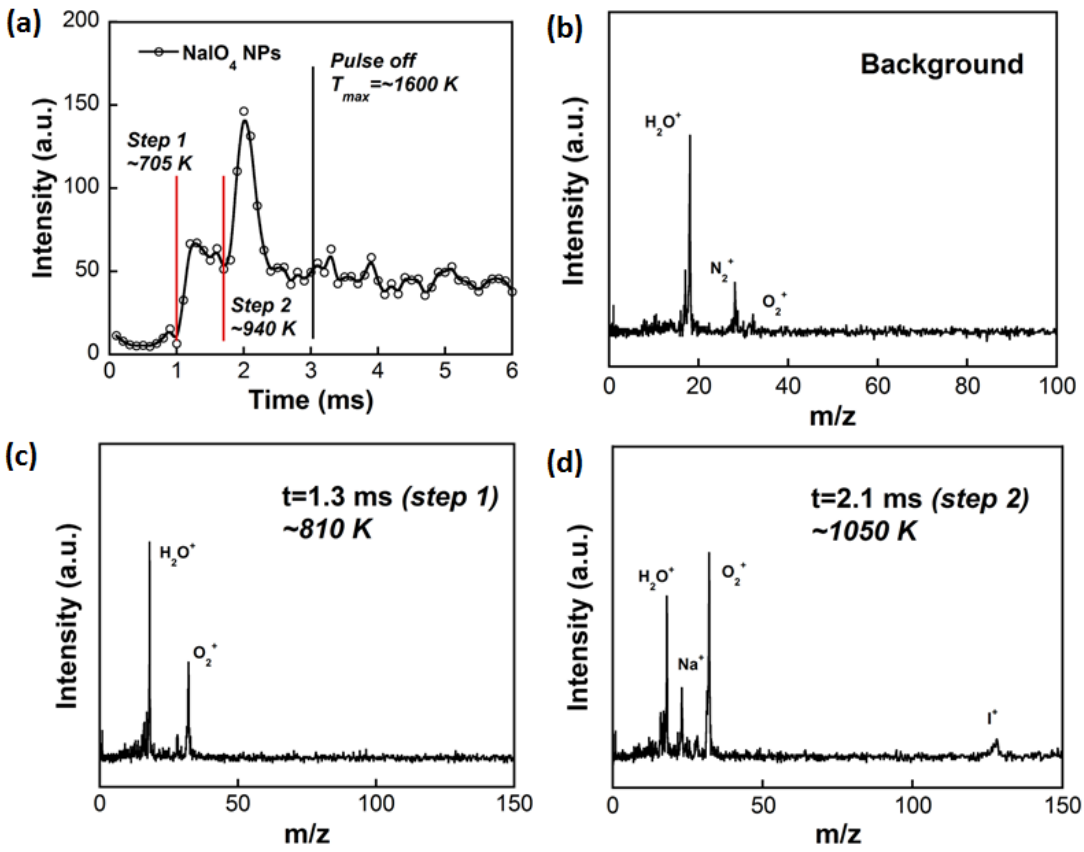


**Figure 6.10.** (a) Temporal profile of oxygen release from $NaIO_4$ nanoparticles. (b) Background mass spectrum. (c, d) The selected time resolved mass spectra of rapid heating of $NaIO_4$ nanoparticles (c-d).

Naturally, we would expect that the superior gas generating behavior and relative low ignition temperatures should be related to the properties of periodate oxidizer nanoparticles upon heating. Since $KIO_4$ and $NaIO_4$ nanoparticles behave similarly, we only analyze $KIO_4$ results in the following ($NaIO_4$ results are shown in Figure 6.10). Figure 6.9a-b show the temperature-jump time of flight mass spectrometer measured species that formed at different stages during the decomposition of $KIO_4$ nanoparticles under rapid heating (~3 ms, heating rate ~$5\times10^5$ K/s). The background spectrum in Figure 6.10b shows $H_2O$, $N_2$ and small amount of $O_2$. Unlike $KClO_4$'s

decomposition which proceeds in a single step (Figure 6.11b), $KIO_4$ appears to decompose in two stages. In the first stage at relatively low temperature <800 K (Figure 6.9a), $O_2$ is the only species detected, while $O_2$, K, and small amount of I are seen at higher temperatures >900 K (Figure 6.9b). The temporal oxygen release profile in Figure 6.9c shows two regimes as demarked in the figure, which are highly reproducible in repeated experiments. We observed an onset temperature for oxygen release of ~740 K, which is also the onset decomposition temperature of $KIO_4$ nanoparticles. The second stage of decomposition shows an increase in oxygen starting at ~900 K, which also corresponds to the first appearance of potassium.

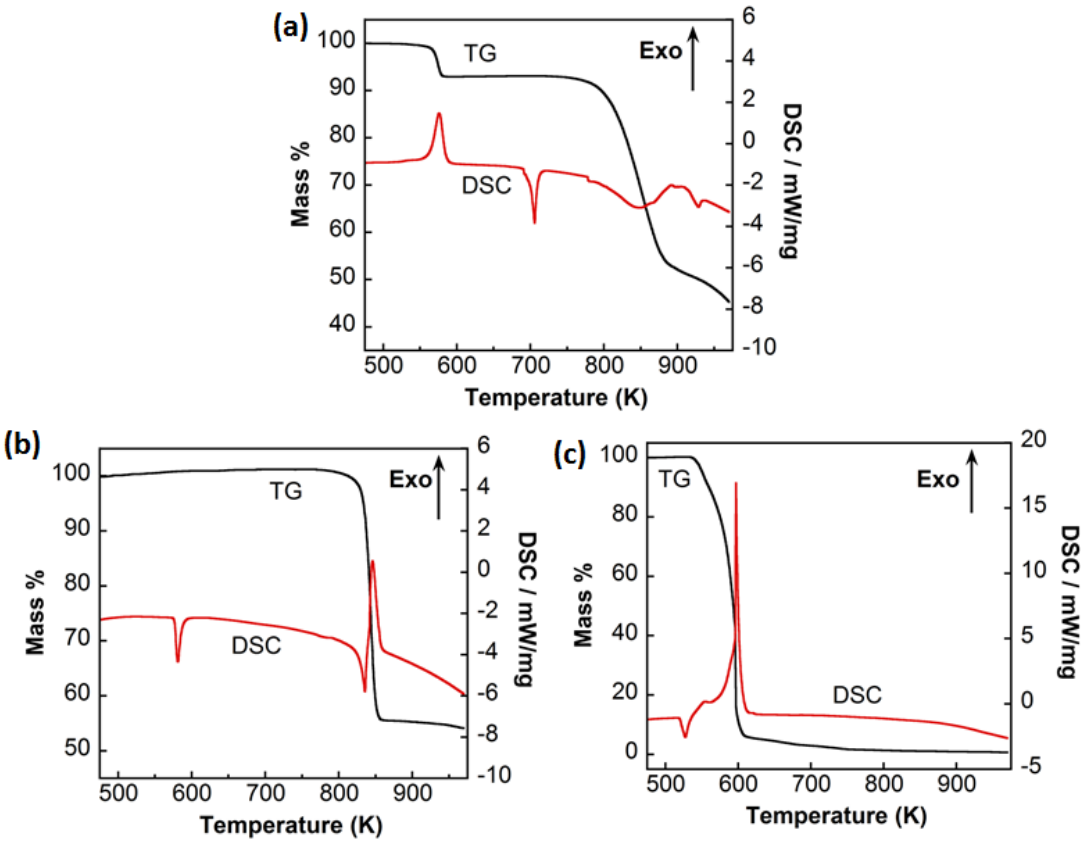

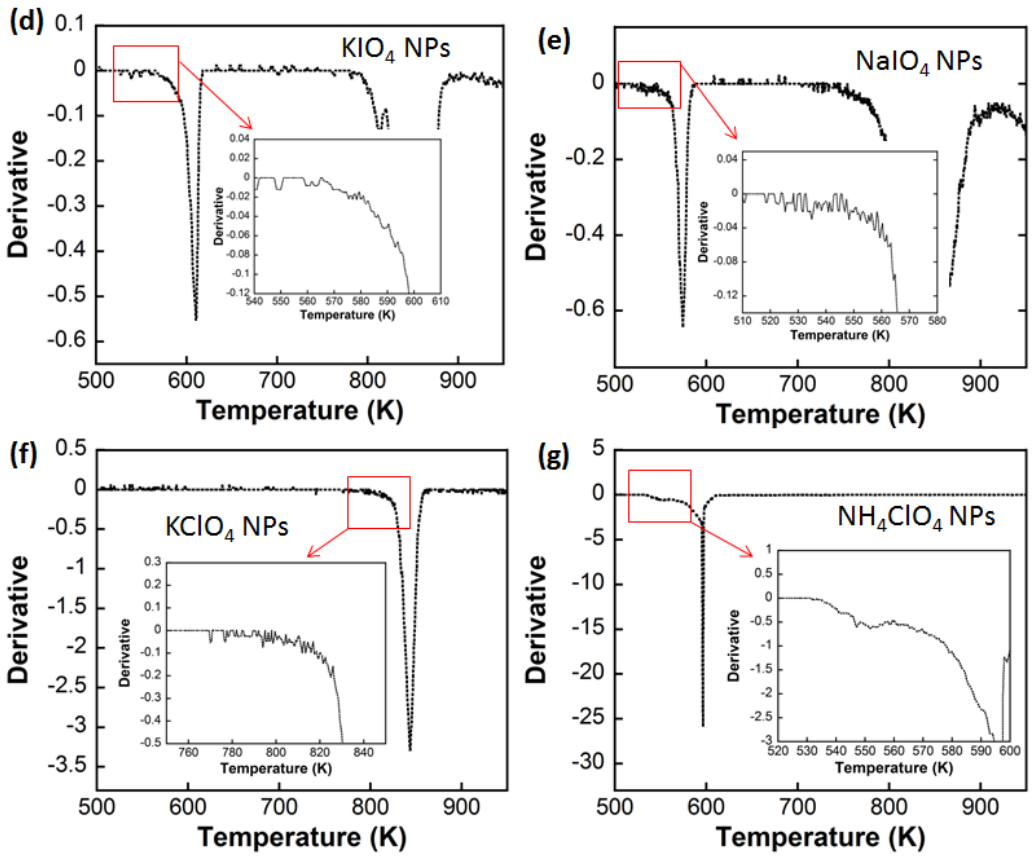


**Figure 6.11.** (a-c) TG/DSC curves of (a) $NaIO_4$ nanoparticles, (b) $KClO_4$ nanoparticles and (c) $NH_4ClO_4$ nanoparticles; d-g) DTG curves of (d) $KIO_4$ nanoparticles, (e) $NaIO_4$ nanoparticles, (f) $KClO_4$ nanoparticles, and (g) $NH_4ClO_4$ nanoparticles.

The decomposition of $KIO_4$ nanoparticles at low heating rate was studied by thermogravimetric analysis (TGA) with simultaneous heat flux by differential scanning calorimetry (DSC), as shown in Figure 6.9d. $KIO_4$ decomposes in two steps in Figure 6.9d, in agreement with high heating rate t-jump measurements in Figure 6.9a-c, and previous slow heating rate thermoanalytical studies. [29] As seen from Figure 6.9d, $KIO_4$ begins to decompose to $KIO_3$ and $O_2$ (~7% weight loss) exothermically at 570 K, while a second endothermic decomposition step begins at

780 K, to form KI and $O_2$ (~20% weight loss). Different from most metal oxide decompositions which are endothermic, periodate decomposition is exothermic which presumably is responsible for the relative low ignition temperature. Indeed we find that perchlorate nanoparticle decomposition is also exothermic, but through a single step decomposition (Figure 6.11b-c).

To further explore initiation mechanisms of periodate nanoenergetic formulations, we rapidly heated them to 1173 K at $10^6$ K/s in a hot-stage SEM with before and after images shown in Figure 6.12a, b for Al/$KIO_4$. Quite surprising, and unlike our prior SEM thermite mixture (Al/CuO, Al/$WO_3$) studies, [30] we found that no obvious fuel-oxidizer reaction is apparent, with only the nanoaluminum left on the sample holder after rapid heating (more evidence shown in Figure 6.13). Considering the fact that the high heating microscope experiments were carried out in high vacuum, we employed the T-Jump wire heating experiments for Al/$KIO_4$ with in-situ high speed imaging and mass spectrometry. These results showed that there was very little if any burning on the wire in contrast to the very violent burning at atmospheric pressure in air (Figure 6.12d) and argon (Figure 6.S2a) environments. Further mass spectrometry results (Figure 6.S4) showed spectra similar to the neat periodate nanoparticles. Since the decomposition of $KIO_4$ nanoparticles, i.e., oxygen release, commences at 740 K (Figure 6.9c), it is reasonable to conclude that oxygen released from the oxidizers in vacuum escapes from the composite energetic sample before reaching its ignition temperature. The results imply that the reaction mechanism of periodate salt based nanoenergetic formulations differ from those of metal oxide nanothermites, [28] and gas phase oxygen is critical to the ignition and burning of periodate nanoenergetics.

We must emphasize this is the first direct evidence of the contribution of gas-phase oxygen on the ignition and combustion of nanoenergetic formulations.

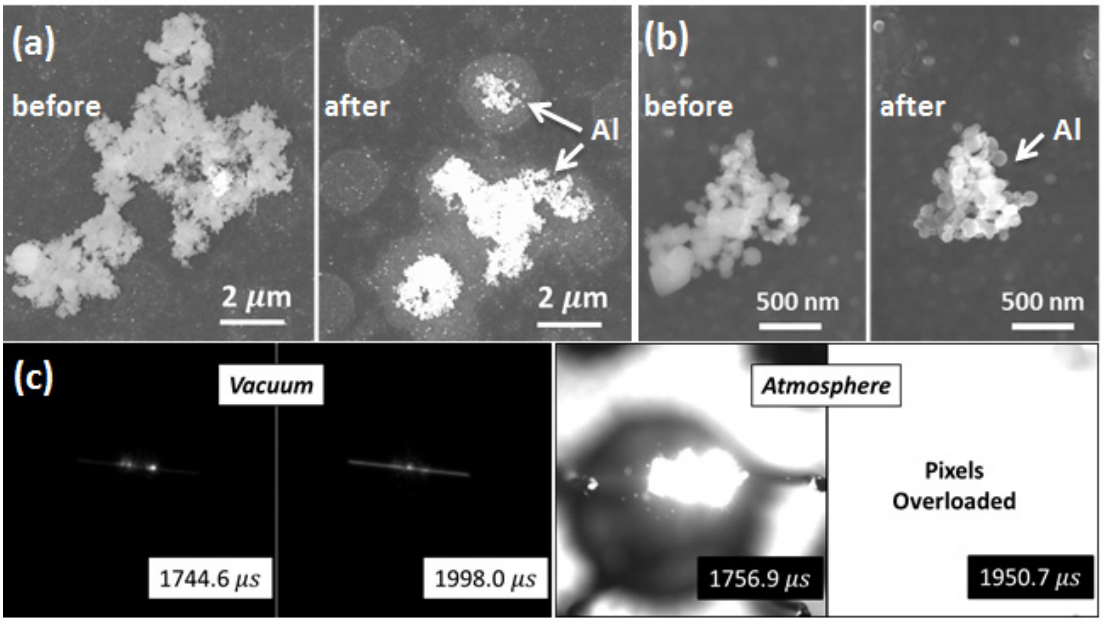


**Figure 6.12.** (a, b) SEM images of $Al/KIO_4$ nanoenergetics before and after rapid heating to 1173 K at $10^6$ K/s and holding for 1 ms. (c, d) High speed imaging of $Al/KIO_4$ nanoenergetic reaction in vacuum (T-Jump/MS) (c) and at atmospheric pressure (air).

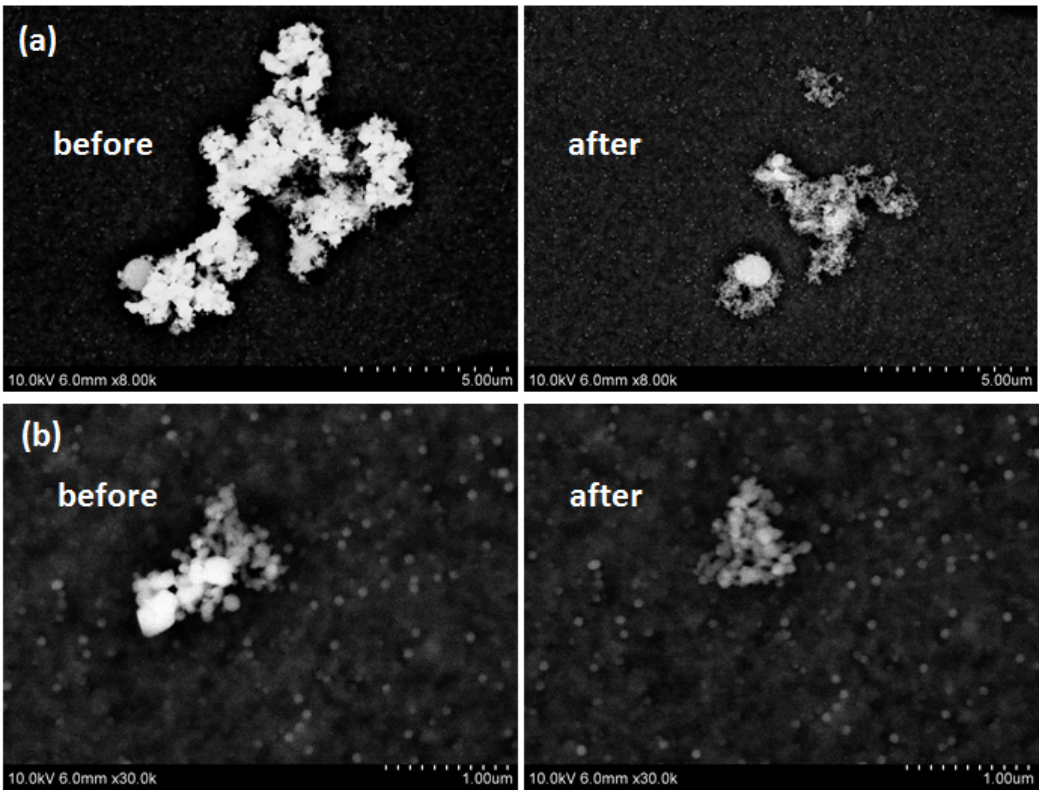


**Figure 6.13.** (a, b) Backscattered electron (BSE) images of Al/$KIO_4$ nanoenergetic formulation before and after rapid heating to 1173 K at $10^6$ K/s. Note: These are the same sample spot sites as shown in Figure 6.12a, b. The bright particles are iodine containing materials; the darker particles are Al/$Al_2O_3$ in the BSE images, confirmed using energy dispersive X-ray spectroscopy (EDS).

## *6.4. Conclusions*

In summary, periodate salt nanoparticles were prepared through an aerosol spray drying process, which demonstrate highly reactive properties when formulated into an aluminum based nanoenergetic. Several in-situ techniques at high heating rates suggest that exothermic decomposition of periodate salts contributes to the low ignition temperature of its nanoenergetic formulations. We also show direct evidence

to support that direct gas phase oxygen release from oxidizer decomposition is critical in the ignition and combustion of periodate nanoenergetic formulations.

## *6.5. Appendix A: Supplemental Information*

### *6.5.1. Supporting Videos.*

Two supporting videos can be downloaded from the following link [31]: http://onlinelibrary.wiley.com/doi/10.1002/anie.201303545/suppinfo

### *6.5.2. Supporting Video Captions.*

#### *6.5.2.1. Materials.*

As received $KIO_4$ (Sigma-Aldrich), CuO nanoparticles (<50 nm, Sigma-Aldrich), and $KIO_4$ nanoparticles (produced in this study) were stoichiometrically mixed with aluminum nanoparticles (Argonide Corp., designated as 50 nm ALEX; 70 wt. % active Al), respectively. Al/$KIO_4$ formulation contains 30.9 wt % aluminum nanoparticles and 69.1 wt % $KIO_4$. Al/CuO formulation contains 24.3 wt % aluminum nanoparticles and 75.7 wt % CuO nanoparticles. Approximately 10 ml of hexane was then added and the mixture was ultrasonicated for 30 min to ensure intimate mixing. After the evaporation of hexane in air, the powder was then gently broken apart. In the following videos, 10.0 mg thermite sample was placed on one aluminum plate and ignited by a multi-purpose lighter on top of the loose powder.

#### *6.5.2.2. Supporting Movie 1: Ignition of Thermite Samples.*

This video was taken with a Canon T2i Digital Camera. This video plays in real time. The sound level measurement was conducted by a sound level meter (Quest Technologies, SoundPro SE 1/1 Octave RTA). The measurable range for sound level

using the A weighting scale is 40-130 dB. The sound level meter was calibrated before, as well as after the experiment, and the tests and the calibration did not change which indicated that the results recorded are accurate. Our results show that nano-Al+as received $KIO_4$ produces a 68.0 dB sound peak, nano-Al+nano-CuO a 103.8 dB, and nano-Al+nano $KIO_4$ over 130 dB. The nano-Al+nano $KIO_4$ was the loudest sample as it surpassed the calibrated sensor range of 130 dB. The results show that nano-Al+nano-$KIO_4$ reaction displays the most powerful explosion.

*6.5.2.3. Supporting Movie 2: High Speed Imaging of Thermite Reactions.*

This video was taken with a Vision Research Phantom® v12.0 digital camera at a resolution of 256×256 and frame rate of 7000 fps (142.9 μs per frame). This video plays at a frame rate of 36.8 fps. The real time in the video is calculated to be: 1s in video = 5.259 ms in real time. The videos show that nano-Al+nano-$KIO_4$ reaction is much more reactive than nano-Al+nano-CuO thermite reaction, and very significantly outperforms nano-Al+as received $KIO_4$ reaction.

**Warning!**

These experiments demonstrated here should only be performed under proper safety protections.

*6.5.3. Electrostatic Discharge (ESD), Friction and Impact Sensitivity*.

The ESD sensitivity tests were carried out by using the ABL Model 150 ESD tester with a 5.785 kV DC voltage. The friction tests were carried out according to STANAG 4487 [32] using the BAM friction tester. The impact sensitivity tests were carried out according to Department of Defense Ammunition and Explosives Hazard Classification Procedures [33] using a Bureau of Explosives (BOE) impact machine.

The experiments were carried out in Indian Head Division, Naval Surface Warfare Center. The authors would like to acknowledge Dr. Greg Young for help in the tests.

***Caution:*** The reported periodate nanoenergetic materials are sensitive towards electric discharge and friction. The electrostatic discharge (ESD) sensitivity of $Al/KIO_4$, $Al/NaIO_4$ and Al/CuO nanoenergetic formulations were measured to be <8.4 mJ, and were beyond our capabilities of measurement. Similar to other nanothermite systems with high ESD sensitivities, the increased sensitivity should be the result of high surface areas that can develop charges.[s1] The friction sensitivity of $Al/KIO_4$ nanoenergetic formulation was measured to be 32 N, while $Al/NaIO_4$ and Al/CuO nanoenergetic formulations were measured to be <6 N. The proper safety precautions must be taken when handling these reactive energetic materials.

The measured impact sensitivity of $Al/KIO_4$, $Al/NaIO_4$ and Al/CuO nanoenergetic formulations were listed below. The nanoenergetic formulations are not very sensitive to impact.

**Table 6.S1.** Bureau of Explosives (BOE) impact sensitivity results.

| *Samples* | *$Al/KIO_4$* | *$Al/NaIO_4$* | *Al/CuO* | *RDX (ref. mat.)* |
|---|---|---|---|---|
| *Results** | *0 out of 10* | *1 out of 10* | *0 out of 10* | *3 out of 10* |

**Based on 10 trial screen tests to determine whether a material is too sensitive or not.*

*6.5.4. SEM images of As-received $KIO_4$ and $NaIO_4$ from Sigma-Aldrich.*

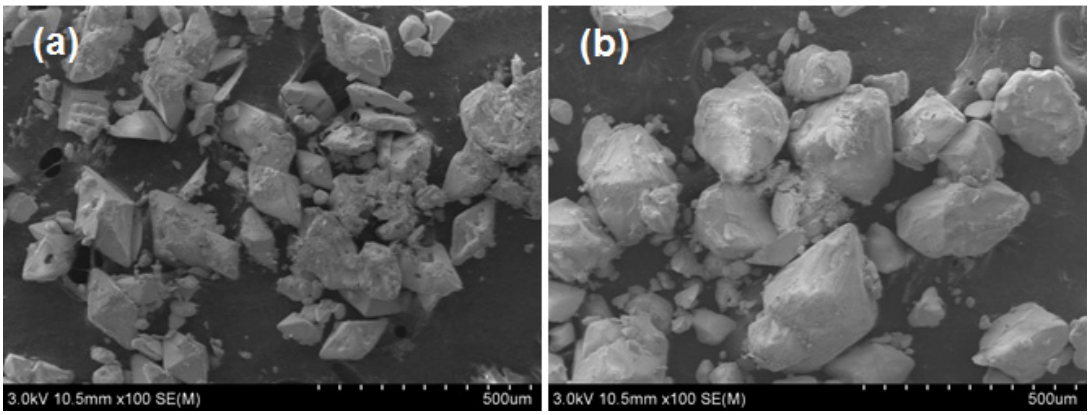


**Figure 6.S1.** SEM images of as received $KIO_4$ (a) and $NaIO_4$ (b) from Sigma-Aldrich.

*6.5.5. High Speed Imaging of Nanoenergetic Formulations Burning on the Rapid Heated Wire in Argon.*

(a) Nano Al+nano $KIO_4$. $T_{ig}$= 920 K.

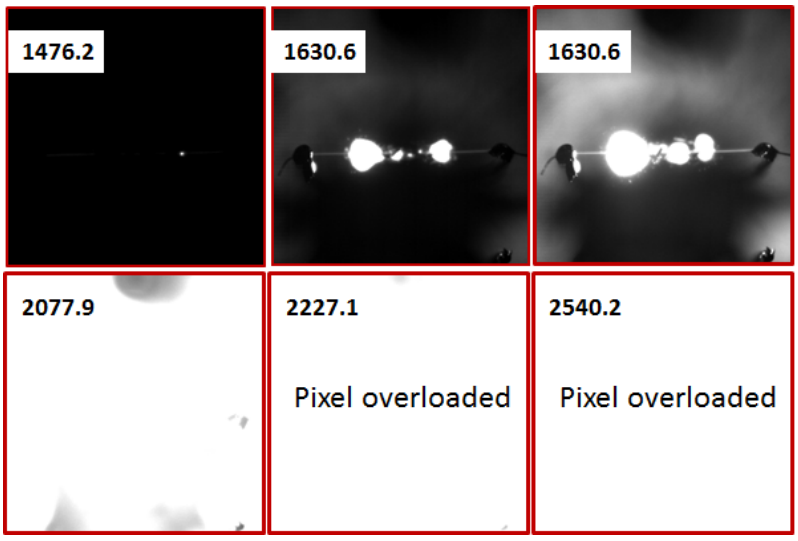

(b) Nano Al+nano $KIO_4$. $T_{ig}$= 855 K.

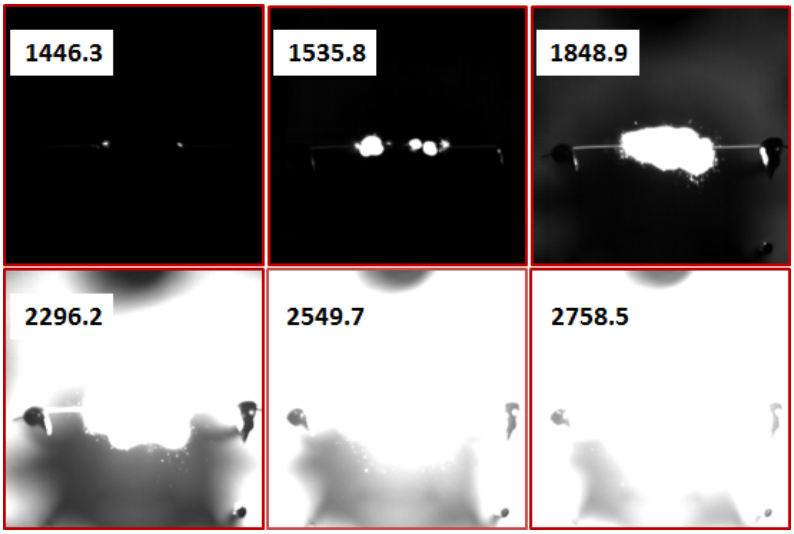


**Figure 6.S2.** (a, b) High speed imaging of nanoenergetic formulations burning on the rapid heated wire. (a) nano Al+nano $KIO_4$, (b) nano Al+nano $NaIO_4$. Note: The wire was rapidly heated to ~1600 K in 3 ms at the atmospheric pressure (argon). Label unit: µs.

*6.5.6. Rapid Heating of Al/$NaIO_4$ Nanoenergetic Formulation in SEM and Vacuum (T-Jump/MS).*

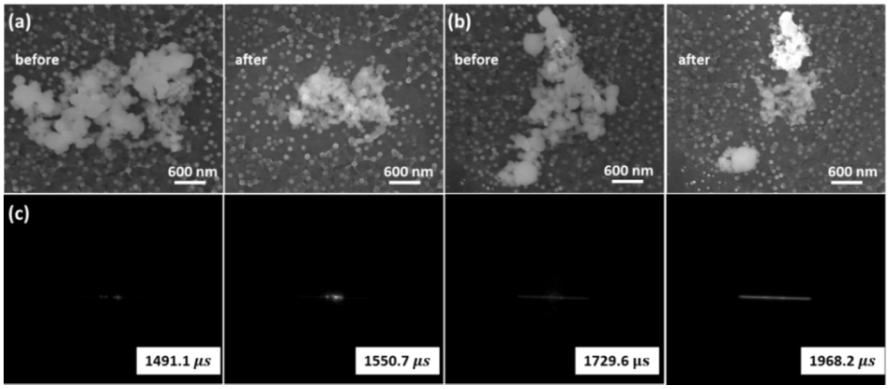


**Figure 6.S3.** (a, b) SEM images of Al/$NaIO_4$ nanoenergetic formulation before and after rapid heating to 1173 K at $10^6$ K/s and holding for 1 ms. (c) High speed imaging of Al/$NaIO_4$ nanoenergetic reaction in vacuum (T-Jump/MS).

*6.5.7. Time Resolved Mass Spectra of Al/KIO4, Al/NaIO4 Nanoenergetic Reactions.*

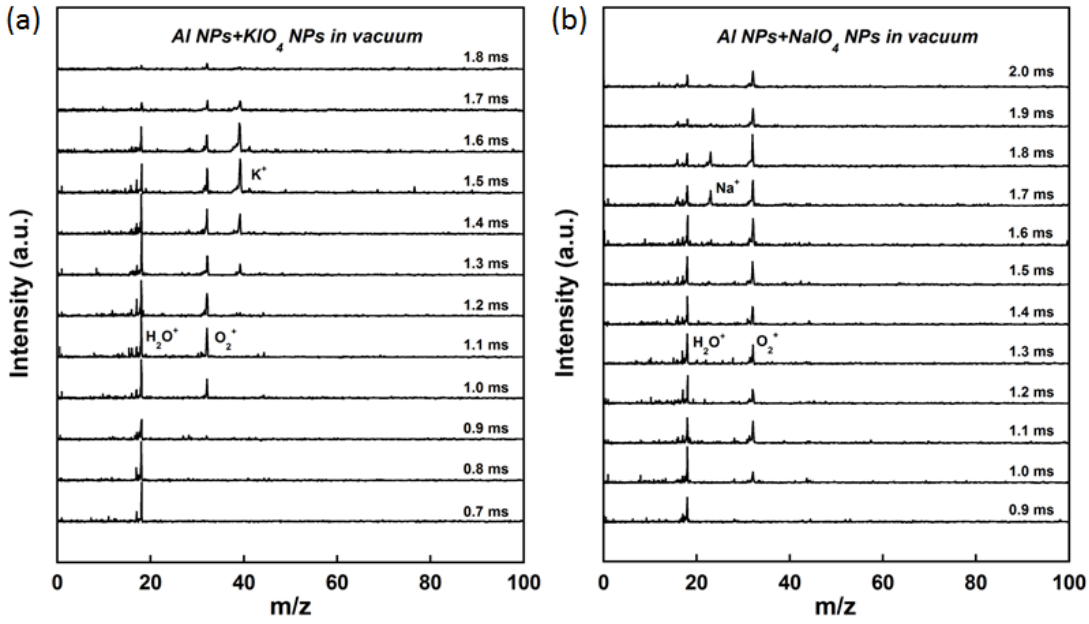


**Figure 6.S4.** (a, b) Time resolved mass spectra of Al/$KIO_4$, Al/$NaIO_4$ nanoenergetic reactions. Note: Heating pulse: 3 ms, heating rate: $4\times10^5$ K/s. The related high speed imagings were shown in Figure 6.12c, Figure 6.S3c.

*6.5.8. Post Combustion Products Analysis.*

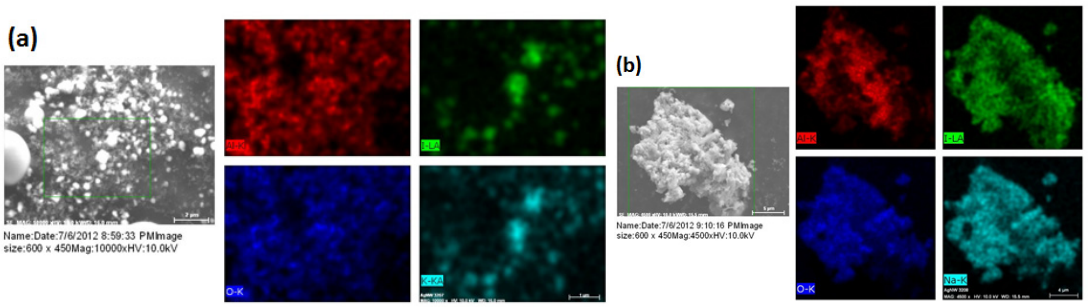


**Figure 6.S5.** (a, b) SEM images and EDS elemental mappings of post combustion products of (a) nano-Al/nano-$KIO_4$ and (b) nano-Al/nano-$NaIO_4$ reactions. The results show that $Al_2O_3$ and KI or NaI are main reaction products.

## *6.6. References*


[1] Aumann, C. E.; Skofronick, G. L.; Martin, J. A. *J. Vac. Sci. Technol. B* **1995**, *13*, 1178-1183.

[2] Rossi, C.; Estéve, A.; Vashishta, P. *J. Phys. Chem. Solids* **2010**, *71*, 57-58.

[3] Zachariah, M. R. *Propellants Explos. Pyrotech.* **2013**, *38*, 7.

[4] Piercey, D.G.; Klapötke, T.M. *Central Europ. J. Energ. Mat.* **2010**, *7*, 115-129.

[5] Rossi, C.; Zhang, K.; Estéve, D.; Alphonse, P.; Thailhades, P.; Vahlas, C. *J. Microelectromech. Syst.* **2007**, *16*, 919-931.

[6] Dreizin, E.L. *Prog. Energy Combust. Sci.* **2009**, *35*, 141-167.

[7] Martirosyan, K.S. *J. Mater. Chem.* **2011**, *21*, 9400-9405.

[8] Yetter, R.A.; Risha, G.A.; Son, S.F. *Proc. Combust. Inst.* **2009**, *32*, 1819-1838.

[9] Yen, N.H.; Wang, L.Y. *Propellants Explos. Pyrotech.* **2012**, *37*, 143-155.

[10] Prakash, A.; McCormick, A.V.; Zachariah, M.R. *Adv. Mater.* **2005**, *17*, 900-903.

[11] Martirosyan, K.S.; Wang, L.; Luss, D. *Chem. Phys. Lett.* **2009**, *483*, 107-110.

[12] Becker, C.R.; Apperson, S.; Morris, C.J.; Gangopadhyay, S.; Currano, L.J.; Churaman, W.A.; Stoldt, C.R. *Nano Lett.* **2011**, *11*, 803-807.

[13] Plummer, A.; Kuznetsov, V.; Joyner, T.; Shapter, J.; Voelcker, N.H. *Small* **2011**, *7*, 3392-3398.

[14] Lide, D.R. *CRC Handbook of Chemistry and Physics*, 85th ed., CRC Press, Boca Raton, **2004**.

[15] Holleman, A.F.; Wiber, E.; Wiberg, N.*Inorganic Chemistry*, Academic Press, New York, **2001**, p. 465.

[16] Wu, C.W.; Sullivan, K.; Chowdhury, S.; Jian, G.Q.; Zhou, L.; Zachariah, M.R. *Adv*. *Funct*. *Mater*. **2012**, *22*, 78-85.

[17] Giles, J. *Nature* **2004**, *427*, 580-581.

[18] Fournier, E. W.; Brady, B. B. *J. Propul. Power* **2005**, *21*, 937-941.

[19] Steinhauser, G.; Klapötke, T.M. *Angew. Chem. Int. Ed.* **2008**, *47*, 3330-3347.

[20] Moretti, J. D.; Sabatini, J.J.; Chen, G. *Angew. Chem. Int. Ed.* **2012**, *51*, 6981-6983.

[21] Boissiere, C.; Grosso, D.; Chaumonnot, A.; Nicole, L.; Sanchez, C. *Adv. Mater.* **2011**, *23*, 599-623.

[22] Carne-Sanchez, A.; Imaz, I.; Cano-Sarabia, M.; Maspoch, D. *Nature Chem.* **2013**, *5*, 203-211.

[23] Zhou, L.; Piekiel, N.; Chowdhury, S.; Zachariah, M. R. *Rapid Commun. Mass Spectrom.* **2009**, *23*, 194-202.

[24] Jian, G.Q.; Piekiel, N.W.; Zachariah, M.R. *J. Phys. Chem. C* **2012**, *116*, 26881-2688.

[25] Sullivan, K.; Zachariah, M.R. *J. Propul. Powe*r **2010**, *26*, 467-472.

[26] Jian, G.Q.; Liu, L.; Zachariah, M.R. *Adv. Funct. Mater.* **2013**, *23*, 1341-1346.

[27] Bazyn, T.; Krier, H.; Glumac, N. *Combust. Flame* **2006**, *145*, 703-713.

[28] Jian, G.Q.; Chowdhury, S.; Sullivan, K.; Zachariah, M.R. *Combust. Flame* **2013**,*160*, 432-437.

[29] Muraleedharan, K.; Kannan, M.P.; Gangadevi, T. *J.Therm.Anal.Calorim.* **2010**, *100*, 177-181.

[30] Sullivan, K.T.; Piekiel, N.W.; Wu, C.; Chowdhury, S.; Kelly, S.T.; Hufnagel, T.C.; Fezzaa, K.; Zachariah, M.R. *Combust. Flame* **2012**, *159*, 2-15.

[31] Jian, G.Q.; Feng, J.Y.; Jacob, R. J.; Egan, G. C.; Zachariah, M.R. *Angew. Chem. Int. Ed.* **2013**, *52*, 9743-9746.

[32] NATO Standardization Agreement (STANAG) on Explosive, Friction Sensitivity Tests, No. 4487, 1st ed., August 22, **2002**.

[33] Technical Bulletin (TB) 700-2/Naval Sea Systems Command Instruction (NAVSEAINST) 8020.8B/Technical Order (TO) 11A-1-47/Defense Logistics Agency Regulations (DLAR) 8220.1, "Department of Defense Ammunition and Explosives Hazard Classification Procedures," January 5, **1998**.

# Chapter 7: Iodine Pentoxide as an Oxidizer in the Thermite Reaction *

## *Highlights*

(a) The ignition and combustion behavior of nano-Al/micro-$I_2O_5$ thermite was systematically studied.

(b) Results suggest that the burning of nano-Al/micro-oxidizer systems in this study is possibly limited by the decomposition of oxidizers.

(c) Considering its potential application as biocides, nano-Al/micro-$I_2O_5$ thermite reactions are an effective way to produce iodine gas via a condensed phase reaction.

## *Overview*

Thermite reactions with high energy release that produce biocidal agents are of interest for their potential applications in bio-agent defense. In this work, we investigated the ignition and combustion of nano-Al/micro-$I_2O_5$ thermite, and studied its potential use in biocidal applications. Cyro-milling was used to produce micro-sized $I_2O_5$ (~2-4 μm), which were used as the oxidizer in this study. The ignition and reaction of the prepared nano-Al/micro-$I_2O_5$ thermite were systematically studied by a rapid fine wire heating technique using a high speed digital camera and a

* The results presented in this chapter have been published in the following conference paper: Jian, G.Q.; Chowdhury, S.; Feng, J.Y.; Zachariah, M.R. In *The Ignition and Combustion Study of Nano-Al and Iodine Pentoxide Thermite*, Proceedings of 8th US National Combustion Meeting, Park City, Utah, USA, 19-22 May, **2013**.

temperature-jump/time-of-flight mass spectrometer (T-Jump/TOFMS). The ignition temperature of nano-Al/micro-$I_2O_5$ thermite in air at atmospheric pressure was found to be ~810 K, lower than ignition temperature ~940 K in vacuum. Time-resolved mass spectra results confirmed that the nano-Al/micro-$I_2O_5$ thermite reaction can produce a lot of iodine species which were suggested to be good biocidal agents. Thermal decomposition of the $I_2O_5$ oxidizer under rapid heating conditions was investigated using T-Jump/TOFMS, and was found to release significant amounts of $O_2$ before its thermite ignition. Constant-volume combustion cell tests were carried out to characterize the pressure rise and optical emissions during the thermite combustion events, and the performance of the $I_2O_5$ containing thermites was compared with other metal oxide thermite systems. The results show that the Al/$I_2O_5$ thermite composite outperforms the traditional Al/CuO and Al/$Fe_2O_3$ thermite systems in terms of peak pressure, pressurization rate, and burning time. Additionally, we observed the concurrent pressure and optical rising for all nano-Al/micro-oxidizer thermites in this study. The results indicate that the pressure rise in the nano-Al/micro-$I_2O_5$ thermite reaction should be from the release of iodine from the thermite reaction with oxygen release being a secondary contributor, suggesting the benefit of using micro sized $I_2O_5$ as a biocidal oxidizer. Transmission electron microscopy with X-ray compositional microanalysis characterization was performed to analyze the post-combustion products. The production of iodine and aluminum oxides were found as main products. Additional studies of the hygroscopic properties of $I_2O_5$ on its thermite reaction will also be discussed. Our study of Al/$I_2O_5$ thermites show that these $I_2O_5$ containing thermite reactions are very reactive, and are

suggested to effectively produce iodine gas, which can be used in microbial agent defense applications.

## *7.1. Introduction*

Global terrorist threats involving the usage of biological agents highlight the need for preemptive neutralization of biological agent munitions, stockpiles, and production facilities. The approaches for effective destruction of biological agents are being considered and an ideal neutralization of biological agents is suggested to possess both a thermal and long-lasting biocidal agent release. [1] Recently, one class of thermite reactions, which exhibit both ideal thermal and chemical characteristics, were proposed to be a promising approach to effectively neutralize this threat. [1-6]

The thermite reaction is a highly exothermic reaction between a metal fuel and metal oxide oxidizer. Aluminum is most often the choice of fuel, due to its high reaction enthalpy, high thermal conductivity, and availability. [7-8] A variety of oxidizers have been used in formulation of thermites, with the most studied oxidizers including $Fe_2O_3$, CuO, $MoO_3$, $Bi_2O_3$, $WO_3$, etc. [9-12] On the other hand, other oxidizers, such as $KMnO_4$, [13] $KClO_4$, [14] $AgIO_3$, [1] are found to be highly reactive. Among these oxidizers, $AgIO_3$ has been considered as a potential biocide due to the large thermal release and the reaction products. Sullivan et al. found that both silver and iodine species, which are known biocides, produced in the Al/$AgIO_3$ thermite reactions were predominantly found in the exterior of the product particle, and thus were bio-available. [1] Another class of oxidizers containing iodine, such as $I_2O_5$ etc., [3, 6, 15] have been suggested as a means to release significant quantities of gas phase iodine. Martirosyan et al. found that Al/$I_2O_5$ nanothermite produced a much

higher transient pressure pulse than traditional metal oxides based nanothermites. [6, 16] Clark and Pantoya tested the biocidal effects of different thermites reactions ($Al+I_2O_5$, $Al+Ag_2O$, and $Al+Fe_2O_3$) on spore neutralization and found that only the iodine containing thermite demonstrated significant spore neutralization. [3]

In this chapter, we aim to further explore the $Al/I_2O_5$ thermite reaction. In particular, ignition and combustion performance along with the final state of the products will be studied. The ignition and reaction process of nano-Al/micro-$I_2O_5$ were characterized by a high speed digital camera and a temperature-jump/time-of-flight mass spectrometer (T-Jump/TOFMS), and whereby thermite reactions can be initiated from a rapidly heated fine wire. The decomposition of iodine pentoxide during rapid heating was also characterized by T-Jump/TOFMS. Constant-volume combustion tests were performed, and compared with traditional thermite formulations. The post combustion products were characterized using transmission electron microscopy and X-ray analysis. The results demonstrate that the iodine containing thermites can produce a lot of iodine species and possess good combustion performance, indicating their potential applications in biocide and energetic gas generators.

## *7.2. Experimental Section*

### *7.2.1. Sample Preparation.*

The nano-aluminum samples used in this study were purchased from the Argonide Corporation, and designated as “50 nm ALEX”. The active aluminum was measured by TGA to be 70% by weight, which was taken into consideration when preparing the stoichiometric samples. Iodine pentoxide powder ($I_2O_5$) was purchased from Sigma-

Aldrich (99.99 % purity) and stored in a glove box to prevent water adsorption. Powder X-ray diffraction (XRD, Bruker D8 Advance using Cu Kα radiation) results in Figure 7.1 show that the as received $I_2O_5$ contains small amount of $HI_3O_8$ which is either from manufacturing process or water adsorption during XRD characterization. Microsized $I_2O_5$ samples were prepared by mechanical milling for 1 hour (Cyromill, Retsch) of the as-received $I_2O_5$ in hexane to prevent water uptake.

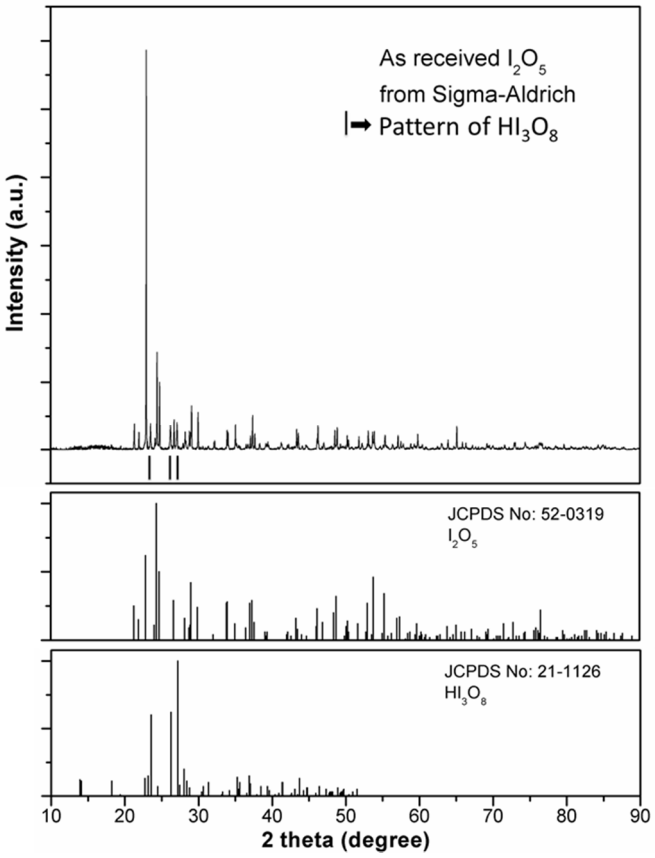


**Figure 7.1.** XRD pattern of as received $I_2O_5$ from Sigma-Aldrich and standard XRD patterns of $I_2O_5$ and $HI_3O_8$. Note: All other peaks without marks in as received $I_2O_5$ are from $I_2O_5$ phase.

The milled $I_2O_5$ samples, as well as as-received $I_2O_5$ were characterized by scanning electron microscopy (SEM, Hitachi SU-70 FEG-SEM), and the images show the particle sizes go down to 2-4 μm after milling, as shown in Figure 7.2. The milled $I_2O_5$ particles were used in the following tests. Microsized $Fe_2O_3$ and CuO powders (<5 μm as specified) used in this study were purchased from Sigma-Aldrich and are summarized in Table 7.1 (in discussion part). These thermite formulations can be thought of as composites comprised of a nanosized fuel and microsized oxidizers.

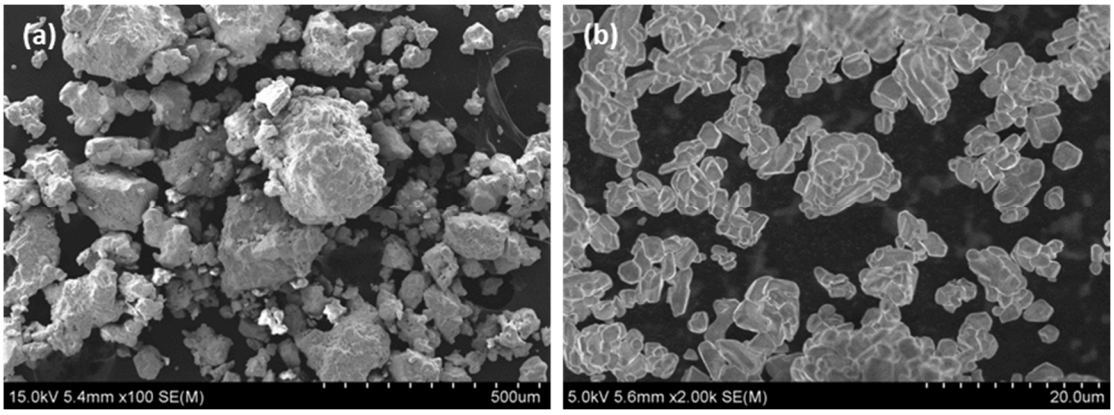


**Figure 7.2.** SEM images of as received (a) and milled (b) $I_2O_5$ particles.

Thermite samples were prepared by mixing of nano-aluminum and $I_2O_5$ powder in stoichiometric ratio. The mixed samples were ultrasonicated in ~10 ml hexane for about 30 min to ensure the mixing between the fuel and oxidizer. For the wire heating experiments, the prepared sample suspension was coated onto a ~10 mm long, 76 μm diameter platinum wire with a micropipette. For the constant volume combustion cell tests, the ultrasonicated thermite sample suspensions were kept in a vacuum oven at 333 K (60 $^oC$) to allow the hexane to fully evaporate. The dry powder was then gently broken apart into a loose powder.

*7.2.2. Time-resolved Mass Spectrometry Measurement and Wire Ignition with High Speed Imaging.*

The recently developed temperature-jump/time-of-flight mass spectrometer (T-Jump/TOFMS) [17] was used to characterize the decomposition of $I_2O_5$ and the thermite reaction between nano-Al and $I_2O_5$. The T-Jump probe (76 μm Pt wire) is directly inserted close to the electron ionization (EI) region of the TOF mass spectrometer, which enables continuously monitoring of a reaction event with a temporal resolution of 100 μs per mass spectrum. Typically, the T-Jump filament (Pt wire, length ~12 mm, diameter ~76 μm) was coated with a thin layer of sample powder (~0.1 mg) and directly inserted close to the electron ionization (EI) region of the mass spectrometer. The coated Pt wire can be rapidly joule heated up to ~ 1800 K in 3 ms, corresponding to a heating rate of $\sim 5\times10^5$ K/s. The Pt wire was replaced after each heating event. From the voltage and current trace, a resistivity measurement can be obtained and related to the instantaneous temperature of the Pt wire, which can be mapped against the time resolved mass spectra. Time-resolved mass spectra combined with the temperature profile were then used for characterization of the decomposition or thermite reaction. A detailed experimental description of T-Jump/TOFMS can be found in Chapter 2 and our previous papers. [17, 18]

High speed imaging of each sample burning on the wire was conducted with a Vision Research Phantom® v12.0 digital camera. The high speed video was taken at a resolution of 256×256 and frame rate of 67065 fps (14.9 μs per frame). The ignition temperature of the thermite sample reaction was obtained from correlating the high speed imaging of the ignition events with the temperature profile of the Pt wire.

*7.2.3. Combustion Cell Test: Simultaneous Pressure and Optical Characterization.*

A constant volume combustion cell [13, 19] was used to characterize the reactivity of bulk thermite samples with the capability of simultaneous pressure and optical measurements. Typically, a fixed mass (25 mg) of the loose thermite sample was placed inside a constant-volume (~13 $cm^3$) pressure vessel and ignited by joule heating of a nichrome coil. A piezoelectric pressure transducer on one port of the cell, together with an in-line charge amplifier and signal conditioner, were employed to measure the temporal pressure change and the pressurization rate (dP/dt). The pressurization rate has been used as a measure of reactivity in thermites since it has been found to correlate with flame propagation velocity, [20] another widely used measurement of thermite reactivity. The optical signal was simultaneously collected by a lens tube assembly attached to another port on the cell, containing a planoconvex lens (f = 50 mm) and a photodetector to collect the broadband emission. The characteristic burn time of thermites in the pressure cell was represented by the full width at half-maximum (FWHM) of the recorded optical signal. For the detailed combustion cell measurement, you can refer to our previous papers. [13, 19]

The measurement of reactivity of the thermites is usually reported as a relative value, which indicates that both the pressurization rate and optical emission measurements should only be thought of in terms of relative performance at the present time.

*7.2.4. Post-combustion Characterization.*

The post-combustion products were collected after combustion test in the combustion cell. The collected sample was dry ground by rubbing the sample between two very clean glass slides. The powder adhered onto a TEM grid (Au mesh/carbon film) for analysis in a transmission electron microscope (TEM, JEOL JEM 2100 FEG). This TEM sample preparation technique was used to avoid any interaction between the combustion products (e.g. iodine) and solvent. The TEM is equipped with an energy dispersive X-ray spectrometer (EDS, Oxford INCA 250) for elemental analysis, which can be operated in scanning mode to perform 1D elemental line scanning and 2D elemental mapping of the sample.

## *7.3. Results and Discussion*

*7.3.1. Time Resolved Mass Spectrometry of Iodine Pentoxide Decomposition and Reaction with Nano-Aluminum.*

$I_2O_5$ particles, as well as thermite samples of nano-Al/micro-$I_2O_5$, were rapidly heated for ~3 ms and up to ~1800 K, at a heating rate of $5\times10^5$ K/s, and the species formed were examined by the time-resolved mass spectrometry. We begin by examining the time resolved mass spectra of milled $I_2O_5$ sample (microsized) decomposition under rapid heating, shown in Figure 7.3a. For spectrum taken at t<1.0 ms (also seen in t=0 s in Figure 7.5), primary peaks of $H_2O$ (m/z=18) and $N_2$ (m/z=28), together with a small amount of $O_2$ (m/z=32) are from the background species in the ionization chamber. At T=800 K (t=1.0 ms), we found a strong signal assigned to $O_2^+$ and other signals assigned to $I^+$, $IO^+$, $IO_2^+$, $I_2^+$, and $I_2O^+$.

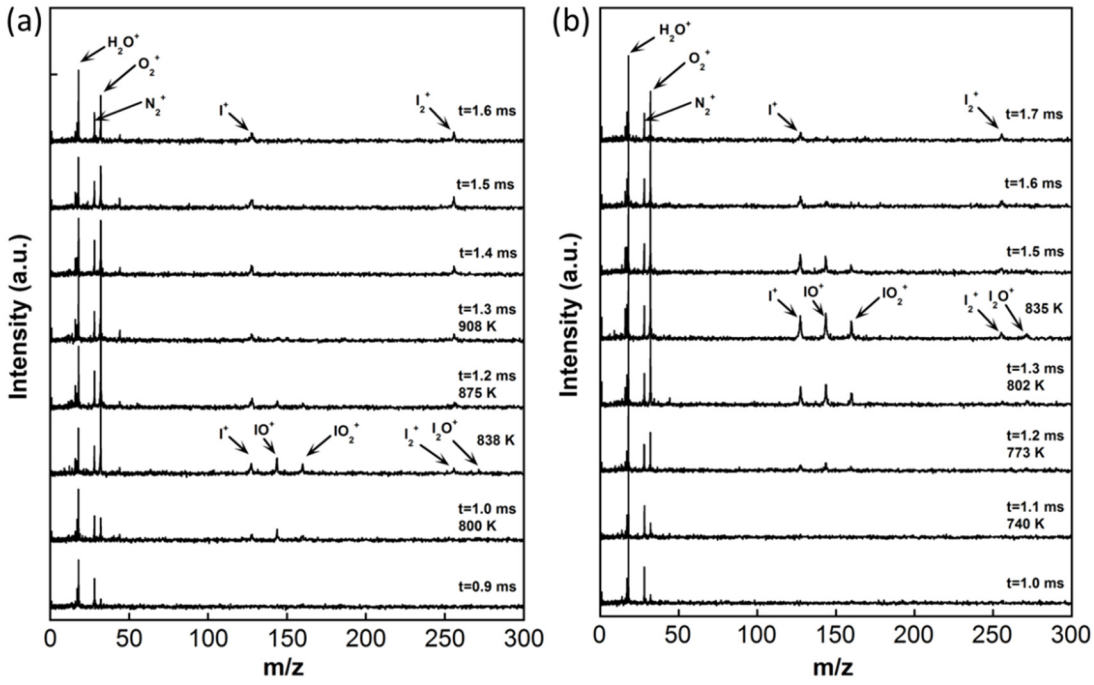


**Figure 7.3.** Time-resolved mass spectra from $I_2O_5$ decomposition (a) milled sample prepared in glove box and (b) milled sample exposed to air for one day.

It is noted that $I^+$, $IO^+$, and $IO_2^+$ were previously reported as the primary species of iodic acid ($HIO_3$) decomposition using mass spectrometry. [21] Given the fact that $I_2O_5$ is hygroscopic, this suggests that the spectrum taken at ~800 K might be from the decomposition of $HI_3O_8$ (also denoted as $HIO_3.I_2O_5$) [22] which forms from the reaction between iodine pentoxide and water ($3I_2O_5+H_2O \rightarrow 2HI_3O_8$). At higher temperatures >910 K (t=1.3 ms), only a very strong $O_2^+$ signal, as well as $I^+$ and $I_2^+$, are observed. We also plot $O_2^+$ and $H_2O^+$ temporal intensity obtained during the rapid heating of milled $I_2O_5$ sample as a function of time and wire temperature shown in Figure 7.4a. From Figure 7.4a, the onset temperature of oxygen release for milled $I_2O_5$ particles is found to be ~760 K.

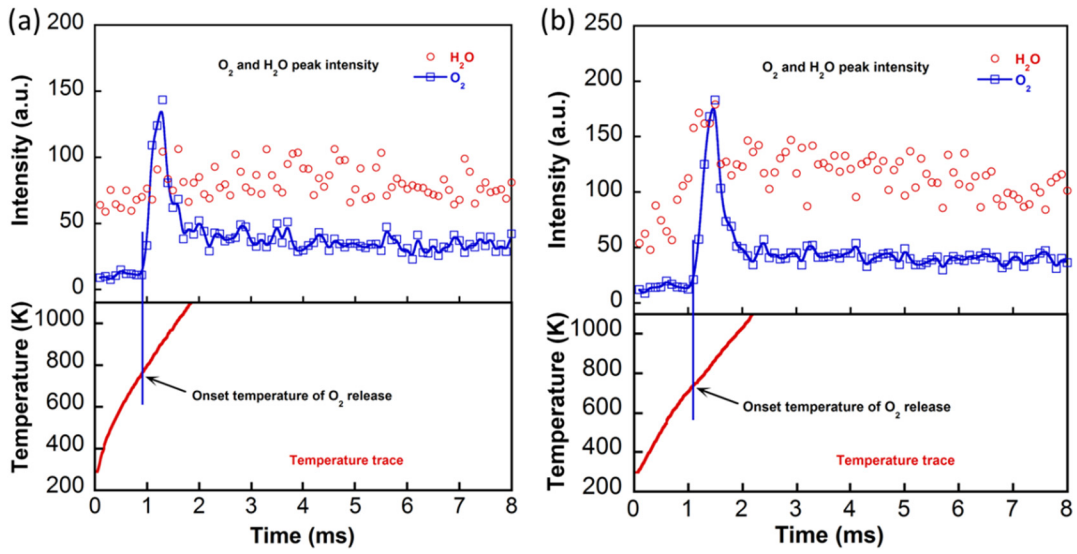


**Figure 7.4.** Temporal profile of oxygen and water peak intensity from heating of $I_2O_5$ samples. (a) Milled sample prepared in glove box and (b) milled sample exposed to air for one day. (Heating rate ~$5\times10^5$K/s)

In Figure 7.3b, we show the mass spectra taken during rapid heating of another milled $I_2O_5$ sample which was exposed to air for one day and expected to absorb much more water than milled $I_2O_5$ sample shown in Figure 7.3a . Comparison of the two samples (Figures 7.4a-b) clearly shows that water evolution in the air exposed sample is significantly above the background. Since the $I_2O_5$ sample shown in Figure 7.4b contains more water, it is not surprising to see a higher intensity of $IO^+$ and $IO_2^+$ in Figure 7.3b. Similar with milled $I_2O_5$ samples shown in Figure 7.3a, only strong $O_2^+$ signal and $I^+$, $I_2^+$ species, which are from the decomposition of $I_2O_5$ ($2I_2O_5 \rightarrow 5O_2+2I_2$), can be seen at higher temperature. The onset oxygen release temperature is ~740 K, as shown in Figure 7.4b.

Figure 7.5 shows the time resolved mass spectra taken at 100 μs intervals for a nano-Al and milled $I_2O_5$ (microsized) thermite reaction. In addition to the mass spectrometry measurement conducted for the thermite reaction, a high speed camera system was coupled with the mass spectrometer to simultaneously capture the emission from the ignition and combustion process. The thermite sample was found to ignite at ~940 K (t=1.70 ms) as optically observed by the high speed camera. We also observe $O_2^+$, $I^+$ and $I_2^+$ prior to ignition, consistent with the straight decomposition of $I_2O_5$. Post ignition, we find strong signals for $O_2^+$ and $I^+$ and weaker signals from $I_2^+$ and $I^{2+}$. A very weak $IO^+$ peak was also observed after ignition, presumably from some water in the sample. The species observed are consistent with the global reaction presented in Eq. 1 and 2. One point of note is that the amount of oxygenated iodine species is reduced in the thermite as compared with the straight decomposition implying, not surprisingly, that the iodine sub-oxides can also act as an aluminum oxidizer.

Secondarily, we also see that ignition (~940 K) occurs after the point of gas phase release of $O_2$ from $I_2O_5$ (~740 K) and essentially at the point that aluminum melts (933 K).

$$2I_2O_5 \rightarrow 2I_2+5O_2 \qquad \text{Eq. (1)}$$

$$10Al+3I_2O_5 \rightarrow 5Al_2O_3+3I_2 \qquad \text{Eq. (2)}$$

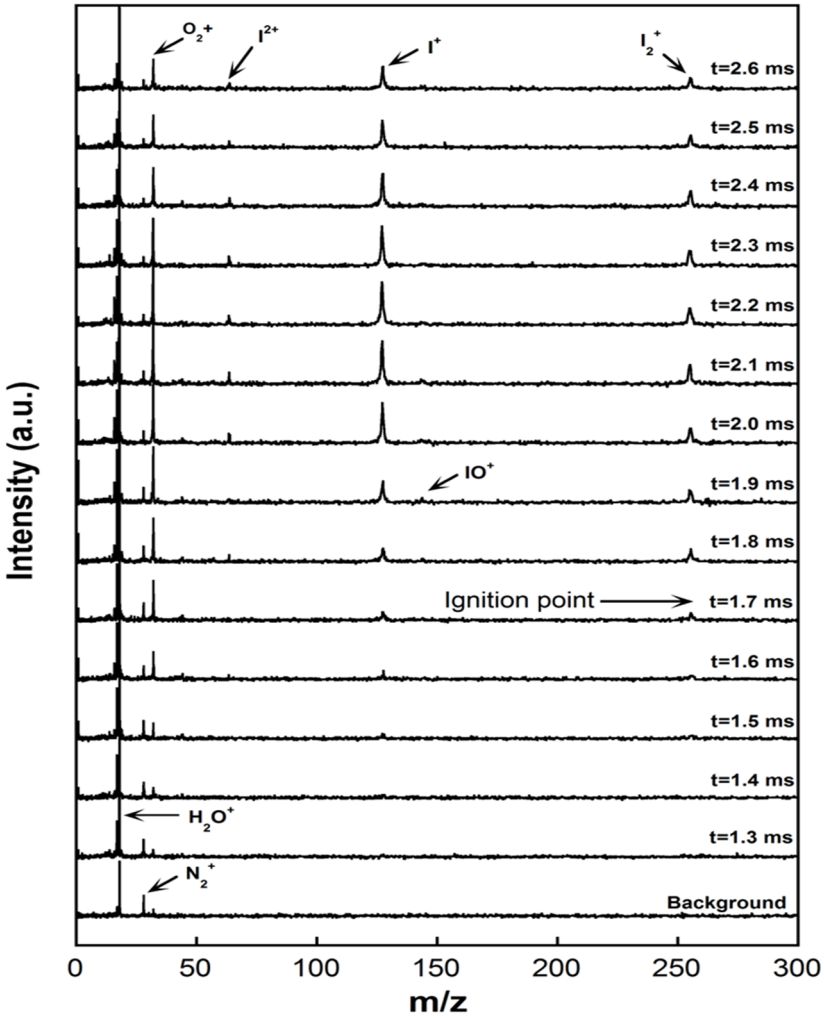


**Figure 7.5**. Time-resolved mass spectra from nano-Al+micro $I_2O_5$ thermite reaction.

*7.3.2. Combustion Characterization of Nano-Al/Micro-$I_2O_5$ Thermites.*

The ignition behavior of nano-Al/micro-$I_2O_5$ thermite samples was examined in atmospheric conditions by high-speed imaging. In Figure 7.6, we show selected temporal snapshots of the violent Al/$I_2O_5$ thermite reactions at atmospheric pressure. The images allow us to assign the point of ignition at t=1.491 ms, corresponding to the wire temperature of ~810 K. The images also show two ignition points that propagate toward each other, and are suggestive of a flame propagation mechanism consistent with hot $O_2$ convective heat transfer effects. In fact, this explanation has

been previously suggested to explain high propagation rates for $Al/AgIO_3$ burning on the wire. [1] Herein, we noted that the ignition temperature for the $Al/I_2O_5$ system in air at atmospheric pressure is found to be 100 degrees lower than the melting point of the aluminum. The low ignition temperature might be explained by the possible exothermic reaction between producing iodine from the oxidizer decomposition and the aluminum oxide shell surrounding the Al nanoparticles. [4]

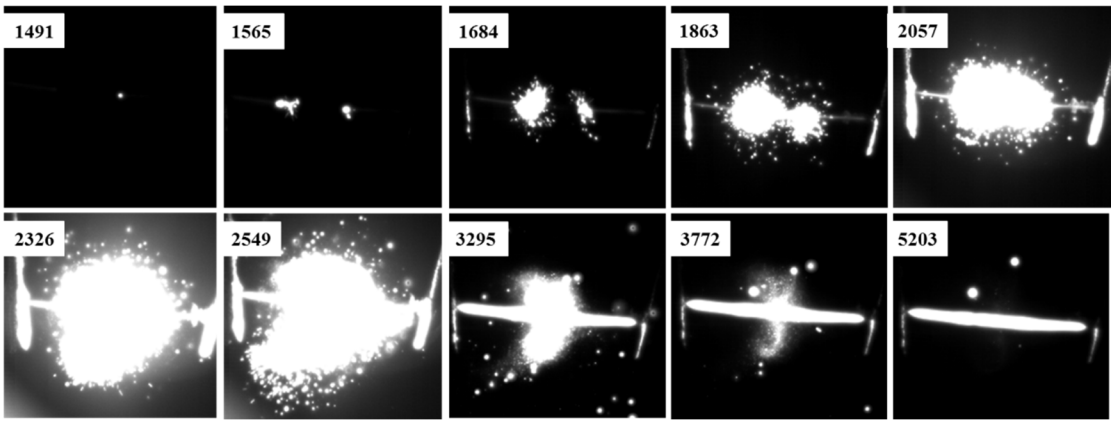


**Figure 7.6.** Sequential snapshots of $Al/I_2O_5$ burning on fast-heating wire in air, as captured by a high-speed video camera. The labeled numbers are time elapsed (μs) after triggering. The thermite is nano-Al (ALEX) and milled $I_2O_5$ (microsized) with an equivalence ratio of 1.0.

In the ionization chamber of mass spectrometer (~$10^{-6}$ Torr), the nano-Al/micro-$I_2O_5$ thermites displayed a much less violent reaction and burning than at atmospheric conditions. It is worth noting that a higher ignition temperature was found for the nano-Al/micro-$I_2O_5$ thermite in vacuum (940 K), compared to~810 K in air at atmospheric pressure. However, ignition temperatures in both cases are still higher than the oxygen release temperature of the $I_2O_5$ particles (~760 K). The differences of reactivity and burning in vacuum and air can be further explained from the following

approach. The mean free path of gas released from the oxidizers in vacuum is orders of magnitude higher than in air, and so some oxygen released from the $I_2O_5$ particles may simply escape from the thermite mixture before it can react with the aluminum nanoparticles.

Constant volume combustion cell tests were performed to evaluate the relative performance of nano-Al/micro-$I_2O_5$ thermites against other thermites under atmospheric conditions. It should be noted that all thermite formulations in this investigation use the same nano-Al fuel. To compare the effects of particle size we plot simultaneous pressure and optical traces for both nano-Al/as received $I_2O_5$ and nano-Al/micro-$I_2O_5$ in Figure 7.7a-b. Quite clearly the micro-$I_2O_5$ thermite outperforms the as received $I_2O_5$ thermite in terms of a higher pressure peak, shorter pressure rise, and burning time.

Direct comparison of the combustion cell tests of nano-Al/micro-$I_2O_5$ and nano-Al/micro-CuO are shown in Figure 7.7c-d. The plots show that $I_2O_5$ has a higher overpressure by a factor of ~ 4 relative to CuO and a shorter burning time. The same trend is also reported elsewhere that Al/$I_2O_5$ displays a much higher peak pressure than Al/CuO combustion in which both fuel and oxidizers are at the nanoscale. [6]

The experimental results of pressure and optical emission data are further tabulated for Al/$I_2O_5$ thermites along with other metal oxides thermite mixtures in Table 7.1. Clearly, the micro-$I_2O_5$ thermite exhibits the highest overpressure and pressurization rate, and shortest burning time among all other nano-Al/micro-oxidizer thermite samples, and even a nano-Al/nano-$Fe_2O_3$ thermite.

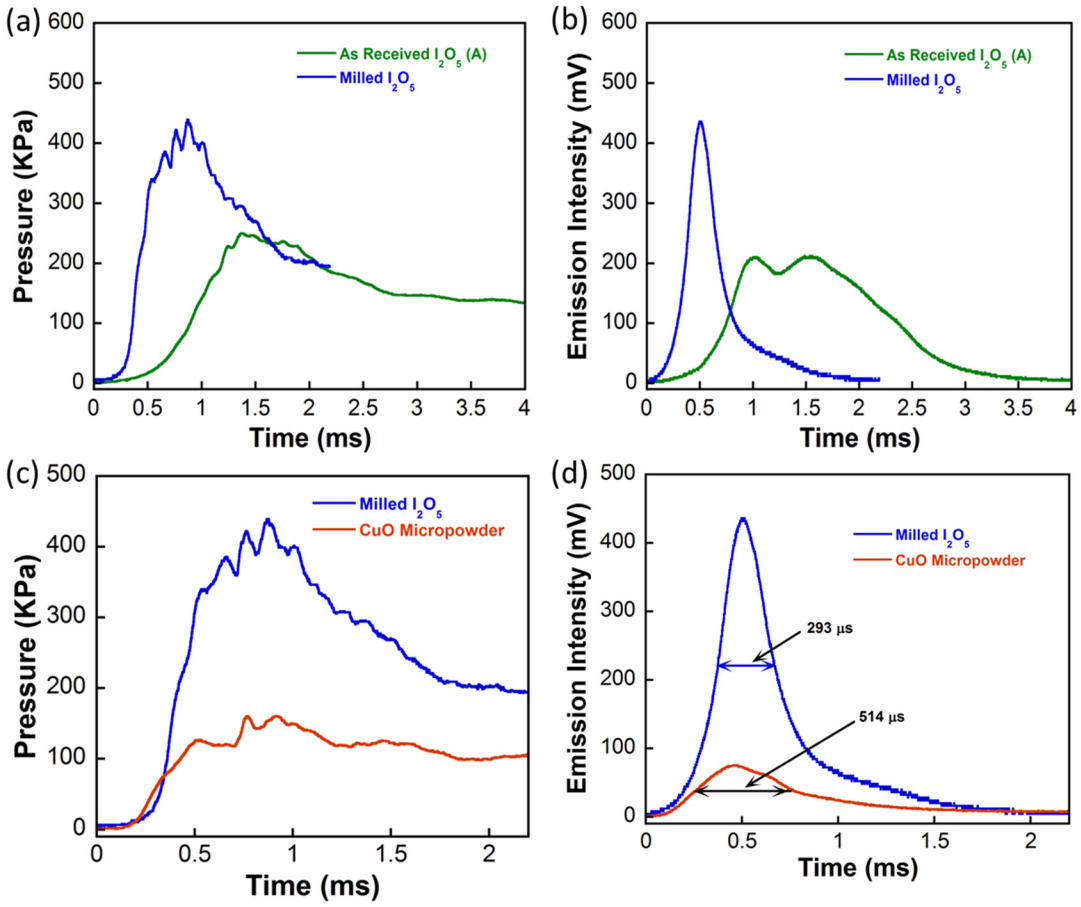


**Figure 7.7.** (a) pressure and (b) optical traces for nano-Al+as received $I_2O_5$ and nano-Al+milled $I_2O_5$ thermites reactions; (c) pressure traces and (d) optical emission traces for nano-Al+milled $I_2O_5$ and nano-Al+micro-CuO thermites reactions. All of the results measured during combustion in a constant-volume combustion cell.

In a previous study of nanothermites, we found that for the Al/CuO nanothermite, the pressure peaks earlier than does the optical emission. i.e., a rapid pressure signal followed by a prolonged optical signal. [17] This result can also be seen in Table 7.1 for nano-CuO, which shows a very short pressure rise time (13 μs) and a relatively long burn time (192 μs). We have argued that the pressurization occurs as a result of the oxygen release from CuO nanoparticles, which can occur well before significant

combustion as associated with the optical emission. This was contrasted in the same study with Al/$Fe_2O_3$ for which the pressure and optical signals occur concurrently for which we concluded that the oxidizer decomposition was the rate-limiting step in Al/$Fe_2O_3$. However, for all nano-Al/micro-oxidizer thermite formulations tabulated in Table 7.1**,** we can see the pressure and optical signals occur almost concurrently, or even earlier. This is very different than that observed in Al/CuO nanothermite system, indicating that the reaction mechanism in the nano-Al/micro-oxidizer system is quite different. Given the only difference between the Al/CuO nanothermite and nano-Al/micro-CuO system is the particle size of the CuO oxidizer, it is reasonable to conclude that the oxidizer decomposition has become the rate-limiting step in nano-Al/micro-CuO thermite reaction. By extension, this argument implies that oxidizer decomposition is limiting in the nano-Al/micro-$I_2O_5$ thermite reaction for which pressure and optical signals occur concurrently.

**Table 7.1.** Combustion cell test data for thermites samples prepared with different oxidizers. All oxidizers were mixed with nano-Al (ALEX). Thermites samples were prepared stoichiometrically assuming complete conversion to $Al_2O_3$.

| Oxidizers (w/Al, φ=1) | $P_{rise}$ (KPa) | Pressure rise time (μs) | Pressurization Rate (KPa/μs) | FWHM burn time (μs) | Note(All materials are from Sigma-Aldrich) |
|---|---|---|---|---|---|
| $I_2O_5$ (A) | 237 | 944 | 0.251 | 1579 | As received, 99.99 % |
| $I_2O_5$ (M) | 366 | 397 | 0.922 | 293 | After 1 hour milling |
| Micro-CuO | 152 | 732 | 0.208 | 514 | <5 μm, 98% |
| Micro-$Fe_2O_3$ | 51.7 | 8350 | 0.00619 | 4394 | <5 μm, ≥99% |
| Nano-CuO | 800 | 13 | 61.5 | 192 | <50 nm |
| Nano-$Fe_2O_3$ | 92.4 | 800 | 0.116 | 936 | <50 nm |

Thermodynamic equilibrium data for Al, $Fe_2O_3$, CuO, and $I_2O_5$ based thermites taken from Fischer and Grubelich's theoretical calculations [23] are shown in Table 7.2. From the data, both the Cu and I based systems should be significant gas producers relative to Fe. This is in fact consistent with the pressurization data presented in Table 7.1. The experiments, however, show that $I_2O_5$ generates a pressure rise more than four times that of nano-Al/micro-CuO system, indicating the faster reaction kinetics. The higher maximum pressure can be explained by the fact that the evaporation of low boiling point iodine (457 K) could increase the pressure inside the reactor while the boiling point of metal products formed during Al/CuO thermite reactions is much higher than iodine. [6]

**Table 7.2.** Constant enthalpy and pressure thermodynamic equilibrium calculations of stoichiometric thermite systems. Data is taken from Fisher and Grubelich (1998) without taking account of the oxide shell on Al.

| Thermite reaction | Adiabatic Temp. (K) | Gas production (mmol/g) | Major gas species | State of metal |
|---|---|---|---|---|
| $2Al+Fe_2O_3 \rightarrow Al_2O_3+2Fe$ | 3135 | 1.4 | Fe | liquid-gas |
| $2Al+3CuO \rightarrow Al_2O_3+3Cu$ | 2843 | 5.4 | Cu | liquid-gas |
| $10Al+3I_2O_5 \rightarrow 5Al_2O_3+3I_2$ | >3253 | 6.3 | $I_2$ | gas |

For all thermite reactions limited by the decomposition of oxidizers, the pressure rise is largely dependent on the final state of the products other than the gas produced during the decomposition of oxidizers. Next, it will be very straightforward for us to understand why the nano-Al/micro-CuO and nano-Al/micro-$I_2O_5$ can even outperform the nano-Al/nano-$Fe_2O_3$ thermite reactions in terms of relative combustion performance shown in Table 7.1.

In addition, from the point of view of Al/$I_2O_5$ thermite's potential application as the biocide, it has been expected that the pressure rise is from the produced hot biocidal species by the very exothermic thermite reaction other than species from the decomposition of oxidizer. Hence, the nano-Al/micro-$I_2O_5$ thermites formulations with concurrent pressure and optical rise signal should be a very good candidate for effective biocides. Since nano-Al/micro-CuO and nano-Al/micro-$I_2O_5$ behave similarly in the combustion cell tests, we would expect similar combustion behavior for nanosized oxidizers. That is to say, the higher pressure rise occurs much earlier than optical emission signal. Of course, we cannot rule out the possibility that two

oxidizers at nanoscale might behave very differently, and more experimental studies are needed to verify this.

*7.3.3. Post-Combustion Characterization of Al/$I_2O_5$ Thermites.*

Not only the combustion performance of thermites, but also the nature and dispersion of the products, matter in biocidal applications. Numerous toxicological studies have shown that small nanoparticles have higher cell cytotoxicity. [24, 25] A good biocide system should be a reaction producing biocidal products which have a high surface area and can be exposed to the environment.

The post combustion products of Al/$I_2O_5$ thermites reaction were collected and added up with the ethanol. The resulted solution displayed a brown color indicating the iodine formed after reaction. The sample was also dry ground by rubbing between two very clean glass slides and prepared for TEM analysis. A representative transmission electron microscopy (TEM) image along with the elemental map of Al, O and I is shown in Figure 7.8 for products from the combustion cell test of Al/$I_2O_5$ thermite. From the elemental mapping, we see particles that contain Al and O, and other particles only contain I. Selected particles with an elemental linescan coupled also confirmed the products are aluminum oxide and iodine, as shown in Figure 7.9. The produced iodine species exist as small nanoparticles (with dark contrast) confirmed by EDS in Figure 7.8-9. The results also excluded the possibility of the $AlI_3$ formation in the final products. In conclusion, Al/$I_2O_5$ thermite reaction is an effective way to produce iodine gas via condensed phase reaction. Furthermore, upon cooling, the iodine condenses to form the high surface area nanoparticles with surface exposure to the environment, thus maximizing its killing potential as a biocidal agent.

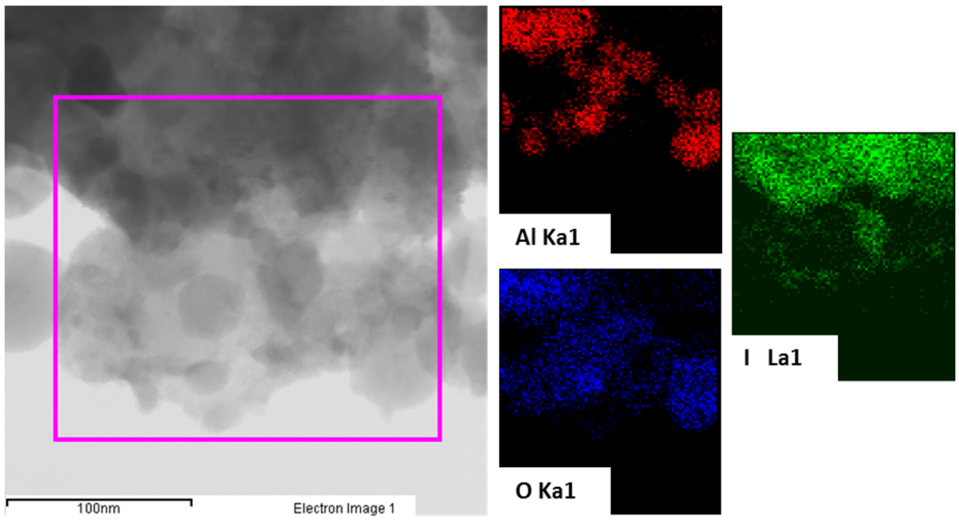


**Figure 7.8.** Representative TEM image and 2D elemental mappings (Al, O, and I, using EDS) of post-combustion products after $Al+I_2O_5$ thermite reaction in the combustion cell. The thermite was nano-Al (ALEX) and milled $I_2O_5$ particles (microsized) with an equivalence ratio of 1.0. Note: Iodine element has a dark contrast in TEM image because of its high atomic number.

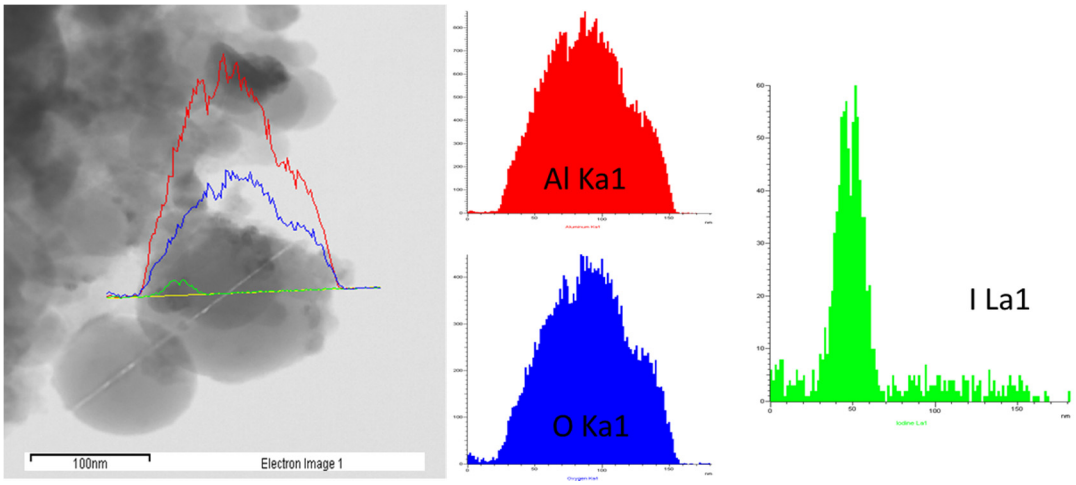


**Figure 7.9.** TEM image and 1D elemental linescan (using EDS) across particles formed after $Al+I_2O_5$ reaction in the pressure cell. Note: Iodine nanoparticles formed and no $AlI_3$ found.

## *7.4. Conclusions*

The ignition and combustion behavior of nano-Al/micro-$I_2O_5$ thermite was systematically studied. Mechanical milling was successfully applied to prepare microsized $I_2O_5$, and the milled $I_2O_5$ thermite system was found to have a higher reactivity compared before mechanical milling. Time resolved mass spectra show that $I_2O_5$ oxidizer starts to decompose at 760 K to produce a lot of oxygen and iodine species, mainly $I^+$ and $I_2^+$. The ignition temperature of nano-Al/micro-$I_2O_5$ thermite reaction in air at atmospheric pressure was determined to be ~810 K. Combustion cell tests show that the nano-Al/micro-$I_2O_5$ system outperforms the nano-Al/micro-CuO system in both pressurization rate and burning time. Concurrent pressure and optical rising was observed for all nano-Al/micro-oxidizer systems in this study. This suggests that the burning of nano-Al/micro-oxidizer systems in this study is possibly limited by the decomposition of oxidizers. Different than the nano-Al/nano-CuO system, the pressure rise in nano-Al/micro-$I_2O_5$, in this study, is from the produced hot biocidal species by very exothermic thermite reactions other than species from the decomposition of oxidizers. TEM coupled with EDS analysis was performed to analyze the post combustion products, and the results indicated that the produced iodine species condensing as small nanoparticles. Considering its potential application as biocides, nano-Al/micro-$I_2O_5$ thermite reactions are an effective way to produce iodine gas via a condensed phase reaction. Furthermore, upon cooling the iodine condensed to form the high surface area nanoparticles with surface exposure to the environment thus could maximize its killing potential as a biocidal agent.

## *7.5. References*


[1] Sullivan, K. T.; Piekiel, N. W.; Chowdhury, S.; Wu, C.; Zachariah, M. R.; Johnson, C. E. *Combust. Sci. Tech.* **2011**, *183*, 285-302.

[2] Johnson, C.E.; Higa, K.T.; Albro, W.R. *Proceedings of the International Pyrotechnics Seminar.* **2008**.

[3] Clark, B.R.; Pantoya, M.L. *Phys. Chem. Chem. Phys.* **2010**, *12*, 12653-12657.

[4] Farley, C.; Pantoya, M. *J. Therm. Anal. Calorim.* **2010**, *102*, 609-613.

[5] Zhang, S.S.; Schoenitz, M.; Dreizin, E.L. *J. Phys. Chem. C* **2010**, *114*, 19653-19659.

[6] Martirosyan, K.S. *J. Mater. Chem.* **2011**, *21*, 9400-9405.

[7] Yetter, R.A.; Risha, G. A.; Son, S. F. *Proc. Combust. Inst*. **2009**, *32*, 1819-1838.

[8] Wen, D.S. *Energy Environ*. *Sci*. **2010**, *3*, 591-600.

[9] Sanders, V. E.; Asay, B. W.; Foley, T. J.; Tappan, B. C.; Pacheco, A. N.; Son, S. F. *J. Propul. Power* **2007**, *23*, 707-714.

[10] Dreizin, E. L. *Prog. Energy Combust. Sci.* **2009**, *35*, 141-167.

[11] Jian, G.Q.; Chowdhury, S.; Sullivan, K.; Zachariah, M.R. *Combust*. *Flame* **2013**, *160*, 432-437.

[12] Jian, G.Q.; Liu, L.; Zachariah, M.R. *Adv. Funct. Mater.* **2013**, *23*, 1341-1346.

[13] Prakash, A.; McCormick, A. V.; Zachariah, M. R. *Adv*. *Mater*. **2005**, *17*, 900-903.

[14] Wu, C.W.; Sullivan, K.; Chowdhury, S.; Jian, G.Q.; Zhou, L.; Zachariah, M. R. *Adv*. *Funct*. *Mater*. **2012**, *22*, 78-85.

[15] Wu, Z.Q.; Kalia, R. K.; Nakano, A.; Vashishta, P. *J. Chem. Phys.* **2011**, *134*, 204501-1-14..

[16] Martirosyan, K.S.; Wang, L.; Luss, D. *Chem*. *Phys*. *Lett*. **2009**, *483*, 107-110.

[17] Zhou, L.; Piekiel, N.; Chowdhury, S.; Zachariah, M. R. *Rapid Commun*. *Mass Spectrom*. **2009**, *23*, 194-202.

[18] Zhou, L.; Piekiel, N.; Chowdhury, S.; Lee, D.; Zachariah, M. R. *J. Appl. Phys.* **2009**, *106*, 083306-1-8.

[19] Sullivan, K.T.; Zachariah, M.R. *J. Propul. Power* **2009**, *26*, 467-472.

[20] Son, S.F.; Busse, J.R.; Asay, B.W.; Peterson, P.D.; Mang, J.T.; Bockmon, B.; Pantoya, M.L. *Proceedings of the International Pyrotechnics Seminar* **2002**, *29*, 203-210.

[21] Studier, M. H.; Huston, J. L. *J. Phys. Chem.* **1967**, *71*, 457-459.

[22] Fischer, A. *Acta Cryst.* **2005**, *E61*, i278-i279.

[23] Fischer, S.H.; Grubelich, M.C. *the 24th International Pyrotechnics Seminar*, Monterey, CA, July **1998**.

[24] Morones, J.R.; Elechiguerra, J.L.; Camacho, A.; Holt, K.; Kouri, J. B.; Ramírez, J. T.; Yacaman, M. J. *Nanotech*. **2005**, *16*, 2346-2353.

[25] Klaine, S.J.; Alvarez, P.J.J.; Batley, G. E.; Fernandes, T.F.; Handay, R. D.; Lyon, Y.; Mahendra, S.; Mclaughlin, M.J.; Lead, J.R. *Environ. Toxicol. Chem.* **2008**, *27*, 1825-1851.

# Chapter 8: Electrospun Energetic Composite Nanofibers*

## *Highlights*

(a) Energetic composite nanofibers (NC/Al, NC/Al-CuO, NC/Al-$Fe_2O_3$, and NC/Al-$Bi_2O_3$) were successfully fabricated using the electrospinning method.

(b) Energetic composite nanofibrous mats showed the enhanced burning rates, compared to the pure nitrocellulose (NC) and nanoaluminum incorporated nanofibrous mats.

## *Overview*

Metal fuels, such as aluminum and magnesium, are principle ingredients in solid composite propellants. Powdered metal fuels are intimately mixed with an oxidizer, and immobilized with polymer binder. In recent years, metallized nanoparticles have been suggested to be potential replacements for conventional metal powders in propellant systems because of their faster oxidation kinetics that could potentially lead to a significantly enhanced burning rate of the propellants and specific impulse. In this chapter, we fabricated energetic composite nanofibrous mats by a one-step electrospinning method. The as prepared energetic composite nanofibers contain both nanoaluminum fuel and oxidizer nanoparticles incorporated in nitrocellulose (NC)

* The results presented in this chapter have been published in the following journal article and conference paper: Yan, S.; Jian, G.Q.; (Co-first author) Zachariah, M.R. *Electrospun Nanofiber-Based Thermite Textiles and their Reactive Properties*, *ACS Appl. Mater. Interfaces* **2012**, *4*, 6432-6435; Jian, G.Q.; Yan, S; Wang, H.Y.; Zachariah, M.R., In *Burning Behavior of Energetic Composite Nanofibers*, Proceedings of 8th US National Combustion Meeting, Park City, Utah, USA, 19-22 May, **2013**. Note: Shi Yan performed most of NC/Al, NC/Al/CuO nanofiber fabrication experiments. Guoqiang Jian performed the experiments of NC/Al/$Fe_2O_3$ and NC/Al/$Bi_2O_3$ nanofibers fabrication and analyzed the data.

binder. By tuning the mass loading and equivalence ratio of nanoaluminum and metal oxide nanoparticles in the precursors, energetic composite nanofibrous mats with different equivalence ratios and mass loadings were successfully fabricated. The energetic composite nanofibrous mats (NC/Al-CuO, NC/Al-$Fe_2O_3$, NC/Al-$Bi_2O_3$) were characterized and tested for their burning behavior and compared with the pure nitrocellulose and nanoaluminum incorporated nanofibers. Energetic composite nanofibrous mats showed enhanced burning rates, which correlate to the mass loading of relative to binder in nanofibers. The energetic composite nanofibers produced by the electrospinning method demonstrate the possibility of avoiding some of the problems associated with melt casting of nanometalized propellants.

## *8.1. Introduction*

Metal fuels, such as aluminum and magnesium, are principle ingredients in modern solid rocket propellants because of their high energy intensity, high combustion temperature, and abundance. [1, 2] Typically, powdered metal fuels are intimately mixed with oxidizer, and immobilized with polymer binder in the propellant system. Although additive micron-sized aluminum fuel can greatly improve the energy release of the propellant, the burning rate have not been found to increase much, resulting in low rates of energy release. [3, 4] Nanoaluminum has been suggested to be a potential replacement for conventional aluminum powders in propellant systems for its faster oxidization kinetics which can lead to, potentially, a significant enhanced burning rate of the propellant and specific impulse.[5-7] However, nanoaluminum suffers from processing challenges, including the increased viscosity of castable

propellant mixes at high volume loading of nanoaluminum, and prevention of aggregation, which hamper its application in the solid propellant systems. [8, 9]

Electrospinning, one of the simplest top down fabrication methods, has been successfully employed to prepare several different polymer based nanofibers [10-14]. Recently, it has been used to create nitrocellulose/nanoaluminum nanofibers for potential propellant applications. [15] Ideally, one would like to integrate both the fuel and oxidizer in an intimate mixture with high volumetric loading and energy density, suggesting a new class of energetic composite nanofibers. [16-19]

The primary motivation of this study is to produce a series of energetic composite nanofibers with different fuel and oxidizer combinations and study their burning behaviors. By tuning the equivalence ratio and mass loading of nanoaluminum and metal oxide nanoparticles in the precursors, energetic composite nanofibrous mats (NC/Al-CuO, NC/Al-$Fe_2O_3$, and NC/Al-$Bi_2O_3$) with different equivalence ratio and mass loading were produced by the electrospinning method and tested for their burning behavior, which were further compared with the pure nitrocellulose and nanoaluminum incorporated nanofibers.

## *8.2. Experimental Section*

### *8.2.1. Materials.*

Aluminum nanoparticles (Al, ALEX, <50nm, Argonide Corp.), copper oxide nanopowder (CuO, <50 nm, Sigma-Aldrich), iron oxide nanopowder ($Fe_2O_3$, <50 nm, Sigma-Aldrich), bismuth oxide ($Bi_2O_3$, 90-210 nm, Sigma-Aldrich), collodion solution (Mallinckrodt Chemical Inc, USP; Fluka-Sigma-Aldrich), diethyl ether (99.8%), and ethanol (99.98%) were all used as received without any further

treatment. The active aluminum in aluminum nanoparticles was measured by thermogravimetric analysis (TGA) to be 70% by weight. The nitrocellulose content of the collodion solution was determined by measuring the solid residue left after evaporating solvent before further experiments.

*8.2.2. Electrospinning Process.*

In a typical experiment with 50 wt % particles in the nanofibers, a suspension was first prepared by dispersing 100 mg nanoaluminum and 100 mg metal oxide nanoparticles in collodion solution (1.3 ml, ~12% nitrocellulose) with additional diethyl ether (0.9 ml) and ethanol (0.9 ml). Nitrocellulose content was kept at ~200 mg for all samples in this study. The suspension was stirred vigorously for 5 min and then ultrasonically mixed for 30 min to allow the initially dispersion of nanoparticles in the solution. The suspension was then magnetically stirred at room temperature for 24 h. The viscous suspension was loaded into a plastic syringe connected with a stainless steel needle (inner dia. 0.8 mm), and electrospun by using a homemade electrospinning setup, as schematically shown in Figure 8.1. The working voltage was set at 18-19 kV, and the distance between needle tip-sample collector substrate was kept at 6 cm. The suspension solution was fed by a syringe pump at a rate of 4.5 ml/h. A rotating collector covered with aluminum foil was used to collect nonwoven energetic composite fibrous mats. The working voltage was chosen below 20 kV to reduce the possibility of spark ignition during the electrospinning process. The operating procedures were the same for all samples in this study. The electrospinning setup was kept and operated in the fume hood, and shielded using insulators to reduce the possible dangers posed by spark ignition.

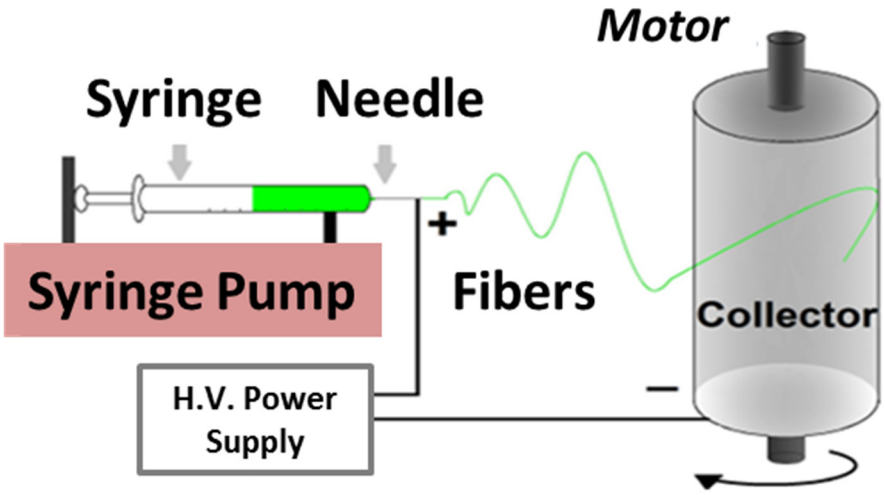


**Figure 8.1.** Schematic illustration of experimental setup for electrospinning.

*8.2.3. Samples Characterization and Burning Rate Measurement.*

The collected samples were characterized by scanning electron microscopy (SEM, Hitachi SU-70 FEG-SEM) and transmission electron microscopy (TEM, JEOL JEM 2100). The SEM is equipped with an energy dispersive X-ray detector (Bruker) for elemental analysis, which can be operated in scanning mode to perform 2D elemental mapping of the sample.

The burning rate experiments of nanofibrous mats (3cm length, 1cm width) were carried out in open air by using a high speed camera (Phantom v12.0) with a frame rate of 10000 frames per second. The mats were ignited by a windproof igniter and recorded using the high speed camera.

## *8.3. Results and Discussion*

*8.3.1. Fabrication and Characterization of Energetic Composite Fibrous Mats.*

Nitrocellulose is chosen as the polymer matrix since it has been previously used as a propellant. The preparation of energetic composite fibrous mats by this

electrospinning method is presented for three systems: NC/Al-CuO, NC/Al-$Fe_2O_3$, and NC/Al-$Bi_2O_3$. We added the same mass of nanoaluminum and metal oxide NPs to form fuel rich thermite formulations, accounting for the presence of nitrocellulose (NC). Pure nitrocellulose and nanoaluminum incorporated nitrocellulose fibrous mats were also prepared using the same approach shown in Figure 8.1. Photographs of nonwoven, pure NC, nanoaluminum incorporated NC, and energetic composite (NC/Al-CuO, NC/Al-$Fe_2O_3$, and NC/Al-$Bi_2O_3$) fibrous mats are shown in Figure 8.2a. As seen from Figure 8.2a, macroscopic non-woven mats on the centimeter scale can be obtained, and the color changes from white (pure NC) to gray (NC/Al), black (NC/Al-CuO), black brown (NC/Al-$Fe_2O_3$) and dark green (NC/Al-$Bi_2O_3$) after incorporating nanoparticles. By tuning the mass loading of nanoaluminum and metal oxide nanoparticles in the precursors, energetic composite fibrous mats with different mass loading were also successfully fabricated. For NC/Al-$Bi_2O_3$, we also produced the energetic composite fibrous mats with different mass equivalent ratios. One example is shown in Figure 8.2b for NC/Al-$Bi_2O_3$, from which we can clearly see that the color of the fibrous mats produced changes by increasing the mass ratio of nano-Al/$Bi_2O_3$ from 1:7 to 1:3 and 1:1 in the precursor solution. With appropriate choice of experimental parameters, the fibrous mats could be produced with nanoparticle loadings up to ~1:1 by weight ratio of nanoparticles to nitrocellulose, and for NC/Al-$Bi_2O_3$ which can be even as high as 3:2.

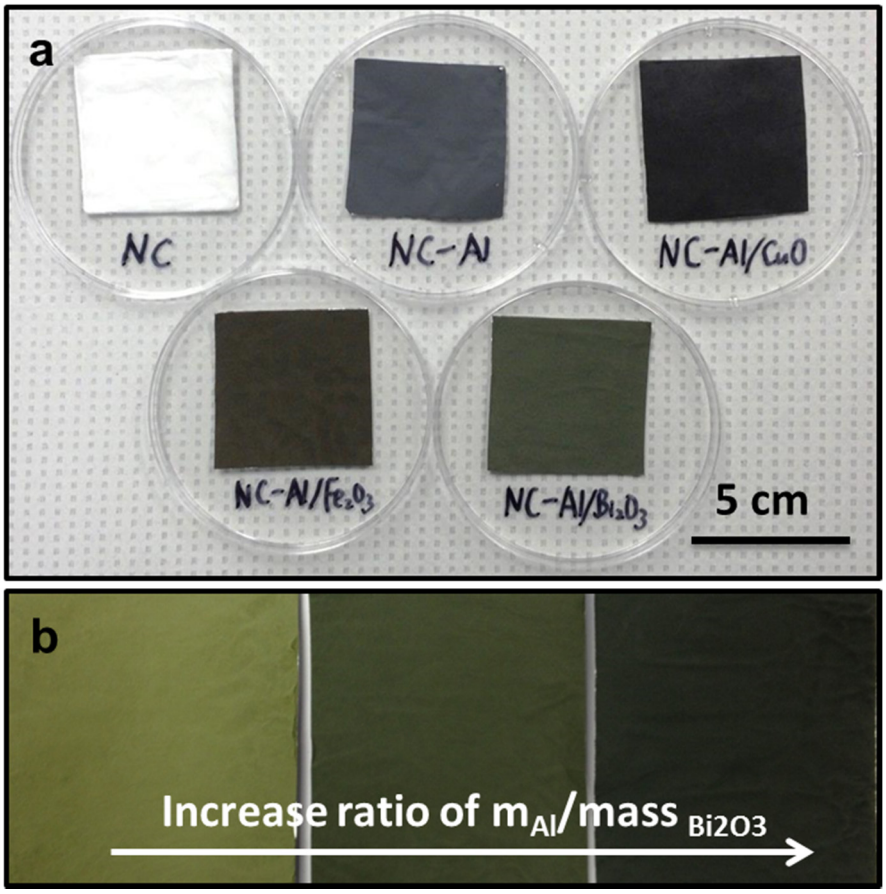


**Figure 8.2.** Photographs of (a) the as prepared fibrous mats (50 wt % particles loadings) and (b) NC/Al-$Bi_2O_3$ fibrous mats with different $m_{Al}/m_{Bi2O3}$ ratio (1:7, 1:3, and 1:1, $m_{Al}+m_{Bi2O3}$=200 mg). Note: The size of all the fibrous mats on the collector is about 10 cm×12.5 cm.

SEM images of the pure NC, NC/Al, and NC/Al-CuO nanofibers are shown in Figure 8.3a-c. As seen from the Figure 8.3a, a uniform and well defined interconnected nitrocellulose fibrous network has been obtained. Considering the fact that the diameter of all fibers could be adjusted by the polymer concentration in the precursor solution, we kept the polymer solution concentration the same for all experiments to reduce the possibility of diameter changing caused by different polymer precursor concentrations.

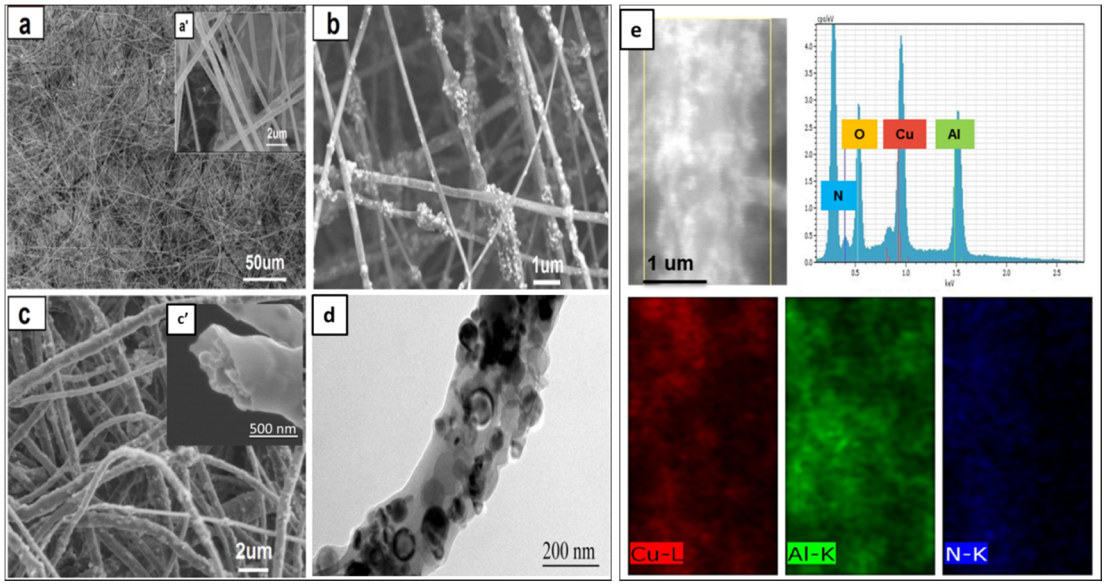


**Figure 8.3.** SEM images of (a) pure NC, (b) NC/Al (50 wt %) and (c) NC/Al-CuO (50 wt %) nanofibers, TEM image (d) and elemental mapping (e) of NC/Al-CuO (50 wt %) nanofibers. Samples in a-c and e are coated with graphite before SEM characterization to prevent melting of NC caused by electron beam irradiation.

Compared to NC fibers with smooth surfaces and diameters of ~300-400 nm, NC/Al and NC/Al-CuO nanofibers are not as uniform and display a relatively wide range of diameters from ~300-1000 nm, which we attribute to the fact that the polymer precursor solution is not as homogeneous as pure nitrocellulose after mixing with nanoparticles. Not surprisingly, the NC/Al and NC/Al-CuO nanofibers in Figure 8.3b-c have a rough, irregular surface morphology, probably due to agglomeration of particles and the increased viscosity of the precursor polymer solution. However, for the same mass loading, NC/Al-CuO nanofibers display a less aggregated surface, while NC/Al nanofibers show substantially more aggregation than NC/Al-CuO. The differences may be due to the higher density of CuO when compared to that of Al and thus occupy less volume than Al. Furthermore, aggregation in solution is greatly

influenced by surface charge states which can significantly alter particle stability during the solvent evaporation stage of electrospinning. For example, Zhang et al. found that the $Fe_3O_4$ nanoparticles with increased surface charge result in the formation of the fibers with smoother surfaces presumably due to increased electrostatic repulsion.[20] Cross sectional SEM (Figure 8.3c') and TEM images (Figure 8.3d) of NC/Al-CuO nanofibers further show that nanoparticles are incorporated inside the fibers and are well dispersed. Elemental mapping of the NC/Al-CuO in Figure 8.3e confirms a homogeneous distribution of the nanoparticles within the nitrocellulose fibers.

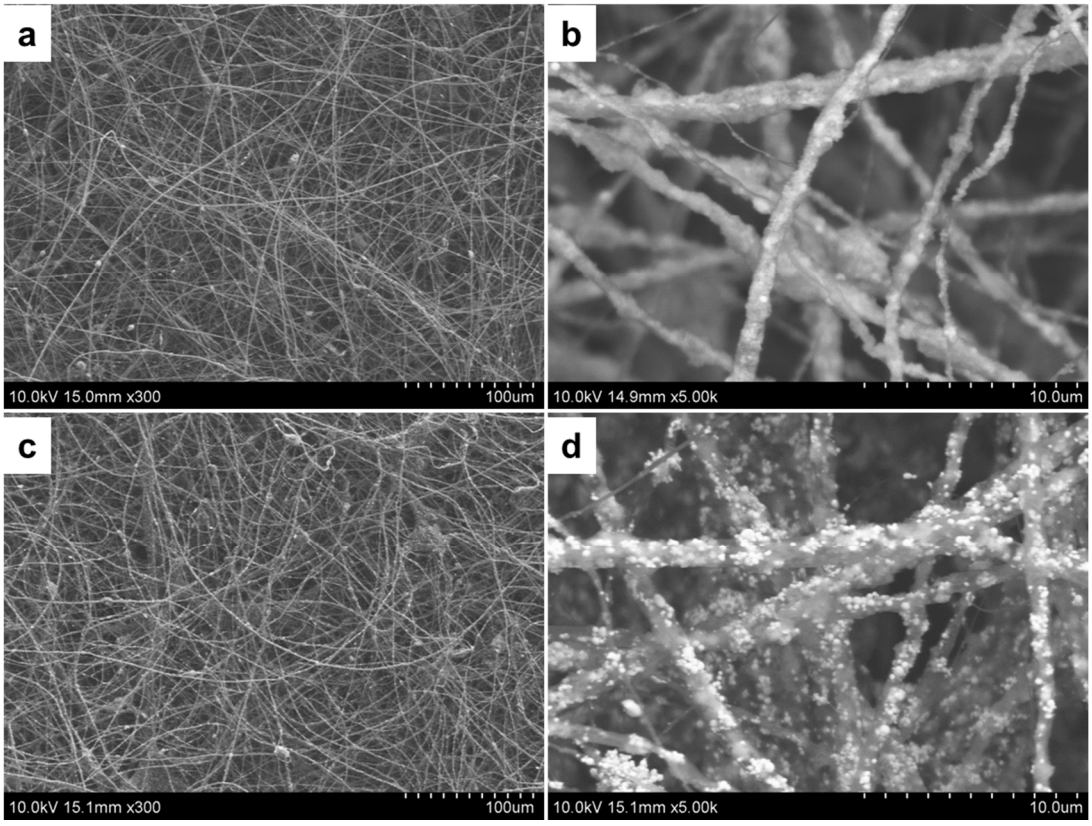


**Figure 8.4.** SEM images of (a-b) NC/Al-$Fe_2O_3$ (50 wt %) and (c-d) NC/Al-$Bi_2O_3$ (60 wt %) nanofibers. Note: $m_{Al}/m_{Fe2O3}$=1:1 in a-b, and $m_{Al}/m_{Bi2O3}$=1:3 in c-d.

Similar to NC/Al-CuO nanofibers, NC/Al-$Fe_2O_3$ and NC/Al-$Bi_2O_3$ nanofibers in Figure 8.4 show a relatively wide range of diameters from ~300-1000 nm and a rough surface morphology. It has been noted from Figure 8.4d that larger particles could be seen incorporated in the nanofibers since $Bi_2O_3$ nanoparticles used in this study are much larger (~90-210 nm) than Al, CuO and $Fe_2O_3$ nanoparticles (<50 nm). In this study, we aim to maximize the mass loading of nanoparticles, and we found that for the solvent mix used in this study, loadings beyond 50 % became increasing difficult to electrospin for NC/Al-CuO and NC/Al-$Fe_2O_3$, and that at ~65 % the instability in the Taylor cone resulted in severe particle agglomeration, as shown in Figure 8.5 for NC/Al-CuO.

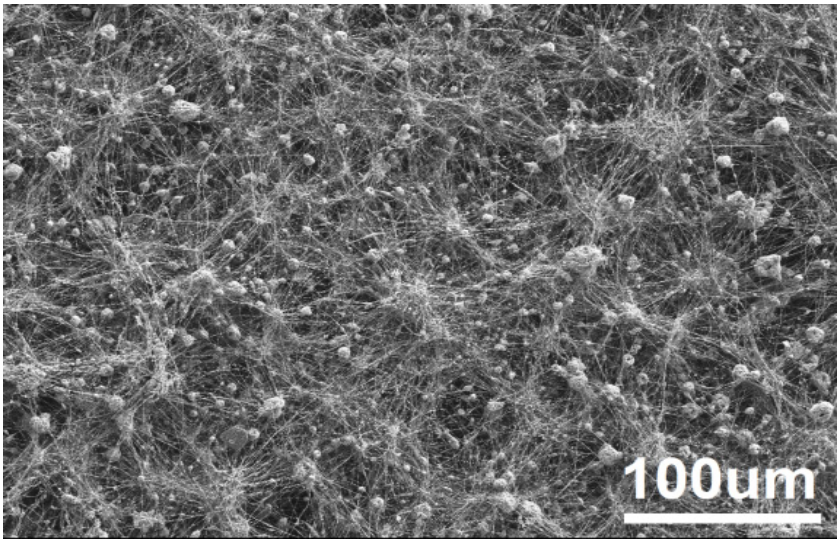


**Figure 8.5.** SEM image of NC/Al-CuO nanofibers with 65 wt % Al-CuO.

However, energetic composite nanofibers with 60 % mass loading of nanoparticles could be easily achieved for NC/Al-$Bi_2O_3$, which might be because $Bi_2O_3$ has a much higher density (8.9 g/cm$^3$) than CuO (6.32 g/cm$^3$) and $Fe_2O_3$(5.24 g/cm$^3$), and thus occupies less space and can be easily incorporated into the nanofibers. The SEM

image and energy-dispersive X-ray spectroscopy (Figure 8.6a, 8.6c) of the NC/Al-$Bi_2O_3$ (60 wt %) show the existence of Al and Bi in the nitrocellulose nanofibers, and elemental mapping of the nanofibers in Figure 8.6d-f confirms a relatively homogenous distribution of the nanoparticles within the nitrocellulose fibers.

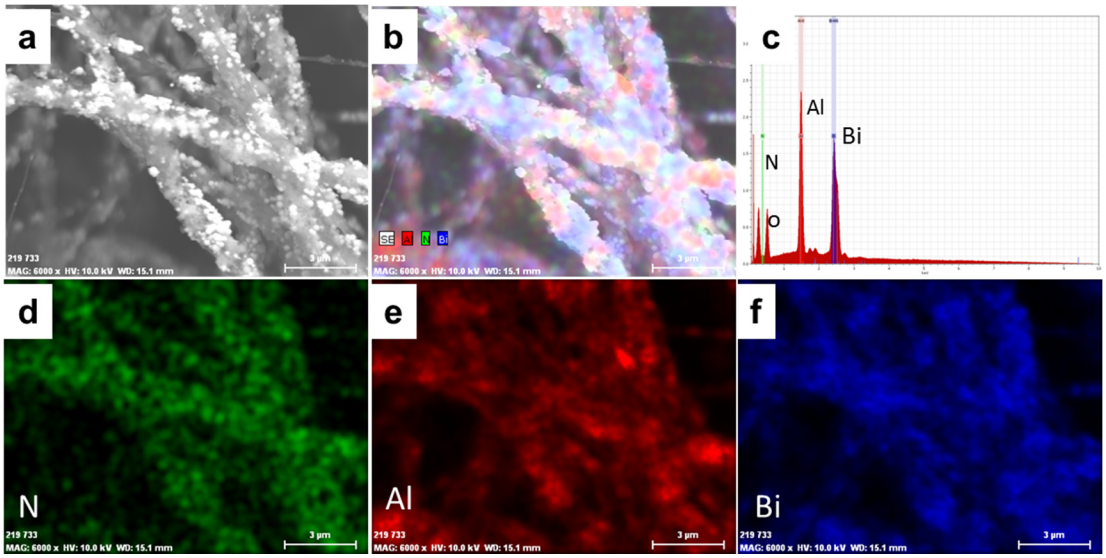


**Figure 8.6.** SEM image (a), energy-dispersive X-ray spectroscopy analysis and elemental mapping (b-f) of NC/Al-$Bi_2O_3$ (60 wt %) nanofibers. Note: Scale bar is 1 μm in a, b and d-f.

*8.3.2. Burning Behavior of Energetic Composite Fibrous Mats.*

The burning behavior of energetic composite nanofibrous mats was characterized using high speed imaging. The representative sequential snapshots of fibrous mats burning in the air are shown in Figure 8.7. Clearly, NC/Al-CuO and NC/Al-$Bi_2O_3$ nanofibrous mats show much more luminous burning when compared with that of NC and NC/Al, and have faster combustion propagation fronts. The burning of NC/Al-$Fe_2O_3$ fibers is similar to NC/Al-CuO and NC/Al-$Bi_2O_3$ nanofibers, with a more luminous burning and faster combustion propagation front. As seen from Figure 8.7,

adding nanoaluminum decreases the combustion propagation velocity of NC nanofibers, presumably due to mass transfer limits in the oxidizer, while incorporating nanothermite significantly increases the combustion propagation velocity.

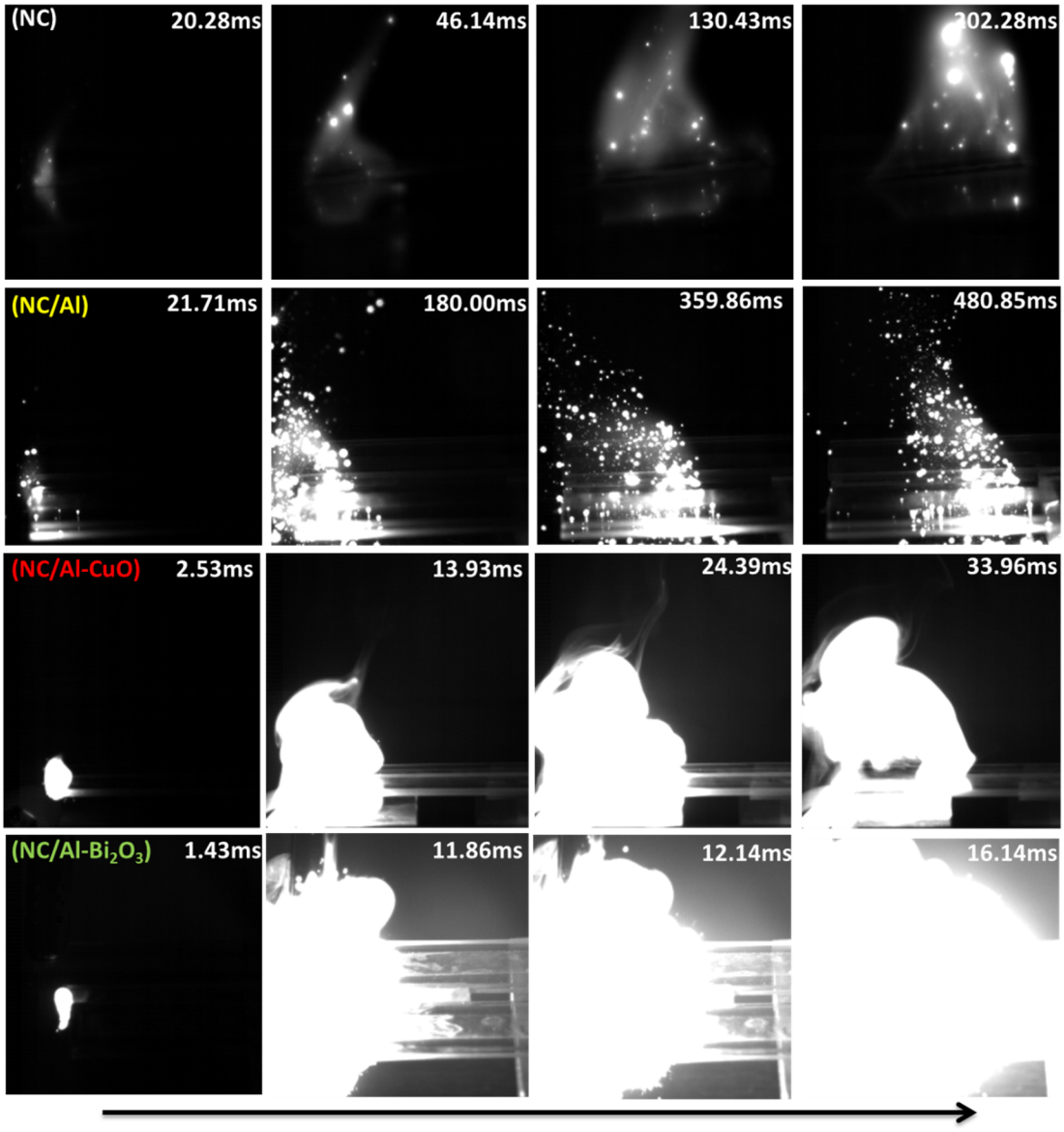


**Figure 8.7.** Sequential snapshots of pure NC, Al/NC with 50 wt % of Al, NC/Al-CuO with 50 wt % of Al-CuO and NC/Al-$Bi_2O_3$ with 60 wt % of Al-$Bi_2O_3$, as captured by high speed video camera.

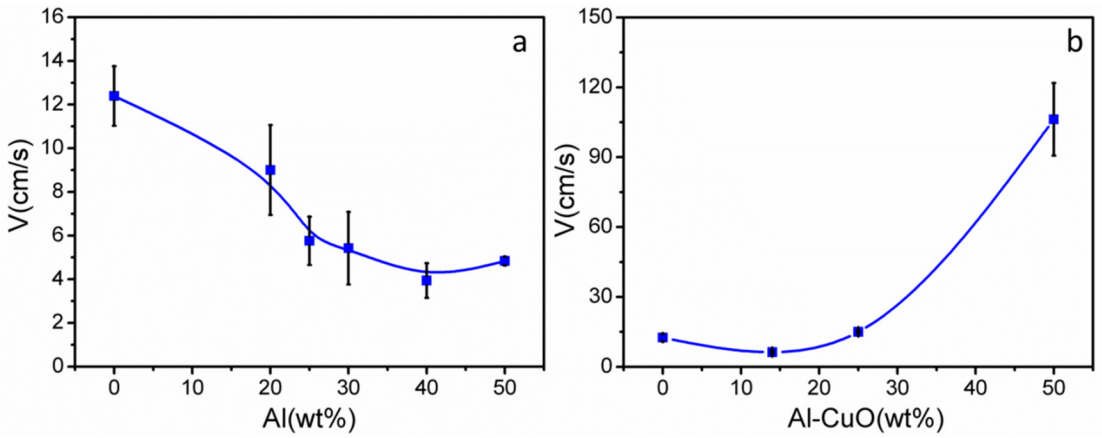


**Figure 8.8.** Combustion propagation velocities of (a) NC/Al and (b) NC/Al-CuO nanofibrous mats as a function of nanoparticles mass loading. Note: Error bars for first three points are too small to be seen in 8b.

To study the effects of mass loading of nanoparticles in the nanofibers on the combustion propagation velocities, the combustion propagation velocities of different NC/Al and NC/Al-CuO fibrous mats have been plotted and shown in Figure 8.8. From Figure 8.8a, pure NC nanofibers (0 wt % point in the plot) show an average velocity of ~12.4 cm/s. By increasing mass loading of nanoaluminum in the NC nanofibers, the combustion propagation velocity of NC/Al nanofibers decreases. This suggests that even though a higher energy density can be achieved with the loading of nanoaluminum in the nitrocellulose nanofibers, this approach results in a lower combustion propagation velocity of the nanofibers. In contrast, the combustion propagation velocities of NC/Al-CuO nanofibers (Figure 8.8b) do not show much change as the mass loading increased to 25 wt %, but jump sharply (~9 time fold increasing) for high mass loading of ~50 wt % NC/Al-CuO nanofibers. A decrease in combustion propagation velocity shows up when the mass loading of Al-CuO is reduced to ~14 %, probably due to the larger distances between Al and CuO

nanoparticles at low mass loadings, thus leading to less intimate contact between Al and CuO nanoparticles. The direct result of less intimate mixture of Al and CuO in a NC matrix is that NC/Al-CuO performs similar to Al/NC nanofibers. The similar results have also been found for NC/Al-$Fe_2O_3$ and NC/Al-$Bi_2O_3$ nanofibrous mats, as can be seen from Table 8.1 and 8.2. In Table 8.1, we can see that by increasing mass loading of nanothermite from 33 wt % to 50 wt %, the combustion propagation velocity changes from 17.1 cm/s to 84.4 cm/s. Similarly, for NC/Al-$Bi_2O_3$ nanofibers with $m_{Al}/m_{Bi2O3}$=1:3, the combustion propagation velocity can be increased from 9.0 cm/s, for 33 wt % loading, to 224.0 cm/s, for 60 wt % loading nanofibrous mats.

**Table 8.1.** Combustion propagation velocities of NC/Al-$Fe_2O_3$ nanofibrous mats.

| Velocity (cm/s) | $m_{Al}/m_{Fe2O3}$=1:1 | | |
|---|---|---|---|
| | $m_{Al}=m_{Fe2O3}$=50 mg | $m_{Al}=m_{Fe2O3}$=75 mg | $m_{Al}=m_{Fe2O3}$=100 mg |
| NC/Al-$Fe_2O_3$ | 17.1 | 22.1 | 84.4 |

Note: Mass of NC is ~200 mg for all samples.

We also studied the effects of equivalence ratio of metal and metal oxide nanoparticles in nanofibers on the combustion propagation velocities, and the results are summarized in Table 8.2. It is seen from Table 8.2 that for the same mass loading of 200 mg, mass ratio of 1:3 can result in a much higher combustion propagation velocity of 64.6 cm/s, compared to 14.0 cm/s and 10.2 cm/s for a mass ratio of 1:1 and 1:7 respectively. This suggests that a fuel rich formulation should be incorporated into nanofibers in order to get a faster burning energetic composite nanofibrous mat. However, too much fuel in nanofibers could also lead to a decreased burning performance, which is similar to the NC/Al burning shown in Figure 8.8a. Further

study is needed to get more appropriate formulations for each energetic composite nanofibers.

**Table 8.2.** Combustion propagation velocities of NC/Al-$Bi_2O_3$ nanofibrous mats.

| Velocity (cm/s) | $m_{Al}/m_{Bi2O3}$=1:1 | $m_{Al}/m_{Bi2O3}$=1:3 | | | $m_{Al}/m_{Bi2O3}$=1:7 |
|---|---|---|---|---|---|
| | $m_{Al}=m_{Bi2O3}$=100 mg | $m_{Al}$=25 mg $m_{Bi2O3}$=75 mg | $m_{Al}$=50 mg $m_{Bi2O3}$=150 mg | $m_{Al}$=75 mg $m_{Bi2O3}$=225 mg | $m_{Al}$=25 mg $m_{Bi2O3}$=175 mg |
| NC/Al-$Bi_2O_3$ | 14.0 | 9.0 | 64.6 | 224.0 | 10.2 |

Note: Mass of NC is ~200 mg for all samples.

## *8.4. Conclusions*

Energetic composite nanofibers have been successfully fabricated using the electrospinning method. By tuning the mass loading and equivalence ratio of nanoaluminum and metal oxide nanoparticles in the precursors, energetic composite nanofibrous mats with different mass loading and equivalence ratio were successfully prepared and evaluated for their combustion performances. Energetic composite nanofibrous mats showed the enhanced burning rates, compared to the pure nitrocellulose and nanoaluminum incorporated nanofibrous mats. The combustion propagation velocities of nanofibrous mats were found to correlate to the mass loading of energetic composite nanoparticles to binder in nanofibers.

Our results show that with the composite energetic nanoparticles being electrospun in the nitrocellulose polymer matrix, the total energy release as well as combustion propagation velocity can be dramatically increased, suggesting its potential application in solid rocket propellant systems.

## *8.5. References*


[1] Arkhipov, V. A.; Korotkikh, A. G. *Combust. Flame* **2012**, *159*, 409-415.

[2] Sadeghipour, S.; Ghaderian, J.; Wahid, M. A. *4th International Meeting of Advances in Thermofluids*, Melaka, Malaysia, Oct 3-4, **2011**.

[3] Bocanegra, P. E.; Chauveau, C.; Gökalp, I. *Aerosp. Sci. Technol.* 2007, 11, 33-38.

[4] Dreizin, E. L. *Prog. Energy Combust. Sci.* **2009**, *35*, 141-167.

[5] Mench, M. M.; Yeh, C. L.; Kuo, K. K. *29th International Annual Conference of ICT*, Inst. Chemische Technologie, **1998**.

[6] Dokhan, A.; Price, E. W.; Seitzman, J. M.; Sigman, R. K. *Proc. Combust. Inst.* **2002**, *29*, 2939-2946.

[7] Armstrong, R. W.; Baschung, B.; Booth, D. W.; Samirant, M. *Nano Lett.* **2003**, *3*, 253-255.

[8] Meda, L.; Marra, G.; Galfetti, L.; Inchingalo, S.; Severini, F.; Luca, L.T.D.; *Compos. Sci. Technol.* **2005**, *65*, 769-773.

[9] Galfetti, L.; Luca, L.T.D.; Severini, F.; Meda, L.; Marra, G.; Marchetti, M.; Regi, M.; Bellucci, S. *J. Phys.: Condens. Matter* **2006**, *18*, S1991-S2005.

[10] Huang, Z. M.; Zhang, Y. Z.; Kotaki, M.; Ramakrishna, S. *Compos. Sci. Technol.* **2003**, *63*, 2223-2253.

[11] Li, D.; Xia, Y.N. *Adv. Mater.* **2004**, *16*, 1151-1170.

[12] Greiner, A.; Wendorff, J. H. *Angew. Chem. Int. Ed.* **2007**,*46*,5670-5703.

[13] Luo, C. J.; Stoyanov, S.D.; Stride, E.; Pelan, E.; Edirisinghe, M. *Chem. Soc. Rev.* **2012**,*41*,4708-4735.

[14] Sovizi, M. R.; Hajimirsadeghi, S. S.; Naderizadeh, B. *J. Hazard. Mater.* **2009**, *168*, 1134-1139.

[15] Xie, L.; Shao, Z. Q.; Wang, W. J.; Wang, F. J. *Integr. Ferroelectr.* **2011**, *127*, 184-192.

[16] Kim, S. H.; Zachariah, M. R. *Adv. Mater.* **2004**, *16*, 1821-1825.

[17] Malchi, J. Y.; Foley, T. J.; Yetter, R. A. *ACS Appl. Mater. Interfaces* **2009**, *1*, 2420-2423.

[18] Séverac, F.; Alphonse, P.; Estève, A.; Bancaud, A.; Rossi, C. *Adv. Funct. Mater.* **2012**, *22*, 323-329.

[19] Jian, G.Q.; Liu, L.; Zachariah, M.R. *Adv. Funct. Mater.* **2013**, *23*, 1341-1346.

[20] Zhang, D.; Karki, A. B.; Rutman, D.; Young, D. P.; Wang, A.; Cocke, D.; Ho, T. H.; Guo, Z.H. *Polymer* **2009**, *50*, 4189-4198.

# Chapter 9: Aerosol Routes to Metal Oxide based Hollow Spheres and their Application as Anode Materials in Lithium-ion Batteries*

## *Highlights*

(a) The aerosol based strategy used to make hollow CuO (Chapter 5) was extended to fabricate $Mn_3O_4$ hollow spheres and carbon coated CuO hollow spheres.

(b) Both $Mn_3O_4$ hollow spheres and carbon coated CuO hollow spheres demonstrated exceptional electrochemical performance, high capacity, excellent rate capability, and long-term cycling stability.

## *Overview*

*Part I: $Mn_3O_4$ Hollow Spheres for Lithium-ion Batteries with High Rate and Capacity.*

Hollow $Mn_3O_4$ spheres were produced at relatively low reactor temperature based on a gas blowing mechanism. In application toward lithium ion batteries (LIBs), the hollow $Mn_3O_4$ spheres show a superior electrochemical performance. These hollow $Mn_3O_4$ structures employed in the LIBs demonstrated high reversible capacity of

* The results presented in this chapter have been submitted/published in the following journal articles: Jian, G.Q.;§ Xu, Y.H.;§ (§ Co-first author) Lai, L-C.; Wang, C.S.; Zachariah, M. R. $Mn_3O_4$ Hollow Spheres for Lithium-ion Batteries with High Rate and Capacity, *J. Mater. Chem. A* **2014**, *2*, 4627-4632; Xu, Y.H.;§ Jian, G.Q.; § (§ Co-first author) Wang, C.S.; Zachariah, M. R. Nano-structured Carbon-coated CuO Hollow Spheres as Stable and High Rate Anodes for Lithium-ion Batteries, *J. Mater. Chem. A* **2013**, *1*, 15486-15490. Note: Guoqiang Jian performed the experiments of materials synthesis and characterization. Dr. Yunhua Xu performed the electrochemical performance test of materials. Guoqiang Jian and Dr. Yunhua Xu analyzed electrochemical performance data.

~980 mAh $g^{-1}$ at 200 mA $g^{-1}$ over 140 cycles and an excellent rate capability by retaining a capacity of 300 mAh $g^{-1}$ at an ultra-high current density of 10000 mA $g^{-1}$ . To the best of our knowledge, this is the best electrochemical performance for $Mn_3O_4$ anode materials to date.

*Part II: Carbon-coated CuO Hollow Spheres as Stable and High Rate Anodes for Lithium-ion Batteries.*

Carbon-coated CuO hollow spheres were synthesized using aerosol spray pyrolysis method. The hollow spherical particles provide a capacity of 670 mAh $g^{-1}$ at 1 C (1 C rate = 670 mA $g^{-1}$) and maintain the capacity for 300 cycles and 400 mAh $g^{-1}$ at 50 C, representing the best performance for CuO anodes in LIBs reported to date.

## *9.1. Introduction*

Rechargeable lithium ion batteries (LIBs) are a key component in portable electronics, and have become the most promising power medium in plug-in electric vehicles and integrated units for grid systems. To meet the demands from these fast growing industries, advanced electrode materials with high energy density and good rate capability are desired to replace the current graphite-based anode materials.[1] Electrode materials for next generation LIBs should be economical to manufacture, pose minimal environmental hazard, possess high capacity, good stability, and excellent rate performance. [2, 3] Pioneering work by Tarascon et al. [4] has demonstrated that nanostructured transition metal oxides can be used as high capacity anode materials via a conversion reaction mechanism ($MO_x+2xLi\leftrightarrow M+xLi_2O$).

*9.1.1. $Mn_3O_4$ as Anode Materials in Lithium-ion Batteries.*

Recently, manganese and cobalt oxides have attracted attention for their high theoretical capacity, and are now among the most explored metal oxide electrode materials. [5-13] Compared with cobalt oxides, manganese oxides have the advantage of nontoxicity, abundance, and low cost. However, although $Mn_3O_4$ has a high theoretical capacity (937 mAh $g^{-1}$) and is isostructural with $Co_3O_4$, its electrochemical performance has been reported to be poor. [14, 15]

Despite these earlier disappointing results, recent progress combining the designing of nanomaterials, with optimized structures and composite components, have greatly improved the electrochemical performance of $Mn_3O_4$, including coating $Mn_3O_4$ with conductive carbon layers, [16] or forming composites with graphene or carbon nanotubes, [17-21] mesoporous $Mn_3O_4$ nanotubes,[22] and spongelike $Mn_3O_4$ nanostructures [23]. The best results show capacities of ~900 mAh $g^{-1}$ at 40 mA $g^{-1}$ [19] and 390 mAh $g^{-1}$ at a high current density of 1600 mA $g^{-1}$ [17]. However, these performance improvements, come at the cost of using expensive components i.e. graphene based materials, or mesoporous architectures to accommodate the volume changes during lithiation/delithiation.

*9.1.2. CuO as Anode Materials in Lithium-ion Batteries.*

CuO has also attracted considerable attention as a promising high capacity (theoretical capacity: 674 mAh $g^{-1}$) anode material because of its low cost and nontoxic nature. [24-28] However, the realization of high capacity and high rate capability for CuO anodes has been impeded by its low conductivity and the severe volume change during the conversion reaction with lithium ions. Recently, to address

these problems, incorporation of carbon materials in nanostructure has been developed and demonstrated with improved electrochemical performance.[28-35] For example, Ko *et al.* reported the enhanced rate capability of CuO/MWCNT nanocomposites, in which the mesoporous CuO particles are threaded with CNTs in the long-axis direction.[28] The enhanced rate capability benefits from the use of CuO nanostructures, CNT conductive networks, as well as the strong binding interaction between NPs and CNTs.

Clearly, the ideal structure of CuO as anode materials in LIBs should have (1) nano-size to mitigate volume change and reduce diffusion length of Li ions to improve cycling stability; (2) a carbon based conductive network (such as graphene/CNTs etc.) to provide a continuous and effective electron transportation pathway to enhance conductivity; (3) good contact between CuO nanograin and the conductive carbon network to maintain the electrochemical activity of CuO materials. However, uniform incorporation of carbon into CuO materials using conventional heat treatment methods is a great challenge due to the reduction property of carbon at high temperature.

*9.1.3. Hollow Metal Oxides Nanostructures as Anode Materials.*

Use of hollow nanostructures has been proposed as an effective approach for high performance electrode materials. [36-38] The unique nature of hollow structures, including high surface area, thin walls, and hollow interior, enables electrode materials with larger electrode-electrolyte contact area, reduced diffusion path, as well as free interior space for alleviating structural strain and volume expansion. [37] Many synthetic efforts have been devoted to the fabrication of the hollow metal

oxides nanostructures; however, most approaches are wet chemistry based methods. [39] Relative to wet chemistry methods, aerosol processes are usually relatively low cost, offer high purity products, and more importantly a continuous production process. [40, 41]We have recently successfully fabricated hollow CuO spheres by aerosol spray pyrolysis route, useful for nanoenergetic gas generators applications. [42]

In this chapter, we extend the aerosol based strategy used to make hollow CuO (Chapter 5), to fabricate $Mn_3O_4$ hollow spheres and carbon coated CuO hollow spheres using a scalable aerosol "droplet to particle" route with the introduction of gas-blowing agents-sucrose and $H_2O_2$. Both $Mn_3O_4$ hollow spheres and carbon coated CuO hollow spheres demonstrated exceptional electrochemical performance, high capacity, excellent rate capability and long-term cycling stability.

## *9.2. Experimental Section*

### *9.2.1. Synthesis of Hollow $Mn_3O_4$ Spheres.*

Hollow $Mn_3O_4$ spheres were synthesized by an aerosol spray pyrolysis method, as illustrated in Figure 9.1. 1.00 g (0.004 mol) manganese (II) nitrate tetrahydrate ($Mn(NO_3)_2.4H_2O$) (≥97.0 %, Sigma-Aldrich), 0.171 g ($5\times10^{-4}$ mol) of sucrose ($C_{12}H_{22}O_{11}$) (Sigma–Aldrich), and 5 ml of hydrogen peroxide solution (30 wt %. $H_2O_2$) (Sigma–Aldrich) were dissolved in 15 ml deionized water as precursor solution. Precursor solution was then atomized to form aerosol droplets by a homemade collision-type atomizer using compressed air (0.24 MPa). The geometric mean diameter of atomized formed aerosol droplets was measured to be ~1 μm using a laser aerosol spectrometer. The aerosol droplets were firstly passed through a silica-

gel diffusion dryer to remove most of the water and then led to a tube furnace set at 600 °C. The normal particle residence time in the heating zone was estimated to be around 1 s. The final products of hollow $Mn_3O_4$ spheres were collected on a 0.4 μm HTTP filter (Millipore).

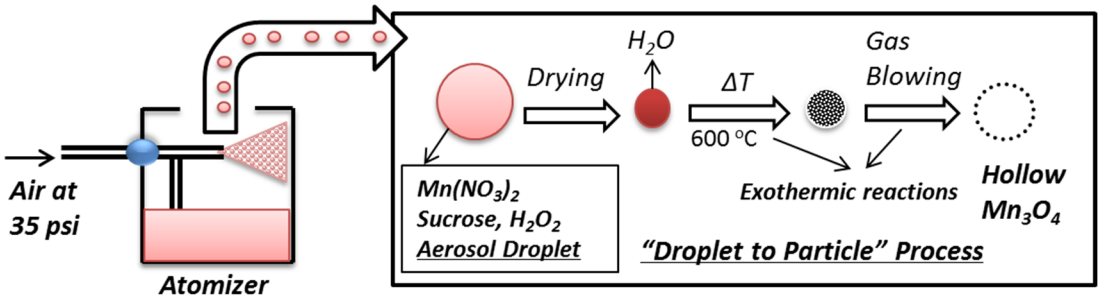


**Figure 9.1.** Schematic formation of hollow $Mn_3O_4$ spheres in a "droplet to particle" aerosol spray pyrolysis process.

*9.2.2. Synthesis of Carbon-Coated Hollow CuO Spheres.*

The setup and method used in the synthesis of carbon-coated hollow CuO spheres is the same to the one used in section 9.2.1 (as illustrated in Figure 9.1). The synthesis of carbon-coated hollow CuO spheres is similar to the synthesis of hollow CuO spheres as described in Chapter 5. The difference is that the precursor solution with higher concentration of copper nitrate and sucrose was used to enable partial carbonization of sucrose, and thus to form a carbon layer on CuO particles. In detail, 2.89 g (0.012 mol) of copper nitrate trihydrate ($Cu(NO_3)_2 \cdot 3H_2O$, Strem Chemical), 0.51 g (0.002 mol) of sucrose ($C_{12}H_{22}O_{11}$, Sigma-Aldrich) and 15 mL of hydrogen peroxide solution (30 wt%. $H_2O_2$, Sigma-Aldrich) were dissolved into 45 mL of distilled water. The furnace temperature was set at 600 °C.

*9.2.3. Materials Characterization.*

Scanning electron microscopy (SEM), transmission electron microscopy (TEM), and selected area electron diffraction (SAED) images were taken by using a Hitachi SU-70 analytical ultra-high resolution SEM and JEOL 2100F field emission TEM, respectively. The powder X-ray diffraction (XRD) was recorded using a Bruker D8 Advance using Cu K α radiation. The thermal analysis experiment (decomposition of $Mn(NO_3)_2.4H_2O$) was conducted in a thermogravimetric analysis (TGA) system (SDT Q600, TA Instruments) under flow of air (100 $cm^3$/min), at a heating rate of 10 $^oC$/min. $N_2$ adsorption/desorption measurement was carried out at 77 K using an Autosorb-iQ analyzer (Quantachrome Instruments). The sample was evacuated overnight at 573 K and 1 mmHg before the measurement.

*9.2.4. Electrochemical Characterization.*

The anode materials (hollow $Mn_3O_4$ spheres/carbon-coated hollow CuO spheres), carbon black and sodium carboxymethyl cellulose (CMC) binder were mixed together at the weight ratio of 70:15:15 to form a slurry and cast onto a copper foil with a loading of 0.5-1.0 mg/$cm^2$ using a doctor blade, followed by an overnight drying in a vacuum oven at 100 $^oC$. Employing a coin cell assembly, lithium foil acts as the counter electrode, 1M $LiPF_6$ in a mixture of ethylene carbonate/diethyl carbonate (EC/DEC, 1/1 by volume) functions as the electrolyte, and Celgard®3501 (Celgard, LLC Corp., USA) as the separator. Cyclic voltammogram (CV) was recorded by a Solatron 1260/1287 Electrochemical Interface (Solartron Metrology, UK) at a scanning rate of 0.1 mV/s between 0-3 V. An Arbin battery test station (BT 2000, Arbin Instruments, USA) was used to test the electrochemical performance. For

hollow $Mn_3O_4$ spheres, rate capability was examined at different current densities from 200 to 10000 mA $g^{-1}$. For carbon coated CuO spheres, rate capability was examined by charging-discharging at different C rates (1C rate = 670 mA $g^{-1}$). For comparison, the commercial CuO nanoparticles (<50 nm, Sigma-Aldrich) were examined under the same cell assembly and test conditions.

## *9.3. Results and Discussion*

### *9.3.1. Synthesis of Hollow $Mn_3O_4$ Spheres and Their Electrochemical Performance.*

The synthesis strategy of the hollow $Mn_3O_4$ spheres is based on an in-situ gas blowing mechanism in single aerosol droplets, as schematically illustrated in Figure 9.1. It consists of atomizing precursor solutions that contains $Mn(NO_3)_2$, sucrose and $H_2O_2$, into aerosol droplets and dispersing them inside a carrier gas-air. The aerosol droplets undergo solvent ($H_2O$) evaporation, chemical reaction and sintering to form hollow particles. Sucrose and $H_2O_2$ in the precursor, act as in-situ gas blowing agents to produce $CO_2$ and $H_2O$. Together with the inherent gas generation properties of the nitrate salt, the gas blowing agents promote the formation of hollow structure, as discussed in chapter 5 and our recent publication. [42]

Figure 9.2a shows a TEM image of the resulting $Mn_3O_4$ materials with a clear hollow structure and ultra-thin walls. The ring pattern selected-area electron diffraction (SAED) in Figure 9.2a indicates the polycrystalline structure of the hollow $Mn_3O_4$ spheres. The SAED pattern show reflections corresponding to *d*-values of $Mn_3O_4$ phase. Some sharp reflections with d-values of ~0.49, 0.31, 0.25, 0.20, 0.15, and 0.14 nm, represent diffraction from (101), (112), (211), (220), (224) and (400) planes of $Mn_3O_4$ phase (Figure 9.2a).

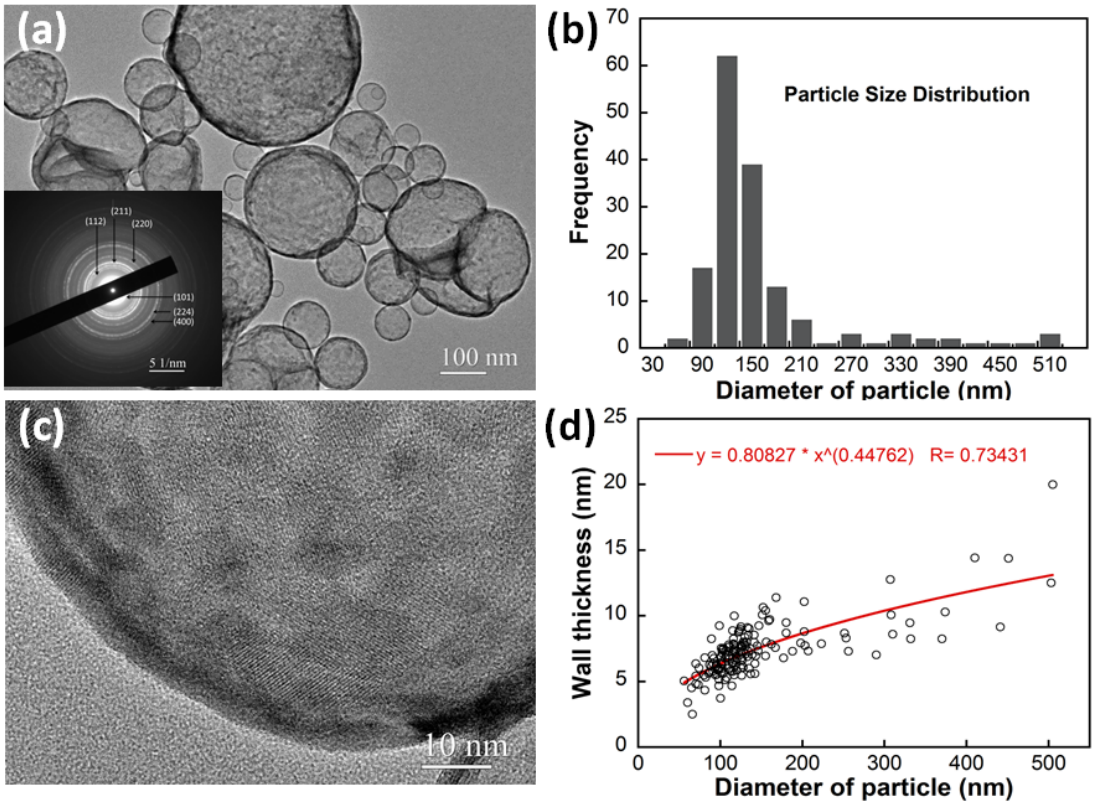


**Figure 9.2.** (a) TEM and SAED images of as collected hollow $Mn_3O_4$ spheres; (b) Particle size distribution of hollow $Mn_3O_4$ spheres based on TEM measurement; (c) High resolution TEM image of hollow $Mn_3O_4$ sphere; (d) The relationship of wall thickness of hollow $Mn_3O_4$ with particle size. Notes: the total counts are 158 in (b, d).

The size distribution of as prepared hollow spheres was obtained by measuring and analyzing a total number of 158 particles in TEM images and plotted in Figure 9.2b. Most particles fall in the range of ~90-210 nm, and the most probable particle size is ~120 nm. Compared to template-based approaches for hollow structures, the aerosol approach in this study shows a relatively wide size distribution, which is typical of the size distribution from the atomization of liquids. $N_2$ adsorption/desorption isothermal curves (Figure 9.3a) show an obvious hysteresis loop, indicating the existence of mesopores within the sample. This is further confirmed by the pore size

distribution (Figure 9.3b) which clearly shows a sharp mesopore peak around 5.6 nm. The specific surface area (calculated by BET method) of the hollow $Mn_3O_4$ spheres is ~96 $m^2$ $g^{-1}$. High resolution TEM image in Figure 9.2c shows that the spheres have ultra-thin walls with thickness of ~5 nm. The wall of the spheres in fact is actually comprised of small nanocrystals (5-10 nm) with pores, in accordance with the $N_2$ adsorption/desorption isothermal results. The shell thickness of 158 hollow spheres in TEM was measured individually. The relationship of shell thickness versus sphere particle size shown in Figure 9.2d indicates that most particles have a shell thickness of 5-10 nm, but that wall thickness increases monotonically with the particle size.

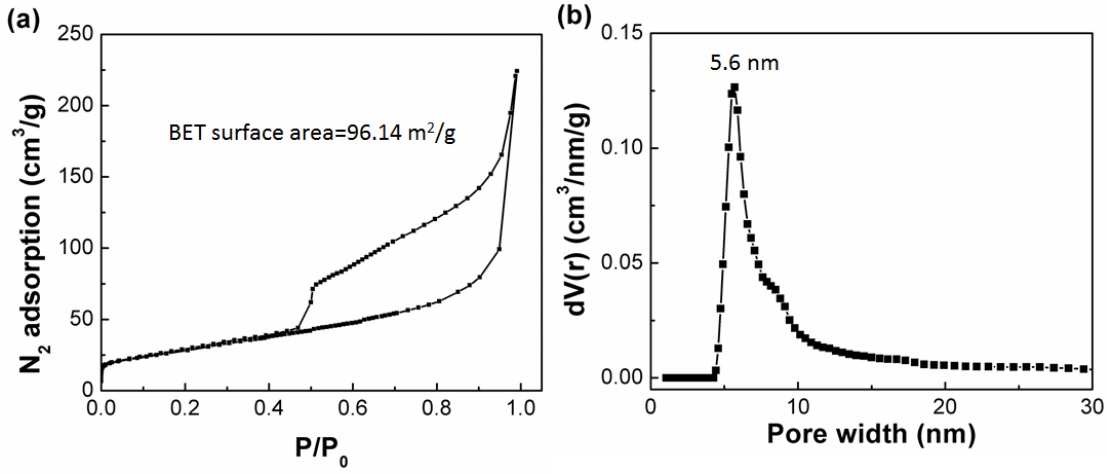


**Figure 9.3.** (a) $N_2$ isothermal curves and (b) NLDFT pore size distribution curve of hollow $Mn_3O_4$ spheres. Note: NLDFT means non-local density functional theory.

Ideally, the wall thickness should be proportional to the initial droplets size if all gases produced during chemical reactions were employed to puff the particles, as schematically shown in Figure 9.4. However, this is not the case shown in Figure 9.2d, where the thickness of the wall does not increase linearly with the change of particle size. Since initial droplets contain the same concentration of solutes, the

amount of gas produced is directly proportional to the droplet volume. However, the amount of gas that should escape a particle during blowing should be proportional to the surface area of the particles. This leads to the result that larger droplets will lose a smaller faction of gas and this gas should result in greater expansion and thinner walls for larger particles.

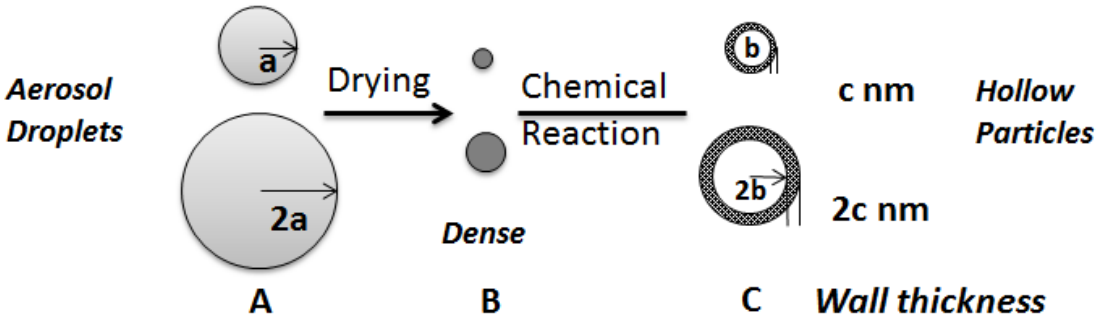


**Figure 9.4.** The ideal relationship of the wall thickness of hollow particle with initial aerosol droplet size. Note: The process is based on an ideal gas blowing assumption that all gases produced in chemical reactions are used for blowing the particles.

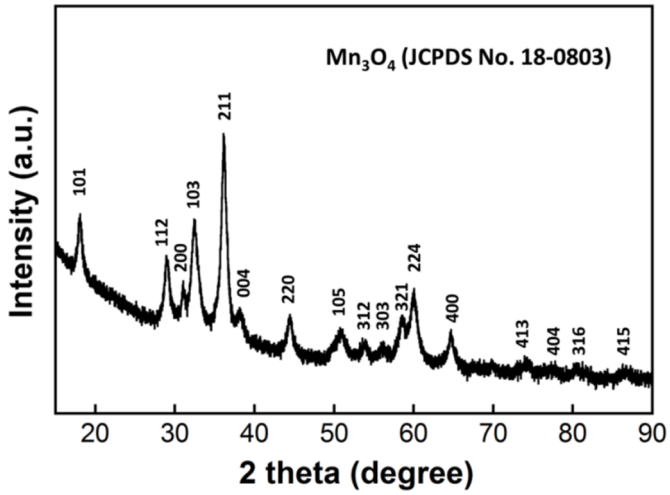


**Figure 9.5.** X-ray diffraction pattern of hollow $Mn_3O_4$ spheres.

Powder diffraction in Figure 9.5 shows the material to be crystalline $Mn_3O_4$ phase (JCPDS No.18-0803), with no observed impurities, which is in agreement with the

SAED analysis. Interestingly, no phase of $Mn_2O_3$ was observed in the product, although $Mn_2O_3$ is the stable phase at 600 °C. [43] To study the decomposition of $Mn(NO_3)_2.4H_2O$, TGA and DSC analysis was performed in air, from room temperature to 1200 °C at a heating rate of 10 °C/min, as shown in Figure 9.6. Beginning at 37 °C, we observe an endotherm with no corresponding mass change which we attribute to melting of $Mn(NO_3)_2.4H_2O$ (m.p.=37 °C). Three mass loss regimes are observed below 250 °C should be from endothermic dehydration and nitrate decomposition. The overall mass loss between 15-250 °C amounts to ~64.4 %, and is close to the 65.3 % expected for the formation of $MnO_2$ from decomposition of $Mn(NO_3)_2.4H_2O$. Upon further heating, further mass loss around 530 and 925 °C, are associated with two endothermic peaks, correspond to the formation of $Mn_2O_3$ and $Mn_3O_4$ respectively. [43]

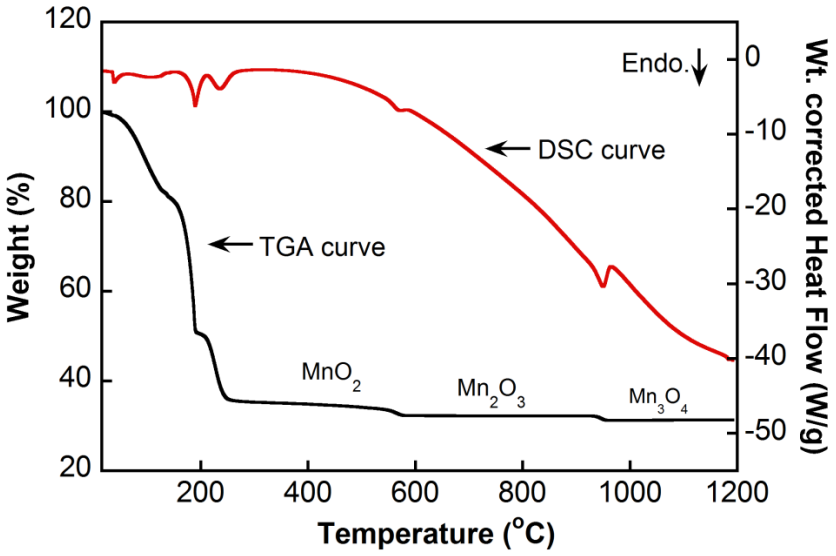


**Figure 9.6.** TGA-DSC curves of $Mn(NO_3)_2.4H_2O$ decomposition in air. (Heating rate: 10 °C/min, air flow: 100 ml/cm$^3$)

We observe single phase $Mn_3O_4$ under our synthesis conditions at 600 $^oC$. During synthesis, the gas generation chemistry which involves the oxidation of sucrose, is exothermic, thus it is quite possible that the actual particle temperature is higher than the reactor temperature. This suggests that the sucrose and $H_2O_2$ in the precursor not only act as gas blowing agents, but may also act as a fast heating source in the particle. In this context, the aerosol spray pyrolysis process in this report is similar to the solution combustion synthesis of metal oxide nanoparticles. [44, 45] In the solution combustion process for producing metal oxide nanoparticles, metal nitrate and glycine ($CH_2NH_2CO_2H$) are ignited in air, and the energy release from the combustion reaction is used to drive the formation chemistry. [45] However, the reaction in our system occurs in a more controlled manner. Firstly, a less reactive fuel-sucrose in place of glycine was used. Secondly, the organic fuel (sucrose) is confined within a single droplet, and the droplet is very fuel lean with a molar ratio of $Mn(NO_3)_2/C_{12}H_{22}O_{11}=8$, with additional oxidizer available from ($2H_2O_2=2H_2O+O_2$), as well as the carrier gas (air). Under such conditions, the combustion is significantly moderated from being violent, which would shatter the droplet/particle, to a condition of a mild exothermic event resulting in gas-blowing. Nevertheless the exothermicity appears sufficient to raise the particle temperature such that $Mn_3O_4$ can be formed at only 600 $^oC$ (reactor temperature), rather than the nominal 925 $^oC$ from $Mn(NO_3)_2.4H_2O$ decomposition.

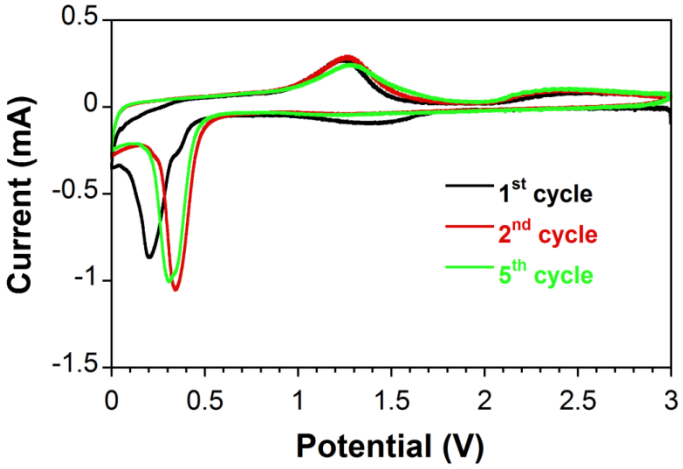


**Figure 9.7.** Cyclic voltammograms of the 1st, 2nd and 5th cycles of hollow $Mn_3O_4$ spheres (scan rate 0.1 mV/s).

Figure 9.7 shows the CV curves in the initial five scans of the hollow $Mn_3O_4$ electrode materials between 0.0 and 3.0 V at a scan rate of 0.1 mV $s^{-1}$. A broad reduction peak around 1.2 V was observed in the first scan and disappeared afterwards, which is ascribed to the decomposition of electrolyte and formation of solid-state interface films and the reduction of $Mn^{3+}$ to $Mn^{2+}$. The main reduction reaction to $Mn^0$ occurred at 0.2 V, in the first cycle. In the following cycles, it shifted to a higher voltage of 0.3 V, which is a common to manganese oxide electrodes, and was attributed to the structure changes during the lithium insertion in the first cycle. [11] In the anodic process, the oxidation of $Mn^0$ to $Mn^{2+}$ occurred at around 1.3 V, while a broad peak appears after 2 V is assigned to the further oxidation of $Mn^{2+}$ to $Mn^{3+}$. The almost identical oxidation/reduction behavior from the second cycle demonstrates good reversibility and stability of the hollow $Mn_3O_4$ spheres.

The charge/discharge profiles of the hollow $Mn_3O_4$ spheres in the first two cycles are shown in Figure 9.8a. The general trend of the charge-discharge profile is

consistent with previous reports on $Mn_3O_4$ anode materials. [17-23] It is seen from the first discharge curve that 1.6 to 0.4 V is due to the formation of solid-electrolyte interface (SEI) and the initial reduction of $Mn_3O_4$.[19] A well-defined voltage plateau at 0.4 V is contributed from the main lithiation reaction of $Mn_3O_4$ hollow spheres. [23] Similar to the CV results, the lithiation plateau moves to a higher voltage of 0.6 V in the second cycle, which implies the structure change in the first cycle lowers the lithiation resistance in the second cycle. The charge curves have two slope plateaus in the ranges of 1-1.5 V and 2.2-3.0 V, corresponding to the oxidation of $Mn^0$ to $Mn^{2+}$ and $Mn^{2+}$ to $Mn^{3+}$ [23], respectively. In the first cycle, the discharge and charge capacities were 1066 and 1609 mAh $g^{-1}$, respectively. The irreversible capacity in the first cycle (34 %) was mainly attributed to the formation of SEI films. In the second cycle, the Coulombic efficiency is higher than 99%. The reversible capacity is around 980 mAh $g^{-1}$, higher than the theoretical value of 937 mAh $g^{-1}$ for the conversion reaction: $Mn_3O_4+8Li^++8e^- \rightarrow 3Mn(0)+4Li_2O$. The extra capacity was also observed for other metal oxide materials and an interfacial mechanism has been proposed, in which the excess lithium was stored in the boundary regions between nanosized metal particles and $Li_2O$ grains produced by the conversion reaction. [46, 47]

The cycling stability of the hollow $Mn_3O_4$ spheres was examined by charging/discharging between 0.0-3.0 V at a current density of 200 mA $g^{-1}$. The cycling performance was shown in Figure 9.8b. The hollow $Mn_3O_4$ sphere anode exhibits a superior stability with no capacity loss except the first two cycles. The capacity retention is ~980 mAh $g^{-1}$ in the $140^{th}$ cycle. The Coulombic efficiency of the hollow $Mn_3O_4$ spheres approaches 100 % after the second cycle, indicating a

stable reversibility. This has drawn attention to the fact that the lithium ion storage of the hollow $Mn_3O_4$ materials in this study is superior to those $Mn_3O_4$ anode materials reported in the literature. [14-23] Apparently, the unique structure of thin-walled hollow structure is responsible for the improved electrochemical performances.

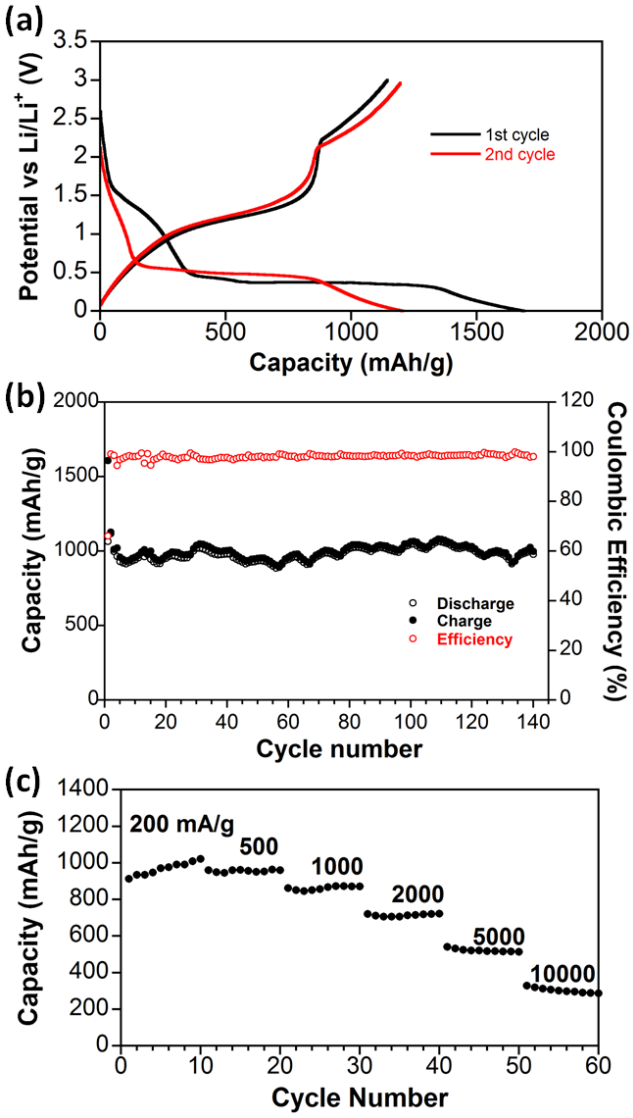


**Figure 9.8.** Electrochemical performance of hollow $Mn_3O_4$ spheres as electrode materials. (a) Charge/discharge profiles for the initial two cycles at a current density of 200 mA $g^{-1}$; (b) Cycling performance at a current density of 200 mA $g^{-1}$; (c) Rate performance at different current densities.

The rate capability of hollow $Mn_3O_4$ materials was evaluated at current rates of 200-10000 mA $g^{-1}$ (Figure 9.8c). At 200 mA $g^{-1}$, it delivers a reversible capacity of ~950 mAh $g^{-1}$, which is comparable to capacity at 200 mA $g^{-1}$. Even at a very high rate of 5000 and 10000 mA $g^{-1}$, the hollow $Mn_3O_4$ spheres can deliver capacities of as high as 520 and 300 mAh $g^{-1}$, respectively. The 300 mAh $g^{-1}$ capacity obtained at the high current of 10000 mA $g^{-1}$ is still comparable to the graphite anode, one currently used in commercial batteries. Such a remarkable rate capability of the $Mn_3O_4$ hollow structure is superior to those with carbon coating and graphene wrapped manganese oxide anode materials, [17-21] represents the best rate performance of $Mn_3O_4$ anode materials. Apparently, the exceptional rate capability is benefited from the unique thin wall hollow structure, which provides a significantly reduced path for both electron and ion diffusion. [37] However, while increasing the lithium ion storage capacity, the hollow structure does inevitably lead to a reduced volumetric energy density.

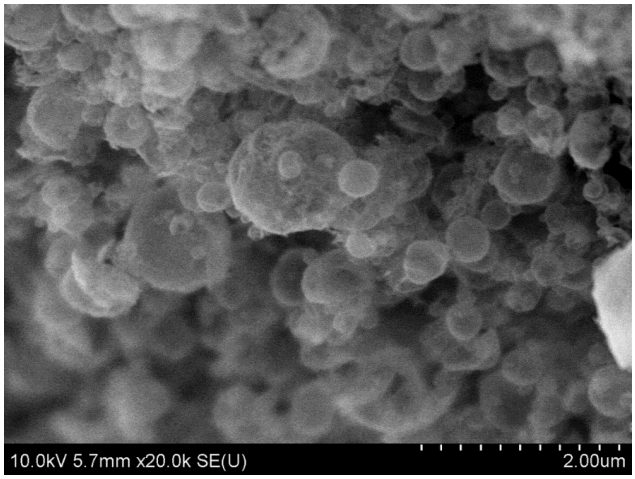


**Figure 9.9.** SEM image of hollow $Mn_3O_4$ spheres after 140 cycles at a current density of 200 mA $g^{-1}$.

As mentioned above, the unique structure of the hollow $Mn_3O_4$ spheres is responsible for the good cycling performance and rate capability. The morphology of the hollow $Mn_3O_4$ spheres after 140 cycles was investigated with SEM (Figure 9.9) and TEM (Figure 9.10). Compared with the TEM image in Figure 9.1, the SEM image of the cycled electrodes shows no obvious morphology changes, demonstrating a robust structure of the hollow spheres, which can effectively alleviate the structural strain and accommodate the large volume change during repeated lithiation/delithiation. TEM images (Figure 9.10) of hollow spheres after cycling show no obvious change regarding the wall thickness compared with the as synthesized hollow spheres. (Figure 9.2)

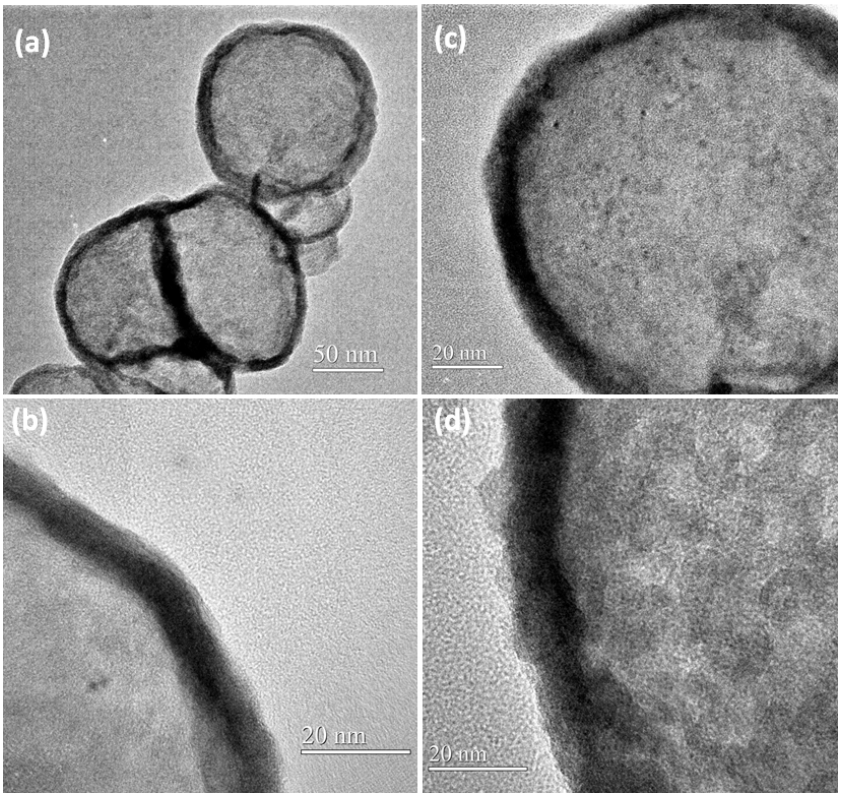


**Figure 9.10.** (a-d) TEM images of hollow $Mn_3O_4$ after 140 cycles. Note: c and d are from different spheres.

*9.3.2. Synthesis of Carbon Coated CuO Hollow Spheres and Their Electrochemical Performance.*

In the aerosol based "droplet to particle" process, the solution of copper nitrate was firstly atomized to form small droplets and then thermally decomposed to form CuO NPs. Meanwhile, sucrose and hydrogen peroxide ($H_2O_2$) in the precursor droplets functioned as gas blowing agents to promote the formation of hollow architectures (similar to process in Figure 9.1). More importantly, by tuning the concentration of sucrose and $H_2O_2$ in the precursor aerosol droplets, partial carbonization of sucrose can be achieved and thus to form carbon coated CuO hollow spheres. Totally different from the previous reports on C/CuO composites that were normally prepared at low temperatures to avoid reduction of CuO by carbon, [24, 27, 32] the aerosol process provides rapid heating of micron sized precursor droplets to a high temperature (600 $^oC$ or higher) in an oxidation environment (air and $H_2O_2$), allowing quick formation of CuO nano-grains, partial carbonization of carbon sources, and generation of gas to puff and form a hollow structure. The short residence time at a high temperature and subsequent fast cooling in an oxidizing environment ensures a rapid precursor decomposition process, thus preventing the reduction reaction.

Figure 9.11a-b show the SEM images of the as-prepared sample in the aerosol spray pyrolysis process. As shown in Figure 9.11a, the particles preserved the spherical morphology of the atomized precursor droplets, while the SEM image of the broken particles (Figure 9.11b) revealed their hollow structure.

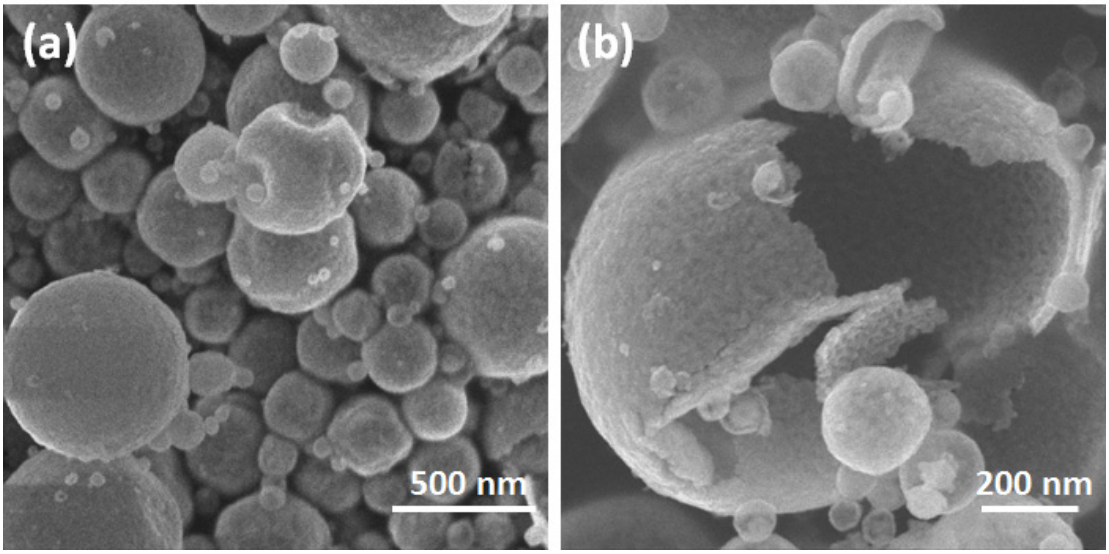


**Figure 9.11.** (a, b) SEM images of the nano-structured carbon-coated CuO hollow spheres.

Similar to the previous findings (see Chapter 5), the wall of the hollow particles consists of a thin layer of NPs with a diameter of ~10 nm, as further confirmed by the TEM image in Figure 9.12a. The high-resolution TEM image in Figure 9.12b clearly shows that the hollow particle was coated with an ultra-thin layer of carbon (~3 nm). Thermogravimetric analysis revealed that the carbon content is less than 3 wt %. The well-defined diffraction rings shown in SAED image in Figure 9.12c indicates that the CuO NPs have a crystalline structure. Powder XRD pattern in Figure 9.12d further confirmed the crystalline product is monoclinic CuO (JCPDS no. 48-1548).

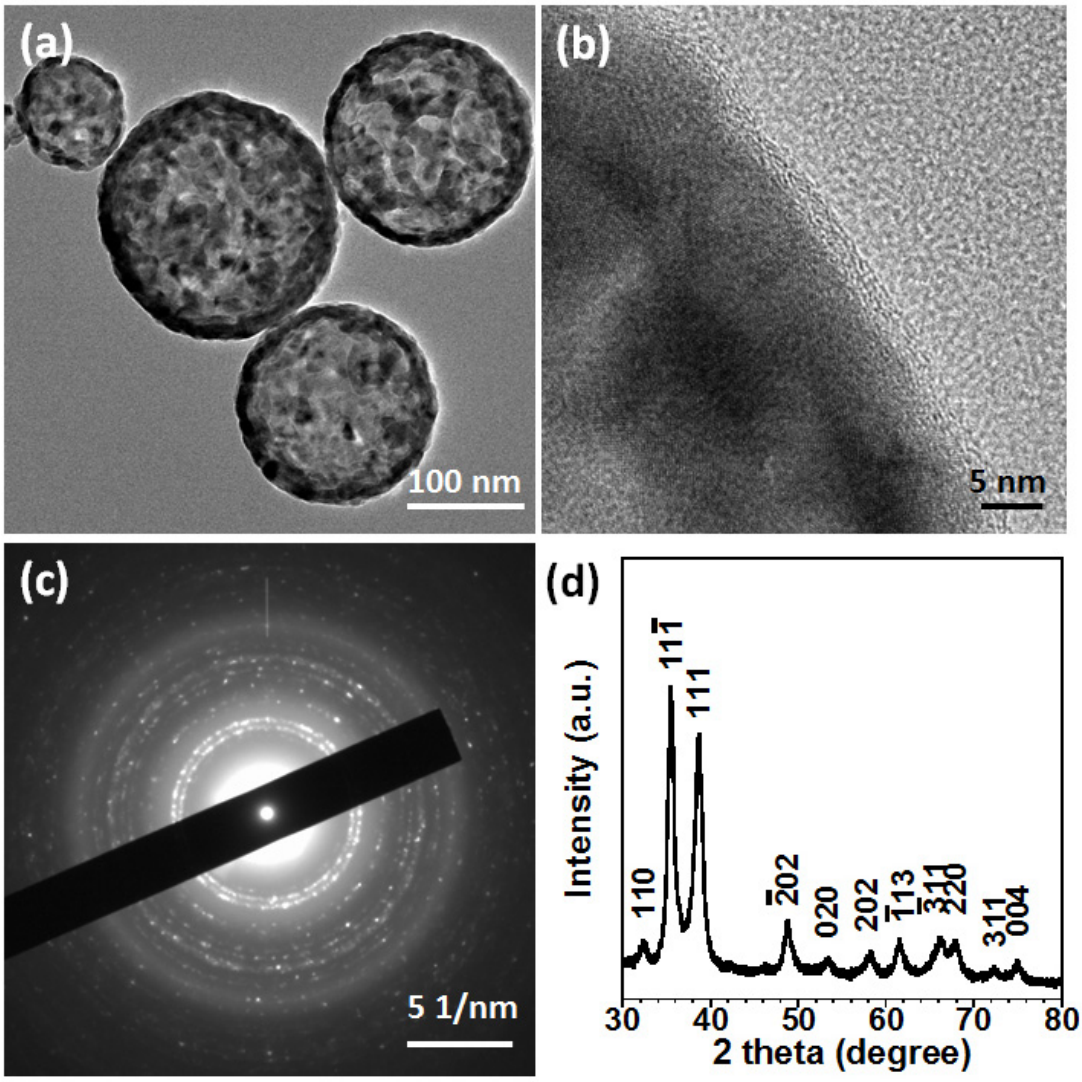


**Figure 9.12.** (a, b) TEM, (c) SAED images and (d) XRD pattern of the nano-structured carbon-coated CuO hollow spheres.

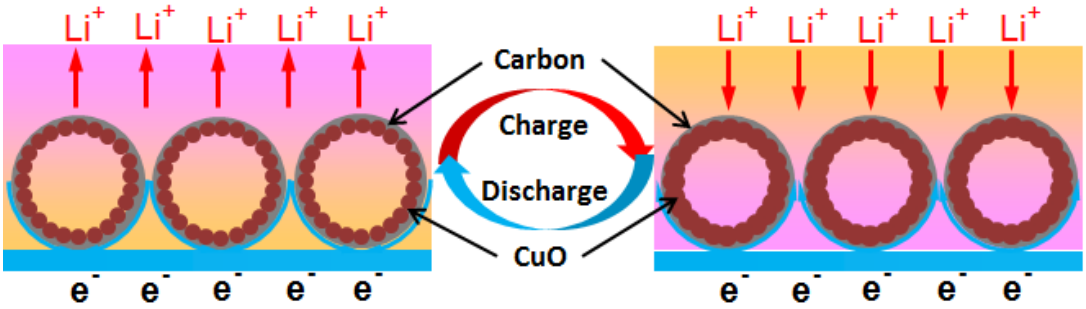


**Figure 9.13.** Schematic illustration of structure change during the charge/discharge processes of the nano-structured carbon-coated CuO hollow spheres.

The unique structure of the carbon-coated CuO hollow spheres brings them a number of advantages as an anode material for LIBs. Figure 9.13 schematically shows these advantages/functions brought by the unique structure. Firstly, the ultra-small NPs can efficiently reduce the stress/strain caused by the volume change during the insertion/extraction processes and the ion diffusion length within the active particles, and thus facilitate the cycling stability and charge transfer reaction. Secondly, the void space in the hollow spheres can accommodate the large volume change induced during charging/discharging. Thirdly, the thin layer CuO nanoparticle structure that is sealed by a carbon layer could help block the penetration of the electrolyte into the center hole reducing the irreversible capacity. Fourthly, the thin carbon coating layer could provide a mechanical support to maintain the integrity of the CuO NPs upon repeated cycling. Finally, the thin layer of carbon can also serve as an electron transportation pathway, enhancing the electrical conductivity of the electrode. Therefore, both long cycling stability and high rate capability are anticipated for nano-structured carbon-coated CuO hollow spheres.

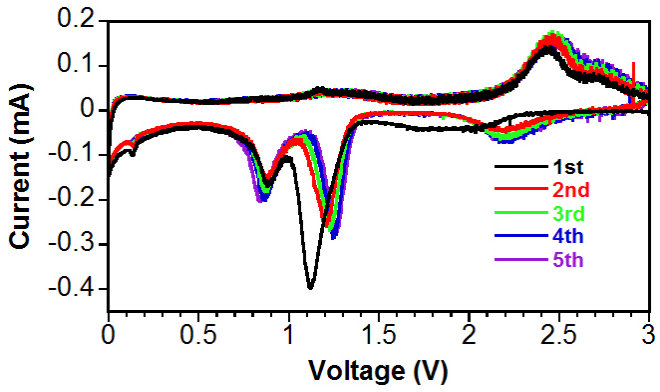


**Figure 9.14.** Cyclic voltammograms curves of the initial five cycles of the nano-structured carbon-coated CuO hollow spheres and commercial CuO NPs. (Scan rate 0.1 mV/s)

Figure 9.14 shows the cyclic voltammogram (CV) curves (initial 5 cycles) of the carbon-coated CuO hollow spheres between 0 and 3 V at a scan rate of 0.1 mV $s^{-1}$. In the first cathodic scan, three peaks were observed at 1.90, 1.12 and 0.88 V, corresponding to the formation of a solid solution of $Cu_{1-x}^{II}Cu_x^{I}O_{1-x/2}$, a phase transition into $Cu_2O$ and the formation of Cu nanograins dispersed into $Li_2O$, respectively. [48] In the following scans, the current peaks at 1.12 and 1.90 V shifted to and maintained at higher potentials of 1.20 and 2.20 V, respectively. The potential shift to more positive potential in the second cycle is a common phenomenon for metal oxide anodes and was attributed to the structure changes during the lithium-ion insertion in the first lithiation. [49] The higher peak current in the first lithiation was partially attributed to the formation of solid electrolyte interface (SEI) films. No obvious difference in the anodic scans was found in the first five cycles. The almost identical lithiation/delithiation behavior after the second cycle demonstrates good reversibility and stability of the carbon-coated CuO hollow spheres.

Figure 9.15a shows the charge-discharge profiles of the carbon-coated CuO hollow spheres in the first 5 cycles. It provides a lithiation capacity of 1003 mA h $g^{-1}$ and a reversible capacity of 551 mA h $g^{-1}$, corresponding to a Coulombic efficiency of 55%, which is higher than a previous report on CuO/C composite anodes.[50] The irreversible capacity is mainly associated with the formation of SEI films. In the following cycles, the capacity slightly increases and the Coulombic efficiency approaches 100 %.

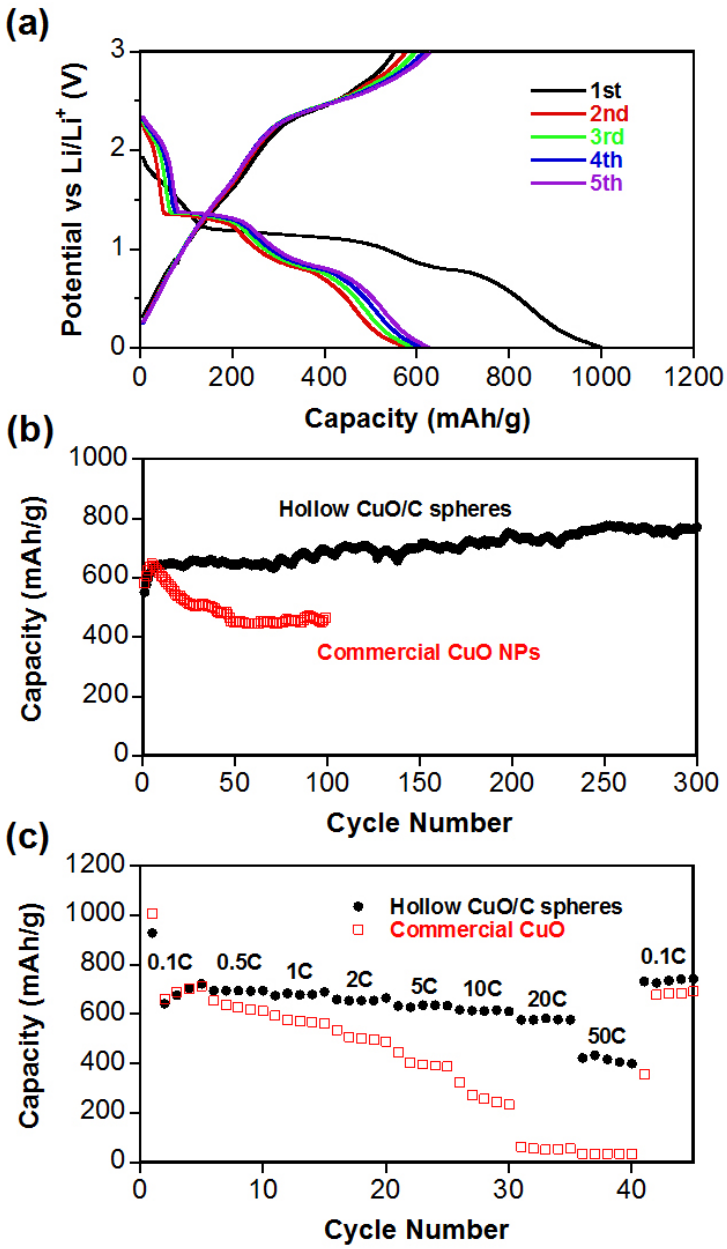


**Figure 9.15.** Electrochemical performance of the nano-structured carbon-coated CuO hollow spherical particles and commercial CuO NPs as electrode materials. (a) Charge/discharge profiles for the initial five cycles at a current density of 670 mA $g^{-1}$; (b) Cycling performance at 1 C rate (670 mA $g^{-1}$); (c) Rate performance.

The cycling performance of the carbon-coated CuO hollow spheres was examined by charge-discharge cycles between 0 and 3.0 V at a 1 C rate (670 mA $g^{-1}$). For comparison, commercial CuO NPs (<50 nm) were also examined under the same conditions. As shown in Figure 9.15b, the charge capacity of carbon-coated CuO hollow spheres quickly increased from ~550 to ~640 mA h $g^{-1}$ in the first five cycles, and then gradually increased to about 750 mA h $g^{-1}$ in the 300$^{th}$ cycle. This is a much better result compared to those reports on CuO anodes in LIBs in the literature. It is noted that the capacity increase during charge-discharge cycles has also been reported on several metal and metal oxide anodes (Sn,[51] $Fe_2O_3$,[52] CoO [53] and CuO[48, 54]), and some of them show higher capacity than their theoretical values. The extra capacity is normally attributed to the reversible formation of gel-like polymeric species in the SEI films due to the catalytic activity of metals in the anodes. [48, 51-54] In this case, the continuous increase in capacity over 300 cycles demonstrates that the volume change of the CuO anodes during the lithium-ion insertion/extraction may build more reversible polymeric species, and thus contributing more extra capacity. The commercial CuO NPs delivered a similar capacity to the carbon-coated CuO hollow spheres in the initial few cycles, but they suffered a rapid capacity decay to ~450 mA h $g^{-1}$ after 50 cycles. These results clearly demonstrate the superior cycling performance of the nano-structured carbon-coated CuO hollow spheres over the commercial NPs.

The rate capability of the nano-structured carbon-coated CuO hollow spheres and the commercial NPs was investigated by charging (delithiation) at 0.1 C and discharging (lithiation) at different C rates, and is shown in Figure 9.15c. The nano-

structured carbon-coated CuO hollow spheres also demonstrated excellent discharge rate capability. Even at a very high rate of 50 C (3.35 A $g^{-1}$), it still retained as high as 400 mA h $g^{-1}$, which means that the carbon-coated CuO hollow sphere anodes can be discharged in 1.2 minutes with higher capacity retention than graphite anodes. To date, this is the best rate performance for CuO anodes we are aware of. In contrast, the commercial CuO NPs failed to provide capacity at 20 C. It was noticed that when the current was changed back to 0.1 C, the commercial CuO NP anodes almost recovered their initial capacity. The reason could be that at low current, the commercial CuO NPs can be fully lithiated and delithiated, resulting in large volume change and severe structure deformation; while at high current density, the low conductivity of commercial CuO NPs induces a large overpotential, thus only partial CuO NPs are lithiated/delithiated, and small volume change and less structure deformation are induced. The less volume change of commercial CuO NPs at a high rate can extend the cycling stability. Therefore, the cycling stability of commercial CuO NPs at a high C rate should be better than that measured at a low C rate. This is the reason why the capacity retention of the commercial CuO NPs at 0.1 C after an aggressive rate test from 1 C to 50 C for 40 cycles (Figure 9.15c) is higher than the capacity retention of commercial CuO NPs after 40 cycles at 1 C (Figure 9.15b). The excellent discharge capability of the nano-structured carbon-coated CuO hollow spheres demonstrated a significant advance in Li-ion battery technologies because the discharge power density is critical for most practical applications. The exceptional electrochemical performance is attributed to the unique structure of the nano-structured carbon-coated hollow particles.

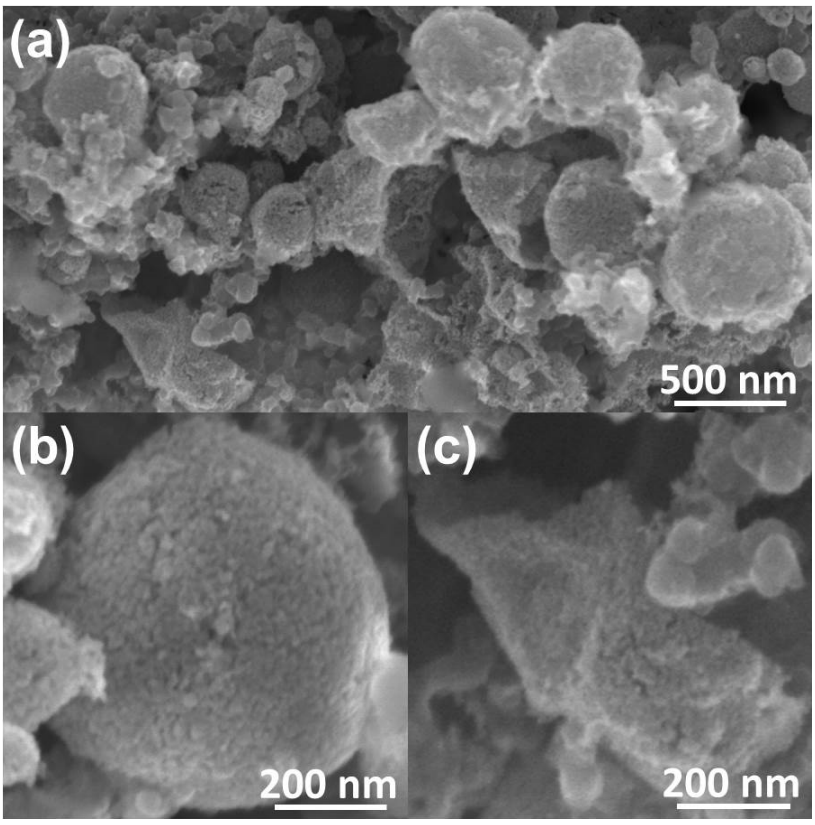


**Figure 9.16.** SEM images of the nano-structured carbon-coated CuO hollow spherical particles after 70 charge/discharge cycles.

The morphology changes of the nano-structured carbon-coated CuO hollow particles after 70 charge-discharge cycles between 0 and 3.0 V at 1 C were investigated using SEM, which is shown in Figure 9.16. Most hollow CuO particles preserved the spherical morphology and the architecture of the as prepared samples (Figure 9.11 and 9.12). Few collapsed particles may be attributed to the mixing/coating process. The integrity of the thin layer of CuO NPs was still maintained (Figure 9.16c). The robust structure is associated with the carbon coating layer and hollow structure, which provides both mechanical support and electrical pathway, thus ensuring good cycling stability and fast rate capability.

## *9.4. Conclusions*

In summary, we successfully synthesized hollow $Mn_3O_4$ spheres and carbon-coated CuO hollow spheres using a one-step, fast, scalable and low-cost synthesis method, aerosol spray pyrolysis.

(a) Hollow $Mn_3O_4$ spheres with an ultra-thin shell demonstrate superior electrochemical performance as anode materials in lithium-ion batteries than any previously reported $Mn_3O_4$ anodes in the literature. The hollow $Mn_3O_4$ spheres exhibited good stability, with high capacity retention of ~980 mAh $g^{-1}$ over 140 cycles, and exceptional rate capability. The outstanding electrochemical performance is attributed to its unique structure, of a hollow interior and ultra-thin wall.

(b) The nano-structured carbon-coated CuO hollow spherical particles showed high capacity, long cycling stability, and excellent rate capability. The exceptional performance is attributed to the unique architecture of the carbon-coated CuO hollow spherical particles. This work provides a facile way to design and develop novel nano-structured electrode materials for high performance rechargeable batteries.

## *9.5. References*

[1] Dunn, B.; Kamath, H.; Tarascon, J-M. *Science* **2011**, *334*, 928-935.

[2] Choi, N.S.; Chen, Z.H.; Freunberger, S.A.; Ji, X.L.; Sun, Y.K.; Amine, K.; Yushin, G.; Nazar, L.F.; Cho, J.; Bruce, P.G. *Angew. Chem. Int. Ed.* **2012**, *51*, 2-33.

[3] Kim, M.G.; Cho, J. *Adv. Funct. Mater.* **2009**, *19*, 1497-1514.

[4] Poizot, P.; Laruelle, S.; Grugeon, S.; Dupont, L.; Tarascon, J-M. *Nature* **2000**, *407*, 496-499.

[5] Reddy, M. V.; Subba Rao, G. V.; Chowdari, B. V. R. *Chem. Rev.* **2013**, *113*, 5364-5457.

[6] Lou, X.W.; Deng, D.; Lee, J.Y.; Feng, J.; Archer, L.A. *Adv. Mater*. **2008**, *20*, 258-262.

[7] Li, Y.G.; Tan, B.; Wu, Y.Y. *Nano Lett*. **2008**, *8*, 265-270.

[8]Yang , X.Y.; Fan ,K.C.; Zhu, Y.H.; Shen, J.H.; Jiang, X.; Zhao, P.; Luan, S.R.; Li, C.Z. *ACS Appl. Mater. Interfaces* **2013**, *5*, 997-1002.

[9] Luo, W.; Hu, X.L.; Sun, Y.M.; Huang, Y.H. *ACS Appl. Mater. Interfaces* **2013**, *5*, 1997-2003

[10] Nayak, S.; Malik, S.; Indris, S.; Reedijk, J.; Powell, A.K. *Chem. Eur. J.* **2010**, *16*, 1158-1162.

[11] Guo, J.C.; Liu, Q.; Wang, C.S.; Zachariah, M.R. *Adv. Funct. Mater.* **2012**, *22*, 803-811.

[12] Xia, H.; Lai, M.O.; Lu, L. *J. Mater. Chem.* **2010**, *20*, 6896-6902.

[13] Chae, C.; Kim, J.H.; Kim, J.M.; Sun, Y.K.; Lee, J.K. *J. Mater. Chem.* **2012**, *22*, 17870-17877.

[14] Pasero, D.; Reeves, N.; West, A.R. *J. Power Sources* **2005**, *141,* 156-158.

[15] Fan Q.; Whittingham, M.S. *Electrochem. Solid-State Lett.* **2007**, *10*, A48-A51.

[16] Wang, C.B.; Yin, L.W.; Xiang, D.; Qi, Y.X. *ACS Appl. Mater. Interfaces* **2012**, *4*, 1636-1642.

[17] Wang, H.L.; Cui, L.F.; Yang, Y.; Casalongue, H.S.; Robinson, J.T.; Liang, Y.Y.; Cui, Y.; Dai, H.J. *J. Am. Chem. Soc.* **2010**, *132*, 13978-13980.

[18] Liu, S.Y.; Xie, J.; Zheng, Y.X.; Cao, G.S.; Zhu, T.J.; Zhao, X.B. *Electrochim. Acta* **2012**, *66*, 271-278.

[19] Li, L.; Guo, Z.P.; Du, A.J.; Liu, H.K. *J. Mater. Chem.* **2012**, *22*, 3600-3605.

[20] Lavoie, N.; Malenfant, P.R.L.; Courtel, F.M.; Abu-Lebdeh, Y.; Davidson, I.J. *J. Power Sources* **2012**, *213*, 249-254.

[21] Wang, Z.H.; Yuan, L.X.; Shao, Q.G.; Huang, F.; Huang, Y.H. *Mater. Lett.* **2012**, *80*, 110-113.

[22] Bai, Z.C.; Fan, N.; Ju, Z.C.; Guo, C.L.; Qian, Y.T.; Tang, B.; Xiong, S.L. *J. Mater. Chem. A* **2013**, *1*, 10985-10990.

[23] Gao, J.; Lowe, M.A.; Abruna, H.D. *Chem. Mater.* **2011**, *23*, 3223-3227.

[24] Zheng, S.-F.; Hu, J.-S.; Zhong, L.-S.; Song, W.-G.; Wan, L.-J.; Guo, Y.-G. *Chem. Mater.* **2008,** *20,* 3617-3622.

[25] Ke, F.-S.; Huang, L.; Wei, G.-Z.; Xue, L.-J.; Li, J.-T.; Zhang, B.; Chen, S.-R.; Fan, X.-Y.; Sun, S.-G. *Electrochim. Acta* **2009**, *54,* 5825-5829.

[26] Park, J. C.; Kim, J.; Kwon, H.; Song, H. *Adv. Mater.* **2009**, *21*, 803-807.

[27] Wang, L.; Cheng, W.; Gong, H.; Wang, C.; Wang, D.; Tang, K.; Qian, Y. *J. Mater. Chem.* **2012**, *22,* 11297-11302.

[28] Ko, S.; Lee, J.; Yang, H. S.; Park, S; Jeong, U. *Adv. Mater.* **2012**, *24*, 4451-4456.

[29] Chen, L.B.; Lu, N.; Xu, C.M.; Yu, H.C.; Wang, T.H. *Electrochim.Acta* **2009**, *54,* 4198-4201.

[30] Xiang, J.Y.; Tu, J.P.; Zhang, J.; Zhong, J.; Zhang, D.; Cheng, J.P. *Electrochem. Commun.* **2010**, *12*, 1103-1107.

[31] Dar, M. A.; Nam, S. H.; Kim, Y. S.; Kim, W. B. *J. Solid State Electrochem.* **2010**, *14*, 1719-1726.

[32] Zhou, J.; Ma, L.; Song, H.; Wu, B.; Chen, X. *Electrochem. Commun.* **2011**, *13*, 1357-1360.

[33] Chen, X.; Zhang, N.; Sun, K. *J. Mater. Chem.* **2012**, *22*, 13637-13642.

[34] Wang, L.; Gong, H.; Wang, C.; Wang, D.; Tang, K.; Qian, Y. *Nanoscale* **2012**, *4*, 6850-6855.

[35] Lee, J.; Choi, S.; Park, S. *Chem. Asian J.* **2013**, *8,* 1377-1380.

[36] Lou, X.W.; Archer, L.A.; Yang, Z.C. *Adv. Mater.* **2008**, *20*, 3987-4019.

[37] Wang, Z.Y.; Zhou, L.; Lou, X.W. *Adv. Mater.* **2012**, *24*, 1903-1911.

[38] Lai, X.Y.; Halpert, J.E.; Wang, D. *Energy Environ. Sci.* **2012**, *5*, 5604-5618.

[39] Hu, J.; Chen, M.; Fang, X.S.; Wu, L.M. *Chem. Soc. Rev.* **2011**, *40*, 5472-5491.

[40] Okuyama, K.; Lenggoro, I.W. *Chem. Eng. Sci.* **2003**, *58*, 537-547.

[41] Boissiere, C.; Grosso, D.; Chaumonnot, A. *Adv. Mater.* **2011**, *23*, 599-623.

[42] Jian, G.Q.; Liu, L.; Zachariah, M.R. *Adv. Funct. Mater.* **2013**, *23*, 1341-1346.

[43] Stobbe, E.R.; Boer, B.A.d.; Geus, J.W. *Catal. Today* **1999**, *47*, 161-167.

[44] Chick, L.A.; Pederson, L.R.; Maupin, G.D.; Bates, J.L.; Thomas, L.E.; Exarhos, G.J. *Mater. Lett.* **1990**, *10*, 6-12.

[45] Mukasyan, A.S.; Epstein, P.; Dinka, P. *Proc. Combust. Inst.* **2007**, *31*, 1789-1795.

[46] Maier, J. *Solid State Ionics* **2002**, *148*, 367-374.

[47] Balaya, P.; Li, H.; Kienle, L.; Maier, J. *Adv. Funct. Mater.* **2003**, *13*, 621-625.

[48] Débart, A.; Dupont, L.; Poizot, P.; Leriche, J-B.; Tarascon, J. M. *J. Electrochem. Soc.* **2001**, *148*, A1266-A1274.

[49] Xu, Y. H.; Jian, G. Q.; Liu, Y. H.; Zhu, Y. J.; Zachariah, M. R.; Wang, C. S. *Nano Energy* **2014**, *3*, 26-35.

[50] Huang, X. H.; Wang, C. B.; Zhang, S. Y.; Zhou, F. *Electrochim. Acta* **2011**, *56*, 6752-6756.

[51] Xu, Y. H.; Guo, J. C.; Wang, C. S. *J. Mater. Chem.* **2012**, *22*, 9562-9567.

[52] Hassan, M. F.; Rahman, M.M.; Guo, Z. P.; Chen, Z. X.; Liu, H. K. *Electrochim. Acta* **2010**, *55*, 5006-5013.

[53] Grugeon, S.; Laruelle, S.; Dupont, L.; Tarascon, J.-M. *Solid State Sci.* **2008**, *5*, 895-904.

[54] Xiang, J. Y.; Tu, J. P.; Qiao, Y. Q.; Wang, X. L.; Zhong, J.; Zhang, D.; Gu, C. D. *J. Phys. Chem. C* **2011**, *115*, 2505-2513.

# Chapter 10: Mesoporous $Fe_2O_3$ Spheres as Anode Materials in Lithium-ion Batteries [*]

## *Highlights*

(a) Crystalline and amorphous mesoporous $Fe_2O_3$ spheres were synthesized using aerosol spray pyrolysis-a scalable "droplet to particle" route.

(b) Both crystalline and amorphous mesoporous $Fe_2O_3$ spheres changed into nano-crystallite porous structure after charge/discharge cycles. As anode materials in LIBs, the crystalline mesoporous $Fe_2O_3$ spheres suffer less structure deformation and show much better electrochemical performance than amorphous $Fe_2O_3$ spheres.

## *Overview*

Mesoporous $Fe_2O_3$ spherical particles with amorphous or crystalline structure were synthesized at different temperatures using a facile and scalable method-aerosol spray pyrolysis. As anode materials in LIBs, the crystalline $Fe_2O_3$ (C-$Fe_2O_3$) spheres synthesized at 800 °C show better electrochemical performance than the amorphous $Fe_2O_3$ (A-$Fe_2O_3$) prepared at 600 °C. Both, however, changed into nano-crystallite porous structure after charge/discharge cycles. The C-$Fe_2O_3$ spheres provided high

[*] The results presented in this chapter have been published in the following journal article: Xu, Y.H.;[§] Jian, G.Q.;[§] ([§]Co-first author) Liu, Y.H.; Zhu, Y.J.; Zachariah, M. R.; Wang, C.S. Superior Electrochemical Performance and Structure Evolution of Mesoporous $Fe_2O_3$ Anodes for Lithium-ion Batteries, *Nano Energy* **2014**, *3*, 26-35. Note: Guoqiang Jian performed the experiments of materials synthesis and characterization. Dr. Yunhua Xu performed the electrochemical performance test of materials. Dr. Yunhua Xu and Guoqiang Jian analyzed electrochemical performance test data.

reversible capacity of 800 mAh $g^{-1}$ at 0.5 C over 300 charge/discharge cycles and retained 300 mAh $g^{-1}$ at 10 C. The excellent cycling stability of the C-$Fe_2O_3$ spheres is mainly attributed to the interior voids in the mesoporous $Fe_2O_3$ particles that provide extra space to accommodate volume change and alleviate structural strain/stress during electrochemical reaction. The high rate performance of mesoporous C-$Fe_2O_3$ is attributed to (1) fast charge transfer reaction at the large interfacial area between electrode and liquid electrolyte and (2) the reduced Li-ion diffusion distances. This work not only provides a simple synthesis approach for electrode materials in lithium ion batteries, but also helps in designing novel and high performance electrode materials.

## *10.1. Introduction*

As the current dominant power source in portable electronic devices, lithium-ion batteries (LIBs) are of great interest for potential application in emerging electric vehicles and renewable clean energy sources. [1-3] However, the low energy density of commercial graphite/$LiCoO_2$ lithium-ion batteries has hampered implementation of a wide array of energy and environmentally desirous technologies. [4, 5] In this regard, extensive efforts have been made to seek anode materials with high capacity, good rate capability and long cycling life. [1, 6, 7] Iron is earth abundant, low cost and nontoxic, making iron oxides a promising candidate for sustainable Li-ion batteries. Compared with conventional graphite anodes, Iron oxides ($Fe_2O_3$) have a three times higher theoretical capacity of 1006 mAh $g^{-1}$. [6, 7]. The large theoretical capacity of $Fe_2O_3$ is delivered by a conversion reaction where one chemical formula unit of $Fe_2O_3$ can react with 6 Li ions to form iron nano-particles dispersed in a $Li_2O$

matrix. [6, 7] However, the insertion/extraction of a large amount of Li ions leads to large volume change, which can adversely impact morphology and mechanical contact during reaction cycling, leading to a rapid decay in capacity.

Creating nano-sized electrode materials is one of the most successful methods to mitigate the volume change of metal oxide anodes. [1, 7-12] Pioneering work by Taroscon's group has demonstrated the significant improvement in cycle stability and rate capacity for nano-sized $Fe_2O_3$ particles in contrast to micro-sized particles. [13, 14] The improved performance of nano-sized electrode materials in LIBs benefits from reduced dimension which could reduce structural strain/stress and improve charge/discharge kinetics. Following these ideas a variety of nano-$Fe_2O_3$ architectures, comprising nanoparticles, nanotubes to hierarchical nanostructures [15-35] have been synthesized using hydrothermal [26-28, 31, 32] and hard-template methods. [15-17, 30] However, easy fabrication of advanced $Fe_2O_3$ electrode materials with high capacity and long cycling life is still a great challenge. One key question arises: What is an ideal model structure for $Fe_2O_3$ as anode materials?

An appealing structural approach is using mesoporous $Fe_2O_3$ particles, which not only take advantage of long cycling life and high rate performance of nano-$Fe_2O_3$ but also have high tapping density. [36-38] Mesoporous spherical particles hold several advantages over nanoparticles and other nanostructures based on purely structural consideration. Specifically, mesoporous $Fe_2O_3$ particles with closed-mesopores have much smaller surface area than that of nanoparticles and open-pore materials, and thus offer high Coulombic efficiency and large taping density. [39] The nano-sized

walls of the mesoporous $Fe_2O_3$ particles offer similar Li-ion diffusion pathway to $Fe_2O_3$ nanoparticles, which ensures fast kinetics and thus high rate capability. Finally, mesopores provide additional voids to effectively accommodate the volume change and alleviate the structural strain/stress during electrochemical reaction, giving rise to longer cycling life and improved cycling stability. Practically, this concept of design has been previously demonstrated in several conversion reaction electrodes, such as $MnO_2$ [40], $Co_3O_4$ [41, 42], as well as $Cr_2O_3$ [43].

Mesoporous $Fe_2O_3$ particles with different morphologies have also been synthesized using complex acidic etching [27], template synthesis [30], hydrothermal synthesis [33] and chimie douce precipitation method [34]. The porous $Fe_2O_3$ particles prepared using these methods, however, can only sustain a short cycling life of 50-100 cycles. [15-32] There has been limited success in low-cost synthesis methods capable of mass production of mesoporous $Fe_2O_3$ with high cycling performance. The question is: how to fabricate the desirable $Fe_2O_3$ electrode materials in a relatively easy way which can enable us to scale up for further application?

In previous works, it has been shown that the aerosol spray pyrolysis is a powerful technique to synthesize kinds of functional materials. [44-47] Aerosol spray pyrolysis is a simple process, whereby a precursor solution is atomized to form aerosol droplets dispersed in a carrier gas, which undergoes thermally-induced evaporation of solvent and solid-state chemical reactions to form the desired particles. [47] Compared with wet-chemistry methods, aerosol spray pyrolysis is relatively low cost, compatible with on-line continuous production processes, thus providing a scalable

manufacturing of particles. In a recent work by our groups, ultrasmall and uniformly sized nano-Sn grain/carbon spheres were successfully produced using this technique. [44] It was shown that the rapid heating and cooling process associated with droplet formation and solvent evaporation can "freeze" the precursor solid particles to create uniformly nano-structured spherical particles, which is hardly achievable by the wet chemistry methods.

In this chapter, we employed a one-step "droplet-to-particle" aerosol spray pyrolysis method to produce crystalline or amorphous mesoporous $Fe_2O_3$ spherical particles by tuning the pyrolysis temperatures. The mesoporous $Fe_2O_3$ spherical particles was investigated as anode materials in LIBs. High reversible capacity of ~800 mAh $g^{-1}$ at 0.5 C over 300 charge/discharge cycles were demonstrated for the crystalline $Fe_2O_3$ anode. The effects of the amorphous and crystal structures on the electrochemical performance and the structure evolution during electrochemical tests were also investigated.

## *10.2. Experimental Section*

### *10.2.1. Synthesis of Mesoporous $Fe_2O_3$ Spherical Particles.*

Mesoporous $Fe_2O_3$ particles were prepared by an aerosol spray pyrolysis method as illustrated in Figure 10.1. Typically, ~3.2 g (0.0075 mol) iron (III) nitrate nonahydrate ($Fe(NO_3)_3 \cdot 9H_2O$, Sigma-Aldrich) and 0.34 g (0.001 mol)sucrose ($C_{12}H_{22}O_{11}$, Sigma-Aldrich) were dissolved into 110 ml water. Aerosol droplets containing the dissolved precursors were generated using compressed air at a pressure of 0.24 MPa in a collision type atomizer. The geometric mean diameter of the droplets was measured to be ~1 μm by a laser aerosol spectrometer. The produced

aerosol droplets were firstly passed through a silica-gel diffusion dryer to remove most of the water, and then passed to a tube furnace at 600 or 800 °C. The normal residence time in the synthesis was around 1 s for a total gas flow rate of 3.5 L $min^{-1}$.The final products were collected on a 0.4 μm (pore size) HTTP Millipore filter.

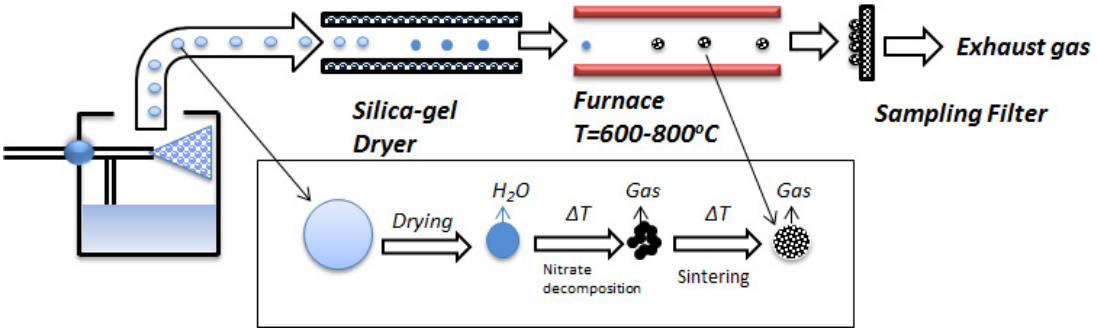


**Figure 10.1.** Schematic illustration of aerosol spray pyrolysis route to mesoporous $Fe_2O_3$.

*10.2.2. Material Characterizations.*

Scanning electron microscopy (SEM), transmission electron microscopy (TEM) and selected area electron diffraction (SAED) images were taken by the Hitachi SU-70 analytical ultra-high resolution SEM and JEOL 2100F TEM, respectively. X-ray diffraction (XRD) pattern was recorded by Bruker Smart1000 (Bruker AXS Inc.) using CuKα radiation. The Brunauer-Emmett-Teller (BET) specific surface area and pore size and volume were analyzed using $N_2$ absorption with Micromeritics ASAP 2020 Porosimeter Test Station.

*10.2.3. Electrochemical Characterization.*

The mesoporous $Fe_2O_3$ spherical particles were mixed with carbon black and sodium carboxymethyl cellulose (CMC) binder to form slurry at the weight ratio of 70:15:15. The electrode was prepared by casting the slurry onto copper foil with active material loading of ~1.0 mg $cm^{-2}$ using a doctor blade and dried in a vacuum oven at 100 °C overnight. Coin cells were assembled with lithium foil as the counter electrode, 1 M $LiPF_6$ in a mixture of ethylene carbonate/diethyl carbonate (EC/DEC, 1:1 by volume) as the electrolyte, and Celgard®3501 (Celgard, LLC Corp., USA) as the separator. Electrochemical performance was tested using Arbin battery test station (BT2000, Arbin Instruments, USA). Rate capability was examined by charging/discharging at different rates from 0.1 C to 30 (C rate=1006 mA $g^{-1}$). Cyclic voltammogram scanned at 0.1 mV/s between 0-3 V was recorded using Solatron 1260/1287 Electrochemical Interface (Solartron Metrology, UK). For comparison, the commercial $Fe_2O_3$ nanoparticles with particle size of 50 nm (Sigma-Aldrich) were examined at the same cell assemble and test conditions. Galvanostatic intermittent titration technique (GITT) measurement was carried out by applying a pulse constant current of 200 mA $g^{-1}$ with duration of 30 min and followed by 6 h relaxation to reach an equilibrium voltage.

## *10.3. Results and Discussion*

*10.3.1. Synthesis and Characterization of Mesoporous $Fe_2O_3$ Spheres.*

A schematic illustration for the synthesis of mesoporous $Fe_2O_3$ spheres is shown in Figure 10.1. The aerosol spray pyrolysis synthesis followed a one-step "droplet-to-particle" process whereby precursor solutions are atomized and thermally

decomposed to form mesoporous particles. The key to the formation of the closed-mesopore structure is the existence of the gas blowing agent in the precursor solution. Both decomposition of nitrate salts and oxidation of sucrose could produce gases which lead to the formation of porous structure. The role of sucrose here is to increase the gas production in the sintering process, as illustrated in Figure 10.1. Two temperatures, 600 °C and 800 °C, were set to synthesize mesoporous $Fe_2O_3$ spheres. The products collected at two reactor temperatures of 600 and 800 °C, were denoted as A-$Fe_2O_3$ (amorphous) and C-$Fe_2O_3$ (crystalline), respectively.

SEM images in Figure 10.2 show the morphology of $Fe_2O_3$ spheres. It can be seen that spherical shape of the precursor droplets was well preserved for both samples of A-$Fe_2O_3$ and C-$Fe_2O_3$, representing the typical feature of materials synthesized by aerosol spray pyrolysis process. The $Fe_2O_3$ spherical particles for both samples are distributed in the diameter range of hundreds of nanometers. The enlarged SEM image in Figure 10.2c clearly reveals open and uniformly distributed nano-sized pores on the surface of the $Fe_2O_3$ spherical particles, implying a porous structure of spherical particles.

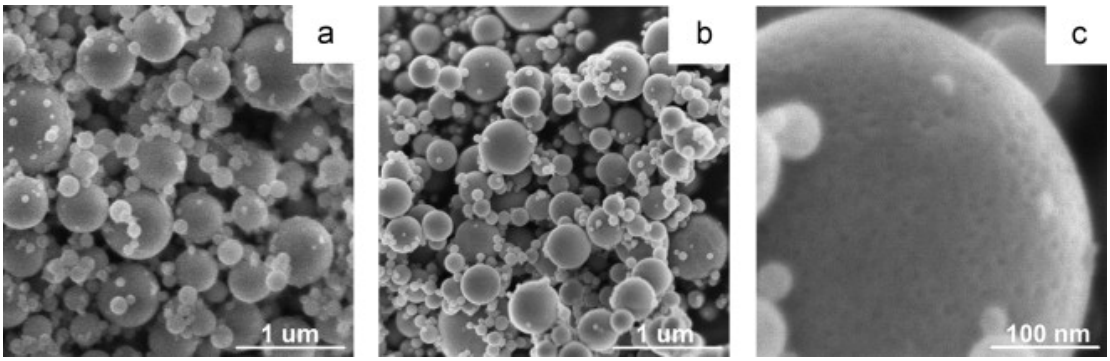


**Figure 10.2.** SEM images of (a) A-$Fe_2O_3$ and (b, c) C-$Fe_2O_3$.

The mesoporous nature within the $Fe_2O_3$ spheres is further evidenced by TEM images in Figure 10.3.

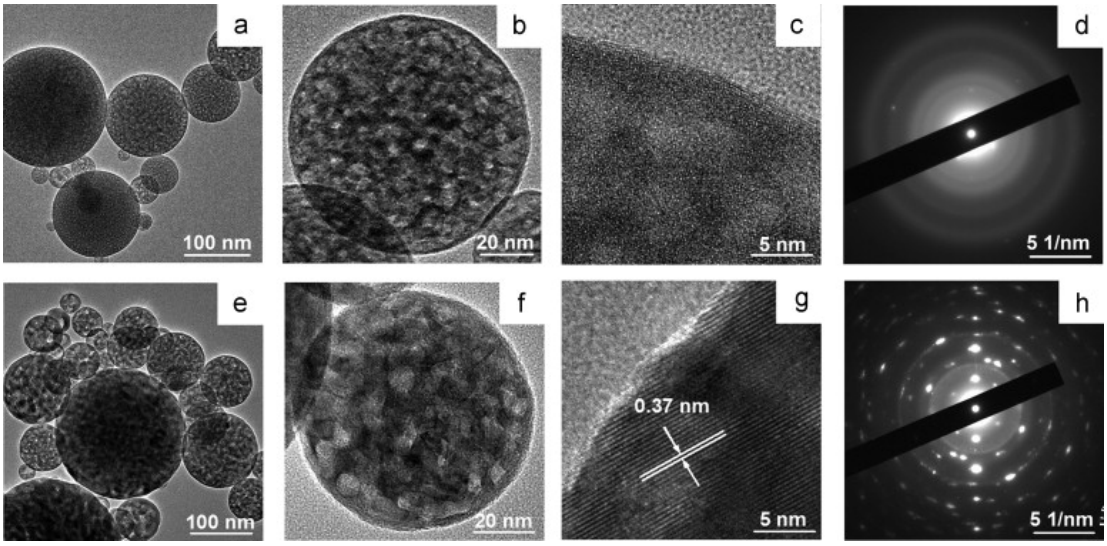


**Figure 10.3.** TEM images of (a-c) A-$Fe_2O_3$ and (e-g) C-$Fe_2O_3$. SAED images of (d) A-$Fe_2O_3$ and (h) C-$Fe_2O_3$.

For both samples of A-$Fe_2O_3$ and C-$Fe_2O_3$, the porous structure is clearly revealed with the contrast between $Fe_2O_3$ walls and mesopores in the TEM images (Figure 10.3). The lighter regions represent pores, while the darker represent $Fe_2O_3$ walls. Both the diameter of pores and the thickness of the $Fe_2O_3$ walls are around 10 nm. Clearly, C-$Fe_2O_3$ shows much stronger contrast and better-defined pore structure than A-$Fe_2O_3$. At higher temperature of 800 °C, much faster and complete decomposition of the precursors occurred, facilitating formation of crystal structure and well-defined pores (Figure 10.3f and 10.3g); while A-$Fe_2O_3$ particles show an amorphous structure (Figure 10.3c). This is further confirmed by the selected area electron diffraction (SAED) images (Figure 10.3d and 10.3h). C-$Fe_2O_3$ (Figure 10.3h) show bright diffraction rings, implying the crystalline structure. Figure 10.3g shows the high-

resolution TEM lattice image. The lattice spacing was measured to be 0.37 nm, which is in good agreement with the *d*-spacing of the (012) plane of crystalline $Fe_2O_3$. However, only broad diffraction rings are observed for A-$Fe_2O_3$ (Figure 10.3d), indicating an amorphous structure.

Both A-$Fe_2O_3$ and C-$Fe_2O_3$ mesoporous particles were characterized using X-ray diffraction (XRD), and the XRD patterns are shown in Figure 10.4. Fine diffraction peaks were displayed for C-$Fe_2O_3$, which can be indexed to the crystal structure of $Fe_2O_3$ (α phase, JCPDS card no.: 33-0664). No impurity peaks were detected, indicating that the thermal decomposition at the synthesis temperature (800 °C) is sufficient to form crystalline $Fe_2O_3$, even though the heating time is as short as a few seconds. In contrast, no obvious diffraction peaks are displayed for A-$Fe_2O_3$, which is in good agreement with the high-resolution TEM and SAED results (Figure 10.3c, d).

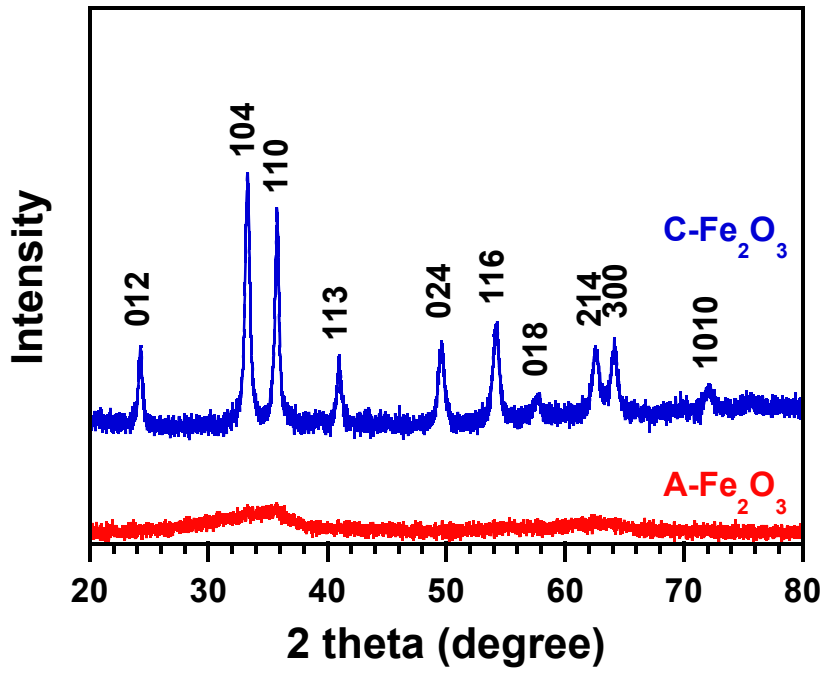


**Figure 10.4.** XRD patterns of the mesoporous $Fe_2O_3$ particles.

Figure 10.5 shows the nitrogen adsorption isotherm curves of mesoporous Fe2O3 spheres. BET specific surface area and pore volume are 23 $m^2$ $g^{-1}$ and 0.015 $cm^3$ $g^{-1}$ for A-$Fe_2O_3$, 58 $m^2$ $g^{-1}$ and 0.15 $cm^3$ $g^{-1}$ for C-$Fe_2O_3$, respectively. The surface areas of both A-$Fe_2O_3$ and C-$Fe_2O_3$ are much smaller than reported porous $Fe_2O_3$ anodes (103-207 $m^2$ $g^{-1}$ for mesoporous $Fe_2O_3$ cocoons and rods [34] and 765.0 $m^2$ $g^{-1}$ for porous $Fe_2O_3$ nanotubes [17]). BJH average open-pore diameter is 10 nm and 11 nm for A-$Fe_2O_3$ and C-$Fe_2O_3$, respectively, which are in consistence with the results by TEM images. The results suggest the closed-mesopore structure of the $Fe_2O_3$ spheres.

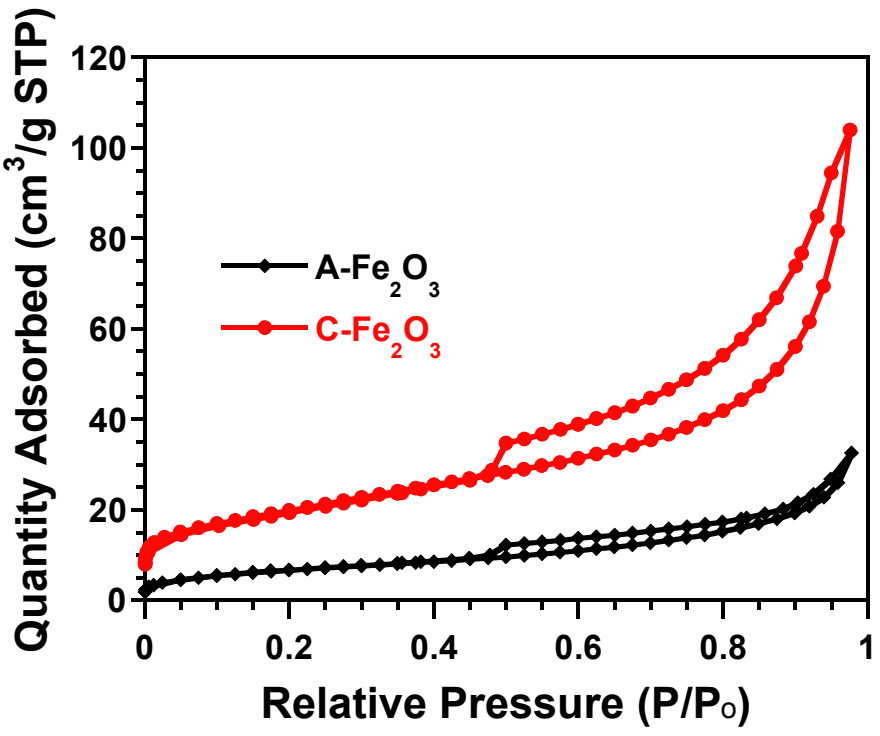


**Figure 10.5.** $N_2$ adsorption/desorption isotherm curves of mesoporous $Fe_2O_3$ spheres.

*10.3.2. Electrochemical Characterization and Performance.*

Electrochemical performance of both A-$Fe_2O_3$ and C-$Fe_2O_3$ electrodes was investigated in coin cells using lithium as the counter electrode, as shown in Figure 10.6. Figure 10.6a and 10.6b show the first two cyclic voltammogram (CV) scans of A-$Fe_2O_3$ and C-$Fe_2O_3$ at a scan rate of 0.1 mV/s between 0 V and 3.0 V.

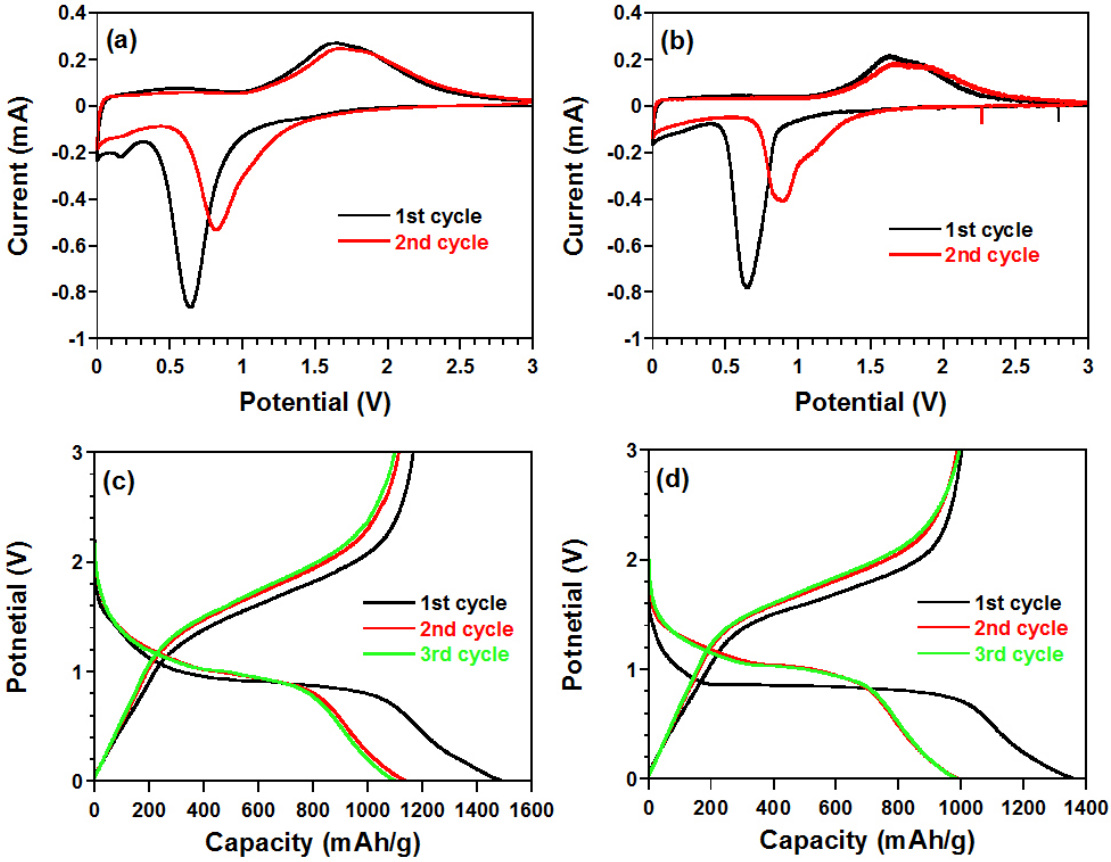


**Figure 10.6.** Cyclic voltammograms of (a) A-$Fe_2O_3$ and (b) C-$Fe_2O_3$ in the initial two cycles scanned between 0-3 V at a rate of 0.1 mV/s, and charge/discharge profiles of (c) A-$Fe_2O_3$ and (d) C-$Fe_2O_3$ at the initial three cycles at 100 mA $g^{-1}$ and 0-3 V.

The strong reduction peaks at 0.65 V for C-$Fe_2O_3$ and 0.7 V for A-$Fe_2O_3$ observed in the first cycle are attributed to the reduction of $Fe^{3+}$ to $Fe^0$. In the second cycle, both peaks shifted to higher voltage of 0.9 V for C-$Fe_2O_3$ and 0.8 V for A-$Fe_2O_3$ with

reduced peak current. The current peak shift to more positive potential in the second cycle is a common phenomenon for iron oxide anodes [15-35] and was attributed to the structure changes during the lithium insertion in the first cycle. The higher peak current in the first lithiation was partially attributed to the formation of solid-electrolyte interface (SEI) films. In the anodic process, similar oxidation curves and peak intensity were presented for A-$Fe_2O_3$ and C-$Fe_2O_3$ in the first cycle with two broad peaks centered at 1.65 V and 1.85 V, respectively. Both peaks are from the oxidation reaction of $Fe^0$ to $Fe^{3+}$. Meanwhile, no significant difference between the first and second anodic scans was observed for both A-$Fe_2O_3$ and C-$Fe_2O_3$ electrodes.

The difference between crystalline and amorphous $Fe_2O_3$ mesoporous spheres can also be observed in galvanic charge/discharge curves. Figure 10.6c and 10.6d illustrate the first three charge/discharge curves of A-$Fe_2O_3$ and C-$Fe_2O_3$ at 100 mA/g from 0 to 3.0 V. The crystalline $Fe_2O_3$ shows a long and flat plateau at 0.8 V in the first discharge (Figure 10.6d), and then shifted to 1.0 V and became a slop line in the subsequent discharges; while the discharge potential profile of amorphous $Fe_2O_3$ in the first discharge is less flat than that of crystalline $Fe_2O_3$ (a typical feature for amorphous electrode materials [48, 49]), and maintain its slope shape but slightly shifted to a higher potential in the following discharges. Similar to the CV curves, potential increase in the second cycles for crystalline $Fe_2O_3$ have been widely reported for iron oxide and other anode materials [7, 14, 50] and were attributed to the structure changes during the lithium insertion in the first cycle. In the first cycle, the volume change due to the conversion reaction produced defects though the mesoporous released some stress/strain and changed the $Fe_2O_3$ from crystalline or

amorphous network structure to nano-crystallite structure, which would facilitate the lithium ion insertion and lower the electrochemical polarization in the subsequent cycles. [7] The nano-crystallite structure after lithiation/delithation cycles was confirmed by the TEM and SAED images after 100 cycles (Figure 10.7).

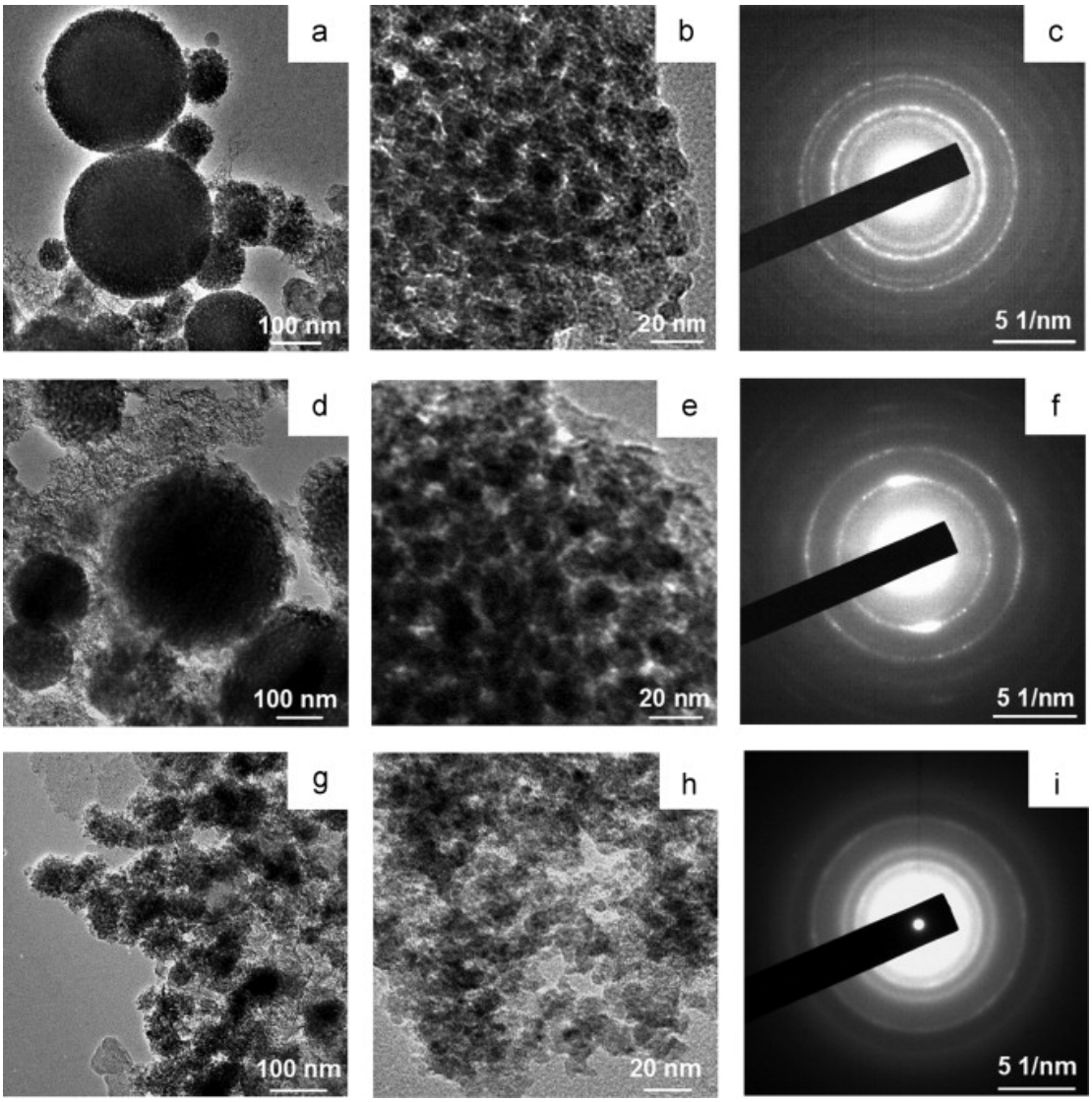


**Figure 10.7.** TEM images of (a, b) A-$Fe_2O_3$, (d, e) C-$Fe_2O_3$ and (g, h) commercial $Fe_2O_3$ nanoparticles, and SAED images of (c) A-$Fe_2O_3$, (f) C-$Fe_2O_3$ and (i) commercial $Fe_2O_3$ nanoparticle anodes taken after 100 cycles.

During delithiation, a plateau-like potential slope at 1.2-2.5 V was observed (Figure 10.6c and 10.6d), which accounts for the oxidation reaction of $Fe^0$-$Fe^{3+}$. There is no obvious difference in the charge processes for the first three cycles. The almost identical charge/discharge behavior from the second cycle demonstrates good reversibility and stability of the mesoporous $Fe_2O_3$ anodes.

The first discharge of C-$Fe_2O_3$ delivered a capacity of 1365 mAh $g^{-1}$, much higher than the theoretical value of 1006 mAh $g^{-1}$. The extra capacity is attributed to the decomposition reaction of the electrolyte. The reversible capacity of C-$Fe_2O_3$ in the first cycle is 1003 mAh $g^{-1}$, corresponding to 99.7 % of the theoretical capacity. The high reversible capacity identifies full utilization of the porous $Fe_2O_3$ through the whole spherical particles. No capacity fading occurred in the following cycles, revealing good stability. In contrast, A-$Fe_2O_3$ delivered higher charge and discharge capacities of 1167 mAh $g^{-1}$ and 1501 mAh $g^{-1}$, respectively. The higher capacity could be associated with the amorphous structure.

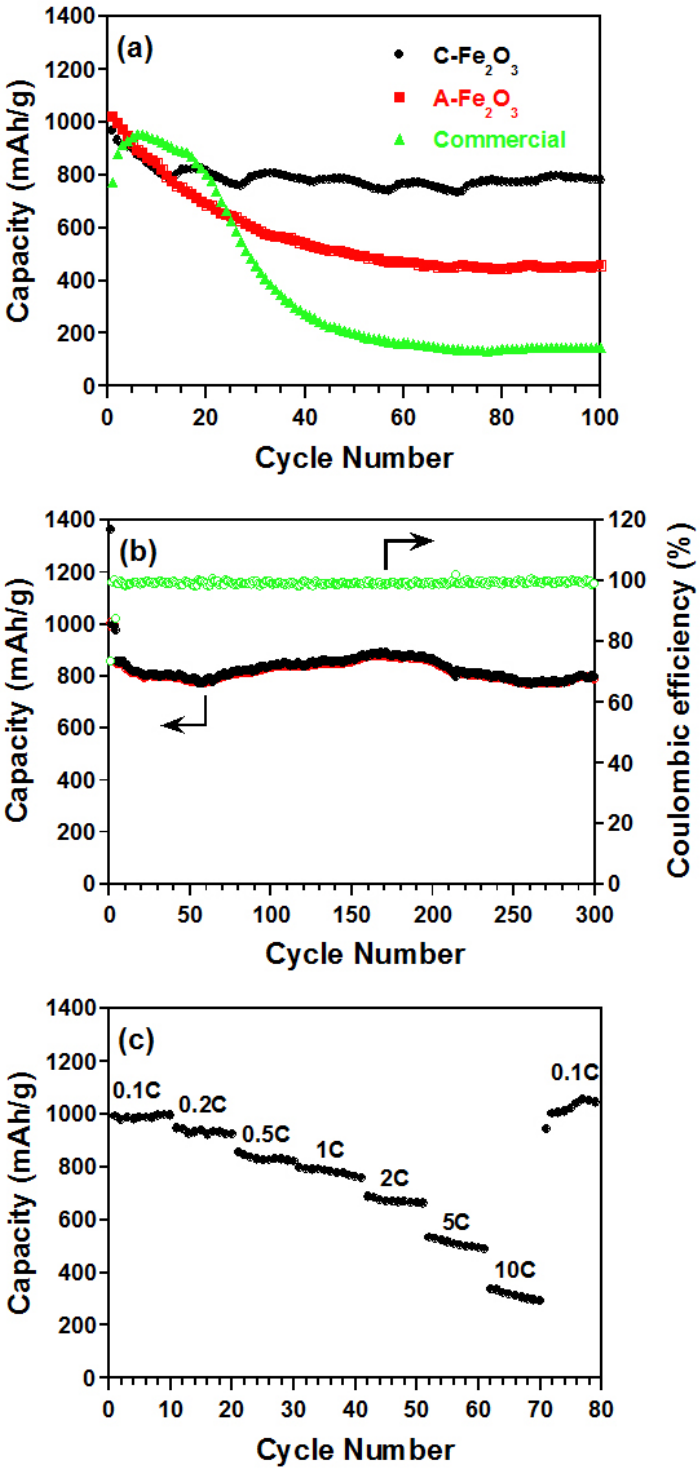


**Figure 10.8.** (a) Comparison of cycling performance of A-$Fe_2O_3$, C-$Fe_2O_3$ and commercial $Fe_2O_3$ nanoparticles. (b) Cycling performance of C-$Fe_2O_3$ at 500 mA $g^{-1}$ and 0-3 V after three cycles at 100 mA $g^{-1}$. (c) Rate capability of C-$Fe_2O_3$.

The cycling stability of both C-$Fe_2O_3$ and A-$Fe_2O_3$ electrodes were investigated by repeated charge/discharge processes between 0 and 3.0 V at a current density of 500 mA $g^{-1}$, as plotted in Figure 10.8a. Commercial $Fe_2O_3$ nanoparticles (<50 nm) were also examined at the same conditions for comparison. C-$Fe_2O_3$ provides a charge capacity of around 1000 mAh $g^{-1}$ in the first cycle follow by slight capacity decay for 15 cycles, and then remains stable at ~800 mAh $g^{-1}$ up to 100 cycles. However, the capacity of A-$Fe_2O_3$ continuously drops to and then stabilizes at ~450 mAh $g^{-1}$, which is only half of the capacity of C-$Fe_2O_3$. Although both C-$Fe_2O_3$ and A-$Fe_2O_3$ altered into the similar nano-crytallite structure after the first cycle, the large overpotential of amorphous A-$Fe_2O_3$ in the first lithiation (Appendix A: Figure 10.10c) implies that more severe structure deformation occurred during the first lithiation, which reduces the cycling stability. The commercial $Fe_2O_3$ nanoparticles provided similar capacity in the initial cycles, but subsequently showed a rapid decay to failure after ~50 cycles (Figure 10.8a). These results clearly demonstrate that the superior cycling performance of the mesoporous C-$Fe_2O_3$ synthesized using aerosol spray pyrolysis over the commercial nanoparticles.

The microstructure of the mesoporous $Fe_2O_3$ anodes and the commercial nanoparticles after 100 charge/discharge cycles between 0 and 3.0 V at 500 mA $g^{-1}$ current were investigated using TEM (Figure 10.7). Both A-$Fe_2O_3$ and C-$Fe_2O_3$ maintain the integrity of the spherical particles after 100 cycles. High resolution TEM images (Figure 10.7b and 10.7e) revealed that the porous structure also survived the lithium ion insertion/extraction reactions for both anodes. Compared to the porous structure with a wall-frame network of the unreacted $Fe_2O_3$ spherical

particles in Figure 10.3, the porous $Fe_2O_3$ spheres converted into more loosed porous structure, featuring by a cluster of small nanoparticles. The diameter of nanoparticles is still around 10 nm and the preservation of the spherical morphology, demonstrating that the mesoporous $Fe_2O_3$ spheres can effectively accommodate the volume change, and alleviate the strain during the electrochemical cycles. As shown in the SAED images (Figure 10.7c and 10.7f) of $Fe_2O_3$ particles after 100 cycles, crystal pattern can be observed for both A-$Fe_2O_3$ and C-$Fe_2O_3$ anodes. Different to the porous $Fe_2O_3$, the commercial nanoparticles suffered much more severe structure and morphology deformation during the charge/discharge cycles as evidenced by the TEM images in Figure 10.7g-h and Figure 10.S1 (as received commercial $Fe_2O_3$ nanoparticles)., As seen from TEM images, the spherical morphology was not kept after cycles, which is consistent with the worse cycling stability.

Due to the high cycling stability of C-$Fe_2O_3$, the extended cycling behavior of C-$Fe_2O_3$ was further evaluated at 500 mA $g^{-1}$ after three cycles at 100 mA $g^{-1}$ (Figure 10.8b). After 300 cycles, no capacity fading occurred with capacity retention of ~800 mAh $g^{-1}$. Such long-life cycling performance has barely been reported in literature. [15-34] The Coulombic efficiency is approaching 100 % over the 300 cycles. These definitely prove that the mesoporous $Fe_2O_3$ sphere electrode synthesized at 800 °C is a promising material for energy storage and rechargeable batteries.

The rate capability of the mesoporous C-$Fe_2O_3$ anodes was examined at different current densities. Excellent rate performance of the mesoporous C-$Fe_2O_3$ anodes was demonstrated in Figure 10.8c. A high capacity of 300 mAh $g^{-1}$ was retained at a 10 C

rate (C rate=1006 mA $g^{-1}$), which is comparable to graphite used in commercial lithium ion batteries. Even at a higher rate of 20 C, the capacity retention is still as high as 120 mAh $g^{-1}$, which is much better than those previously reported solid iron oxide nanoparticles. [18] Remarkably, the rate capability of the mesoporous C-$Fe_2O_3$ anodes is superior to that of those conductive additive-incorporated iron oxide anodes, such as amorphous carbon, graphene as well as carbon nanotubes. [31, 51-53] The excellent rate capability is believed to be associated with the mesoporous structure.

Clearly, the unique porous spherical structure of the mesoporous $Fe_2O_3$ anodes is responsible for the enhanced electrochemical performance. As is well known, the porous structure provides extra space to accommodate the large volume change during lithium ion insertion/extraction, which helps alleviate the absolute strain on the surface and avoid mechanical crack and maintains the integrity of the whole particle and good electric pass within the spherical particles, and thus improving the cycling stability and rate performance. In addition, the reduced dimension of $Fe_2O_3$ electrode (nano-sized walls) not only offers further assistance to reduce the strain led by lithiation/delithiation reaction, but also provides short transport distances for lithium ions and electrons, allowing fast kinetics. Along with the nano-sized dimension, this porous spherical structure enables an excellent rate capability. Finally, compared with amorphous structure, the crystal structure is another factor to provide a strong mechanical support. As a result, the mesoporous crystalline $Fe_2O_3$ spheres not only enable full utilization of $Fe_2O_3$ to store lithium ions, thus providing high capacity, but also improve the cycling stability and rate capability.

## *10.4. Conclusions*

Mesoporous $Fe_2O_3$ spherical particles were synthesized at different temperatures of 600 °C and 800 °C using aerosol spray pyrolysis as anode materials for lithium-ion batteries. A-$Fe_2O_3$ is amorphous, while C-$Fe_2O_3$ has a fine crystal structure. High capacity, good cycling stability as well as excellent rate capability were demonstrated for C-$Fe_2O_3$. The TEM results revealed that the electrochemical cycles converted the wall-frame porous structure into nano-crystallite structure for both crystalline and amorphous $Fe_2O_3$. The better stability of C-$Fe_2O_3$ suggests that mesoporous crystal structure is promising for high performance anode materials in LIBs.

## *10.5. Appendix A: The Influence of Structure Change on Electrochemical Performance.*[a]

The CVs in Figure 10.6 and images in Figure 10.7 show that the structure change from crystal or amorphous to nano-crystallite in the first charge/discharge cycle influences the electrochemical behavior (equilibrium potential and overpotential) in the following cycles. To understand how the structure change influences the thermodynamic equilibrium potential and kinetic overpotential of the mesoporous $Fe_2O_3$ electrodes, GITT technique was used to investigate the equilibrium potential and overpotential of the $Fe_2O_3$ anodes in the first two charge/discharge cycles. The GITT curves are shown in Figure 10.9. Since the capacity of A-$Fe_2O_3$ is larger than C-$Fe_2O_3$ (Figure 10.6c and 10.6d), the capacities were normalized to the state of discharge (SOD) to obtain the intrinsic electrochemical property.

[a] The analysis in this part (Section 10.5) was mainly contributed by Dr. Yunhua Xu and Prof. Chunsheng Wang at the Department of Chemical and Biochemical Engineering.

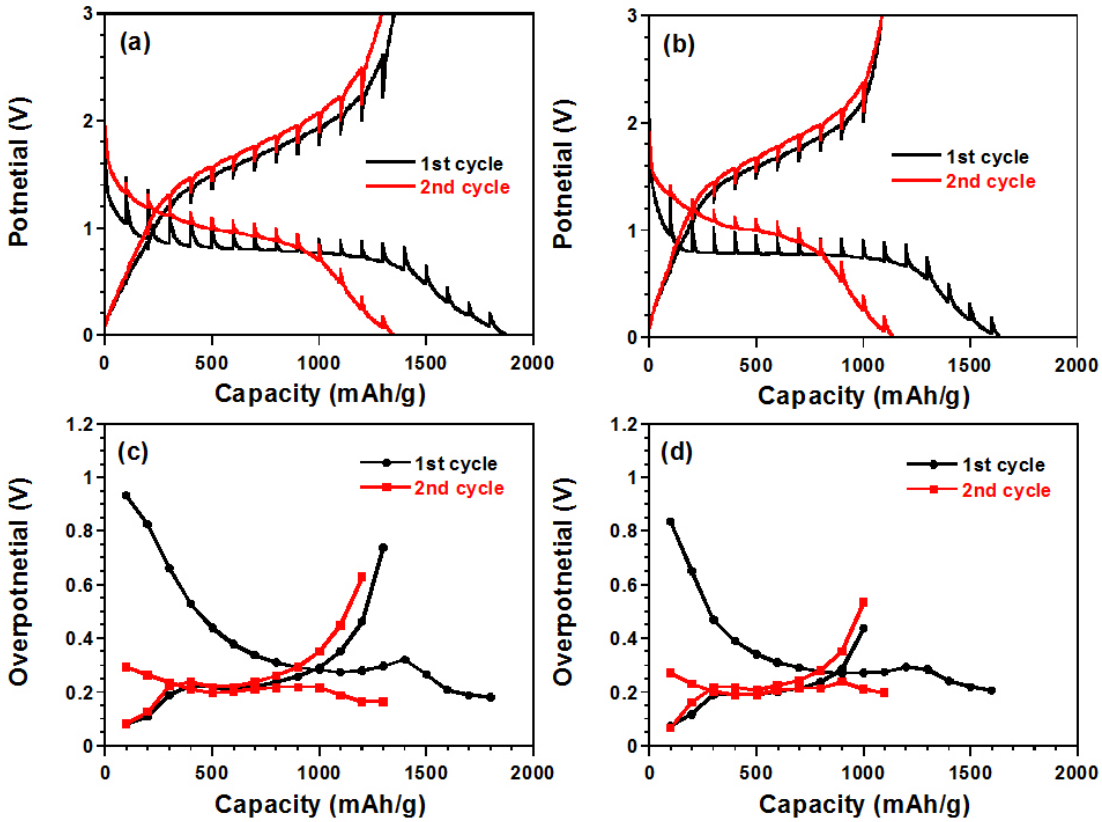


**Figure 10.9.** Potential response of the mesoporous (a) A-$Fe_2O_3$ and (b) C-$Fe_2O_3$ anodes in the first and second cycles during GITT measurement. Overpotential of (c) A-$Fe_2O_3$ and (d) C-$Fe_2O_3$ in the first two cycles.

Figure 10.10 compares the equilibrium potentials and overpotentials of C-$Fe_2O_3$ and A-$Fe_2O_3$ in the initial two cycles. In the first cycle (Figure 10.10a), the initial discharge equilibrium potential of the crystalline $Fe_2O_3$ is slightly lower than that of amorphous $Fe_2O_3$ but reaches similar value after 50 % of discharge. Charge equilibrium potentials of the two $Fe_2O_3$ electrodes appear similar, implying that the structure change occurred in the early stage of the first discharge. In the second cycle, both C-$Fe_2O_3$ and A-$Fe_2O_3$ show the same charge/discharge equilibrium potential

because both crystalline and amorphous $Fe_2O_3$ were altered into nano-crystallite structure in the first cycle.

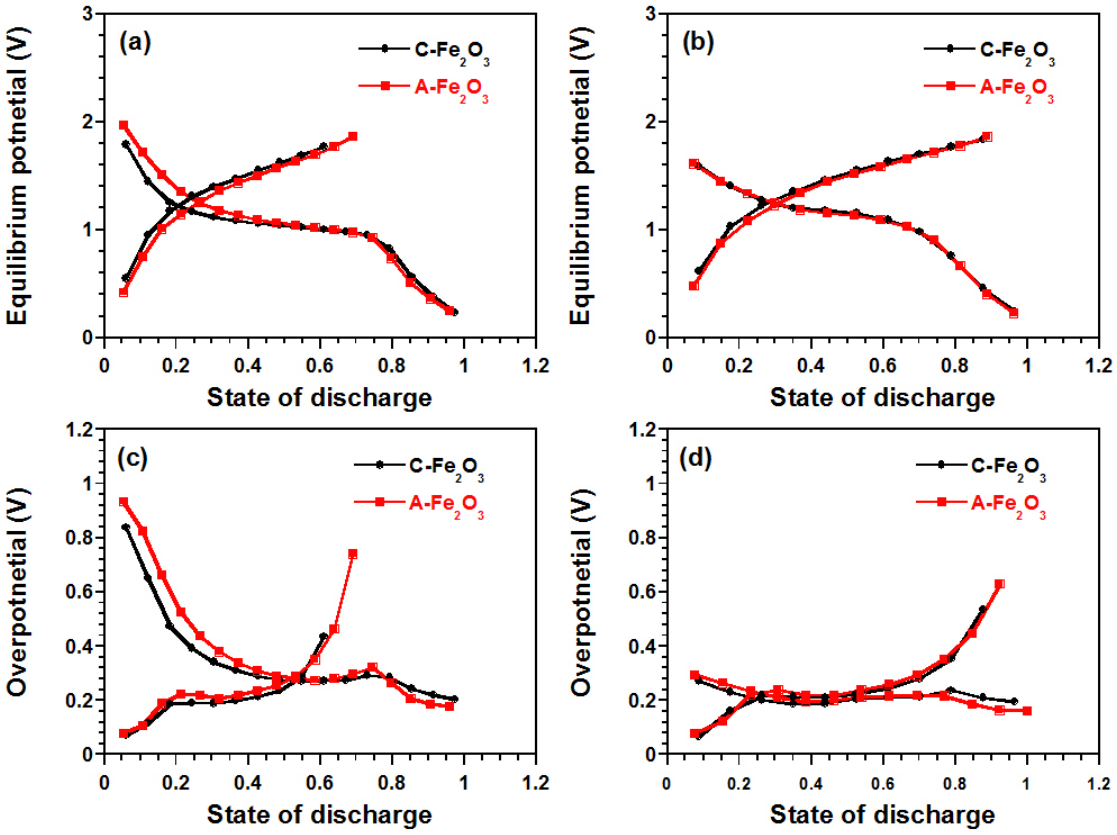


**Figure10.10.** Equilibrium charge/discharge profiles of the mesoporous $Fe_2O_3$ anodes in the (a) first and (b) second cycles. Overpotential of the mesoporous $Fe_2O_3$ in the (c) first and (d) second cycles.

The overpotentials of both C-$Fe_2O_3$ and A-$Fe_2O_3$ decrease with SOD but the amorphous $Fe_2O_3$ shows a slightly larger value than that of the crystalline $Fe_2O_3$ at the beginning of the first discharge, indicating that the structure change from amorphous to nano-crystallite is more difficulty than from crystalline to nano-crystallite. The discharge overpotentials for the two $Fe_2O_3$ electrodes in the second charge/discharge cycles are similar and much lower than those in the first cycle.

Therefore the formation of nano-crystallite structure enhanced the lithiation /delithiation kinetics of $Fe_2O_3$ electrodes.

## *10.6. Appendix B: Supplemental Information*

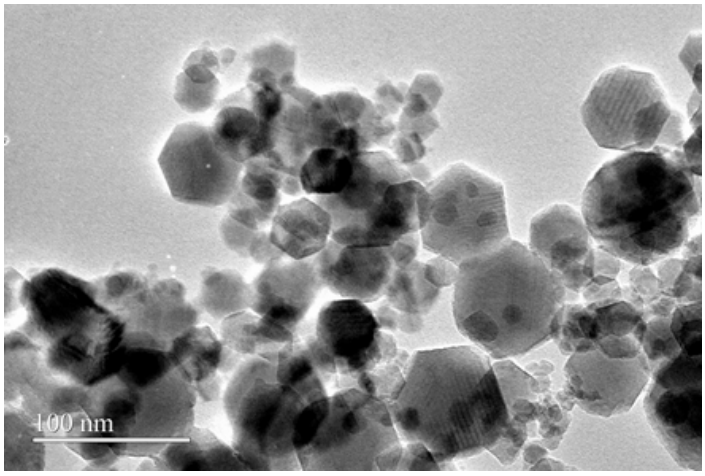


**Figure 10.S1** TEM image of the commercial $Fe_2O_3$ nanoparticles.

## *10.7. References*

[1] Kasavajjula, U.; Wang, C. S.; Appleby, A. J. *J. Power Sources* **2007**, *163*, 1003-1039.

[2] Dunn, B.; Kamath, H.; Tarascon, J.-M. *Science* **2011**, *334*, 928-935.

[3] Yang, Z.; Zhang, J.; Kintner-Meyer, M. C. W.; Lu, X.; Choi, D.; Lemmon, J. P.; Liu, J. *Chem. Rev.* **2011**, *111*, 3577-3613.

[4] Dahn, J. R.; Zheng, T.; Liu, Y.; Xue, J. S. *Science* **1995**, *270*, 590-593.

[5] Dresselhaus, M. S.; Dresselhaus, G. *Adv. Phys.* **1981**, *30*, 139-326.

[6] Cabana, J.; Monconduit, L.; Larcher, D.; Palacín M. R. *Adv. Mater.* **2010**, *22*, E170-E192.

[7] Poizot, P.; Laruelle, S.; Grugeon, S.; Dupont, L.; Tarascon, J.-M. *Nature* **2000**, *407*, 496-499.

[8] Lou X. W.; Archer, L. A.; Yang Z. *Adv. Mater.* **2008**, *20*, 3987-4019.

[9] Aricò, A. S.; Bruce, P.; Scrosati, B.; Tarascon, J.-M.; Schalkwijk, W. V. *Nat. Mater.* **2005**, *4*, 366-377.

[10] Guo, Y.-G.; Hu, J.-S.; Wan, L.-J. *Adv. Mater.* **2008**, *20*, 2878-2887.

[11] Bruce, P.; Scrosati, B.; Tarascon, J.-M. *Angew. Chem. Int. Ed.* **2008**, *47*, 2930-2946.

[12] Song, M.-K.; Park, S.; Alamgir, F. M.; Cho, J.; Liu, M. *Mater. Sci. Eng. R* **2011**, *72*, 203-252.

[13] Larcher, D.; Masquelier, C.; Bonnin, D.; Chabre, Y.; Masson, V.; Leriche, J.-B.; Tarascon, J.-M. *J. Electrochem. Soc.* **2003**, *150*, A133-A139.

[14] Larcher, D.; Bonnin, D.; Cortes, R.; Rivals, I.; Personnaz, L.; Tarascon, J.-M. *J. Electrochem. Soc.* **2003**, *150*, A1643-A1650.

[15] Chen, J.; Xu, L.; Li, W.; Gou, X. *Adv. Mater.* **2005**, *17*, 582-586.

[16] Wang, Z.; Luan, D.; Madhavi, S.; Li, C. M.; Lou, X. W. *Chem. Commun.* **2011**, *47*, 8061-8063.

[17] Kang, N.; Park, J. H.; Choi, J.; Jin, J.; Chun, J.; Jung, I. G.; Jeong, J.; Park, J.-G.; Lee, S. M.; Kim, H. J.; Son, S. U. *Angew. Chem. Int. Ed.* **2012**, *51*, 6626-6630.

[18] Lin, Y.-M.; Abel. P. R.; Heller, A.; Mullins, C. B. *J. Phys. Chem. Lett.* **2011**, *2*, 2885-2891.

[19] Tartaj, P.; Amarilla, J. M. *J. Power Sources* **2011**, *196*, 2164-2170.

[20] Ortiz, G. F.; Hanzu, I.; Lavela, P.; Tirado, J. L.; Knauth, P.; Djenizian, T. *J. Mater. Chem.* **2010**, *20*, 4041-4046.

[21] Chaudhari, S.; Srinivasan, M. *J. Mater. Chem.* **2012**, *22*, 23049-23056.

[22] Kim, H. S.; Piao, Y.; Kang, S. H.; Hyeon, T.; Sung, Y. E. *Electrochem. Commun.* **2010**, *12*, 382-385.

[23] Zhou, J. S.; Song, H. H.; Chen, X. H.; Zhi, L. J.; Yang, S. Y.; Huo, J. P.; Yang, W. T. *Chem. Mater.* **2009**, *21*, 2935-2940.

[24] Zhong, J.; Cao, C.; Liu, Y.; Li, Y.; Khan, W. S. *Chem. Commun.* **2010**, *46*, 3869-3871.

[25] Chou, S.-L.; Wang, J.-Z.; Chen, Z.-X.; Liu, H.-K.; Dou, S.-X. *Nanotechnology* **2011**, *22*, 265401-1-5.

[26] Wang, B.; Chen, J. S.; Wu, H. B.; Wang, Z.; Lou, X. W. *J. Am. Chem. Soc.* **2011**, *133*, 17146-17148.

[27] Chen, J. S.; Zhu, T.; Yang, X. H.; Yang, H. G.; Lou, X. W. *J. Am. Chem. Soc.* **2010**, *132*, 13162-13164.

[28] Zhang, L.; Wu, H. B.; Madhavi, S.; Hng, H. H.; Lou, X. W. J *J. Am. Chem. Soc.* **2012**, *134*, 17388-17391.

[29] Koo, B.; Xiong, H.; Slater, M. D.; Prakapenka, V. B.; Podsiadlo, M. P.; Johnson, C. S.; Rajh, T.; Shevchenko, E. V. *Nano Lett.* **2012**, *12*, 2429-2435.

[30] Xu, X.; Cao, R.; Jeong, S.; Cho, J. *Nano Lett.* **2012**, *12*, 4988-4991.

[31] Ma, Y.; Ji, G.; Lee, J. Y. *J. Mater. Chem.* **2011**, *21*, 13009-13014.

[32] Han, Y.; Wang, Y.; Li, L.; Wang, Y.; Jiao, L.; Yuan, H.; Liu, S. *Electrochim. Acta* **2011**, *56*, 3175-3181.

[33] Zhang, J.; Sun, Y.; Yao, Y.; Huang, T.; Yu, A. *J. Power Source* **2013**, *222*, 59-65.

[34] Ang W. A.; Gupta N.; Prasanth, R.; Madhavi, S. *ACS Appl. Mater. Interfaces* **2012**, *4*, 7011-7019.

[35] Jia, X.; Chen, J.-J.; Xu, J.-H.; Shi, Y.-N.; Fan, Y.-Z.; Zheng, M.-S.; Dong, Q.-F. *Chem. Commun.* **2012**, *48*, 7410-7412.

[36] Ren, Y.; Armstrong, A. R.; Jiao, F.; Bruce, P. G. *J. Am. Chem. Soc.* **2010**, *132*, 996-1004.

[37] Jiao, F.; Bao, J.; Bruce, P. G. *Electrochem. Solid-State Lett.* **2007**, *10*, A264-A266.

[38] Ren, Y.; Ma, Z.; Bruce, P. G. *Chem. Soc. Rev.* **2012**, *41*, 4909-4927.

[39] Guo, J. C.; Liu, Q.; Wang, C.S.; Zachariah, M.R. *Adv. Funct. Mater.* **2012**, *22*, 803-811.

[40] Luo, J.-Y.; Zhang, J.-J.; Xia, Y.-Y. *Chem. Mater.* **2006**, *18*, 5618-5623.

[41]Shaju, K. M.; Jiao, F.; Débart, A.; Bruce, P. G. *Phys. Chem. Chem. Phys.* **2007**, *9*, 1837-1842.

[42] Li, Y.; Tan, B.; Wu, Y. *Nano Lett.* **2008**, *8*, 265-270.

[43] Dupont, L.; Laruelle, S.; Grugeon, S.; Dickinson, C.; Zhou, W.; Tarascon, J.-M. *J. Power Sources* **2008**, *175*, 502-509.

[44] Xu, Y. H.; Liu, Q.; Zhu, Y. J.; Liu, Y. H.; Langrock, A.; Zachariah, M. R.; Wang, C. S. *Nano Lett.* **2013**, *13*, 470-474.

[45] Langrock, A.; Xu, Y. H.; Liu, Y. H.; Manivannan, A.; Wang, C. S. *J. Power Sources* **2013**, *223*, 62-67.

[46] Prakash, A.; McCormick, A. V.; Zachariah, M. R. *Chem. Mater.* **2004**, *16*, 1466-1471.

[47] Jian, G. Q.; Liu, L.; Zachariah, M. R. *Adv. Funct. Mater.* **2013**, *23*, 1341-1346.

[48] Yin, Y.; Hu, Y.; Wu, P.; Zhang, H.; Cai, C. *Chem. Commun.* **2012**, *48*, 2137-2139.

[49] Liu, Y.-L.; Xu, Y. H.; Han, X. G.; Pellegrinelli, C.; Zhu, Y. J.; Zhu, H. L.; Wan, J. Y.; Chung, A. C.; Vaaland, O.; Wang, C. S.; Hu, L. B. *Nano Lett.* **2012***, 12,* 5664-5668.

[50] Chan, C.; Peng, H.; Liu, G.; McIlwrath, K.; Zhang, X. F.; Huggins, R. A.; Cui, Y. *Nat. Nanotechnol.* **2008**, *3*, 31-35.

[51] Chou, S.-L.; Wang, J.-Z.; Wexler, D.; Konstantinov, K.; Zhong, C.; Liu, H.-K.; Dou, S.-X. *J. Mater. Chem.* **2010**, *20*, 2092-2098.

[52] Zhu, X.; Zhu, Y.; Murali, S.; Stoller, M. D.; Ruoff, R. S. *ACS Nano* **2011**, *4*, 3333-3338.

[53] Yu, W.-J.; Hou, P.-X.; Li, F.; Liu, C. *J. Mater. Chem.* **2012**, *22*, 13756-13763.

# Chapter 11: Summary

## *11.1. Conclusions*

The objective of this dissertation study was to enhance our understanding and tuning of nanostructured materials that might find application toward energetic materials and electrode materials in lithium ion batteries. This dissertation work investigates the chemical energy conversion systems involving energetic materials and lithium ion batteries from both a mechanistic and application standpoint. The conclusions are made in two separate parts regarding the two different energy conversion systems.

***Part I.*** *Chapter 2-8: Nanocomposite energetic materials*

As discussed in Chapter 1, nanocomposite energetic materials (e.g., nanothermites) have several advantages over their micro counterparts and traditional organic energetic materials. However, their applications in the fields of propellant, explosives and fast power sources are partially limited by the lack of understanding about the fast and intense reaction processes.

In chapter 2, I gave an overview of the development and key features of a series of ultra-high heating rate diagnostic tools used in our group. In particular, temperature-jump/time-of-flight mass spectrometry, one of the main techniques used in this dissertation, was presented as a tutorial. The progress made by using these techniques to understand the role of gas phase oxygen generation from the oxygen carrier in the ignition event was reviewed.

In chapter 3 and 4, a temperature-jump/time-of-flight mass spectrometer was used to study the ignition of aluminum nanoparticles, nanothermite reaction mechanism, and metal oxides nanoparticles decomposition under rapid heating conditions.

In chapter 3, T-Jump/TOFMS was used to investigate Al-NPs and nano-Al/CuO thermite reactions at high heating rates ~$10^5$-$10^6$ K/s. Time-resolved mass spectra were obtained for rapid heating of Al-NPs and fuel rich nano-Al/CuO thermite mixtures in which for the first time, four Al-containing intermediate species have been observed (Al, $Al_2O$, AlO, $Al_2O_2$). Time-resolved mass spectra of rapidly heated Al-NPs support the hypothesis that Al containing species diffuse outwards through the oxide shell under high heating rate conditions.

In chapter 4, T-Jump/TOFMS was employed to study the kinetics of decomposition for three metal oxide nanoparticles (CuO, $Fe_2O_3$ and $Co_3O_4$) at high heating rates of ~$10^5$K/s. The isoconversion effective activation energies were calculated based on the time-resolved mass spectra information and temperature profiles, and are found to be significantly lower than activation energies at slow heating rates. The lower activation energies obtained in this study imply that even for nanoparticles, which have small diffusional length scales, high heating rates can result in a situation where mass transfer constraints are observed. This should have implication on how systems that employ metal oxides as oxygen carriers are selected.

Chapter 5-8 presented the efforts to make new nanoenergetic composite materials using different methods, including aerosol spray pyrolysis/drying, milling and electrospinning. Rapid heating diagnostic tools including T-jump/TOFMS, high speed

imaging and/or using a high heating rate SEM holder were employed to study the ignition and reaction mechanisms.

Chapter 5 reported on the development of an Al/CuO nanocomposite which showed better performance than previous composites adopted with nanoparticles. The hollow CuO spheres with thin shell thickness employed in the nanocomposite were prepared by a simple aerosol spray pyrolysis method with the introduction of gas-blowing agents in the synthesis procedure. In Chapter 6, periodate salt nanoparticles were prepared through an aerosol spray drying process, which demonstrated highly reactive properties when formulated into an aluminum based nanoenergetic. Several in-situ techniques at high heating rates suggested that exothermic decomposition of periodate salts contributes to the low ignition temperature of its nanoenergetic formulations. Direct evidence support that direct gas phase oxygen release from oxidizer decomposition is critical in the ignition and combustion of periodate nanoenergetic formulations.

In Chapter 7, the ignition and combustion behavior of nano-Al/micro-$I_2O_5$ thermite was systematically studied. The study of Al/$I_2O_5$ thermites shows that these $I_2O_5$ containing thermite reactions are very reactive and are suggested to effectively produce iodine gas, which can be used in microbial agent defense applications.

In Chapter 8, energetic composite nanofibrous mats with different mass loading and equivalence ratio were successfully prepared and evaluated for their combustion performances. Energetic composite nanofibrous mats showed the enhanced burning rates when compared to the pure nitrocellulose and nanoaluminum incorporated nanofibrous mats. The combustion propagation velocities of nanofibrous mats were

found to correlate to the mass loading of energetic composite nanoparticles to binder in nanofibers. The results show that with the composite energetic nanoparticles being electrospun in the nitrocellulose polymer matrix, the total energy release as well as combustion propagation velocity can be dramatically increased, suggesting its potential application in solid rocket propellant systems.

***Part II.*** *Chapter 9-10: Anodes materials for LIBs*

In Chapter 9, the aerosol based strategy used to make hollow CuO (Chapter 5) was extended to fabricate $Mn_3O_4$ hollow spheres and carbon coated CuO hollow spheres. Both $Mn_3O_4$ hollow spheres and carbon coated CuO hollow spheres demonstrated exceptional electrochemical performance, high capacity, excellent rate capability and long-term cycling stability.

In Chapter 10, mesoporous $Fe_2O_3$ spherical particles were synthesized using aerosol spray pyrolysis as anode materials for lithium-ion batteries. High capacity, good cycling stability, as well as excellent rate capability were demonstrated for crystalline-$Fe_2O_3$. The TEM results revealed that the electrochemical cycles converted the wall-frame porous structure into a nano-crystallite structure for both crystalline and amorphous $Fe_2O_3$. The better stability of crystalline-$Fe_2O_3$ suggests that mesoporous crystal structure is promising for high performance anode materials in LIBs.

## *11.2. Recommendations for Future Work*

### *11.2.1. Further Developments of Ultra-high Heating Rate Diagnostic Tools.*

*a. Calorimetry measurements during rapid heating in T-Jump/TOFMS.*

While I was able to measure the Pt wire temperature, calorimetry measurement of ignition events and a thermite reaction remains a challenge. I attempted to study the thermal effects during rapid heating using current T-Jump system. Some of my preliminary results (not included in previous chapters) are listed as below:

(1). Using the same Pt wire, a temperature difference can be observed before and after coating of nanothermite sample, as shown in Figure 11.1. A temperature jump was found at ~1000 K for the wire coated with Al/CuO nanothermite.

The temperature jump was confirmed to happen at the ignition temperature by simultaneous high speed imaging.

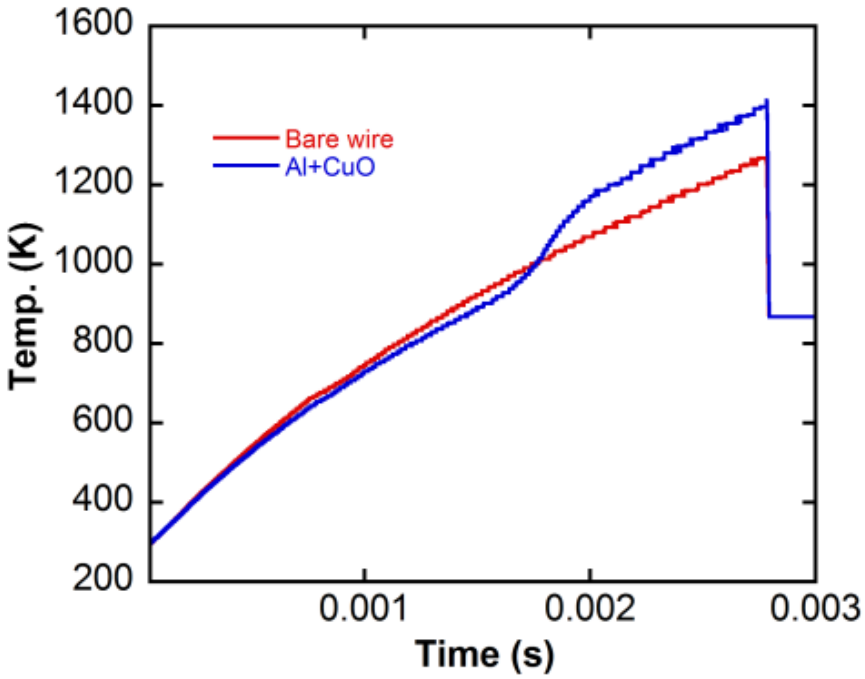


**Figure 11.1.** The temperatures of the Pt wire with/without coating of Al/CuO nanothermite during rapid heating. (Heating rate: ~$5\times10^5$ K/s)

(2). Figure 11.2 shows that the wire with more thermite sample loading has a larger power difference, indicating a higher energy release.

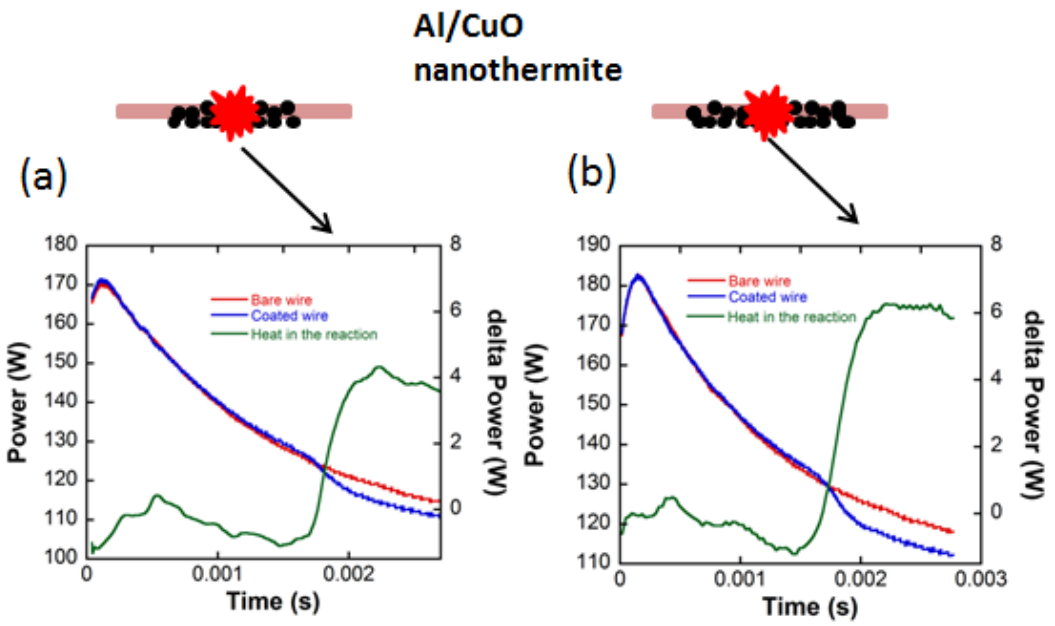


**Figure 11.2.** Power differences between the Pt wire with and without thermite coating during rapid heating. Note: (a) and Figure 11.1 are from the same experiment. The amount of materials on the wire: $m_b/m_a$~1.5.

However, the current T-Jump wire system cannot provide a quantitative calorimetry measurement for nanothermite reactions. There are several issues, even for a qualitative comparison of two reaction systems, such as:

(1) A thick coating of sample is needed; (2) Nanothermite reaction is very violent, and sample will leave the wire upon ignition (see Figure 2.3b in Chapter 2); (3) In principle, it cannot compare the heat release from two systems in which one release few gas and the other not; (4) No viable way to estimate the percent of heat left the system etc.

Recent development of chip-based nanocalorimeters could potentially be able to realize a quantitative calorimetry measurement of nanothermite reactions at high heating rates. Nanocalorimetry methods only need a very small mass of sample (μg to

*n*g) and have the capability of rapidly heating a sample to a high temperature. [1] Combined with T-Jump/TOFMS, it is expected that species, temperature, calorimetry and optical emission can be measured simultaneously. In fact, we have recently initiated the collaboration with Dr. LaVan on this project; some promising results have been obtained.

*b. Improvement of T-Jump/TOFMS.*

The T-Jump/TOFMS technique is still in a stage of continuous development. Several future technical improvements could include:

(1) increase sampling rate, which can be achieved by updating the data acquisition approach; it is more desirable to be able to get time resolved mass spectra in every 20 μs; (2) enable the capability of laser heating, such as $CO_2$ laser. One benefit of using laser heating is that some samples are very difficult to coat onto the wire; (3) add a skimmer between sample probe and ionization chamber; (Figure 11.3) it is expected that the design of skimmer will reduce the effect of the flux of intensely charged species and system contamination; (4) introduce gas inlet into the sample loading chamber, this upgrade can allow the study of gas-solid reactions at high heating rates. A pulse valve series 9 from Parker Precision Fluid, which can operate as fast as 160 μs, can be used to produce gas pulses. The pulse generator of the T-Jump/TOFMS system can trigger both the pulsed valve and the heating pulse among other accessories. With a skimmer between the two chambers and employment of the pulse valve, the local pressure of the ionization region and mass spectrometer signal are expected to be relatively stable and not affected by the gas pulse.

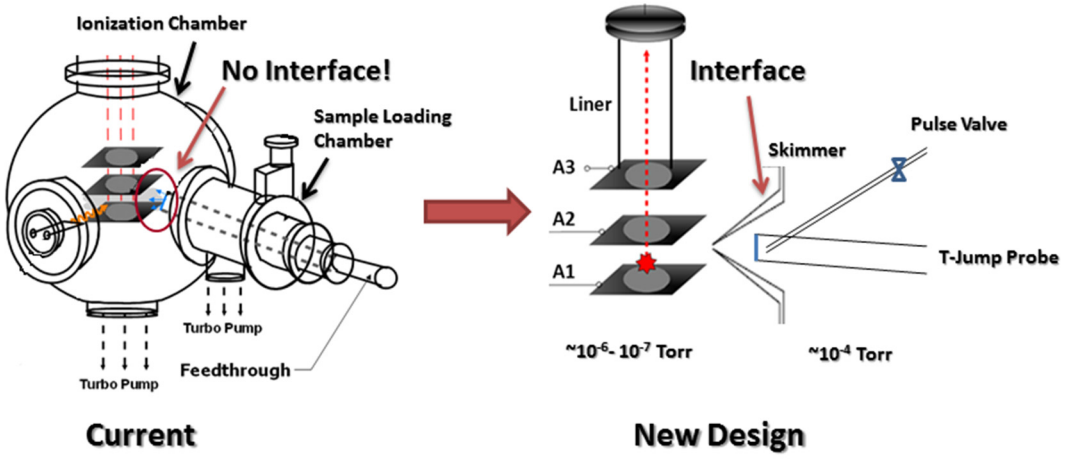


**Figure 11.3.** One upgrade choice for the T-Jump/TOFMS system.

Continuous efforts should also be put into the combination of other diagnostic tools with T-Jump/TOFMS. In view of the convenience of combining T-Jump/TOFMS with other diagnostic tools, more applications in a wide range of condensed phase materials are expected in the near future.

*11.2.2. Ignition and Reaction Mechanism of Al/$Co_3O_4$ Nanothermite.*

In Chapter 2, I summarized the progress made by using T-Jump based techniques to understand the role of gas phase oxygen generation from the oxygen carrier in the ignition event. Based on the results shown in Figure 11.4, we conclude that the initiation of nanothermite (ignition) before oxygen release or without oxygen release is likely a result of direct interfacial contact between fuel and oxidizer, leading to condensed state mobility of reactive species. However, there is one particular system which deserves our attention, that is, Al-$Co_3O_4$. In this system, Al-$Co_3O_4$ nanothermite has an ignition temperature which is higher than the temperature of

oxygen release from $Co_3O_4$. More experiments are needed to further understand this system, such as combustion cell and rapid heating electron microscopy experiments.

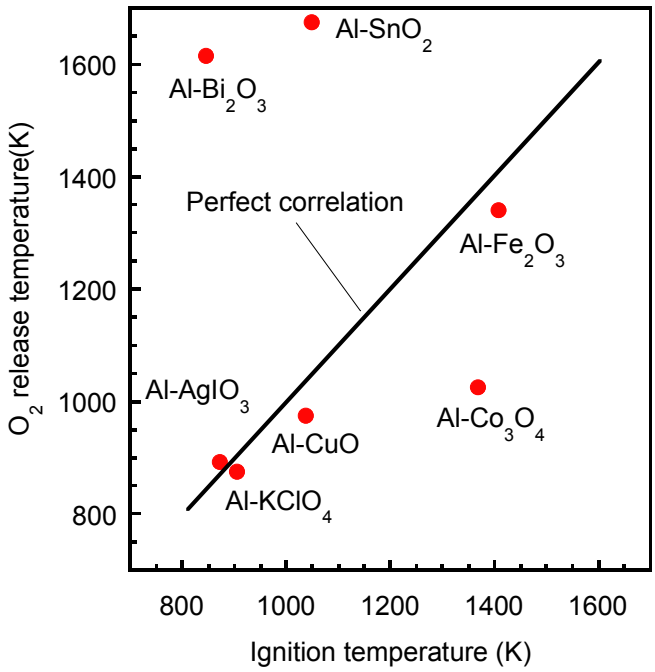


**Figure 11.4.** Oxygen release temperature from bare oxidizers vs. ignition temperature for various Al based nanothermites. [2]

*11.2.3. Other recommendations*

*a. Reactivity Tuning and Development of New Nanocomposite Energetic Materials.*

Our recent efforts in the application of T-Jump/TOFMS and other ultra-high heating rate diagnostic tools in aluminum nanothermite research greatly improve our understanding of decomposition, ignition and combustion of nanoaluminum based thermite reactions at high heating rates. Application of this technique in other metal/oxidizer systems is expected. Some nanoenergetic materials systems involving the use of Si, Ta nanoparticles etc., can be studied using rapid heating diagnostic tools.

There are also a variety of choices for oxidizers, such as salt based nanoparticles. Interesting systems include Si/$KIO_4$, Ta/CuO etc.

*b. Synthesis of Cathode Materials by Aerosol Spray Pyrolysis.*

In my dissertation, I focused on the synthesis of anode materials using aerosol spray pyrolysis. Aerosol spray pyrolysis is a "droplet-to-particle" process. Multicomponent particles can be easily formed by only controlling the starting precursor solution. I expect that by using a similar approach to what is presented in my dissertation, hollow and mesoporous multiple transition metal oxide spheres with controllable composition could be synthesized by an aerosol spray pyrolysis method. The materials of interests include multiple transition metal oxides which can be used as cathode materials in rechargeable batteries, such as $LiMn_{1.5}Ni_{0.5}O_4$ [3] and $Na_x[Fe_{0.5}Mn_{0.5}]O_2$ [4], nanostructured materials of these complex metal oxides are relatively difficult to synthesize by wet chemistry methods.

## *11.3. References*


[1] Yi, F.; LaVan, D.A. *Thermochim. Acta* **2013**, *569*, 1-7.

[2] Jian, G.Q.; Chowdhury, S.; Sullivan, K.; Zachariah, M.R. *Combust*. *Flame* **2013**, *160*, 432-437.

[3] Yabuuchi, N.; Kajiyama, M; Iwatate, J; Nishikawa, H; Hitomi, S; Okuyama, R.; Usui, R.; Yamada, Y.; Komaba, S. *Nature Mater.* **2012**, *11*, 512-517.

[4] Xu, J.T.; Dou, S.X.; Liu, H.K.; Dai, L.M. *Nano Energy* **2013**, *2*, 439-442.

# List of References

Format: [A-B]. A=Chapter number, and B=Reference number in each chapter.


[1-1] Wink, D. J. *J. Chem. Educ.* **1992**, 69, 108-111.

[1-2] Akhavan, J. *The Chemistry of Explosives*. 2nd ed: The Royal Society of Chemistry, **2004**.

[1-3] Dreizin, E.L. *Prog. Energy Combust. Sci.* **2009**, *35*, 141-167.

[1-4] Fischer, S.H.; Grubelich, M.C. In:*32nd AIAA/ASME/SAE/ASEE Joint Propulsion Conference*. Lake Buena Vista, FL; **1996**.

[1-5] Aumann, C. E.; Skofronick, G. L.; Martin, J. A. *J. Vac. Sci. Technol. B, Microelectron. Process. Phenom.* **1995**, *13*, 1178-1183.

[1-6] Rossi, C.; Zhang, K.; Estéve, D.; Alphonse, P.; Thailhades, P.; Vahlas, C. *J. Microelectromech. Syst.* **2007**, *16*, 919-931.

[1-7] Yetter, R. A.; Risha, G. A.; Son, S. F. *Proc*. *Combust*. *Inst*. **2009**, *32*, 1819-1838.

[1-8] Piercey, D. G.; Klapötke, T. M. *Central Europ. J. Energ. Mat.* **2010**, *7*, 115-129.

[1-9] Martirosyan, K. S. *J. Mater. Chem.* **2011**, *21*, 9400-9405.

[1-10] Rossi, C.; Estéve, A.; Vashishta, P. *J. Phys. Chem. Solids* **2010**, *71*, 57-58.

[1-11] Zachariah, M. R. *Propellants Explos*. *Pyrotech*. **2013**, *38*, 7.

[1-12] Kim, S. H.; Zachariah, M. R. *Adv. Mater.* **2004**, *16*, 1821-1825.

[1-13] Malchi, J. Y.; Foley, T. J.; Yetter, R. A. *ACS Appl. Mater. Interfaces* **2009**, *1*, 2420-2423.

[1-14] Shende, R.; Subramanian, S.; Hasan, S.; Apperson, S.; Thiruvengadathan, R.; Gangopadhyay, K.; Gangopadhyay, S.; Redner, P.; Kapoor, D.; Nicolich, S.; Balas, W. *Propellants Explos. Pyrotech.* **2008**, *33*, 122-130.

[1-15] Séverac, F.; Alphonse, P.; Estève, A.; Bancaud, A.; Rossi, C. *Adv. Funct. Mater.* **2012**, *22*, 323-329.

[1-16] Dunn, B.; Kamath, H.; Tarascon, J-M. *Science* **2011**, *334*, 928-935.

[1-17] Choi, N.S.; Chen, Z.H.; Freunberger, S.A.; Ji, X.L.; Sun, Y.K.; Amine, K.; Yushin, G.; Nazar, L.F.; Cho, J.; Bruce, P.G. *Angew. Chem. Int. Ed.* **2012**, *51*, 2-33.

[1-18] Poizot, P.; Laruelle, S.; Grugeon, S.; Dupont, L.; Tarascon, J-M. *Nature* **2000**, *407*, 496-499.

[1-19] Arico, A.S.; Bruce, P.; Scrosati, B.; Tarascon, J-M.; Schalkwijk, W.V. *Nature Mater.* **2005**, *4*, 366-377.

[1-20] Cabana, J.; Monconduit, L.; Larcher, D.; Rosa Palacin, M. *Adv. Mater.* **2010**, *22*, E170-E192.

[1-21] Zhang, Q.F.; Uchaker, E.; Candelaria, S.L.; Cao, G.Z. *Chem. Soc. Rev.* **2013**, *42*, 3127-3171.

[1-22] Wang, Z.Y.; Zhou, L.; Lou, X.W. *Adv. Mater.* **2012**, *24*, 1903-1911.

[1-23] Wu, H.B.; Chen, J.S.; Hng, H.H.; Lou, X.W. *Nanoscale* **2012**, *4*, 2526-2542.

[1-24] Reddy, M. V.; Subba Rao, G.V.; Chowdari, B.V.R. *Chem. Rev.* **2013**, *113*, 5364-5457.

[2-1] Vyazovkin, S.; Wight, C. A. *Annu. Rev. Phys. Chem.* **1997**, *48,* 125-149.

[2-2] Rossi, C.; Estéve, A.; Vashishta, P. *J. Phys. Chem. Solids* **2010**, *71*, 57-58.

[2-3] Jian, G. Q.; Zhao, Y.; Wu, Q.; Yang, L. J.; Wang, X. Z.; Hu Z. *J. Phys. Chem.C* **2013**, *117*, 7811-7817.

[2-4] White, D.R.; White, R.L. *J. Appl. Polym. Sci.* **2005**, *95*, 351-357.

[2-5] Pérez-Ramírez, J.; Mul, G.; Kapteijn, F.; Moulijn, J. A. *J. Mater. Chem*. **2001**, *11*, 821-830.

[2-6] Pérez-Ramírez, J.; Abelló, S.; Van der Pers, N. M. *Chem. Eur. J.* **2007**, *13*, 870-878.

[2-7] Beattie, S. D.; Setthanan, U.; McGrady, G. S. *Int. J. Hydrogen Energy* **2011**, *36*, 6014-6021.

[2-8] Xu, D. G.; Yang, Y.; Cheng, H.; Li, Y. Y.; Zhang, K. L. *Combust. Flame* **2012**, *159*, 2202-2209.

[2-9] Puszynski, J.A. *J. Therm. Anal .Calorim.* **2009***, 96*, 677-685.

[2-10] Moore, D. S.; Son, S.F.; Asay, B. W. *Propellants Explos. Pyrotech.* **2004,** *29*, 106-111.

[2-11] Zamkov, M.A.; Conner, R.W.; Dlott, D.D. *J. Phys. Chem. C* **2007**, *111,* 10278-10284.

[2-12] Granier, J.J.; Pantoya, M.L. *Combust. Flame* **2004**, *138*, 373-383.

[2-13] Brill, T.B.; Brush, P.J.; James, K.J.; Shepherd, J.E.; Pfeiffer, K.J. *Appl. Spectros.* **1992**, *46*, 900-911.

[2-14] Brill, T.B.; Ramanathan, H. *Combust. Flame* **2000**, 122, 165-171.

[2-15] Brill, T.B.; Arisawa, H.; Brush, P. J.; Gongwer, P. E.; Williams, G. K. *J. Phys.Chem.* **1995**, *99*, 1384-1392.

[2-16] Zhou, L.; Piekiel, N.; Chowdhury, S.; Zachariah, M. R. *Rapid Commun*. *Mass Spectrom*. **2009**, *23*, 194-202.

[2-17] Zhou, L.; Piekiel, N.; Chowdhury, S.; Zachariah, M. R. *J. Phys*. *Chem*. *C* **2010**, *114*, 14269-14275.

[2-18] Jian, G.Q.; Piekiel, N.W.; Zachariah, M.R. *J. Phys. Chem. C* **2012**, *116*, 26881-26887.

[2-19] Jian, G.Q.; Chowdhury, S.; Sullivan, K.; Zachariah, M.R. *Combust*. *Flame* **2013**, *160*, 432-437.

[2-20] Childs, P. R. N. *Practical Temperature Measurement,* Butterworth Heinemann: London, **2001**.

[2-21] Chowdhury, S. Ph.D. Dissertation, *University of Maryland*, **2012**.

[2-22] Young, G.; Jian, G.Q.; Jacob, R.; Zachariah, M.R. to be submitted.

[2-23] Sullivan, K.T.; Piekiel, N.W.; Wu, C.; Chowdhury, S.; Kelly, S.T.; Hufnagel, T.C.; Fezzaa, K.; Zachariah, M.R. *Combust. Flame* **2012**, *159*, 2-15.

[2-24] Wang, Y.J.; Liu, X.; Im, K-S.; Lee, W-K.; Wang, J.; Fezzaa, K.; Hung, D.L.S.; Winkelman, J.R. *Nature Phys.* **2008**, *4*, 305-309.

[2-25] Sullivan, K. T.; Chiou, W. A.; Fiore, R.; Zachariah, M. R. *Appl. Phys. Lett.* **2010**, *97*, 133104-1-3.

[2-26] Kim, J.S.; LaGrange, T.; Reed, B.W.; Taheri, M.L.; Armstrong, M.R.; King, W.E.; Browning, N.D.; Campbell, G.H. *Science* **2008**, 321, 1472-1475.

[2-27] Egan, G. C.; Sullivan, K.T.; LaGrange, T.; Reed, B. W.; Zachariah, M. R. *J. App. Phys.* **2014**, 115, 084903.

[2-28] Sullivan, K.; Zachariah, M.R. *J. Propul. Powe*r **2010**, *26*, 467-472.

[3-1] Yetter, R. A.; Risha, G. A.; Son, S. F. *Proc. Combust. Inst.* **2009**, *32*, 1819-1838.

[3-2] Dreizin, E. L. *Prog. Energy Combust. Sci.* **2009**, *35*, 141-167.

[3-3] Wen, D. S. *Energy Environ. Sci.* **2010**, *3*, 591-600.

[3-4] Trunov, M. A.; Schoenitz, M.; Dreizin , E. L. *Combust. Theor. Model.* **2006**, *10*, 603-623.

[3-5] Firmansyah, D. A.; Sullivan, K.; Lee, K. S.; Kim, Y. H.; Zahaf, R.; Zachariah, M. R.; Lee, D. G. *J. Phys. Chem. C* **2012**, *116*, 404-411.

[3-6] Granier, J. J.; Pantoya, M. L. *Combust. Flame* **2004**, *138*, 373-383.

[3-7] Huang, Y.; Risha, G. A.; Yang, V.; Yetter, R. A. *Combust. Flame* **2009**,*156*, 5-13.

[3-8] Rai, A.; Park, K.; Zhou, L.; Zachariah, M. R. *Combust. Theor. Model* **2006**, *10 (5)*, 843-859.

[3-9] Chowdhury, S.; Sullivan, K.; Piekiel, N.; Zhou, L.; Zachariah, M. R. *J. Phys. Chem. C* **2010**, *114*, 9191-9195.

[3-10] Levitas, V. I.; Asay, B. W.; Son, S. F.; Pantoya, M. *Appl. Phys. Lett.* **2006**, *89*, 071909-1-3.

[3-11] Levitas, V. I.; Asay, B. W.; Son, S. F.; Pantoya, M. *J. Appl. Phys.* **2007**, *101*, 083524-1-20.

[3-12] Levitas, V. I.; Pantoya, M. L.; Dikici, B. *Appl. Phys. Lett.* **2008**, *92*, 011921-1-3.

[3-13] Zhou, L.; Piekiel, N.; Chowdhury, S.; Zachariah, M. R. *Rapid Commun. Mass Spectrom.* **2009**, *23*, 194-202.

[3-14] Zhou, L.; Piekiel, N.; Chowdhury, S.; Lee, D. G.; Zachariah, M. R. *J. Appl. Phys.* **2009**, *106*, 083306-1-8.

[3-15] Childs, P. R. N. *Practical Temperature Measurement,* Butterworth Heinemann: London, **2001**.

[3-16] Wimber, R.T.; Halvorson, J.J. *Journal of Materials, JMLSA* **1972**, *7*, 564-567.

[3-17] Hilpert, K. *Rapid Commun. Mass Spec.* **1991**, *5*, 175-187.

[3-18] Deutsch, H.; Hilpert, K.; Becker, K.; Probst, M.; Märk, T. D. *J. Appl. Phys.* **2001**, *89*, 1915-1-7.

[3-19] Drowart, J.; Chatillon, C.; Hastie, J.; Bonnell, D. *Pure Appl. Chem.* **2005**, *77*, 683-737.

[3-20] Chervonnyi, A. D. *Russ. J. Inorg. Chem.,* **2010**, *55*, 556-559.

[3-21] Zhou, L.; Piekiel, N.; Chowdhury, S.; Zachariah, M. R. *J. Phys. Chem. C* **2010**, *114*, 14269-14275.

[3-22] Sullivan, K. T.; Chiou, W. A.; Fiore, R.; Zachariah, M. R. *Appl. Phys. Lett.* **2010**, *97*, 133104-1-3.

[3-23] Chakraborty, P.; Zachariah, M. R. *Combust. Flame* **2013**, DOI: 10.1016/j.combustflame.2013.10.017.

[3-24] McHale, J. M.; Auroux, A.; Perrotta, A. J.; Navrotsky, A. *Science*, **1997**, *277*, 788-791.

[3-25] Sullivan, K. T.; Piekiel, N. W.; Wu, C.; Chowdhury, S.; Kelly, S. T.; Hufnagel, T. C.; Fezzaa, K.; Zachariah, M. R. *Combust. Flame* **2012**, *159*, 2-15.

[3-26] Henz, B. J.; Hawa, T.; Zachariah, M. R. *J. Appl. Phys.* **2010**, *107*, 024901-1-9.

[3-27] Yuasa, S.; Zhu, Y. X.; Sogo, S. *Combust. Flame* **1997**, *108*, 387-396.

[3-28] Pangilinan, G. I.; Russell, T. P. *J. Chem. Phys.* **1999**, *111*, 445-448.

[3-29] Wang, S. F.; Yang, Y. Q.; Sun, Z. Y.; Dlott, D. D. *Chem. Phys. Lett.* **2003**, *368*, 189-194.

[3-30] Moore, D. S.; Son, S. F.; Asay, B. W. *Propellants Explos. Pyrotech.* **2004,** *29*, 106-111.

[3-31] Piehler, T. N.; DeLucia, F. C.; Munson, C. A.; Homan, B. E.; Miziolek, A. W.; McNesby, K. L. *Appl. Opt.*. **2005**, *44*, 3654-3660.

[3-32] Lynch, P.; Fiore, G.; Krier, H.; Glumac, N. *Combust. Sci. and Tech.* **2010**, *182*, 842-857.

[3-33] Goroshin, S.; Mamen, J.; Higgins, A.; Bazyn, T.; Glumac, N.; Krier, H. *Proc. Combust. Inst.* **2007**, *31*, 2011-2019.

[3-34] Wang, W. Q.; Clark, R.; Nakano, A.; Kalia, R. K.; Vashishta, P. *Appl. Phys. Lett.* **2010**, *96*, 181906-1-3.

[3-35] Campbell, T. J.; Aral, C.; Ogata, S.; Kalia, R. K.; Nakano, A.; Vashishta, P. *Phy. Rev. B* **2005**, *71*, 205413-1-14.

[3-36] Puri, P.; Yang, V. *J Nanopart Res*. **2010**, *12*, 2989-3002.

[3-37] Wang, W. Q.; Clark, R.; Nakano, A.; Kalia, R. K.; Vashishta, P. *Appl. Phys. Lett.* **2009**, *95*, 261901-1-3.

[3-38] Kim, Y. K.; Irikura, K.K.; Rudd, M.E.; Ali, M.A.; Stone, P.M.; Chang, J.; Coursey, J.S.; Dragoset, R. A.; Kishore, A. R.; Olsen, K. J.; Sansonetti, A. M.; Wiersma, G. G.; Zucker, D. S.; Zucker, M. A. NIST Electron-Impact Cross Section Database, http://physics.nist.gov/PhysRefData/Ionization/molTable.html (accessed January 16, 2014).

[4-1] Cho, P.; Mattisson, T.; Lyngfelt, A. *Fuel* **2004**, *83*, 1215-1225.

[4-2] Dreizin, E. L. *Prog. Energy Combust. Sci.* **2009**, *35*, 141-167.

[4-3] Steinfeld, A. *Solar Energy* **2005**, *78*, 603-615.

[4-4] Vyazovkin, S.; Wight, C.A. *Annu*. *Rev*. *Phys*. *Chem*. **1997**, *48*, 125-149.

[4-5] Vyazovkin, S. *Int*. *Rev*. *Phys*. *Chem*. **2000**, *19*, 45-60.

[4-6] Zhou, L.; Piekiel, N.; Chowdhury, S.; Zachariah, M. R. *Rapid Commun. Mass Spectrom.* **2009**, 23, 194-202.

[4-7] Zhou, L.; Piekiel, N.; Chowdhury, S.; Zachariah, M. R. *J. Phys*. *Chem*. *C* **2010**, *114*, 14269-14275.

[4-8] Jian, G.Q.; Piekiel, N.W.; Zachariah, M.R. *J. Phys. Chem. C* **2012**, *116*, 26881-26887.

[4-9] Jian, G.Q.; Chowdhury, S.; Sullivan, K.; Zachariah, M.R. *Combust*. *Flame* **2013**, *160*, 432-437.

[4-10] Vyazovkin, S.; Goryachko, V.; Bogdanova, V.; Guslev, V. *Thermochim*. *Acta* **1993**, *215*, 325-328.

[4-11] Bonnet, E.; White, R.L. *Thermochim*. *Acta* **1998**, *311*, 81-86.

[4-12] White, D.R.; White, R.L. *J. Appl. Polym. Sci.* **2005**, *95*, 351-357.

[4-13] White, R.L. *Int. J. Mass Spectrom.* **2009**, *287*, 128-133.

[4-14] White, D.R.; White, R.L. *Appl. Spectrosc.* **2008**, *62*, 116-120.

[4-15] Ozawa, T. *Bull. Chem. Soc. Jpn.* **1965**, *38*, 1881-1886.

[4-16] Flynn, H.; Wall, L.A. *J. Res. Natl. Bur. Stand.* **1966**, *70A*, 487-523.

[4-17] Ozawa, T. *Thermochim. Acta* **1992**, *203*, 159-165.

[4-18] Vyazovkin, S.; Sbirrazzuoli, N. *Macromol. Rapid Commun.* **2006**, *27*, 1515-1532.

[4-19] Doyle, C. D. *J. Appl. Polym. Sci.* **1962**, *6*, 639-642.

[4-20] Roberts, H. S.; Smyth, F.H. *J. Am. Chem. Soc.* **1921**, *43*, 1061-1079.

[4-21] Galvita, V.V.; Poelman, H.; Rampelberg, G.; Schutter, B.D.; Detavenier, C.; Marin, G.B. *Catal. Lett.* **2012**, *142*, 959-968.

[4-22] Arjmand, M.; Keller, M.; Leion, H.; Mattisson, T.; Lyngfelt, A. *Energy Fuels* **2012**, *26*, 6528-6539.

[4-23] Tiernan, M.J.; Barnes, P.A.; Parkes, G.M.B. *J.Phys.Chem.B* **1999**, *103*, 338-345.

[4-24] Kim, J.Y.; Rodriguez, J.A.; Hanson, J.C.; Frenkel, A.I.; Lee, P.L. *J. Am. Chem. Soc.* **2003**, *125*, 10684-10692.

[4-25] Pineau, A.; Kanari, N.; Gaballah, I. *Thermochim. Acta* **2006**, *447*, 89-100.

[4-26] Chadda, D.; Ford, J.D.; Fahim, M.A. *Int. J. Energy Res.* **1989**, *13*, 63-73.

[4-27] Malinin, G.V.; Tolmachev, Y.M. *Russian Chemical Reviews* **1975**, *44*, 392-397.

[4-28] Malecki, A.; Prochowska-Klisch, B. *J. Therm. Anal.* **1994**, *41*, 1109-1117.

[4-29] Maciejewski, M. *J. Therm. Anal*. **1992**, *38*, 51-70.

[4-30] Vyazovkin, S. *Thermochim. Acta* **2003**, *397*, 269-271.

[4-31] Yue, L.H.; Shui, M.; Xu, Z.D. *Thermochim. Acta* **1999**, *335*, 121-126.

[4-32] Song, P.X.; Wen, D.S.; Guo, Z. X.; Korakianitis, T. *Phys. Chem. Chem. Phys.* **2008**, *10*, 5057–5065.

[4-33] Navrotsky, A.; Ma, C.C.; Lilova, K.; Birkner, N. *Science* **2010**, *330*, 199-201.

[4-34] Navrotsky, A. *ChemPhysChem* **2011**, *12*, 2207-2215.

[4-35] Piekiel, N.W.; Cavicchi, R.E.; Zachariah, M.R. *Thermochim. Acta* **2011**, *521*, 125-129.

[4-36] Choi, Y.; Jung, M.; Lee, Y.K. *Electrochem. Solid-State Lett.* **2009**, *12*, F17-F19.

[4-37] Fushimi, C.; Araki, K.; Yamaguchi, Y.; Tsutsumi, A. *Ind. Eng. Chem. Res.* **2003**, *42*, 3922-3928.

[4-38] Chen, D.T.Y. *J. Therm. Anal.* **1975**, *7*, 61-64.

[4-39] Galwey, A.K.; Brown, M.E. *Thermal Decomposition of Ionic Solids, Volume 86: Chemical Properties and Reactivities of Ionic Crystalline Phases* (Studies in Physical and Theoretical Chemistry), Elsevier Science, **1999**, 1st edition.

[4-40] Bergermayer, W.; Schweiger, H.; Wimmer, E. *Phys.Rev.B* **2004**, *69*, 195409-1-12.

[4-41] Li, J.; Wang, S.Q.; Mayer, J.W.; Tu, K.N. *Phys. Rev. B* **1989**, *39*, 12367-12372.

[4-42] Li, J.; Mayer, J.W. *Mater. Chem. Phys.* **1992**, *32*, 1-24.

[4-43] Sullivan, K.T.; Piekiel, N.W.; Wu, C.; Chowdhury, S.; Kelly, S.T.; Hufnagel, T.C.; Fezzaa, K.; Zachariah, M.R. *Combust. Flame* **2012**, *159*, 2-15.

[4-44] Perinet, F.; Duigou, J.L.; Monty, C. *in Non-Stoichiometric Compounds Surfaces, Grain Boundaries and Structural Defects;* Nowotny, J.; Weppner, W., Ed.; Kluwer Academic Publishers: Boston, **1989**; Vol. *276*; p 387-397.

[4-45] Moore,W.J.; Selikson, B. *J. Chem. Phys.* **1951**, *19*, 1539-1543.

[4-46]Hill, C.G. *An Introduction to Chemical Engineering Kinetics and Reactor Design*, Wiley: **1977**.

[5-1] Lou, X.W.; Archer, L.A.; Yang, Z.C. *Adv. Mater.* **2008**, *20*, 3987-4019.

[5-2] Zhang, Q.; Wang, W. S.; Goebl, J.; Yin, Y. D. *Nano Today* **2009**, *4*, 494-507.

[5-3] Hu, J.; Chen, M.; Fang, X.S.; Wu, L.M. *Chem. Soc. Rev.* **2011**, *40*, 5472-5491.

[5-4] Liu, J.; Qiao, S.Z.; Chen, S.J.; Lou, X.W.; Xing, X.R.; Lu, G.Q. *Chem. Commun.* **2011**, *47*, 12578-12591.

[5-5] Lai, X. Y.; Halpert, J. E.; Wang, D. *Energy Environ. Sci.* **2012**, *5*, 5604-5618.

[5-6] Wang, Z.Y.; Zhou, L.; Lou, X.W. *Adv. Mater.* **2012***, 24,* 1903-1911.

[5-7] Lee, J.H. *Sens. Actuators, B* **2009***, 140,* 319-336.

[5-8] Yin, Y.D.; Rioux, R.M.; Erdonmez, C.K.; Hughes, S.; Somorjai, G.A.; Alivisatos, A.P. *Science* **2004,** 304, 711-714.

[5-9] Railsback, J.G.; Johnston-Peck, A.C.; Wang, J.W.; Tracy, J.B. *ACS Nano* **2010**, 4, 1913-1920.

[5-10] Yang, H.G.; Zeng, H.C. *J. Phys. Chem. B* **2004**, *108*, 3492-3495.

[5-11] Lou, X.W.; Wang, Y.; Yuan, C.; Lee, J.Y.; Archer, L.A. *Adv. Mater.* **2006**, *18*, 2325-2329.

[5-12] Kruis, F.E.; Fissan, H.; Peled, A. *J. Aerosol Sci.* **1998**, *29*, 511-535.

[5-13] Mariotti, D.; Sankaran, R.M. *J. Phys. D: Appl. Phys.* **2010** *43,* 323001-21.

[5-14] Schimmoeller, B.; Pratsinis, S.E.; Baiker, A. *ChemCatChem* **2011**, *3*, 1234-1256.

[5-15] Okuyama, K.; Lengoro, I.W. *Chem. Eng.Sci.* **2003**, 58, 537-547.

[5-16] Boissiere, C.; Grosso, D.; Chaumonnot, A.; Nicole, L.; Sanchez, C. *Adv. Mater.* **2011***, 23,* 599-623.

[5-17] Dreizin, E.L. *Prog. Energy Combust. Sci.* **2009**, *35*, 141-167.

[5-18] Piercey, D.G.; Klapötke, T.M. *Central Europ. J. Energ. Mat.* **2010**, *7*, 115-129.

[5-19] Rossi, C.; Zhang, K.; Estéve, D.; Alphonse, P.; Thailhades, P.; Vahlas, C. *J. Microelectromech. Syst.* **2007**, *16*, 919-931.

[5-20] Aumann, C. E.; Skofronick, G. L.; Martin, J. A. *J. Vac. Sci. Technol. B,Microelectron. Process. Phenom.* **1995**, *13*, 1178-1183.

[5-21] Kim, S. H.; Zachariah, M. R. *Adv. Mater.* **2004**, *16*, 1821-1825.

[5-22] Malchi, J. Y.; Foley, T. J.; Yetter, R. A. *ACS Appl. Mater. Interfaces* **2009**, *1*, 2420-2423.

[5-23] Shende, R.; Subramanian, S.; Hasan, S.; Apperson, S.; Thiruvengadathan, R.; Gangopadhyay, K.; Gangopadhyay, S.; Redner, P.; Kapoor, D.; Nicolich, S.; Balas, W. *Propellants, Explos., Pyrotech.* **2008**, *33*, 122-130.

[5-24] Séverac, F.; Alphonse, P.; Estève, A.; Bancaud, A.; Rossi, C. *Adv. Funct. Mater.* **2012**, *22*, 323-329.

[5-25] Martirosyan, K.S. *J. Mater. Chem.* **2011**, *21*, 9400-9405.

[5-26] Zhou, L.; Piekiel, N.; Chowdhury, S.; Zachariah, M.R. *J. Phys. Chem. C* **2010**, *114*, 14269-14275.

[5-27] Sullivan, K.; Zachariah, M. R. *J. Propul. Power* **2010***, 26,* 467-472.

[5-28] Amarilla, J. M.; Rojas, R. M.; Rojo, J. M. *J. Power Sources* **2011**, *196*, 5951-5959.

[5-29] Prakash, A.; McCormick, A.V.; Zachariah, M.R *Adv. Mater.* **2005**, *17*, 900-903.

[5-30] Wu, C.W.; Sullivan, K.; Chowdhury, S.; Jian, G.Q.; Zhou, L.; Zachariah, M.R. *Adv. Funct. Mater.* **2012**, *22*, 78-85.

[5-31] Navrotsky, A.; Ma, C.C.; Lilova, K.; Birkner, N. *Science*, **2010**, *330*, 199-201.

[5-32] Jian, G.Q.; Zhou, L. Piekiel, N.; Zachariah, M.R. Probing Oxygen Release Kinetics of Nanosized Metal Oxides by Temperature-Jump Time of Flight Mass Spectrometry. Fall Meeting, the Eastern States Section of the Combustion Institute, Storrs, CT, Oct 9-12, **2011**.

[6-1] Aumann, C. E.; Skofronick, G. L.; Martin, J. A. *J. Vac. Sci. Technol. B* **1995**, *13*, 1178-1183.

[6-2] Rossi, C.; Estéve, A.; Vashishta, P. *J. Phys. Chem. Solids* **2010**, *71*, 57-58.

[6-3] Zachariah, M. R. *Propellants Explos. Pyrotech.* **2013**, *38*, 7.

[6-4] Piercey, D.G.; Klapötke, T.M. *Central Europ. J. Energ. Mat.* **2010**, *7*, 115-129.

[6-5] Rossi, C.; Zhang, K.; Estéve, D.; Alphonse, P.; Thailhades, P.; Vahlas, C. *J. Microelectromech. Syst.* **2007**, *16*, 919-931.

[6-6] Dreizin, E.L. *Prog. Energy Combust. Sci.* **2009**, *35*, 141-167.

[6-7] Martirosyan, K.S. *J. Mater. Chem.* **2011**, *21*, 9400-9405.

[6-8] Yetter, R.A.; Risha, G.A.; Son, S.F. *Proc. Combust. Inst.* **2009**, *32*, 1819-1838.

[6-9] Yen, N.H.; Wang, L.Y. *Propellants Explos. Pyrotech.* **2012**, *37*, 143-155.

[6-10] Prakash, A.; McCormick, A.V.; Zachariah, M.R. *Adv. Mater.* **2005**, *17*, 900-903.

[6-11] Martirosyan, K.S.; Wang, L.; Luss, D. *Chem. Phys. Lett.* **2009**, *483*, 107-110.

[6-12] Becker, C.R.; Apperson, S.; Morris, C.J.; Gangopadhyay, S.; Currano, L.J.; Churaman, W.A.; Stoldt, C.R. *Nano Lett*. **2011**, *11*, 803-807.

[6-13] Plummer, A.; Kuznetsov, V.; Joyner, T.; Shapter, J.; Voelcker, N.H. *Small* **2011**, *7*, 3392-3398.

[6-14] Lide, D.R. *CRC Handbook of Chemistry and Physics*, 85th ed., CRC Press, Boca Raton, **2004**.

[6-15] Holleman, A.F.; Wiber, E.; Wiberg, N.*Inorganic Chemistry*, Academic Press, New York, **2001**, p. 465.

[6-16] Wu, C.W.; Sullivan, K.; Chowdhury, S.; Jian, G.Q.; Zhou, L.; Zachariah, M.R. *Adv*. *Funct*. *Mater*. **2012**, *22*, 78-85.

[6-17] Giles, J. *Nature* **2004**, *427*, 580-581.

[6-18] Fournier, E. W.; Brady, B. B. *J. Propul. Power* **2005**, *21*, 937-941.

[6-19] Steinhauser, G.; Klapötke, T.M. *Angew. Chem. Int. Ed.* **2008**, *47*, 3330-3347.

[6-20] Moretti, J. D.; Sabatini, J.J.; Chen, G. *Angew. Chem. Int. Ed.* **2012**, *51*, 6981-6983.

[6-21] Boissiere, C.; Grosso, D.; Chaumonnot, A.; Nicole, L.; Sanchez, C. *Adv. Mater.* **2011**, *23*, 599-623.

[6-22] Carne-Sanchez, A.; Imaz, I.; Cano-Sarabia, M.; Maspoch, D. *Nature Chem.* **2013**, *5*, 203-211.

[6-23] Zhou, L.; Piekiel, N.; Chowdhury, S.; Zachariah, M. R. *Rapid Commun. Mass Spectrom.* **2009**, *23*, 194-202.

[6-24] Jian, G.Q.; Piekiel, N.W.; Zachariah, M.R. *J. Phys. Chem. C* **2012**, *116*, 26881-2688.

[6-25] Sullivan, K.; Zachariah, M.R. *J. Propul. Powe*r **2010**, *26*, 467-472.

[6-26] Jian, G.Q.; Liu, L.; Zachariah, M.R. *Adv. Funct. Mater.* **2013**, *23*, 1341-1346.

[6-27] Bazyn, T.; Krier, H.; Glumac, N. *Combust. Flame* **2006**, *145*, 703-713.

[6-28] Jian, G.Q.; Chowdhury, S.; Sullivan, K.; Zachariah, M.R. *Combust. Flame* **2013**,*160*, 432-437.

[6-29] Muraleedharan, K.; Kannan, M.P.; Gangadevi, T. *J.Therm.Anal.Calorim.* **2010**, *100*, 177-181.

[6-30] Sullivan, K.T.; Piekiel, N.W.; Wu, C.; Chowdhury, S.; Kelly, S.T.; Hufnagel, T.C.; Fezzaa, K.; Zachariah, M.R. *Combust. Flame* **2012**, *159*, 2-15.

[6-31] Jian, G.Q.; Feng, J.Y.; Jacob, R. J.; Egan, G. C.; Zachariah, M.R. *Angew. Chem. Int. Ed.* **2013**, *52*, 9743-9746.

[6-32] NATO Standardization Agreement (STANAG) on Explosive, Friction Sensitivity Tests, No. 4487, 1st ed., August 22, **2002**.

[6-33] Technical Bulletin (TB) 700-2/Naval Sea Systems Command Instruction (NAVSEAINST) 8020.8B/Technical Order (TO) 11A-1-47/Defense Logistics Agency Regulations (DLAR) 8220.1, "Department of Defense Ammunition and Explosives Hazard Classification Procedures," January 5, **1998**.

[7-1] Sullivan, K. T.; Piekiel, N. W.; Chowdhury, S.; Wu, C.; Zachariah, M. R.; Johnson, C. E. *Combust. Sci. Tech.* **2011**, *183*, 285-302.

[7-2] Johnson, C.E.; Higa, K.T.; Albro, W.R. *Proceedings of the International Pyrotechnics Seminar.* **2008**.

[7-3] Clark, B.R.; Pantoya, M.L. *Phys. Chem. Chem. Phys.* **2010**, *12*, 12653-12657.

[7-4] Farley, C.; Pantoya, M. *J. Therm. Anal. Calorim.* **2010**, *102*, 609-613.

[7-5] Zhang, S.S.; Schoenitz, M.; Dreizin, E.L. *J. Phys. Chem. C* **2010**, *114*, 19653-19659.

[7-6] Martirosyan, K.S. *J. Mater. Chem.* **2011**, *21*, 9400-9405.

[7-7] Yetter, R.A.; Risha, G. A.; Son, S. F. *Proc. Combust. Inst*. **2009**, *32*, 1819-1838.

[7-8] Wen, D.S. *Energy Environ*. *Sci*. **2010**, *3*, 591-600.

[7-9] Sanders, V. E.; Asay, B. W.; Foley, T. J.; Tappan, B. C.; Pacheco, A. N.; Son, S. F. *J. Propul. Power* **2007**, *23*, 707-714.

[7-10] Dreizin, E. L. *Prog. Energy Combust. Sci.* **2009**, *35*, 141-167.

[7-11] Jian, G.Q.; Chowdhury, S.; Sullivan, K.; Zachariah, M.R. *Combust*. *Flame* **2013**, *160*, 432-437.

[7-12] Jian, G.Q.; Liu, L.; Zachariah, M.R. *Adv. Funct. Mater.* **2013**, *23*, 1341-1346.

[7-13] Prakash, A.; McCormick, A. V.; Zachariah, M. R. *Adv*. *Mater*. **2005**, *17*, 900-903.

[7-14] Wu, C.W.; Sullivan, K.; Chowdhury, S.; Jian, G.Q.; Zhou, L.; Zachariah, M. R. *Adv*. *Funct*. *Mater*. **2012**, *22*, 78-85.

[7-15] Wu, Z.Q.; Kalia, R. K.; Nakano, A.; Vashishta, P. *J. Chem. Phys.* **2011**, *134*, 204501-1-14..

[7-16] Martirosyan, K.S.; Wang, L.; Luss, D. *Chem*. *Phys*. *Lett*. **2009**, *483*, 107-110.

[7-17] Zhou, L.; Piekiel, N.; Chowdhury, S.; Zachariah, M. R. *Rapid Commun*. *Mass Spectrom*. **2009**, *23*, 194-202.

[7-18] Zhou, L.; Piekiel, N.; Chowdhury, S.; Lee, D.; Zachariah, M. R. *J. Appl. Phys.* **2009**, *106*, 083306-1-8.

[7-19] Sullivan, K.T.; Zachariah, M.R. *J. Propul. Power* **2009**, *26*, 467-472.

[7-20] Son, S.F.; Busse, J.R.; Asay, B.W.; Peterson, P.D.; Mang, J.T.; Bockmon, B.; Pantoya, M.L. *Proceedings of the International Pyrotechnics Seminar* **2002**, *29*, 203-210.

[7-21] Studier, M. H.; Huston, J. L. *J. Phys. Chem.* **1967**, *71*, 457-459.

[7-22] Fischer, A. *Acta Cryst.* **2005**, *E61*, i278-i279.

[7-23] Fischer, S.H.; Grubelich, M.C. *the 24th International Pyrotechnics Seminar*, Monterey, CA, July **1998**.

[7-24] Morones, J.R.; Elechiguerra, J.L.; Camacho, A.; Holt, K.; Kouri, J. B.; Ramírez, J. T.; Yacaman, M. J. *Nanotech*. **2005**, *16*, 2346-2353.

[7-25] Klaine, S.J.; Alvarez, P.J.J.; Batley, G. E.; Fernandes, T.F.; Handay, R. D.; Lyon, Y.; Mahendra, S.; Mclaughlin, M. J.; Lead, J. R. *Environ. Toxicol. Chem.* **2008**, *27*, 1825-1851.

[8-1] Arkhipov, V. A.; Korotkikh, A. G. *Combust. Flame* **2012**, *159*, 409-415.

[8-2] Sadeghipour, S.; Ghaderian, J.; Wahid, M. A. *4th International Meeting of Advances in Thermofluids*, Melaka, Malaysia, Oct 3-4, **2011**.

[8-3] Bocanegra, P. E.; Chauveau, C.; Gökalp, I. *Aerosp. Sci. Technol.* 2007, 11, 33-38.

[8-4] Dreizin, E. L. *Prog. Energy Combust. Sci.* **2009**, *35*, 141-167.

[8-5] Mench, M. M.; Yeh, C. L.; Kuo, K. K. *29th International Annual Conference of ICT*, Inst. Chemische Technologie, **1998**.

[8-6] Dokhan, A.; Price, E. W.; Seitzman, J. M.; Sigman, R. K. *Proc. Combust. Inst.* **2002**, *29*, 2939-2946.

[8-7] Armstrong, R. W.; Baschung, B.; Booth, D. W.; Samirant, M. *Nano Lett.* **2003**, *3*, 253-255.

[8-8] Meda, L.; Marra, G.; Galfetti, L.; Inchingalo, S.; Severini, F.; Luca, L.T.D.; *Compos. Sci. Technol.* **2005**, *65*, 769-773.

[8-9] Galfetti, L.; Luca, L.T.D.; Severini, F.; Meda, L.; Marra, G.; Marchetti, M.; Regi, M.; Bellucci, S. *J. Phys.: Condens. Matter* **2006**, *18*, S1991-S2005.

[8-10] Huang, Z. M.; Zhang, Y. Z.; Kotaki, M.; Ramakrishna, S. *Compos. Sci. Technol.* **2003**, *63*, 2223-2253.

[8-11] Li, D.; Xia, Y.N. *Adv. Mater.* **2004**, *16*, 1151-1170.

[8-12] Greiner, A.; Wendorff, J. H. *Angew. Chem. Int. Ed.* **2007**, *46*, 5670-5703.

[8-13] Luo, C. J.; Stoyanov, S.D.; Stride, E.; Pelan, E.; Edirisinghe, M. *Chem. Soc. Rev.* **2012**,*41*,4708-4735.

[8-14] Sovizi, M. R.; Hajimirsadeghi, S. S.; Naderizadeh, B. *J. Hazard. Mater.* **2009**, *168*, 1134-1139.

[8-15] Xie, L.; Shao, Z. Q.; Wang, W. J.; Wang, F. J. *Integr. Ferroelectr.* **2011**, *127*, 184-192.

[8-16] Kim, S. H.; Zachariah, M. R. *Adv. Mater.* **2004**, *16*, 1821-1825.

[8-17] Malchi, J. Y.; Foley, T. J.; Yetter, R. A. *ACS Appl. Mater. Interfaces* **2009**, *1*, 2420-2423.

[8-18] Séverac, F.; Alphonse, P.; Estève, A.; Bancaud, A.; Rossi, C. *Adv. Funct. Mater.* **2012**, *22*, 323-329.

[8-19] Jian, G.Q.; Liu, L.; Zachariah, M.R. *Adv. Funct. Mater.* **2013**, *23*, 1341-1346.

[8-20] Zhang, D.; Karki, A. B.; Rutman, D.; Young, D. P.; Wang, A.; Cocke, D.; Ho, T. H.; Guo, Z.H. *Polymer* **2009**, *50*, 4189-4198.

[9-1] Dunn, B.; Kamath, H.; Tarascon, J-M. *Science* **2011**, *334*, 928-935.

[9-2] Choi, N.S.; Chen, Z.H.; Freunberger, S.A.; Ji, X.L.; Sun, Y.K.; Amine, K.; Yushin, G.; Nazar, L.F.; Cho, J.; Bruce, P.G. *Angew. Chem. Int. Ed.* **2012**, *51*, 2-33.

[9-3] Kim, M.G.; Cho, J. *Adv. Funct. Mater.* **2009**, *19*, 1497-1514.

[9-4] Poizot, P.; Laruelle, S.; Grugeon, S.; Dupont, L.; Tarascon, J-M. *Nature* **2000**, *407*, 496-499.

[9-5] Reddy, M. V.; Subba Rao, G. V.; Chowdari, B. V. R. *Chem. Rev.* **2013**, *113*, 5364-5457.

[9-6] Lou, X.W.; Deng, D.; Lee, J.Y.; Feng, J.; Archer, L.A. *Adv. Mater*. **2008**, *20*, 258-262.

[9-7] Li, Y.G.; Tan, B.; Wu, Y.Y. *Nano Lett*. **2008**, *8*, 265-270.

[9-8]Yang , X.Y.; Fan ,K.C.; Zhu, Y.H.; Shen, J.H.; Jiang, X.; Zhao, P.; Luan, S.R.; Li, C.Z. *ACS Appl. Mater. Interfaces* **2013**, *5*, 997-1002.

[9-9] Luo, W.; Hu, X.L.; Sun, Y.M.; Huang, Y.H. *ACS Appl. Mater. Interfaces* **2013**, *5*, 1997-2003

[9-10] Nayak, S.; Malik, S.; Indris, S.; Reedijk, J.; Powell, A.K. *Chem. Eur. J.* **2010**, *16*, 1158-1162.

[9-11] Guo, J.C.; Liu, Q.; Wang, C.S.; Zachariah, M.R. *Adv. Funct. Mater.* **2012**, *22*, 803-811.

[9-12] Xia, H.; Lai, M.O.; Lu, L. *J. Mater. Chem.* **2010**, *20*, 6896-6902.

[9-13] Chae, C.; Kim, J.H.; Kim, J.M.; Sun, Y.K.; Lee, J.K. *J. Mater. Chem.* **2012**, *22*, 17870-17877.

[9-14] Pasero, D.; Reeves, N.; West, A.R. *J. Power Sources* **2005**, *141,* 156-158.

[9-15] Fan Q.; Whittingham, M.S. *Electrochem. Solid-State Lett.* **2007**, *10*, A48-A51.

[9-16] Wang, C.B.; Yin, L.W.; Xiang, D.; Qi, Y.X. *ACS Appl. Mater. Interfaces* **2012**, *4*, 1636-1642.

[9-17] Wang, H.L.; Cui, L.F.; Yang, Y.; Casalongue, H.S.; Robinson, J.T.; Liang, Y.Y.; Cui, Y.; Dai, H.J. *J. Am. Chem. Soc.* **2010**, *132*, 13978-13980.

[9-18] Liu, S.Y.; Xie, J.; Zheng, Y.X.; Cao, G.S.; Zhu, T.J.; Zhao, X.B. *Electrochim. Acta* **2012**, *66*, 271-278.

[9-19] Li, L.; Guo, Z.P.; Du, A.J.; Liu, H.K. *J. Mater. Chem.* **2012**, *22*, 3600-3605.

[9-20] Lavoie, N.; Malenfant, P.R.L.; Courtel, F.M.; Abu-Lebdeh, Y.; Davidson, I.J. *J. Power Sources* **2012**, *213*, 249-254.

[9-21] Wang, Z.H.; Yuan, L.X.; Shao, Q.G.; Huang, F.; Huang, Y.H. *Mater. Lett.* **2012**, *80*, 110-113.

[9-22] Bai, Z.C.; Fan, N.; Ju, Z.C.; Guo, C.L.; Qian, Y.T.; Tang, B.; Xiong, S.L. *J. Mater. Chem. A* **2013**, *1*, 10985-10990.

[9-23] Gao, J.; Lowe, M.A.; Abruna, H.D. *Chem. Mater.* **2011**, *23*, 3223-3227.

[9-24] Zheng, S.-F.; Hu, J.-S.; Zhong, L.-S.; Song, W.-G.; Wan, L.-J.; Guo, Y.-G. *Chem. Mater.* **2008,** *20,* 3617-3622.

[9-25] Ke, F.-S.; Huang, L.; Wei, G.-Z.; Xue, L.-J.; Li, J.-T.; Zhang, B.; Chen, S.-R.; Fan, X.-Y.; Sun, S.-G. *Electrochim. Acta* **2009**, *54,* 5825-5829.

[9-26] Park, J. C.; Kim, J.; Kwon, H.; Song, H. *Adv. Mater.* **2009**, *21*, 803-807.

[9-27] Wang, L.; Cheng, W.; Gong, H.; Wang, C.; Wang, D.; Tang, K.; Qian, Y. *J. Mater. Chem.* **2012**, *22,* 11297-11302.

[9-28] Ko, S.; Lee, J.; Yang, H. S.; Park, S; Jeong, U. *Adv. Mater.* **2012**, *24*, 4451-4456.

[9-29] Chen, L.B.; Lu, N.; Xu, C.M.; Yu, H.C.; Wang, T.H. *Electrochim.Acta* **2009**, *54,* 4198-4201.

[9-30] Xiang, J.Y.; Tu, J.P.; Zhang, J.; Zhong, J.; Zhang, D.; Cheng, J.P. *Electrochem. Commun.* **2010**, *12*, 1103-1107.

[9-31] Dar, M. A.; Nam, S. H.; Kim, Y. S.; Kim, W. B. *J. Solid State Electrochem.* **2010**, *14*, 1719-1726.

[9-32] Zhou, J.; Ma, L.; Song, H.; Wu, B.; Chen, X. *Electrochem. Commun.* **2011**, *13*, 1357-1360.

[9-33] Chen, X.; Zhang, N.; Sun, K. *J. Mater. Chem.* **2012**, *22*, 13637-13642.

[9-34] Wang, L.; Gong, H.; Wang, C.; Wang, D.; Tang, K.; Qian, Y. *Nanoscale* **2012**, *4*, 6850-6855.

[9-35] Lee, J.; Choi, S.; Park, S. *Chem. Asian J.* **2013**, *8,* 1377-1380.

[9-36] Lou, X.W.; Archer, L.A.; Yang, Z.C. *Adv. Mater.* **2008**, *20*, 3987-4019.

[9-37] Wang, Z.Y.; Zhou, L.; Lou, X.W. *Adv. Mater.* **2012**, *24*, 1903-1911.

[9-38] Lai, X.Y.; Halpert, J.E.; Wang, D. *Energy Environ. Sci.* **2012**, *5*, 5604-5618.

[9-39] Hu, J.; Chen, M.; Fang, X.S.; Wu, L.M. *Chem. Soc. Rev.* **2011**, *40*, 5472-5491.

[9-40] Okuyama, K.; Lenggoro, I.W. *Chem. Eng. Sci.* **2003**, *58*, 537-547.

[9-41] Boissiere, C.; Grosso, D.; Chaumonnot, A. *Adv. Mater.* **2011**, *23*, 599-623.

[9-42] Jian, G.Q.; Liu, L.; Zachariah, M.R. *Adv. Funct. Mater.* **2013**, *23*, 1341-1346.

[9-43] Stobbe, E.R.; Boer, B.A.d.; Geus, J.W. *Catal. Today* **1999**, *47*, 161-167.

[9-44] Chick, L.A.; Pederson, L.R.; Maupin, G.D.; Bates, J.L.; Thomas, L.E.; Exarhos, G.J. *Mater. Lett.* **1990**, *10*, 6-12.

[9-45] Mukasyan, A.S.; Epstein, P.; Dinka, P. *Proc. Combust. Inst.* **2007**, *31*, 1789-1795.

[9-46] Maier, J. *Solid State Ionics* **2002**, *148*, 367-374.

[9-47] Balaya, P.; Li, H.; Kienle, L.; Maier, J. *Adv. Funct. Mater.* **2003**, *13*, 621-625.

[9-48] Débart, A.; Dupont, L.; Poizot, P.; Leriche, J-B.; Tarascon, J. M. *J. Electrochem. Soc.* **2001**, *148*, A1266-A1274.

[9-49] Xu, Y. H.; Jian, G. Q.; Liu, Y. H.; Zhu, Y. J.; Zachariah, M. R.; Wang, C. S. *Nano Energy* **2014**, *3*, 26-35.

[9-50] Huang, X. H.; Wang, C. B.; Zhang, S. Y.; Zhou, F. *Electrochim. Acta* **2011**, *56*, 6752-6756.

[9-51] Xu, Y. H.; Guo, J. C.; Wang, C. S. *J. Mater. Chem.* **2012**, *22*, 9562-9567.

[9-52] Hassan, M. F.; Rahman, M.M.; Guo, Z. P.; Chen, Z. X.; Liu, H. K. *Electrochim. Acta* **2010**, *55*, 5006-5013.

[9-53] Grugeon, S.; Laruelle, S.; Dupont, L.; Tarascon, J.-M. *Solid State Sci.* **2008**, *5*, 895-904.

[9-54] Xiang, J. Y.; Tu, J. P.; Qiao, Y. Q.; Wang, X. L.; Zhong, J.; Zhang, D.; Gu, C. D. *J. Phys. Chem. C* **2011**, *115*, 2505-2513.

[10-1] Kasavajjula, U.; Wang, C. S.; Appleby, A. J. *J. Power Sources* **2007**, *163*, 1003-1039.

[10-2] Dunn, B.; Kamath, H.; Tarascon, J.-M. *Science* **2011**, *334*, 928-935.

[10-3] Yang, Z.; Zhang, J.; Kintner-Meyer, M. C. W.; Lu, X.; Choi, D.; Lemmon, J. P.; Liu, J. *Chem. Rev.* **2011**, *111*, 3577-3613.

[10-4] Dahn, J. R.; Zheng, T.; Liu, Y.; Xue, J. S. *Science* **1995**, *270*, 590-593.

[10-5] Dresselhaus, M. S.; Dresselhaus, G. *Adv. Phys.* **1981**, *30*, 139-326.

[10-6] Cabana, J.; Monconduit, L.; Larcher, D.; Palacín M. R. *Adv. Mater.* **2010**, *22*, E170-E192.

[10-7] Poizot, P.; Laruelle, S.; Grugeon, S.; Dupont, L.; Tarascon, J.-M. *Nature* **2000**, *407*, 496-499.

[10-8] Lou X. W.; Archer, L. A.; Yang Z. *Adv. Mater.* **2008**, *20*, 3987-4019.

[10-9] Aricò, A. S.; Bruce, P.; Scrosati, B.; Tarascon, J.-M.; Schalkwijk, W. V. *Nat. Mater.* **2005**, *4*, 366-377.

[10-10] Guo, Y.-G.; Hu, J.-S.; Wan, L.-J. *Adv. Mater.* **2008**, *20*, 2878-2887.

[10-11] Bruce, P.; Scrosati, B.; Tarascon, J.-M. *Angew. Chem. Int. Ed.* **2008**, *47*, 2930-2946.

[10-12] Song, M.-K.; Park, S.; Alamgir, F. M.; Cho, J.; Liu, M. *Mater. Sci. Eng. R* **2011**, *72*, 203-252.

[10-13] Larcher, D.; Masquelier, C.; Bonnin, D.; Chabre, Y.; Masson, V.; Leriche, J.-B.; Tarascon, J.-M. *J. Electrochem. Soc.* **2003**, *150*, A133-A139.

[10-14] Larcher, D.; Bonnin, D.; Cortes, R.; Rivals, I.; Personnaz, L.; Tarascon, J.-M. *J. Electrochem. Soc.* **2003**, *150*, A1643-A1650.

[10-15] Chen, J.; Xu, L.; Li, W.; Gou, X. *Adv. Mater.* **2005**, *17*, 582-586.

[10-16] Wang, Z.; Luan, D.; Madhavi, S.; Li, C. M.; Lou, X. W. *Chem. Commun.* **2011**, *47*, 8061-8063.

[10-17] Kang, N.; Park, J. H.; Choi, J.; Jin, J.; Chun, J.; Jung, I. G.; Jeong, J.; Park, J.-G.; Lee, S. M.; Kim, H. J.; Son, S. U. *Angew. Chem. Int. Ed.* **2012**, *51*, 6626-6630.

[10-18] Lin, Y.-M.; Abel. P. R.; Heller, A.; Mullins, C. B. *J. Phys. Chem. Lett.* **2011**, *2*, 2885-2891.

[10-19] Tartaj, P.; Amarilla, J. M. *J. Power Sources* **2011**, *196*, 2164-2170.

[10-20] Ortiz, G. F.; Hanzu, I.; Lavela, P.; Tirado, J. L.; Knauth, P.; Djenizian, T. *J. Mater. Chem.* **2010**, *20*, 4041-4046.

[10-21] Chaudhari, S.; Srinivasan, M. *J. Mater. Chem.* **2012**, *22*, 23049-23056.

[10-22] Kim, H. S.; Piao, Y.; Kang, S. H.; Hyeon, T.; Sung, Y. E. *Electrochem. Commun.* **2010**, *12*, 382-385.

[10-23] Zhou, J. S.; Song, H. H.; Chen, X. H.; Zhi, L. J.; Yang, S. Y.; Huo, J. P.; Yang, W. T. *Chem. Mater.* **2009**, *21*, 2935-2940.

[10-24] Zhong, J.; Cao, C.; Liu, Y.; Li, Y.; Khan, W. S. *Chem. Commun.* **2010**, *46*, 3869-3871.

[10-25] Chou, S.-L.; Wang, J.-Z.; Chen, Z.-X.; Liu, H.-K.; Dou, S.-X. *Nanotechnology* **2011**, *22*, 265401-1-5.

[10-26] Wang, B.; Chen, J. S.; Wu, H. B.; Wang, Z.; Lou, X. W. *J. Am. Chem. Soc.* **2011**, *133*, 17146-17148.

[10-27] Chen, J. S.; Zhu, T.; Yang, X. H.; Yang, H. G.; Lou, X. W. *J. Am. Chem. Soc.* **2010**, *132*, 13162-13164.

[10-28] Zhang, L.; Wu, H. B.; Madhavi, S.; Hng, H. H.; Lou, X. W. J *J. Am. Chem. Soc.* **2012**, *134*, 17388-17391.

[10-29] Koo, B.; Xiong, H.; Slater, M. D.; Prakapenka, V. B.; Podsiadlo, M. P.; Johnson, C. S.; Rajh, T.; Shevchenko, E. V. *Nano Lett.* **2012**, *12*, 2429-2435.

[10-30] Xu, X.; Cao, R.; Jeong, S.; Cho, J. *Nano Lett.* **2012**, *12*, 4988-4991.

[10-31] Ma, Y.; Ji, G.; Lee, J. Y. *J. Mater. Chem.* **2011**, *21*, 13009-13014.

[10-32] Han, Y.; Wang, Y.; Li, L.; Wang, Y.; Jiao, L.; Yuan, H.; Liu, S. *Electrochim. Acta* **2011**, *56*, 3175-3181.

[10-33] Zhang, J.; Sun, Y.; Yao, Y.; Huang, T.; Yu, A. *J. Power Source* **2013**, *222*, 59-65.

[10-34] Ang W. A.; Gupta N.; Prasanth, R.; Madhavi, S. *ACS Appl. Mater. Interfaces* **2012**, *4*, 7011-7019.

[10-35] Jia, X.; Chen, J.-J.; Xu, J.-H.; Shi, Y.-N.; Fan, Y.-Z.; Zheng, M.-S.; Dong, Q.-F. *Chem. Commun.* **2012**, *48*, 7410-7412.

[10-36] Ren, Y.; Armstrong, A. R.; Jiao, F.; Bruce, P. G. *J. Am. Chem. Soc.* **2010**, *132*, 996-1004.

[10-37] Jiao, F.; Bao, J.; Bruce, P. G. *Electrochem. Solid-State Lett.* **2007**, *10*, A264-A266.

[10-38] Ren, Y.; Ma, Z.; Bruce, P. G. *Chem. Soc. Rev.* **2012**, *41*, 4909-4927.

[10-39] Guo, J. C.; Liu, Q.; Wang, C.S.; Zachariah, M.R. *Adv. Funct. Mater.* **2012**, *22*, 803-811.

[10-40] Luo, J.-Y.; Zhang, J.-J.; Xia, Y.-Y. *Chem. Mater.* **2006**, *18*, 5618-5623.

[10-41]Shaju, K. M.; Jiao, F.; Débart, A.; Bruce, P. G. *Phys. Chem. Chem. Phys.* **2007**, *9*, 1837-1842.

[10-42] Li, Y.; Tan, B.; Wu, Y. *Nano Lett.* **2008**, *8*, 265-270.

[10-43] Dupont, L.; Laruelle, S.; Grugeon, S.; Dickinson, C.; Zhou, W.; Tarascon, J.-M. *J. Power Sources* **2008**, *175*, 502-509.

[10-44] Xu, Y. H.; Liu, Q.; Zhu, Y. J.; Liu, Y. H.; Langrock, A.; Zachariah, M. R.; Wang, C. S. *Nano Lett.* **2013**, *13*, 470-474.

[10-45] Langrock, A.; Xu, Y. H.; Liu, Y. H.; Manivannan, A.; Wang, C. S. *J. Power Sources* **2013**, *223*, 62-67.

[10-46] Prakash, A.; McCormick, A. V.; Zachariah, M. R. *Chem. Mater.* **2004**, *16*, 1466-1471.

[10-47] Jian, G. Q.; Liu, L.; Zachariah, M. R. *Adv. Funct. Mater.* **2013**, *23*, 1341-1346.

[10-48] Yin, Y.; Hu, Y.; Wu, P.; Zhang, H.; Cai, C. *Chem. Commun.* **2012**, *48*, 2137-2139.

[10-49] Liu, Y.-L.; Xu, Y. H.; Han, X. G.; Pellegrinelli, C.; Zhu, Y. J.; Zhu, H. L.; Wan, J. Y.; Chung, A. C.; Vaaland, O.; Wang, C. S.; Hu, L. B. *Nano Lett.* **2012***, 12,* 5664-5668.

[10-50] Chan, C.; Peng, H.; Liu, G.; McIlwrath, K.; Zhang, X. F.; Huggins, R. A.; Cui, Y. *Nat. Nanotechnol.* **2008**, *3*, 31-35.

[10-51] Chou, S.-L.; Wang, J.-Z.; Wexler, D.; Konstantinov, K.; Zhong, C.; Liu, H.-K.; Dou, S.-X. *J. Mater. Chem.* **2010**, *20*, 2092-2098.

[10-52] Zhu, X.; Zhu, Y.; Murali, S.; Stoller, M. D.; Ruoff, R. S. *ACS Nano* **2011**, *4*, 3333-3338.

[10-53] Yu, W.-J.; Hou, P.-X.; Li, F.; Liu, C. *J. Mater. Chem.* **2012**, *22*, 13756-13763.

[11-1] Yi, F.; LaVan, D.A. *Thermochim. Acta* **2013**, *569*, 1-7.

[11-2] Jian, G.Q.; Chowdhury, S.; Sullivan, K.; Zachariah, M.R. *Combust. Flame* **2013**, *160*, 432-437.

[11-3] Yabuuchi, N.; Kajiyama, M; Iwatate, J; Nishikawa, H; Hitomi, S; Okuyama, R.; Usui, R.; Yamada, Y.; Komaba, S. *Nature Mater.* **2012**, *11*, 512-517.

[11-4] Xu, J.T.; Dou, S.X.; Liu, H.K.; Dai, L.M. *Nano Energy* **2013**, *2*, 439-442.